Autonomous Underwater Vehicle Design Considering Energy Source Selection and Hydrodynamics.

by

Kieran Thomas Rutherford

A thesis
presented to the University of Southampton
in fulfilment of the thesis requirement
for an Engineering Doctorate

Southampton, United Kingdom

UNIVERSITY OF SOUTHAMPTON

ABSTRACT

FACULTY OF ENGINEERING, SCIENCE & MATHEMATICS

SCHOOL OF ENGINEERING SCIENCES

Engineering Doctorate

AUTONOMOUS UNDERWATER VEHICLE DESIGN CONSIDERING ENERGY SOURCE SELECTION AND HYDRODYNAMICS.

by Kieran Thomas Rutherford.

An autonomous underwater vehicle (AUV) is an unmanned submersible that carries out specific scientific, commercial or military missions without an umbilical connection to the surface. Fulfilment of its mission depends upon a clear appreciation of required payload, endurance, depth and speed.

AUVs are a continually developing technology. Many reviewed AUVs are of a similar shape and draw heavily on previous designs. The development of formal design methodology should encourage AUV development through increased understanding of the key decisions and the compromises necessary to meet AUV requirements. One area of improvement is AUV endurance.

AUV endurance is determined by the onboard energy capacity, the power required by operating subsystems and propulsion power to overcome hydrodynamic resistance. Greater endurance can be achieved by increasing the amount of energy stored or by decreasing the power draw.

Presented physical measurements confirm that a lithium polymer battery type is pressure tolerant. Utilisation of such batteries can reduce the required volume and mass of the AUV pressure vessel and for deep diving AUVs permit an increased energy source within the AUV. As a consequence of this research Autosub 6000 has incorporated pressure tolerant lithium polymer cells and can operate at greater depths than Autosub 3.

Computational investigations of AUV hull shapes allows simple truncated Taylor series based relationships to be developed linking drag force and hull shape geometric parameters. The empirical equations have been incorporated within the presented design method. Hence propulsion power of a candidate hull shape can be quickly estimated and compared against available AUV energy capacity.

The presented structured AUV design method encourages innovation by starting with a design procedure focused on fulfilling the mission specifications. The design method can explore such options as reducing pressure vessel volume, and create a hull shape based upon practical arrangements of the internal subsystems.

Acknowledgements.

I would like to express my thanks to all those who have provided help and encouragement throughout my work. Thanks to my supervisors, Prof. Gwyn Griffiths and Prof. Grant Hearn for their guidance, support and patience when presented with another half-written Chapter. In particular Gwyn for offering me the chance of a lifetime to travel aboard the RSS James Clark Ross into the Arctic circle and gain invaluable experience into the Autosub and ship work.

Thanks to all my friends and family for putting up with me during both the highs and lows of research work. Whether that be some useful advice on a particular problem, going for another coffee break or just letting me vent my thoughts.

My utmost thanks must go to Anne, who has been with me offering support and encouragement throughout. I am a better person for knowing her.

Table of Contents.

List of Figures.

List of Tables.

Nomenclature.

a	Elliptical minor axis
A_i	Area of the i^{th} panel.
Al - HP or Al - H_2O_2	Aluminium/ hydrogen peroxide
A_{Slice}	Area of cross-sectional slice in yz plane
b	Elliptical major axis
B	Buoyancy
C	M_E to M_{AUV} ratio
C_{12}	Short time constant capacitor
C_{DSa}	Coefficient of drag based on surface area
$C_{D\nabla}$	Volumetric coefficient of drag
C_F	Coefficient of friction
C_{Fi}	Coefficient of friction of the i^{th} panel.
C_{Long}	Long time constant capacitor
C_P	Coefficient of pressure
C_{Pi}	Coefficient of pressure of the i^{th} panel.
C_Θ	Cylindrical coefficient
E	Young's modulus
F	Faraday's constant
$F_{Induced}$	Induced drag
$F_{Pressure}$	Pressure force
$F_{Viscous}$	Viscous force
g	gravity = 9.81 ms^{-2}
H	Boundary layer shape factor
I_D	Discharging current
k	Hull shape form factor

K	Pressure vessel material constant
L_{AUV}	Length of AUV
L_{Bow}	Length of bow from leading edge of bow to middle body transition
L_{Foam}	Lever arm of foam buoyancy
L_{PVC}	Length of pressure vessel cylinder
m_i	First geometric input parameter of candidate hull shape
m_{Base}	First geometric input parameter of base hull shape
$Mass_{internalsystems}$	Mass of pressure sensitive subsystems to pack within pressure vessel
$Mass_{PV}$	Empty pressure vessel mass
M_{AUV}	AUV mass
M_B	Buoyancy mass
M_E	Energy mass
M_{Hotel}	Hotel mass
$M_{Payload}$	Payload mass
M_{Prop}	Propulsion mass
M_{PV}	Pressure vessel mass
$M_{Structure}$	Structure mass
M_x	Mass at point along x
n_i	Second geometric input parameter of candidate hull shape
n_i	Unit surface normal of A_i panel
n_{Base}	Second geometric input parameter of base hull shape
n_{Bow}	Power of bow curvature
p_i	Third geometric input parameter of candidate hull shape
p_{Base}	Third geometric input parameter of base hull shape
P_{Buckle}	Pressure vessel buckling pressure

$P_{Collapse}$	Pressure vessel collapse pressure
P_{Hotel}	Hotel electrical power
$P_{Payload}$	Payload electrical power
P_{Prop}	Propulsion electrical power
Q_0	Total charge a battery can hold
Q_r	Energy remaining within battery
Q_t	Energy extracted from battery
r_{PVi}	Inner pressure vessel radius
r_{PVo}	Outer pressure vessel radius
R	Universal gas constant
R_{01}	Instantaneous battery resistance
R_{12}	Short time constant resistor
Re	Reynold's number based on AUV length
Re_{Crit}	Critical Reynold's number for boundary layer transition
Re_S	Reynold's number based on profile length
Re_x	Reynold's number local to position x
Re_θ	Reynold's number based on θ
$Re_{\theta Palisupan}$	Reynold's number based on θ as found by Palisupan
Re_∇	Reynold's number based on cube root of AUV volume
R_{Long}	Long time constant resistor
R_{Max}	Maximum radius of hull shape
R_P	Battery self discharge resistance
R_{PV}	Pressure vessel radius
R_S	Radius of hull shape stern
s	Distance along the surface of hull shape profile
s_m	Lengthwise mesh density

S_F	Safety factor
Spe	Specific energy of battery
t	Pressure vessel wall thickness
t_m	Circumferential mesh density
T	Absolute temperature
u	Local velocity
U	Flow velocity at edge of boundary layer
U_∞	Flow velocity before disturbed by a body
v	Fluid viscosity
V	Unit vector in direction of local flow
V	Voltage
V_0	Voltage when on load
V_1	Voltage after instantaneous voltage rise
V_2	Voltage after gradual time dependant voltage rise
V_h	Battery voltage at half useful life
V_t	Terminal voltage
V_T	Total velocity vector
x	Lengthwise axis of hull shape
x_{crit}	Critical x distance for boundary layer transition
y	Radial axis of hull shape
z	Radial axis of hull shape
χ	Moment wake area
δ_{Lam}	Laminar boundary layer thickness
δ_{Turb}	Turbulent boundary layer thickness
ϕ	Battery specific constant
η_a	Anodic overpotential

η_c	Cathodic overpotential
η_{pt}	Efficiency of the power train
λ	Universal function in Thwaites laminar boundary layer
θ	Boundary layer momentum thickness
ρ_B	Density of buoyancy material
ρ_E	Energy gravimetric density
ρ_W	Water density
∇_B	Volume of buoyancy material
∇_E	Energy source volume
∇_{PV}	Pressure vessel displaced volume
∇_S	Hull shape volume
∇_{SS}	Volume of subsystems
σ_{yield}	Yield stress
υ	Poisson's ratio

Abbreviations.

ABE	Autonomous Benthic Explorer
ADCP	Acoustic Doppler current profiler
Ag - Zn	Silver – Zinc
Al - HP or Al - H_2O_2	Aluminium/ hydrogen peroxide
Aoa	Angle of attack.
ATUV	Advances of Technology for Underwater Vehicles
AUSI	Autonomous Undersea Systems Institute
AUV	Autonomous Underwater Vehicle
BMT	Bow to middle body transition for the parallel middle body hull shape.
CFD	Computational Fluid Dynamics
CFRP	Carbon Fibre Reinforced Plastic
CoB	Centre of buoyancy
CoG	Centre of gravity
CTD	Conductivity Temperature Depth
GFRP	Glass Fibre Reinforced Plastic
GPS	Global Positioning Satellite
ISE	International Submarine Engineering
ITTC	International towing tank conference
JaMSTeC	Japan Marine Science and Technology Centre
MIT	Massachusetts Institute of Technology
Mn - Al	Manganese Alkaline
MST	Middle body to stern transition for the parallel middle body hull shape
NACA	National Advisory Committee for Aeronautics

Ni - Cd	Nickel Cadmium
NOCS	National Oceanography Centre Southampton
OCV	Open Circuit Voltage
SAMS	Subsurface Autonomous Mapping System
SES	School of Engineering Sciences
SAUCE	Student Autonomous Underwater Challenge – Europe
SoC	Battery State of Charge
UUST	Unmanned Untethered Submersible Technology
VTB	Virtual Test Bed
WHOI	Woods Hole Oceanographic Institute

Chapter 1
Introduction.

An autonomous underwater vehicle (AUV) is an unmanned and untethered submersible that carries out specific scientific, commercial or military missions without umbilical based communication and power from the surface. The fulfilment of the mission requires a clear appreciation of its requirements on payload, range, depth and speed, and how these affect the necessary operational requirements of the AUV.

The National Oceanography Centre, Southampton (NOCS) designed and built the AUV Autosub. This Engineering Doctorate was sponsored by NOCS and the School of Engineering Sciences (SES) University of Southampton, thus enabling close observation and operational experience of Autosub and it is used as the basis for examples.

1.1 Problem statement.

One option to improve an AUV is to increase both endurance and diving depth. How can these goals be achieved and expressed in order to aid the initial AUV design? What are the conflicts between the energy carried onboard, the operational depth and the actual hull shape of the AUV?

1.2 Why this problem exists.

As of 2007, over 400 AUVs have been made. Of these, 156 were produced by Hydroid Inc (Newman, *et al.* 2007) as part of the Remus range and are scaled versions of the same AUV hull shape. Over half of the 400 existing AUVs weigh less than 100 kg and are restricted in payload and endurance. AUV technology is considered to be still in its infancy and is capable of more.

Another 500 AUVs are anticipated to be required over the next decade, though there is potential for the demand to be much higher (Newman, *et al.* 2007). To encourage this market to grow, AUV technology and capabilities must improve. One improvement is to increase the endurance of the AUV, allowing it to carry a greater payload or travel further.

AUV endurance is determined by the energy capacity carried onboard and the power draw of all subsystems. Greater endurance can be achieved by increasing the amount of energy stored or decreasing the power required by the subsystems. To increase the energy stored, the energy per unit mass (energy density, measured in Wh kg^{-1}) or the total mass of the energy source or both must be increased. Increasing the energy per unit mass requires a change in the type of energy source, and may have economic and design implications. Most AUVs have a neutral buoyancy condition, which limits vehicle mass to the mass of the water displaced. Increasing the size of

energy source will increase the mass and volume of the AUV. A larger AUV will have a larger drag force, requiring greater propulsion power and so use more energy unless hull shape refinement takes place.

Different AUV hull shapes of the same volume can experience different drag forces. Consequently hull shape and volume should both be considered when attempting to reduce AUV propulsion power. Additionally, the cruising velocity of the AUV will influence the propulsion power.

The conflict between increasing endurance, increasing vehicle volume and hull shape should be resolved as the AUV design evolves. Without a formal design methodology, an AUV design is usually driven by an engineer's personal experience, previously built AUVs and compatibility with existing systems. Therefore design innovation is hindered by uncertainty. As a consequence AUVs rarely deviate from known workable solutions. Options that become available through improved technology might be overlooked. For example, Autosub 6000's concept design was radically different from previous Autosub models and as a result of this research a new pressure tolerant energy source was adopted. However, the energy storage was retrofitted to Autosub 3's bow and stern to create Autosub 6000. Hull shape options made possible by the pressure tolerant energy source did not progress further than the adaptation of an existing design.

AUV designers are faced with the problem of how to create the hull shape and select an energy source for an AUV, whilst resolving any decision that will impact other areas of the design.

1.3 A specific proposed solution.

A structured design method is presented that creates a technically feasible concept AUV based upon a specific mission and seeks to reduce the influence of the existing base of AUVs. A structured design methodology would guide decisions, lend confidence to the results and encourage innovation. This allows an AUV to be created from a 'blank sheet' and focuses design on fulfilling the mission specifications. Innovation is encouraged by understanding the implication of decisions made in the design process. Two decisions, the energy source and hull shape, have been investigated in detail within this research.

The energy source can be made pressure tolerant and so not require protection by a pressure vessel. Pressure vessel mass increases with depth and becomes less buoyant (Griffiths, *et al.* 2004). Loss of buoyancy must be compensated by an increase in displaced volume to maintain neutral buoyancy. Consequently the AUV displaced volume will increase. Pressure tolerant

batteries will allow extra mass to be allocated to the energy source or payload, and provide greater flexibility regarding the hull shape.

The design methodology will determine the AUV hull shape by first investigating the arrangement of internal subsystems. The propulsion power of the candidate hull shape is quickly estimated and compared against AUV energy capacity. The concept design is evaluated against mission objectives and the design iterated to fulfil these objectives.

The creation of a design method, the potential for mass savings allowed through use of pressure tolerant batteries and an increased understanding of AUV hull shape upon hydrodynamic characteristics will all contribute to the improvement of AUV knowledge.

1.4 Research objectives.

The intended outcomes of this research are summarised in three primary objectives and the subsequent subsidiary tasks.

Primary Objective list:

I – Creation of a structured design methodology incorporating energy source and hull shape influences.

This objective will add guidelines and structure to the decision process of designing an AUV from an initial mission specification, by selection of an energy source and hull shape based on an increased understanding of both.

II – Improve the prediction of lithium polymer battery behaviour at high hydrostatic pressure.

This objective will provide improved estimations of energy use at an earlier design stage by characterising the battery voltage with the remaining battery capacity. Characterisation tests will include different pressure and temperature environments.

III - Investigate the hydrodynamic shape of rotationally symmetric AUV hull shapes to parameterise drag change with shape change.

From investigating AUV hull shapes and variants a relationship between drag force and hull shape might be found. This relationship will be expressed as guidelines or formulae that can be utilized by a design method.

These primary objectives are broken down to subsidiary tasks that guide the research and permit the consideration of alternative plans should conflicts arise.

Subsidiary questions encountered.

The design methodology is a very large area of research and needs to be limited to the provision of a workable tool within the time constraints of this research. It was anticipated there would be little structured design in place for an AUV. However this freedom was itself a problem - where to begin the process and how to break it into manageable work tasks? This was surmounted by restricting the design methodology to concept design and guidelines. There will be more than one unique approach to AUV design. The logic flow within the process should be well defined, and key decisions that would benefit from engineering experience will be discussed.

Objective I is now expanded to provide a list of related tasks to be addressed:

- Identify analytic equations that quantify AUV behaviour.
- Investigate the logic flow and identify key decisions.
- Create a constrained design method.
- Generate example missions and necessary subsystem packages.
- Test the design method with challenging case studies.

Expanding objective II gives a list of subsidiary tasks:

- Test a significant number of lithium polymer batteries at pressure to establish pressure tolerance.
- Establish a characterisation approach.
- Complete physical tests of batteries at pressure and low temperature and varying current.
- Quantify the affect of the environment on battery voltage.
- Suggest a method of utilising knowledge as a design tool.

The physical testing of the batteries is necessary to establish performance at pressure. If found not to be pressure tolerant then the research would concentrate on design cycle based on the use of a pressure sensitive energy source.

Objective III is expanded to give a list of tasks:

- Identify common AUV shapes.

- Model these shapes in panel code and verify the results.
- Generate likely shape variants and create drag predictions.
- Incorporate drag predictions into design methodology.

A computational approach was selected to model different AUV hull shapes and estimate drag force. Results are verified against published results for comparable hull shapes. A fluid boundary layer model was available that would simulate laminar and turbulent boundary layers. This level of modelling detail is required by the selected laminar flow hull shape.

Contingency plans included a simpler boundary layer model and the author of the computational potential method was available to offer valuable advice.

The success of these objectives and tasks will be discussed in the associated Chapters and summarised in the conclusions (Chapter 9).

1.5 Development of the presented research.

An understanding of the current state of AUV technology is needed in order to create the design process.

A selection of existing AUVs are described in Chapter 2, in particular their operational use, energy source carried, hull shape and vehicle size. The dominance of pressure sensitive batteries as an AUV energy source is shown. Pressure vessel mass is significant, especially when operating at deep depth. Mass savings are to be made by removing or downsizing the pressure vessel. A relationship between AUV mass and energy mass is established. Energy source types are then described, concentrating on energy density and practical concerns for each. A look at engineering design approaches follows and concludes that design is specific to the system, yet no complete design methodologies exist for AUVs. Furthermore, automated geometric shape packing techniques are not fully three dimensional and cannot accommodate the hydrostatic mass balance required for AUV stability. This review highlights the need to improve the design methodology of AUVs.

AUV hull shape design is heavily influenced by the need for a pressure vessel to protect pressure sensitive subsystems and energy source. Pressure vessels have a preferential cylindrical or spherical shape and the AUV hull shape is often an extension of this. There would be an increased number of options for the AUV hull shape should the pressure vessel be reduced in size or removed completely. Additionally the saved mass of the pressure vessel could be allocated to another subsystem or the total AUV mass reduced.

Having established the current technology, Chapter 3 considers the parameters that influence AUV endurance and the conflicts between them. It aids understanding of the balance within AUV design and identifies the energy source and hull shape as areas for research. The principal equations that estimate range are presented and then the parameters of velocity, volume, energy capacity and hull shape are discussed. This analysis illustrates how AUV endurance is controlled. The interdependencies of the design decisions are explored using design flow charts. These design logic flow charts form the skeleton of the proposed design method generated in Chapter 7.

In order to remove the pressure vessel the energy source must be made tolerant of pressure at AUV operation depth. Conducted practical experiments of pressurising lithium polymer batteries are described in Chapter 4. The test methodology is described in Doerffel's paper (Doerffel and Abu Sharkh 2004) and this is modified to suit the selected battery chemistry.

Measurements obtained in this research show the batteries are pressure tolerant at 6000 m depth and so confirm that reduction of the pressure vessel is physically possible. An industrial outcome of this work is that Autosub 6000 incorporated the pressure tolerant lithium polymer cells and can operate at greater depths than its predecessor.

Lithium polymer battery performance is established and expressed as an equivalent circuit in order to generate a battery model. The experiments included environmental temperature and power draw and the affects on equivalent circuit parameters are analysed. The battery model can predict the energy source voltage over the mission duration and contribute towards a fuel gauge. The fuel gauge is validated against Autosub 6000's energy source performance during a trial mission.

Removing the pressure vessel is established as an option, so research explores the implication on the hull shape. This requires understanding drag force variation with associated hull shape variation. A variety of axis-symmetric hull shapes are modelled using a potential theory based computational method. Chapter 5 summarises the program theory, two possible boundary layer models and the literature relevant to the shapes modelled. Three families of AUV hull shape are considered: a parallel middle body and two laminar flow shapes. The parallel middle body is based upon Autosub and is a common shape amongst existing AUVs. The laminar flow shape has a low drag by careful control of the boundary layer over the hull. This boundary layer flow constrains the hull shape, and so impacts upon the volume available for internal subsystems.

Chapter 6 provides the hydrodynamic results of the computational investigation. Within each hull shape family presented in turn are hull shape variant profile definitions and drag predictions resulting from differing boundary layer models at increasing velocities. The results are discussed

and guidelines generated for altering hull shape geometry parameters. These relationships are expressed by volumetric coefficient of drag as a function of input hull shape profile parameters. The hull shapes are compared against each other, and the application for a design method is discussed.

Chapter 7 brings the previous Chapters together through the creation of a formal design methodology. This method operates within boundary specifications drawn from the AUV mission. The required subsystems are arranged such that the AUV is hydrostatically balanced. Hull shape profile parameters are defined by the subsystem arrangement, enabling a quick estimate of drag. The required key decisions are highlighted and the automation of stages within the methodology is described.

Chapter 8 critically analyses the design method, showing its application and limitations. Two challenging AUV missions are described, along with an overview of required AUV payloads. The first mission requires an AUV to operate at high velocity, presenting a challenge to the AUV energy source. The second mission will create a deep diving AUV at a lower mass and greater endurance than existing AUVs. The design method is applied to each mission to produce a concept AUV.

Chapter 9 summarises the Thesis conclusions and contributions. The outcomes are compared to the research objectives. Future work and industrial applications are discussed.

The Appendices occur last. The first Appendix reproduces two publications that have resulted from this research. The first paper "*Energy storage for long endurance AUVs*" by Griffiths, G., J. Jamieson, S. Mitchel and K. Rutherford. (2004), is a result of the work within Chapter 2. The second paper "*Performance of Lithium-Polymer Cells at High Hydrostatic Pressure.*" by K. Rutherford, D. Doerffel (2005) is a result of the work in Chapter 4. Appendix B discusses pressure vessel design, volume and mass.

Appendix C summarises the least squares approximation for finding the battery internal resistance in Chapter 4. Appendix D provides an overview into hydrodynamic computational methods used in Chapters 5 and 6. Appendix E gives the Matlab code used in generating and filtering subsystem arrangements as created in Chapter 7.

Chapter 2
Literature review.

This Chapter summarises the key characteristics of existing AUVs, the different available and developing energy sources and AUV design methodology. Insight of the existing published state of technology and design is essential for providing a basis for this research to build upon. This background provides the motivation for improving AUV performance through a more structured design methodology.

Existing AUVs are reviewed in terms of their hull shape, energy source and mission capabilities. AUV mass is important to the energy carried, and a relationship between energy mass and AUV mass is established. The energy sources available to an AUV are described together with their limitations and their applicability to underwater operation is considered. Autosub's history and design evolution is described, and an alternative laminar hull shape is introduced.

A look at design methodology illustrates that design is specific to the system, furthermore no specific design methodologies exist for AUVs. A general design review is conducted and literature dealing with manned submarine design is discussed. Automated packing methods for payloads and internal subsystems are considered. The intention was to find a method of representing AUV subsystems and to find an approach of efficiently packing them within a hull shape.

2.1 Existing AUVs.

As indicated in Chapter 1, a number of AUVs are in use within commercial industry, and many more are to be developed. The operation, hull shape and energy source of a selection of these AUVs are discussed to identify similarities and possible reasons for any significant design differences.

2.1.1 Test bed AUVs.

Most AUVs are in some way used as development vehicles. In marine terms they are a relatively new technology and consistently being upgraded and revised. Some AUVs are further along this process than others and therefore will be discussed in section 2.1.2. A few of the older or more experimental AUVs are discussed here.

International Submarine Engineering (ISE), based in Canada, produce the explorer range of AUVs, discussed in section 2.1.2. ISE's first AUV, named ARCS, is owned by the Department

of National Defence – Canada (Figure 2.1*i*). This serves as a test bed to develop technology for the Theseus AUV. ARCS is interesting because of a successful continuous 35 hour mission with a 100 kWh aluminium - oxygen fuel cell in 1997 (www1). ARCS is cylindrical with a large parallel middle body similar to Autosub although ARCS has both fore and aft control surfaces.

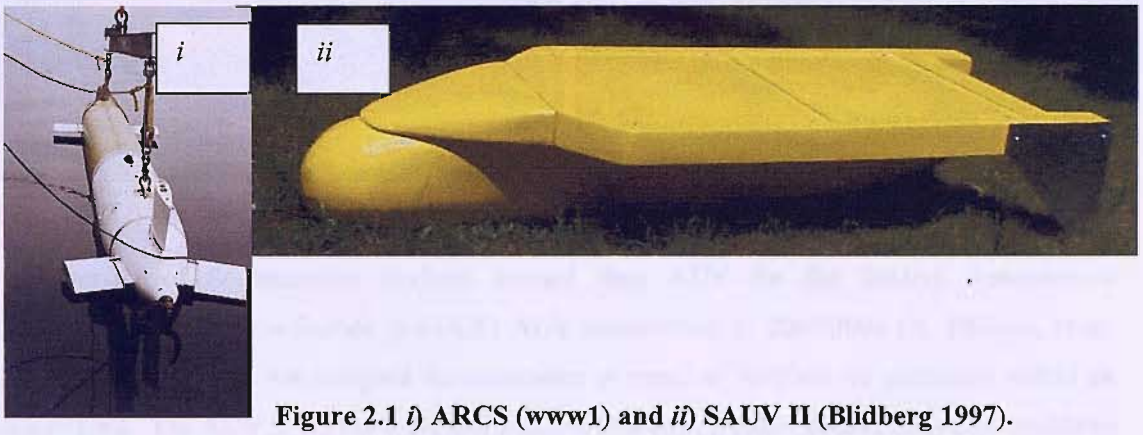

Figure 2.1 *i*) ARCS (www1) and *ii*) SAUV II (Blidberg 1997).

Falmouth Scientific Instruments has an experimental solar powered long endurance AUV (SAUV II, Figure 2.1*ii*). This means spending long periods at the surface recharging its lithium ion batteries. SAUV II is designed to give operational endurance of several months using its rechargeable energy source, but is limited to a daily range of 50 km to ensure sufficient recharge time (Blidberg 1997). SAUV II has a large flat wing above the torpedo main body to accommodate the solar cells. The lifting forces generated by this wing make manoeuvring very challenging. James Jalbert et al found the wing to be a primary source of drag, and it was possible to reduce drag to 40 % of the original model by tapering the wing shape (Jalbert, *et al.* 2003). The vehicle's control system has to cope with the manoeuvring challenges and battery charging from an inconsistent power source. The predecessor was created by D. R. Blidberg and M.D.Adeev at the Autonomous Undersea Systems Institute (AUSI) (Blidberg 1997).

The Underwater Robotics & Application laboratory (www2) in Tokyo have a number of research AUVs; Manta-Ceresia, R-1, Pteroa 150 and Tri-dog. Pteroa 150 is the same hull shape as the Manta-Ceresia, which is a test bed AUV (Figure 2.2*i*). It has a NACA 0030 aerofoil cross-section, so that the whole AUV hull generates lift force at non zero incidence to allow for better altitude control. This is a different approach for an AUV hull form as opposed to a rotationally symmetric body and seems to be based on hydrodynamic performance. The flow properties about a NACA section have been very well studied, and so the hydrodynamic performance should be predicable given a smooth hull surface, but will have manoeuvrability affects and increased lift to drag ratio when at an angle. No detail is reported about the internal construction of pressure vessel or energy source.

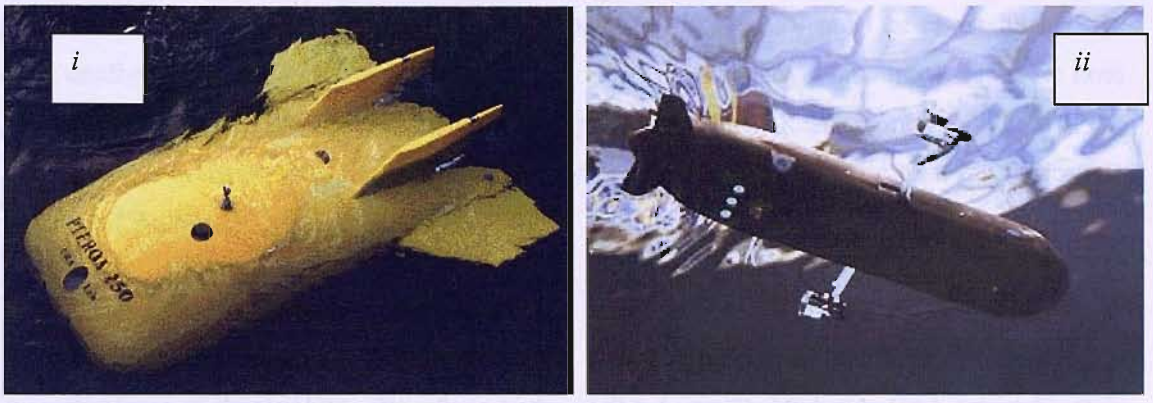

Figure 2.2 *i*) Pteroa 150 (www2) and *ii*) Soton AUV (Akhtman, *et al.* 2007).

University of Southampton students created their AUV for the Student Autonomous Underwater Challenge – Europe (SAUCE) AUV competition in 2005/2006 (A. Phillips, *et al.* 2007). Soton AUV is not designed for endurance or speed as its trials are contained within an indoor pool. The AUV is 1.33 m long, and consists of a bow, parallel middle body and cruciform stern (Figure 2.2*ii*). There are two large wings midway along the body which mount two thrusters, and two more thrusters are recessed within the parallel middle body to provide vertical motion. The four thrusters give the vehicle high manoeuvrability. The student team did very well in solving the challenges of the structure, power system, control and waterproofing the vehicle. A single large pressure vessel is situated in the parallel middle body, and contains all the pressure and water sensitive components, such as the electronics and energy source. The hull is not rotationally symmetric as the vertical thrusters require the hull surface to be flat about the entrance to the thruster tunnel.

Gavia is created by Hafmynd in Iceland. This is a small modular AUV, less than 2.5 m long, a diameter of 0.2 m and weighing up to 75 kg (Figure 2.3).

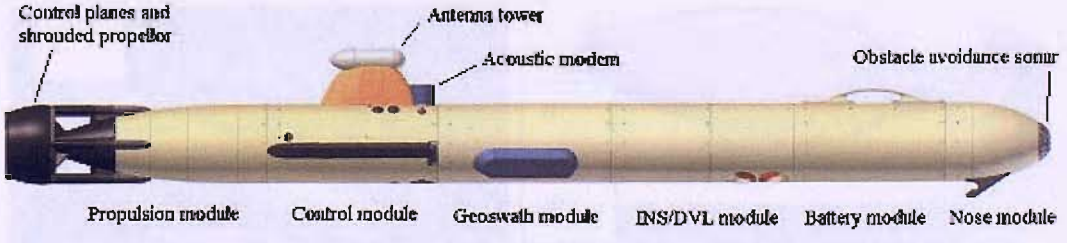

Figure 2.3 *i*) Gavia showing modular components (Yeo 2007).

Gavia is rated to 2000 m depth and can operate for 6 hours on one battery module. Physically Gavia is arranged into cylindrical modules, with each module lying along the central axis, and of known mass and displacement (Yeo 2007). This means that the module order can be rearranged

for different configurations and the hydrostatic balance of the AUV must be re-established for each configuration. The modules are all parallel sided leaving only a small bow (specific nose module) and the stern occurs within the final propulsion module. Rearranging modules will not alter the bow or stern, only the overall length of the parallel middle body and the hydrostatic balance of the vehicle.

2.1.2 Commercial AUVs.

AUVs are used for commercial projects by the oil industry and the military. There are few manufacturers of these AUVs (Bluefin robotics- USA (www3); Hydroid- USA (www4); ISE-Canada (www1); Konsberg – Norway (www5)). Many commercial AUVs are built by institutions as a single vehicle (NOCS- UK (www6), Subsea 7 –UK (www7)), or as a showcase AUV to build more in future (DeepC, Germany (www8)).

Hydroid inc. creates the REMUS AUV, designed as a low cost and lightweight vehicle for monitoring and mine counter measures for the US Navy (McCarthy 2003) and hydrographic surveys (Figure 2.4*i*). Hydroid have shipped over 70 REMUS (Remote Environmental Measuring UnitS) vehicles and have expanded to produce 3 difference size of vehicle (www4). The Remus 100 is relatively small (1.6 m long, 0.19 m diameter, 37 kg and operating depth of 100 m) and consists of an elliptical bow, parallel mid body and tapering stern, with a standard sensor payload package which can be customized to user specifications. The largest vehicle, Remus 6000 has the same profile shape as the Remus 100, but is much larger (0.71 m diameter, 3.84 m long, 862 kg and operating depth of 6000 m). Both vehicles use rechargeable lithium ion batteries housed within cylindrical pressure vessels. The payload is mounted within the bow, except the side scan sonar, conductivity temperature depth (CTD) profiler and global positioning satellite (GPS) system, which are mounted within the parallel middle body.

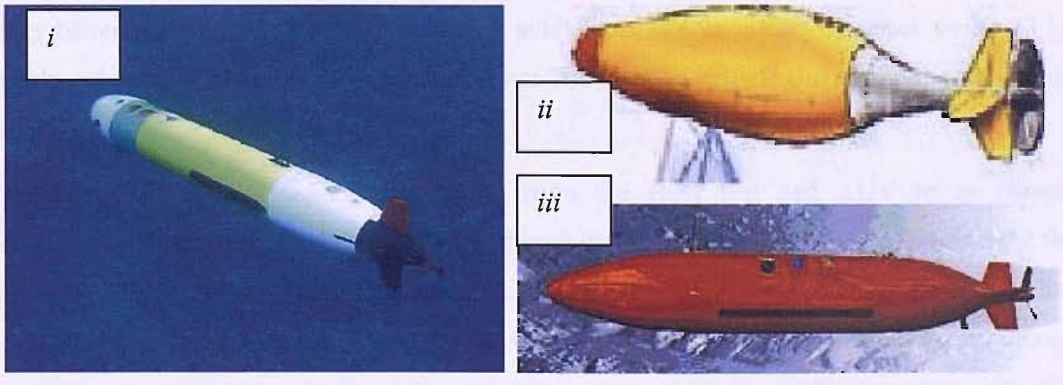

Figure 2.4 *i*) REMUS (www4) *ii*) Hugin I and *iii*) Hugin 3000 (www5).

Kongsberg (www5) have made a number of vehicles for military and offshore survey applications. Hugin I was a test bed vehicle, using a laminar flow hull shape and Ni-Cd batteries (Figure 2.4*ii*). Hugin II has been used by the Norwegian Underwater Intervention AS under the name NUI Explorer for detailed mapping of the sea bed in water depths of 600m (Hasvold, *et al.* 1999). It also tested a hydrogen peroxide (Al – HP) battery as a pressure tolerant rechargeable energy source (Hasvold, *et al.* 1999). This will be discussed further in section 2.3.2. Hugin 3000 (Figure 2.4*iii*)is the deepest diving AUV produced by Kongsberg, capable of 3000 m and 60 hr endurance (Hasvold, *et al.* 2005). It has a 5.35 m long rotationally symmetric body, a long bow, short parallel middle body and then a sinusoidal profile stern. The total vehicle weighs 1400 kg in air, although it has a 2.4 m^3 hull displacement. It appears likely that the laminar flow hull of Hugin I was split in two and extended with the parallel middle body. Kleiner and Northcutt observe that although the use of Hugin 3000 has met its requirements and conducted 25,000 km of surveys, its operation time has been decreasing (Kleiner and Northcutt 2004). In 2001 it was utilised for 100 days, and in 2003 it was utilised for 53 days. Kleiner and Northcutt then comment that despite Hugin being five times more efficient than traditional deep tow methods, industry has not appeared keen to support the vehicle.

Hugin 1000 was initially aimed at naval use, but has since been brought into commercial surveys. It is the latest of the Hugin vehicles, and builds on the Hugin 3000 system. It is the same shape as the Hugin 3000, but is designed to minimise volume whilst carrying a comparable payload. The vehicle can vary in length depending on the payload and system configuration (body length of 4.0 m – 5.0 m) and is limited to 1000 m depth (www5). The optional payload section sits before the middle body and extends into the bow, so the vehicle length variation comes from increasing the parallel middle body length. With a pressure tolerant primary or secondary lithium energy source, the secondary batteries can achieve 24 hrs endurance and the primary batteries have almost twice the energy available. The secondary batteries weigh 83 kg per pack and are capable of 5 kWh, or 20 hours at 700 W. The vehicle carries three such battery packs.

This family of AUVs display progression from the early test bed AUV to its current incarnation. None have stopped being used, and so fulfil their initial design specification, but the design continues to evolve over each generation. The initial design was a laminar flow body, but when creating a higher endurance and larger vehicle, a parallel middle body was introduced rather than scaling the whole body. This approach is most likely due to the economic cost of a complete redesign and manufacture.

In addition to ARCS, ISE also produce a customisable explorer AUV. Two diesel powered snorkelling surface AUVs designated, Dolphin and Dorado were developed. All ISE AUVs are torpedo shaped with a long parallel middle body. Dolphin and Dorado have a mast through which the AUV draws air to supply its engine. The Explorer AUV is modular and the customer can specify payload. The AUV is then scaled to decide optimum velocity for the required payload and endurance. This is a quick and easy method for the customer; but requires a lot of experience within ISE to translate the customer's desires and realise the AUV specification.

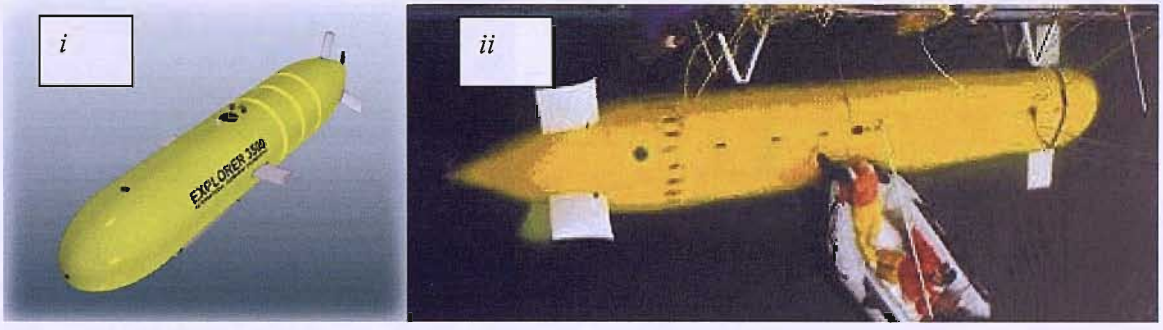

Figure 2.5 *i*) Explorer and *ii*) Theseus (both from www1).

Theseus is a large AUV that was designed by ISE (and operated by the Canadian Department of National Defence) to autonomously lay cable at depth. It successfully completed missions under ice around Canada's Ellesmere Island. On its longest mission the AUV managed 360 km of unaided travel, taking 51 hours, with depths up to 600 m (Ferguson, *et al.* 1999 pg. 65 - pg. 70). It's longest single mission to date was 262 km in 50 hours, conducted in 1998. Theseus is a large vehicle with a parallel middle body making up 70% of its length. The design driver for such a body was the requirement for a very large payload bay. Like other AUVs its sensors are mounted in the bow and the energy source located in the middle body, but the user payload (in this case the cable to be laid) fits into the middle body. This is also the only reviewed vehicle that stores a disposable payload, yet it still has a shape common to many other vehicles.

Bluefin Robotics Corporation is an off shoot company of the Massachusetts Institute of Technology (MIT) Autonomous Underwater Vehicle laboratory. They produce the Bluefin 9, 12, and 21 AUV (www3). These are mostly for American battlespace research, though some also conduct offshore oil seafloor surveys. The number in the AUV name indicates the vehicles diameter in inches, so the Bluefin 21 is the largest AUV they produce. The Bluefin 9 is small and light, sufficient to be carried by one person. The AUVs have an axis-symmetric parallel middle body shape, due to modularity and ease of manufacture, and the user configured payload is fitted in the parallel middle body, making the vehicle length variable. All these vehicles are powered

by a pressure tolerant lithium polymer energy source manufactured by Bluefin (and discussed in section 2.3.1). With this energy source, the 21 AUV can achieve an 18 hour mission, and as the lithium packs are not housed within a pressure vessel they can be swapped out more easily so the AUV turnaround is 2 hours on deck.

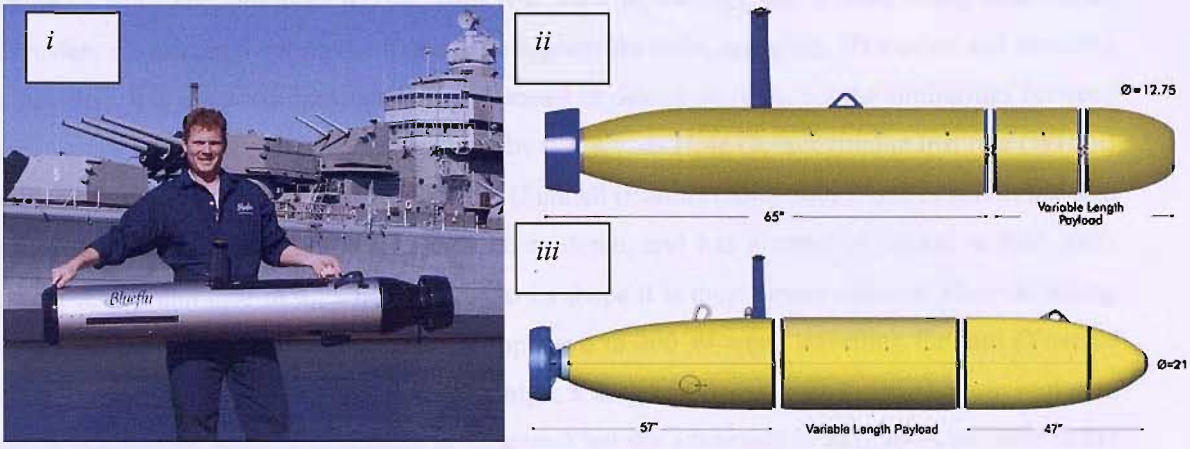

Figure 2.6 *i*) Hugin 9 *ii*) Hugin 12 and *ii*) Hugin 21 AUV (all from www3).

Geosub is an AUV developed by Subsea 7 after close work with NOCS and Autosub (discussed in section 2.1.3). Geosub is the same base AUV as Autosub and externally looks identical, it is 6.82 m long, has a diameter of 0.9 m, weighs 2400 kg in air, and can operate at 3000 m (www7). The energy source has been upgraded to lithium ion secondary batteries for a total of 66 kWh weighing 600 kg, and 30 to 60 hours endurance depending on payload configuration. The operating speed is 1 to 2 ms^{-1}, so hydrodynamically this is very similar to Autosub2.

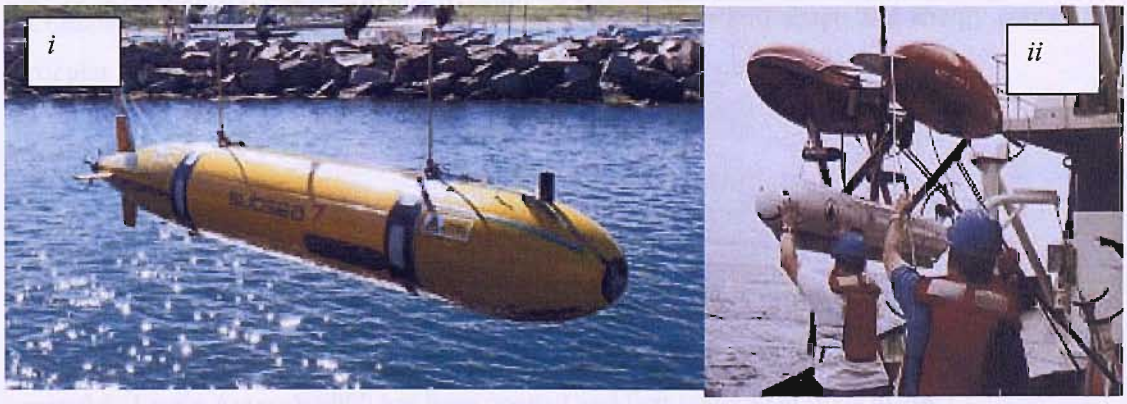

Figure 2.7 *i*) Geosub (www7) and *ii*) ABE (Yoerger 2007).

The design of Geosub further illustrates AUV design based on technology that is known to work coupled with slight design modifications. The alternate energy source is a direct move to

increase range, and reduce downtime assuming the time to recharge the lithium ion batteries is less than the time to replace all Autosub2's primary batteries.

Two of the more different AUV shapes are seen in Autonomous Benthic Explorer (ABE) and DeepC. Both are multihull AUVs, with two hulls at the top, and a third slung underneath. Thrusters are mounted within the frame that supports the hulls, and gives 3D motion and hovering capability. It is unknown how much DeepC based its design on ABE, but the similarities between the two are very noticeable. ABE was built by the Woods Hole Oceanographic Institute (WHOI) and was first operated in deep water in 1993 (Funnell (Editor) (2001-2002)) and is still in use as a research vehicle. ABE can operate at 5500 m depth, and has a range of 10 km at 0.65 ms^{-1}, giving it an endurance of 4.25 hours. Due to its shape it is most power efficient when travelling forwards, 350W when travelling sideways opposed to 200 W when travelling forward (Yoerger 2007). The drag profile of such a shape is high, a drag coefficient based of 0.31 on frontal area (for a model body without propellers or thrusters) but the advantage is its manoeuvrability in 3D space (Kinsey 1998). The power source for ABE consists of 378 lithium ion secondary batteries, for a 5.4 kWh pack, which replaced a 1.2 kWh lead-acid (Pb-acid) battery pack. A proportional increase in endurance was found (Abu Sharkh, *et al.* 2003 pp. 19 - 35).

DeepC is an AUV created with Atlas-Electronik as a project for Bundsministerium fur Bildűng und Forshung. It was a Tri-hull vehicle similar to ABE, with the top two hulls forming pressure vessels for a fuel cell energy source. It was designed for 4000m depth, weighed 2.4 tonnes, and claimed up to 60 hours operation at 1.8 ms^{-1} (Hornfeld 2004). The project has now been terminated by Atlas Electronik (www8).

Commercial AUVs have been considered with a focus on hull shape and energy source. A particular AUV is then discussed in greater detail due to accessibility of data.

2.1.3 Autosub.

NOCS built the Autosub AUV which was designed to be a scientific instrument platform, carrying a scientific payload of biological, chemical and physical sensors to depth. The design has been through four generations, Autosub 1 to Autosub 2 improved the centre section and energy source. Autosub 3 was created following the loss of Autosub 2, and the propeller was improved. Lastly Autosub 6000 has been created and first underwent trials in 2007.

Autosub 1 was first tested in June 1996 along the dockside at NOCS (Stevenson, *et al.* 2002), it completed 382 missions covering over 5000 km, most of which was unescorted, and 708 km under ice before its loss in February 2005 under the Fimbul ice sheet in Antarctica. Autosub 2's longest single mission to date was conducted in 1998, when it travelled 262 km in 50 hours.

A profile schematic of Autosub 2 is shown in Figure 2.8 and a cross section of the parallel middle body showing the pressure vessels that contain the energy source can be seen in Figure 2.9. Unless specified, references in this Thesis to Autosub refer to Autosub 2.

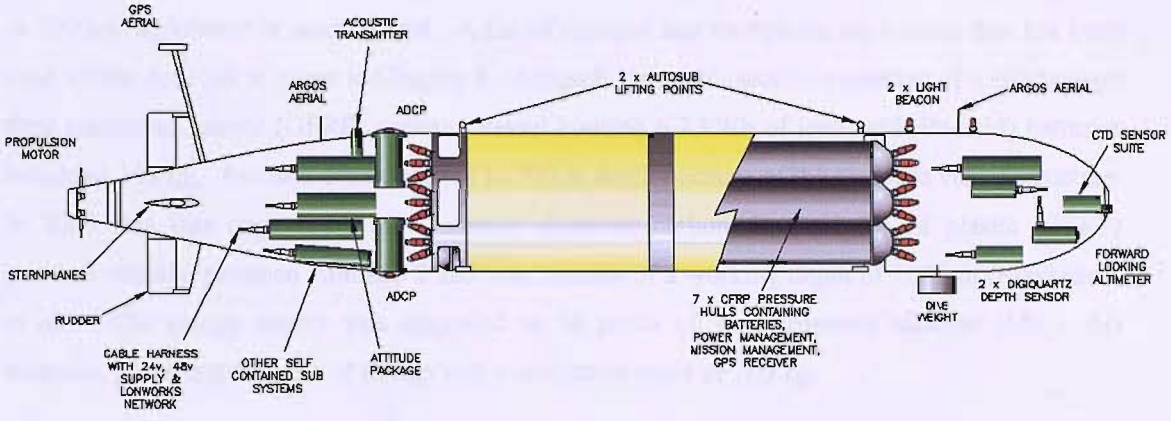

Figure 2.8 Schematic of Autosub 2

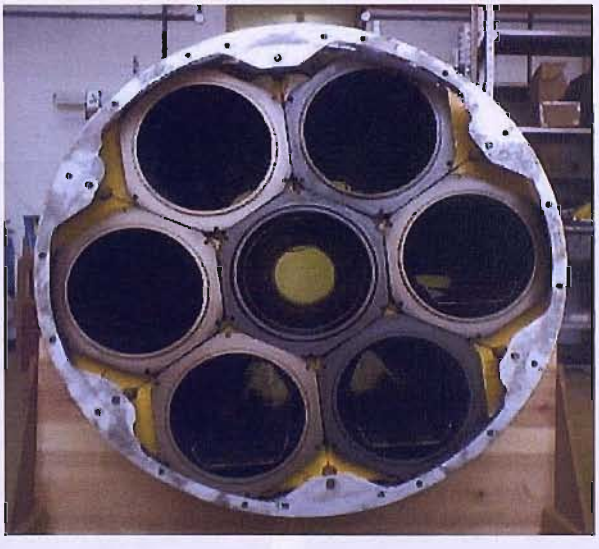

Figure 2.9 Cross section of Autosub 2's parallel middle body, showing arrangement of pressure vessels.

Autosub is almost 7.0 m long, 0.9 m in diameter, weighs 2400 kg in air and is almost neutrally buoyant in water. A slightly positive buoyancy force is preferable so that the AUV will return the sea surface should electrical power fail. Autosub has a drop weight suspended by a solenoid to

increase buoyancy if electrical power fails. There are additional buoyancy concerns with local water density variation and volume lost due to buoyancy foam compression with diving depth.

Autosub has an envelope volume of 3.5 m^3 meaning that approximately 1 m^3 of the hull volume is free flooding. It has room in the bow and stern to accommodate payload totalling 1 m^3 or 100 kg, whichever is reached first. A list of payload and navigation equipment that has been used within Autosub is given in Chapter 8. Autosub 1's centre section consisted of a single glass fibre reinforced plastic (GFRP) pressure vessel housing 6.7 kWh of lead acid (Pb-acid) batteries weighing 160 kg. Autosub 1 was limited to 500 m depth because of the pressure vessel structure. In 2000 this was upgraded with 7 smaller diameter carbon fibre reinforced plastic (CFRP) pressure vessels, renamed Autosub 2 and was capable of a working depth of 1600 m (Stevenson, *et al.*). The energy source was upgraded to 58 packs of 75 manganese alkaline (Mn – Al) batteries, providing 61 kWh of energy and a maximum mass of 700 kg.

Figure 2.10 shows the Mn – Al batteries used in Autosub 2. Figure 2.10*i* shows an individual battery pack, and Figure 2.10*ii* shows a line of packs connected together ready to be fit within a pressure vessel. Although individual battery batteries are cylindrical (Commercial 'D' batteries), once arranged the packs are hexagonal to allow packing within the cylindrical pressure vessel. These were then placed on sliders to allow the packs to be removed for replacement and maintenance.

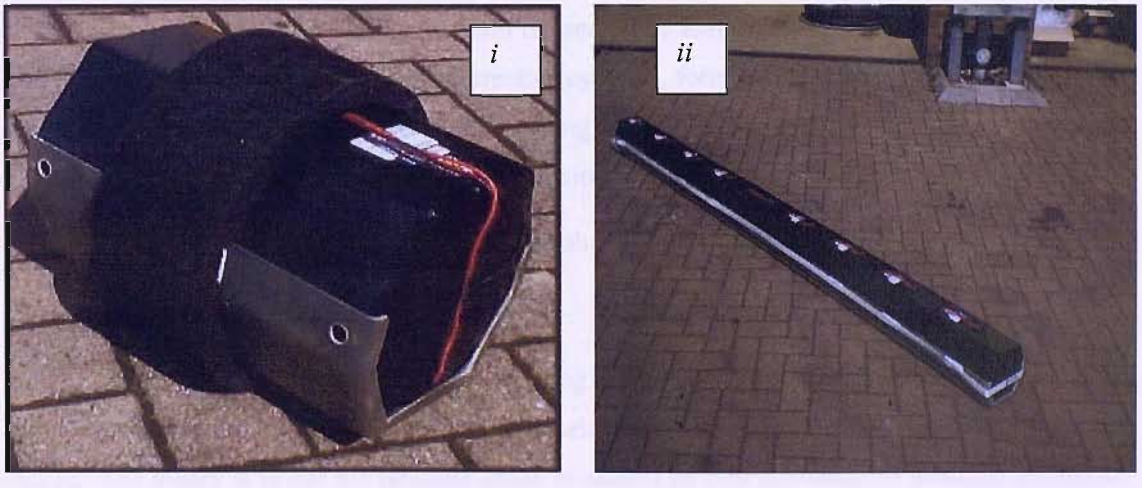

Figure 2.10 i) Double pack of 72 Mn - Al D shape batteries and ii) 14 double battery packs wired in series.

The batteries are insulated as the water temperatures of most Autosub 2 missions were colder than average. Within the single pressure vessel of Autosub 1 the batteries would overheat and required a heat sink as the surrounding water was much warmer with surface temperatures over

30 °C. When the move was made to colder waters the heat sink became a problem and the energy source packing was redesigned.

Autosub is an evolving vehicle, so adaptations are made as problems arise and are solved. Two such examples are the bow weight and side fins. The bow weight was added before the Pine Island Bay cruise in early 2003 (Millard, *et al.* 2003). Autosub dives by running along the surface until the aft control planes create sufficient force to push the bow down. Launching in an ice field meant that there is a risk of collision on the surface, so the bow dive weight pull's the bow down and is released once the vehicle is fully submerged and controllable. The side fins added in 2004 are placed along the parallel middle body (Dowdeswell 2004). When working near glaciers a layer of fresh water is present at the surface. This fresh water is less dense than seawater, and so Autosub would become negatively buoyant at the surface. Weight was removed such that Autosub was neutrally buoyant at the surface, and the side fins would act as control surfaces to give a downwards force when Autosub reached denser seawater.

The concept Autosub 6000 relied on the spherical pressure vessels to provide buoyancy, with syntactic foam supplying any additional required buoyancy. The subsystems were to be fitted about the buoyancy spheres to fill free-flooding volume within a smooth external shape. The original design of Autosub 6000 used a laminar flow hull shape and so had an external envelope in which to fit the foam. The existing Autosub 6000 design does not have spherical pressure vessels so a larger volume of syntactic foam is used. The foam is fitted about the cuboid energy source and the external face is shaped to create a cylinder, forming a parallel middle section. The parallel middle section radius was defined by using existing Autosub 3 bow and stern sections, in effect, Autosub 6000's hull shape is a shorter version of Autosub 3.

An alternative to the parallel middle body hull shape is discussed next.

2.1.4 Laminar flow body.

The concept of reducing shape drag by controlling the boundary layer of the body is not new. It has been used in aeronautics for wings and fuselages, and has been considered for AUV hull shapes. The theory is to use the pressure gradient caused by bow curvature to maintain a laminar boundary layer flow and its inherently lower coefficient of friction.

The concept of a laminar flow AUV was presented by Parsons *et al.* (Parsons, *et al.* 1974). An iterative approach was used to create the shape with a 4^{th} degree polynomial for the bow, and 5^{th} degree polynomials for the middle body and stern. The profile is for a shape of unit length, so can be scaled to suit when maintaining the fineness ratio (length / diameter) of 4.84. The profile is shown in Figure 2.11.

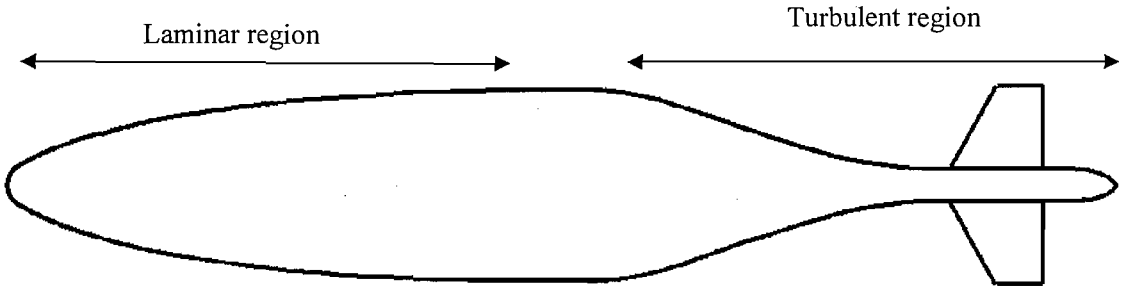

Figure 2.11 Laminar flow hull shape as defined by Parsons with a cruciform control surface arrangement.

Parsons *et al.*'s approach will form the basis for a hull shape geometry in this Thesis. The hydrodynamic modelling of this shape by other researchers is given in Chapter 5, and the hydrodynamic results from additional computational modelling are given in Chapter 6.

Having discussed geometric form and energy sources within different AUVs the masses contributing the AUVs total displaced mass are now reviewed.

2.2 AUV mass.

A key constraint to AUV design is the condition of neutral buoyancy, which means that the AUV must displace the same mass of water as the AUV total mass. If the AUV displaces less than its mass, then the AUV will sink (negatively buoyant), and if it displaces more then it will float (positively buoyant). Either condition will mean the AUV has to consume power to maintain level flight.

In practice an AUV is unlikely to be completely neutrally buoyant, and positive buoyancy is preferred in case of AUV malfunction. Such imbalance can be addressed during AUV manufacture and whilst in service, as local water conditions will affect buoyancy. This research will aim to design neutrally buoyant concept AUVs.

There are AUVs that are not designed to be neutrally buoyant, for example the Slocum thermal glider. Variable buoyancy provides the propulsion for the glider. A glider alters its buoyancy to become negatively buoyant, as the glider sinks the control surfaces provide a force forward. At the designated depth the glider becomes positively buoyant, changing its attitude and then gliding to the surface. The Slocum thermal glider is discussed further in Section 2.3.3.

2.2.1 Mass of energy source to vehicle mass.

An investigation of many AUVs was conducted by the author during 2003 – 2004. This created a spreadsheet containing the AUV mass, energy source mass and capacity, and information on the power outputs. This was used to try and identify any trends concerning the proportion of the AUV mass dedicated to the energy source.

Batteries, either primary or secondary, are by far the most common choice of energy storage for past and present AUVs. In Jane's Underwater Technology (Funnell (Editor) (2001-2002)) information on the energy source is available for 61 different AUVs. Batteries were used in 53 of these vehicles (3 primary, 42 secondary, 4 primary or secondary, 4 of unspecified type). Aluminium oxygen semi-fuel batteries were used in four vehicles (for example Hugin); only one vehicle claimed to use a hydrogen-oxygen fuel cell (Urashima); an air-breathing diesel was used by two semi-submersibles (Dolphin and Dorado) and a closed cycle diesel engine was used by one vehicle (R1 Robot). Other options found in other sources include the thermal engine of the Slocum glider (Webb, *et al.* 2001) or to recharge onboard supplies as in a solar-powered AUV (Blidberg and Mikhail 2003 pg. 59 - pg. 76). Since this study, more vehicles have been built, and others have been retired, but this study has not been updated since 2004. Autosub 6000 has been presented here from results in 2007, as the Autosub series are used as examples throughout this research.

Given the importance of these batteries and the effect of increasing the energy on endurance, how best can the energy source of a vehicle be improved? Either the quantity (and hence mass) of component batteries, or the energy stored per kg of mass must be increased. The numerical implications of either option will be discussed in Chapter 3. This section will discuss the energy source mass of current vehicles.

The mass of an AUV (M_{AUV}) has to include structure ($M_{Structure}$), payload ($M_{Payload}$), control systems (M_{Hotel}), propulsion (M_{Prop}), any pressure vessels (M_{PV}), energy source (M_E) and buoyancy (M_B). This can be shown in equation 2.1.

$$M_{AUV} = M_{Structure} + M_{Payload} + M_{Hotel} + M_{Prop} + M_{PV} + M_E + M_B \qquad 2.1$$

The total mass of the AUV should equal the mass of water displaced. The faired volume might be greater than the displaced volume, and this will entrain water mass, implying a low packing efficiency of the vehicle. Most batteries have a density greater than the density of water (ρ_W) and so M_E will be negatively buoyant.

$M_{Payload}$ may change for each mission but is primarily constrained by the mission objectives, much the same as M_{Hotel} being constrained by navigational requirements. $M_{Structure}$ reflects the design detail of the vehicle. It is assumed that there are sufficient design options to allow this to be addressed after the conceptual stage. The propulsion mass is defined by the required thrust, making minimal mass a secondary design objective. The pressure vessel performs two functions, buoyancy and protection of pressure sensitive components. The pressure vessel volume is determined by the volume of pressure sensitive components and its mass determined by volume and operation depth.

Research commenced with a survey of the mass proportions of other vehicles. A non-dimensional ratio selected was to divide the M_E by the M_{AUV} as indicated in equation 2.2.

$$Mass\ Ratio = \frac{M_E}{M_{AUV}} \qquad 2.2$$

This ratio allows comparisons to be drawn from AUVs as large as the United States Navy large scale vehicle, Cutthroat; 200 tonnes (Fox 2001), to as small as Nekton research's Ranger; 3.5 kg (www9). In many cases, M_E was not explicitly provided so therefore is estimated from existing data on energy source capacity and battery chemistry. The *Mass Ratio* for existing vehicles in relation to their diving depth and range are provided Figure 2.12 and Figure 2.13. The unlabelled data points generally refer to test AUVs.

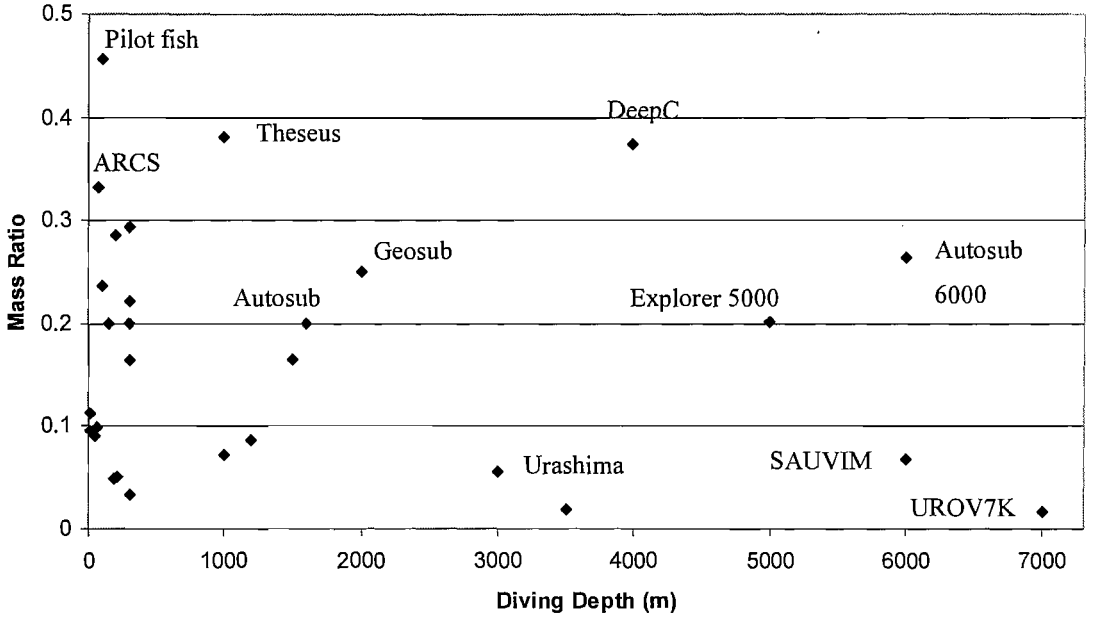

Figure 2.12 Mass ratio with increasing diving depth for 30 AUVs.

The most immediate conclusion from Figure 2.12 and Figure 2.13 is that no current vehicle has a *Mass Ratio* greater than 0.5. At the time of the Advances of Technology for Underwater Vehicles 2004 (ATUV) conference, where the first paper in Appendix A was presented, no vehicle capable of diving greater than 1500 m had a *Mass Ratio* greater than 0.25. However information about the retired DeepC AUV (www8) has since become available and its fuel cell energy source gave a *Mass Ratio* of 0.375. Autosub6000 has now been created and has a potential mass ratio of 0.264, when fully loaded with 12 battery packs, and is capable of diving to deeper depths.

Many of the vehicles with a *Mass Ratio* of below 0.15 are test or demonstrator vehicles, where maximum stored energy was not a design requirement. However, the vehicle with the highest *Mass Ratio*, the Pilot Fish, is a shallow diving test vehicle (Fish, *et al.* 2003).

Comparing AUVs such as Geosub and Autosub or DeepC or Theseus, it is possible to observe a trade off between the AUVs diving depth and its range. E.g. in Figure 2.12 Autosub has a lower diving depth than Geosub, but has a greater range (Figure 2.13).

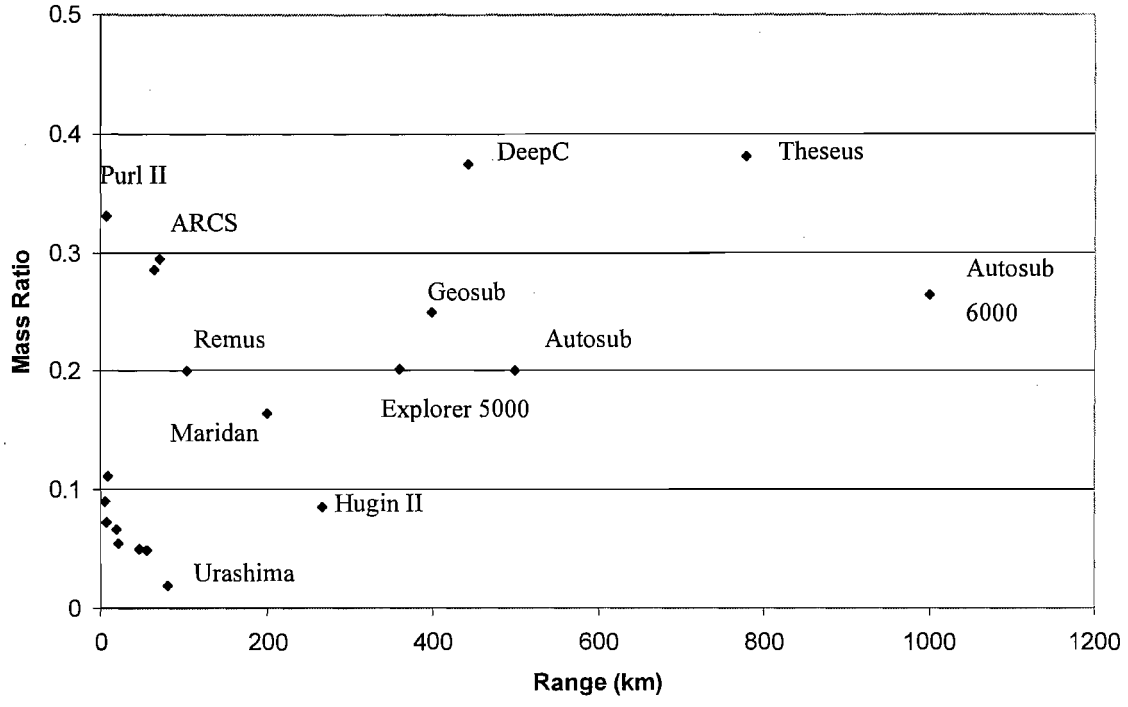

Figure 2.13 Mass ratio with increasing range for 20 AUVs.

A short description of some of the vehicles and what might contribute to their mass ratio is now discussed.

- *ARCS* This is a testbed vehicle and a predecessor to Thesus. M_E is based on 20 kWh Nickel Cadmium (Ni-Cd) batteries, though a 60 kWh fuel cell has been tested. The batteries occupy 29 % of the vehicle mass, it dives to 300 m and has a maximum range of less than 100 km. A high energy content for limited range could imply that most of the AUV power goes to the payload, appropriate for a test vehicle which is testing equipment, not actually travelling great distances.

- *Autosub 2* This was an operational vehicle carrying a payload of scientific equipment. 20 % of the AUV is the mass of the energy source, and the power is balanced between auxiliary power and propulsion power. The CFRP pressure vessels have been operated to 1600 m, though due to a large safety factor the pressure vessels are heavy for their depth rating. The maximum range of the AUV is high for an average mass ratio, but is based upon a low power draw and optimal running conditions.

- *Autosub 6000* Has twelve 44 kg battery packs (McPhail 2006a) totalling, with a vehicle mass of 2000 kg (McPhail 2007a), for a mass ratio of 0.264. Using very similar

navigation technology to its predecessor, Autosub 6000 is projected to be capable of 1000km range at 1.0 ms^{-1}, 660 km at 1.6 ms^{-1}, and is built to withstand 60 MPa pressure. For the higher velocity Autosub 6000 is still an improvement over Autosub. Autosub 6000 will be discussed further in Chapter 4.

- *Geosub* This is an operational AUV derived from Autosub 2. It uses CFRP pressure vessels rated to 2000 m, and a lithium ion energy source (110 Wh kg^{-1}). The pressure vessels and payloads are similar, though the mass ratio is higher than Autosub 2. The range of Geosub is less than that of Autosub's optimal range, but may be a less optimistic estimate, or dependant on a higher average payload power.

- *Pilot fish* This is a shallow diving (<100 m) test vehicle, with a single plastic pressure vessel, built to demonstrate oscillating fin thrusters. A design requirement was to achieve a power-to-weight ratio similar to marine creatures, 25 W kg^{-1}, and so has little in the way of additional mass from payload, instrumentation and pressure vessels. This is an example of a mass driven design, discussed in Chapter 3.

- *Theseus* This is an operational vehicle carrying 220 km of fibre optic cable. The proportion of mass allocated to the energy source has increased by 9 %, the overall mass increased by a factor of 6 and the battery chemistry has changed from nickel cadmium (Ni - Cd) to silver – zinc (Ag - Zn), doubling the specific energy (110 Wh kg^{-1} from 50Whkg^{-1}). This corresponds to a thirteen fold increase in energy, and the range has increased approximately by an order of magnitude (780 km from 72 km). This would imply that the increase in range is not proportional to the increase of energy and one of the systems is not as efficient as tested in ARCS.

- *Urashima* A test vehicle from Japan Marine Science and Technology Centre (JaMSTeC) (Tamura, *et al.*). Tamura et al state that a large pressure hull increases its mass with pressure, due to increasing wall thickness to increase structural strength, and so is not a suitable structure for depths below 1000 m. The AUV is made from a titanium structure, solid foam buoyancy and multiple small pressure vessels and a lithium ion energy source (150 Wh kg^{-1}).

- *USS Cutthroat* A 0.294 scale model of the USS Virginia and contains 25 tonnes of Pb - acid batteries, making it the largest existing AUV. It does not carry a payload as such this is possibly the only AUV which does not have the payload in its design boundary. The large scale model was required for hydrodynamic testing, as the Froude and Reynolds numbers are more representative of the actual submarine. With an AUV

volume as large as 203 m^{-3}, it would be possible to achieve high endurance, but the economics of running such an AUV is beyond all but military budgets.

Figure 2.13 illustrates that increasing the proportion of mass ratio within the AUV will increase the range, and so increasing the mass of the vehicle. There is nearly always a finite limit on the mass of the vehicle, for practical manufacture, launch and transport reasons if not specified in the mission boundary, so another subsystem of the vehicle will have to decrease in mass. The pressure vessel was identified for investigation due to its close relationship with the energy source.

The 0.25 mass ratio could be useful in estimating the energy included in a conceptual design. This will enable the endurance and range to be estimated given a mass or displaced volume, without a detailed design of the navigation systems, payload or propulsion power.

Improving the 0.25 mass ratio can be achieved by reducing the mass of structure and systems. This could increase the mass available for the energy source, or reduce the required displaced volume. A decrease in displaced volume could then alter the shape of the AUV changing drag force or internal arrangements of components. For example, two small radius pressure vessels may allow for a more optimal hull shape than one large pressure vessel of the same volume.

One option to improve the mass ratio of the AUV is to reduce the mass of other components. One such component is the pressure vessel, whose mass increases with diving depth. The pressure vessel design and associated mass is described next.

2.2.2 Pressure vessel mass.

The mass of the pressure vessel can be a significant proportion of M_{AUV}. A pressure vessel supplies an area of ambient pressure within the AUV regardless of depth. This is used to house pressure sensitive equipment and computer parts. Adding equipment inside the pressure vessel will increase the pressure vessel mass and reduce its buoyancy. Appendix B gives further details on pressure vessel creation approach used for the case studies.

Figure 2.14*i* is a sketch of a cylindrical pressure vessel with nomenclature definition and Figure 2.14*ii* indicated the volume assumed to be available for packing sub systems.

The empty pressure vessel mass is determined by the thickness of its walls. The thickness of its walls is determined by the pressure at which the pressure vessel fails. The equations and discussion of designing a pressure vessel is given in Appendix B. The yield pressure (P_{Yield}) and buckling (P_{Buckle}) pressure equations are reiterated here in equation 2.8 and equation 2.9.

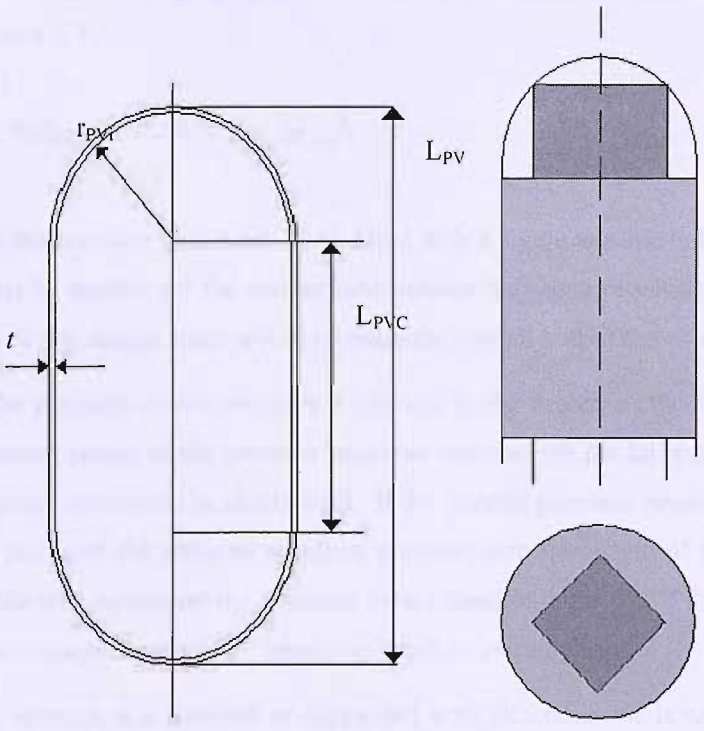

Figure 2.14 *i*) Pressure vessel shape and nomenclature and *ii*) pressure vessel packing volume.

The displacement and mass of the pressure vessel is given in equations 2.4 and 2.5, the total mass of the pressure vessel with pressure sensitive subsystems is given in equation 2.6.

$$r_{PVo} = r_{PVi} + t \tag{2.3}$$

$$\nabla_{PV} = \frac{4}{3}\pi r_{PVo}^{\ 3} + L_{PVC}\pi r_{PVo}^{\ 2} \tag{2.4}$$

$$Mass_{PVS} = \rho_{material}\left[\left(\frac{4}{3}\pi r_{PVo}^{\ 3} + L_{pvc}\pi r_{PVo}^{\ 2}\right) - \left(\frac{4}{3}\pi r_{PVi}^{\ 3} + L_{PVC}\pi r_{PVi}^{\ 2}\right)\right] \tag{2.5}$$

$$M_{Pv} = Mass_{PVS} + Mass_{internal\ systems} \tag{2.6}$$

∇_{PV} is the displaced pressure vessel volume, $Mass_{PVS}$ the mass of the empty pressure vessel and $Mass_{internalsystems}$ the mass of the pressure sensitive subsystems that are packed within.

Packing the pressure vessel and determining its length is more of a challenge, and shows scope for packing algorithms. The hemi-spherical ends can be used for storing smaller subsystems. The subsystem that defines the required radius should be placed within the cylindrical section, and the heaviest subsystem placed near the centre of buoyancy (*CoB*) of the pressure vessel. The

internal volume available for packing is assumed to be consistent with Figure 2.14*ii* and expressed in equation 2.7.

$$Internal\ Volume = \frac{8r_{PVi}^3}{3^{\frac{3}{2}}} + L_{PVC}\pi r_{PVi}^{\ 2} \qquad 2.7$$

The endcaps of the pressure vessel are 37 % filled with a single useable volume. The volume in the endcaps will be needed for the connections outside the pressure vessel, but leaving them completely empty at this design stage would increase the overall size of the pressure vessel.

The packing of the pressure vessel becomes a concern in the design methodology. If the total volume and maximum radius of the pressure sensitive components are known, then the required volume of the pressure vessel can be determined. If the internal pressure vessel radius is the same as the maximum radius of the pressure sensitive systems, then the length of the pressure vessel can be found. This will determine the pressure vessel fineness ratio (L_{PV} / diameter) and allow the required wall thickness for the AUV operating depth to be calculated.

Pressure vessel strength is a function of shape and wall thickness. S_F is safety factor scaling constant, σ_{yield} is the yield strength of the material, t is wall thickness, R_{PV} is the average radius of the pressure vessel, E is Young's modulus of the material and v is poisons ratio. The collapse equation is true for a "thin walled" pressure vessel, that is, wall thickness t is less than 10 % of R_{PV}. The buckling pressure is true for a long thin pressure vessel. A rule of thumb estimates the fineness ratio (length over diameter) of a long thin pressure vessel to be greater than 10. Below a fineness ratio of 10, the failure mode will depend on material stiffness. Equation 2.8 is the equation for pressure vessel yield and equation 2.9 is the equation for buckling pressure (Ross 1990).

$$P_{Yield} = S_F \sigma_{yield} \frac{t}{R_{PV}} \qquad 2.8$$

$$P_{Buckle} = S_F \frac{Et^3}{4(1-\upsilon^2)R_{PV}^3} \qquad 2.9$$

For cylindrical pressure vessels buckling is the most likely method of failure and spherical pressure vessels will fail by material yield. Low fineness ratio cylinders could buckle or yield depending on exact geometry and the presence of ring stiffeners.

Using multiple small pressure vessels as opposed to a single pressure vessel was considered. If multiple pressure vessels are required to give the same internal volume, then the radius of each reduces as the number of pressure vessels increases. This may present more design options when

arranging numerous small pressure vessels rather than one large pressure vessel. There also might be greater challenge in mounting and connecting all the pressure vessels. There is a mass saving when considering multiple pressure vessels, but this does not account for the mass cost of an increased number of connections. These connections have not been investigated and it is unknown how they might scale over multiple pressure vessels. The connections are modelled in Chapter 8 by a single increase in mass and only a single pressure vessel is considered. The next stage is to investigate how the operating depth affects the pressure vessel mass.

Indicative graphs and figures for the mass to displacement ratio and densities of pressure vessels and buoyancy foams (Stevenson and Graham 2003 pp. 77 - 92) were used by Griffiths to derive equation 2.10 (Griffiths, *et al.* 2004).

$$\frac{M_B}{B} = \frac{\rho_B}{(\rho_w - \rho_B)} = \frac{P_{Collapse}}{K - P_{Collapse}} \qquad 2.10$$

In equation 2.10 B is the buoyancy (kg), $P_{Collapse}$ the collapse pressure (MPa) and K a material dependent constant representing the collapse pressure (by whichever failure method) when the mass is equal to the buoyancy: ~75 for titanium, 100-120 for CFRP and ~67 for aluminium (Griffiths, *et al.* 2004). The resulting mass to buoyancy ratio for aluminium, titanium and CFRP ring-stiffened cylindrical pressure vessels are shown in Figure 2.15 together with different buoyancy foams.

The data used to derive equation 2.10 and Figure 2.15 is based upon pressure vessels that have a fineness ratio greater than 10. A pressure vessel with a fineness ratio less than 10 may have a greater buckling pressure, e.g. a sphere has a fineness ratio of 1, the strongest shape possible.

This paper by Griffiths *et al.* is provided in Appendix A. Here key conclusions are restated. For AUVs that dive to depths greater than 3500 m (35 MPa), the pressure vessel becomes a poor choice because mass is increased. A better choice is syntactic foam, such as HisynH4k, or ceramic spheres, as produced by Deepsea power and light (www10). The foam used in Autosub 6000 is the Emerson & Cuming EL34 foam (McPhail 2007b). This is included in Figure 2.15. At low depths, less than 2000 m (20 MPa), the pressure vessels offer more buoyancy than foam, so remain a suitable subsystem choice.

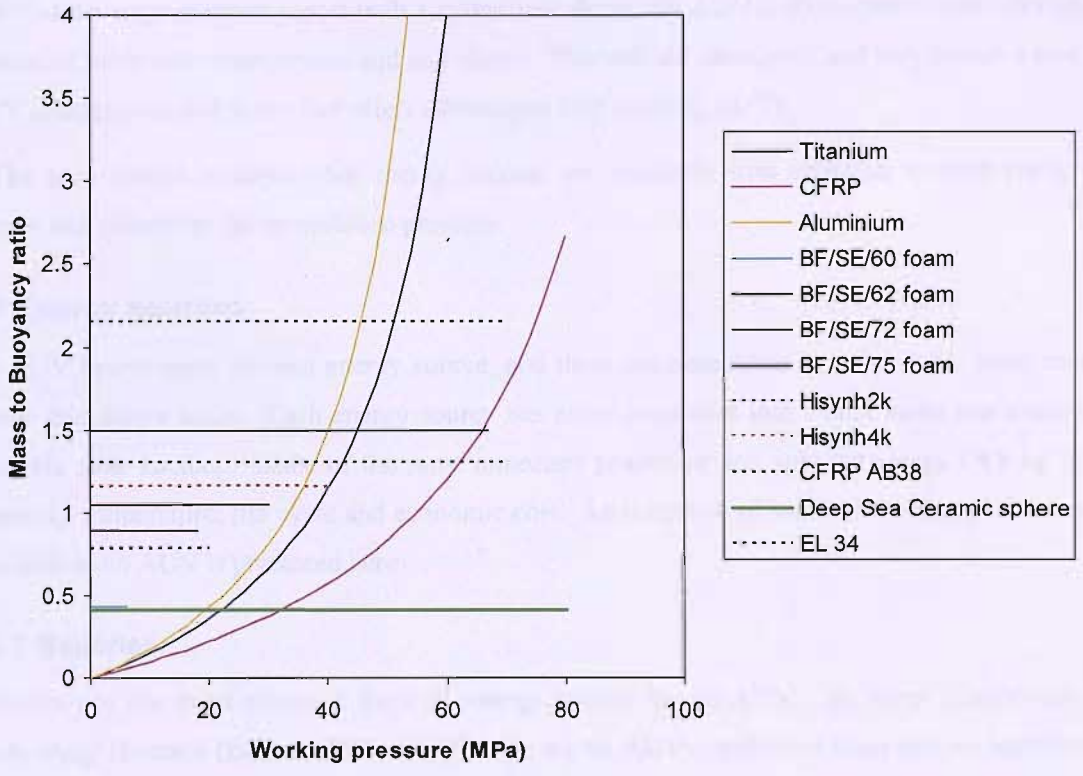

Figure 2.15 Mass to buoyancy ratio for buoyancy foams, glass spheres and ring-stiffened cylindrical pressure vessels in titanium and CFRP (Griffiths, *et al.* 2004). Updated to include Emerson & Cuming EL34 foam.

2.2.3 Implications of removing the pressure vessel.

The pressure vessel is a candidate for reduction in size or removal from the AUV. To achieve size reduction requires a pressure tolerant energy source with the benefit of reducing its diameter, wall thickness and overall pressure vessel mass.

Removing the pressure vessel will affect the mass balance and buoyancy of the AUV. At shallow depths, the pressure vessel may provide buoyancy, and so removing it gives little benefit. At deep depths, where the pressure vessel gives little buoyancy, removal may give a mass saving and improve the AUV mass ratio.

Pressure tolerant energy sources will only appeal in the correct workspace. A high energy density pressure sensitive battery source within a shallow diving AUV may, as a system, have an improved energy density than a pressure tolerant energy source. A deep diving AUV would benefit from removing the pressure vessel and utilising pressure tolerant batteries.

Without a large pressure vessel with a cylindrical shape, the AUV is then open to more design options of subsystem arrangement and hull shape. This will aid innovation and may enable a new AUV arrangement and shape that offers advantages over existing AUVs.

The next section reviews what energy sources are available with attention to their energy density and suitability for operation at pressure.

2.3 Energy sources.

An AUV has to carry its own energy source, and there are constraints on what type, mass and power this source takes. Each energy source has many properties that would make one source desirable over another. Some of the most important properties are: specific energy (Wh kg^{-1}), operating temperature, life cycle and economic cost. An overview of some of the energy sources available to an AUV is presented here.

2.3.1 Batteries.

Batteries are the most common form of energy source for an AUV. In Janes' Underwater Technology (Funnell (Editor) (2001-2002)) there are 61 AUVs, and 53 of them rely on batteries for their energy source. Technology has progressed during this research, and some of the battery chemistries initially investigated have almost dropped out of the commercial market. It appears that lithium technology (in all forms, primary and secondary, pressure tolerant and pressure sensitive) and fuel cells are more accepted. Each has been implemented in different vehicles.

Deciding between the two types of battery, primary or secondary remains a difficult choice during the AUV design and is driven by risk versus economic cost. Primary batteries, such as Mn-Al, are not rechargeable, though in general have higher specific energy and are a lower initial economic cost. Secondary batteries such as Pb - acid or lithium polymer are rechargeable. These generally have a lower specific energy, and are a higher initial economic cost, but recover in value with each charge/discharge cycle to give improved economic return.

Unique to the underwater application is the consideration of high pressure. Batteries with internal voids or manufactured from materials with very different elasticity ratios or require gas venting would not operate at pressure and may even be hazardous. Batteries, such as Pb-acid, can operate at pressure and so do not require a pressure resistant housing.

Table 2.1 shows a selection of energy sources and their properties of specific energy, energy density, energy cost and additional notes. This highlights the potential use of the diesel engine as an energy source, and also the potential benefits of fuel cells if they are developed into reliable

energy sources. Where original costs were specified in dollars, a conversion of 1.7 $/£ has been used.

The two units of Wh kg^{-1} and Wh dm^{-1} are a measure of the energy per unit weight and energy per unit volume. A Wh rating of 1 would mean that the battery is capable of 1 W (Joule per second) for an hour, a total of 3600 joules of energy. Doubling the power draw to 2 W will half the endurance to 30 minutes.

Pb - acid batteries have low energy densities and issues with environmental impact and material recyclability. They are available off the shelf, are inexpensive and a known technology. Autosub 1 successfully used Pb - acid for coastal trials, 7.5 kWh of energy was sufficient for 10 hours operation over 70 km.

Ag - Zn batteries require careful maintenance, have a limited life and are economically expensive (Abu Sharkh, *et al.* 2003 pp. 19 - 35), but have been used in AUVs. Odyssey IIb had a 10 kg pack that supplied 6 hours of vehicle operation (Bradley, *et al.* 2001).

Ni - Cd batteries are also understood, available off the shelf and can withstand physical and electrical abuse, however suffer from memory effects and cadmium is a restricted poisonous material (Shukla, *et al.* 2001).

Zebra batteries are a class of batteries invented in 1985 by Coetzer in Pretoria-South Africa, the technical name is Na-$NiCl_2$ (Shukla, *et al.* 2001). Liquid sodium metal is paired with other metals and in theory can reach 750 Wh kg^{-1} (Abu Sharkh, *et al.* 2003 pp. 19 - 35) though once insulation and structure has been added the results might be nearer that shown in Table 2.1 for the 'Rolls-Royce' produced Zebra battery. These batteries operate at 300 °C internally, and so require careful heat management even outside the battery, which would be a drawback when operating in Arctic or deep water (Bradley, *et al.* 2001).

Lithium polymer or lithium ion batteries are characterised by the electrolyte storing lithium salt, which moves from anode to cathode and back as the battery capacity is used. In a lithium ion this salt can be dissolved in a liquid or solid organic solvent, and in lithium polymer batteries the lithium salt is contained within a conductive solid polymer sheet. Lithium can be a fire risk and needs to be treated carefully, but with a suitable battery management system this should be controllable (www11).

Energy Source	Specific Energy [Wh kg^{-1}]	Energy Volumetric Density [Wh dm^{-3}]	Economic Cost [£ / Wh]	Notes
Pb-Acid[a,b]	20-35	60-90-	0.03[a] to 0.76[e]	Secondary battery, pressure tolerant. Used in test vehicles.
Ni-Cd[a,b]	40-55	60-130	1 to 1.71[e]	Secondary battery, environmental concerns. Not used anymore
Ag-Zn[a]	220	400	3 to 1.63[e]	Secondary battery, ~5 cycles of charge / discharge, Hydrogen generation.
Mn-Al	128	316	0.056 to 0.09 [e,g]	Autosub 2 energy source, now replaced
Lithium polymer[c]	190 varies with chemistry	360 varies with chemistry	1.6[c] to 1.76[e]	Secondary battery, Fire risk, experimental in 2003 (section 2.2), but increasing commercial usage
Zebra[d]	114	168.2		300°C internally, very slow to reheat if turned off.
Al-HP (Al-H_2O_2)[f]	101			Semi fuel cell for Hugin II and 3000, Safety and thermal concerns
Mg-AgCl[f]	200			"seawater battery" low power output, but efficient.
PEM fuel cell[a]	225-1000	200-800	5 to 15	Still experimental, operational fuel cells have lower energy characteristics, fire risk.
Internal combustion engine[a]	75	170	0.05 to 0.1	Fuel fire. Storage of fuel and oxygen will lower this estimate.
Diesel engine[a]	125	75	0.1 -0.2	Fuel fire. Storage of fuel and oxygen will lower this estimate.

References: a) National Research Council ("*National Research Council*" 2001)
b)S. Abu Sharkh (Abu Sharkh, *et al.* 2003 pp. 19 - 35)
c) Kokam website (www11)
d) Zebra battery factsheet (www12)
e) P.Stevenson (Stevenson, *et al.* 2002)
f) O. Hasvold (Hasvold and Storkerson 2001)
g) G.Griffiths (Griffiths 2005)

Table 2.1 Selection of available energy sources.

Lithium batteries are an attractive possibility for AUV designers, with high energy and power densities and operate both primary and secondary sources. They have been successfully used in ABE vehicle, where a 5.4 kWh pack gave the vehicle 30 hours for sea floor operation. Parallel plate lithium batteries are geometrically flexible, and present an option of producing unique battery shapes at manufacture. R. Gitzendanner *et al.* show that a lithium ion battery was manufactured as a semi-circle, and so could be packed within a cylindrical pressure vessel with 100 % packing density (Gitzendanner, *et al.* 2004). However this presented the problem that the energy source was overweight and required too much buoyancy for Gitzendanner's application.

Bluefin robotics have been developing and commercially marketing pressure tolerant lithium batteries. Whilst information has been scarce on the testing due to military funding, recent papers have been published by Bluefin in 2006, after the research in this thesis was presented. The packs created are 3.5kWh, have a mass of 31 kg have a specific energy of 116 Wh kg^{-1} or 360 Wh dm^{-3} (Robinson 2007). Battery and foam have a neutral energy density of 105 Wh kg^{-1} at 300 m (Banner, *et al.* 2006). Neutral energy density accounts for sufficient mass of foam to bring the battery back to neutral buoyancy. This form of energy density specified is not particularly useful here as it is dependant on the foam used and may not be a strict comparison method of battery technologies. These batteries were safety tested for physical and electrical abuse according to US Navy requirements. Safety was the first priority, and Bluefin have worked with their manufacturers to improve the battery design and have now tested upwards of 20,000 batteries (Robinson 2007). The analysis of batteries offers some life information. According to Robinson (2007) the average capacity fade is 2.67 % over 100 cycles.

Lithium polymer batteries have been identified as an area of research for Autosub and so an improved understanding is required. This includes confirming their operation at pressure and characterising them for energy source evaluation. To do this a testing methodology is required, and Doerffel presents a fast method for testing lithium – ion batteries (Doerffel and Abu Sharkh 2004). These batteries are similar to lithium polymer, so the method was examined and modified to a smaller lithium polymer battery. This theory and the author's experimental results are described in Chapter 4.

2.3.2 Fuel cells.

Fuel cells are a possible energy source once practical issues have been addressed, and present the prospect of electrical energy that can be recharged by refilling the fuel tank. This is preferable to a battery in that the energy transferable is enormous compared to recharging batteries. This technology comes in various types (Hasvold and Storkerson 2001) and most are still

experimental. This Thesis does not consider fuel cells specifically. They are included in the literature search because fuel cells are a developing technology and an appreciation of their capabilities and limitations will be useful for a design methodology. The design method in Chapter 3 could include fuel cells with some assumptions on the fuel cell representation within the method.

One major consideration of a fuel cell is that the fuel, especially hydrogen, has to be stored somehow, either as a gas (pressurised cylinders) or as a liquid (requiring cryogenic temperatures and thermal insulation). This presents safety concerns and requires much more system architecture to thermally insulate the liquid gas. Methanol is a preferred fuel for smaller fuel cells, as it is more easily acquired and stored, though for a hydrogen powered road vehicle the proton exchange membrane hydrogen based fuel cell is still seen as the leading candidate (Rand and Dell 2005).

NOCS has practical experience in a Ballard Nexa 1.2 kW fuel cell, and Griffiths gives an approximation of economic cost and performance (Griffiths 2005). A fuel cell could be fitted within a pressure vessel, with pressurised cylinders containing hydrogen, and cryogenically stored oxygen at a cost of £0.033 per Wh. This is competitive to most energy types in Table 2.1. The primary cost driver for batteries is the internal chemistry, the packing, storage and control system is a smaller cost that is similar for every battery pack of similar size. The fuel cell cost drivers come from adapting it to a marine environment and the storage of the fuel.

The Norwegian Defence Research Establishment and Kongsberg – Simrad operate the Hugin series of vehicles. Hugin 1 carried a Ni-Cd 3kWh battery (6 hours endurance) and a semi fuel-cell was developed for Hugin II. Hugin II uses an alkaline Aluminium/ hydrogen peroxide (Al - HP or Al - H_2O_2) semi fuel cell (Hasvold and Storkerson 2001). After finding that a magnesium /dissolved oxygen seawater battery could not provide sufficient energy for an AUV with a design range of 1852 km (1000 nautical miles) and more than the most basic low power payloads, another energy source was required. During the development of this AUV it was noted that near-term users were not interested in long range, but wished for more power for sensors and instrumentation (Hasvold, *et al.* 1999). The Al – HP fuel cell offers high power and energy densities though the system is complex in construction.

Hugin tried to make use of the advantages of operating an energy source at ambient pressure by removing the mass of the pressure vessel. This concept is also the motivation for the research presented in Chapter 3. Carrying compressed oxygen onboard within pressure vessels was considered but the need for a deep diving AUV would make these pressure vessels very heavy.

Furthermore oxygen from the cylinder would be increasingly inefficient at depth. Gas from pressurised cylinders must be delivered against the ambient pressure of the system. Pressure inside the gas bottle can be up to 20 MPa, so for depths greater than 2000 m, the pressure outside the bottle will be greater than pressure inside and so require a pump to remove gas, reducing the efficiency of the energy source (Hasvold, *et al.* 1999).

Hydrogen peroxide based fuel cells can be operated at ambient temperature as the hydrogen peroxide does not require a pressure cylinder, or special temperature storage. Hydrogen peroxide can be broken down into water and oxygen, at a rate of 47 % oxygen per kilogram of hydrogen peroxide. Hydrogen peroxide is a liquid and so can be stored within a deformable bag at ambient pressure, reducing the mass of the energy source. As the hydrogen peroxide is consumed a change in buoyancy of the energy source will occur, so an active buoyancy system will be needed for the vehicle. By carrying hydrogen peroxide as a fuel, Hugin II was able to reach 36 hours endurance after only a 1 hour deck time.

However concentrated hydrogen peroxide is unstable and very exothermic. Due to hydrogen formation from aluminium corrosion in the presence of oxygen, its use is limited to low concentrations, restricting the fuel cell energy density. Thermal control of the energy source is also required as it can corrode at warm temperatures, or fail at low temperatures, so needs to be kept at 30 °C to 40 °C. The personnel operating the AUV when launching, recovering and when refuelling also need special safety equipment to protect them from liquids such as waste electrolyte, for health and safety reasons (Hasvold and Johansen 2002). Unlike batteries, a fuel cell's voltage does not drop off during operation, but will vary with slight fuel flow changes, making the fuel cell more useful at the end of a long mission. As long as there is fuel remaining then the fuel cell can operate at full power, whereas a battery vehicle may have to consider low available voltage.

The 1.2 m^3 Hugin II vehicle at 2 ms^{-1} consumes 300 W for propulsion and 220 W for the hotel, and including a 65 % efficient DC / DC converter (the greatest loss in the system) the load on the semi-fuel cell was 800 W (Hasvold, *et al.* 1999). For the Hugin 3000 the DC/DC converter was replaced and the 2.4 m^3 vehicle endurance increased to 48 hours at 900 W power draw. The system weighs 472 kg and has a nominal energy of 50 kWh, and so estimated to have an energy density of 105 Wh kg^{-1} (Hasvold and Johansen 2002). In parallel to this fuel cell, it also has 21 F-class Ni-Cd batteries, which when included with a DC/DC converter and then added to the energy source mass, the specific energy falls to 100 Wh kg^{-1}. The conclusion is that pressure tolerant batteries at 3000 m offer a 50 % increase in energy density, though this is dependant on the exact construction of a protective pressure vessel. The semi-fuel cell was chosen for the Hugin 3000,

though pressure tolerant lithium batteries would become the energy source of choice in later years (Hasvold and Storkerson 2001).

JaMSTeC have developed a fuel cell for "Urashima" (Sawa, *et al.* 2004). This is a 4 kW closed cycle solid polymer electrolyte fuel cell where hydrogen is stored within a metal hydride. The hydride removes the need for pressure vessels to store the hydrogen, making the energy source safer, but requires a mass of metal to store the hydrogen. The hydride type (AB_5 – a mix of nickel and rare earth) used for Urashima absorbs hydrogen at 0 °C, and requires over 50 °C to release hydrogen, constraining the fuel cell to work at this temperature. Urashima adopts a hot water system, where the fuel cell needs to dissipate 50 % of its energy as heat, which is absorbed by water and passed over the hydride to warm the fuel source. With this fuel cell, the Urashima was able to autonomously cruise for 21 km over 6 hours and consuming about 10 % of its hydrogen capacity. A peak power draw was reached, and so a lithium – ion battery pack was included to handle peak power draws. In June 2003 Urashima achieved a world first 220 km continuous cruise with a fuel cell, and then in July 2005 extended this distance to 317 km (www13).

Fuel cells are becoming more prominent in land vehicles, and may provide power for AUVs, however, the energy storage presents a problem. Compressed hydrogen cylinders are pressure vessels, and suffer all the same drawbacks as a pressure vessel when operating at depth. Solid hydride has been tested, but it is still an experimental storage method.

2.3.3 Other energy sources and future developments.

In the early manned submarines, and the AUVs Dolphin, Dorado (Funnell (Editor) 2001-2002), R1 Robot (www14) and SASS (S. Phillips, *et al.* 2007) power was supplied by a diesel engine, either directly or by charging a battery pack. This would require running at the surface with access to the air via a snorkel, and then charging a battery bank. The energy used whilst submerged comes from these batteries. This method was inexpensive using the technology available, though is not mass efficient. The diesel engine would not be used during the dive, and so becomes an added mass.

Closed cycle diesel engines use known technology operating on air supplied from pressurized cylinders, such as in the R1 robot AUV (www14). The closed cycle diesel engine would still have to operate within a pressure vessel, as the engine block has to retain ambient pressure. At 5 kW output and a mass of 5 tonnes, the closed cycle diesel engine would operate for 60 hours, and generate an effective specific energy of 60 Wh kg^{-1}. The closed cycle diesel engine will have a higher specific energy compared to Pb - acid batteries (25 Wh kg^{-1}) though not as high as Mn - Al

batteries (128 Wh kg^{-1}). Unlike batteries, a closed cycle diesel engine has a minimum mass of engine, before fuel mass is added, so there is a minimum mass for the energy source. The time to refuel the diesel tank is much shorter than to recharge batteries, due to the high calorific value of diesel (44,000 kJ kg^{-1}), and a high energy delivery rate (W).

Modern internal combustion engines are becoming more efficient, currently about 35% efficient for diesel engines. The American Department of Energy have announced that they are contributing $85 million to 12 projects worth $175 million, investigating advanced combustion engine and waste heat recovery technologies (American Department of Energy press release (www15 2005)). Due to ongoing research, low cost and easy repair of diesel engines, the concept of a closed cycle diesel engine as a power source should not be completely ignored as a near term available technology.

There is another power system used in the Slocum thermal glider built by Webb Research Corporation. This employs a special hydrocarbon fluid, which changes state over the range of temperatures found in the ocean. The change of state means a change in volume, and hence a change in buoyancy. This engine is quite inefficient, but due to the large heat sinks (the ocean itself) used in the thermal reaction, this is not a significant factor. When installed in a vertical profiler, doing nothing more than changing the depth of the buoy, the thermal engine lasted 240 days. Webb research predicted an endurance of 5 years for the Slocum thermal glider (Webb 1999). If the endurance of the AUV is as long as five years, it is likely that the energy will no longer constrain the AUV, rather the guidance method, mechanical failure or corrosion will limit the AUV. The thermal glider is a prototype vehicle and was first tested in the ocean in December 2007 (Woods Hole Oceanographic Institution, 2008). This energy source would only be suitable for a gliding AUV that does not require neutral buoyancy.

Looking to the future, what is the likely path for energy source research? Fuel cells are still being researched, and there could be large jumps in energy and efficiency meaning that they could become the energy source of choice. Currently the nature of their power production means that the power fluctuates with time. It is likely that batteries will have to be placed in series to add power and smooth the output.

The original source of the energy can be a concern, especially renewable energy sources: solar; thermal; and wave. An AUV could surface or dock within a garage, charge its batteries and then continue its work. At the surface the AUV could either charge from solar energy, or from wave motion. Geothermal energy stations or methane pumps supplying turbines with fuel to then

generate electricity could be mounted on the sea bed, allowing an AUV to dock, recharge and download data without having to surface.

Most research into environmental energy is at the source; how to create the energy in a sustainable fashion? The AUV will still need to store the energy in some manner, hence battery technology or hydrogen based fuel cells will have critical roles in the future.

2.3.4 Energy source conclusions.

The mass of the pressure vessel has been considered by a number of authors as a limiting factor on the diving depth of a vehicle. The prospect of a pressure tolerant energy source would reduce the volume of ambient pressure space required, and hence the mass of the pressure vessel.

A. Bradley *et al.* conclude after a careful review of available battery systems, that a pressure tolerant battery system would be "the biggest improvement for the AUV community for the near future" (Bradley, *et al.* 2001). This was written in 2001, and pressure tolerant lithium batteries have been the subject of this research, and of intensive research by Bluefin robotics, who now manufacture battery packs commercially. AUVs do now exist with pressure tolerant energy sources, either in fuel cell (Urashima) or battery form (Autosub 6000, Bluefin 9, 12 and 21). The technology is available for pressure tolerant energy sources and the beginning of the next generation of AUVs with them are appearing. These are often retrofitted to an AUV, Autosub6000, or the AUV shape still follows previous designs, Bluefin.

Batteries are likely to remain the technology of choice for the near future, and will likely continue to serve in hybrid energy sources for a time after that. Although there are alternative energy sources, such as fuel cells or renewable energy, the economics of the energy source has to be considered. A battery energy source has the advantages of being a proven technology, and so the factors of cost, safety, maintenance and supply are established and understood. Even when technology has advanced sufficiently to create proven and economically viable alternatives, the battery will likely be included in the system, either as a method to stabilise the power output of a fuel cell, or to store energy created by renewable sources.

From talking to industry at the Unmanned Underwater Vehicle Showcase (annually 2003 - 2007) it was possible to get some feedback from industrial end users and manufacturers. During the course of this research, lithium technology has become much more accepted commercially, and there are more vehicles and systems using them in 2007 than in 2003.

This has provided an overview of energy sources available to AUVs. The concept of a pressure tolerant battery pack and is revisited in Chapter 4 with the advantages of removing or

reducing the pressure vessel in Chapter 7. The design methods found in literature are reviewed next.

2.4 Design methods.

2.4.1 Engineering design methods.

General engineering design methodology is reviewed first, to show the fundamental iterative nature of design. As no bespoke AUV design methods are available this progresses to the design of manned submarines which represent a major underwater vehicle. Since AUV design is also concerned with efficient use of internal space, mathematical and computational packing methods are considered, to find if any exist that might assist with the challenges of AUV design and be transferred to an AUV design method.

Many phases of a design process have a feedback element, as problems are solved, to refine previous decisions and specifications. Pahl and Beitz represent this process as a flow chart with work progressing down the chart, and feedbacks leading to a previous step (Pahl and Beitz 1988). Cross adopts the design flow (Cross 2000), see Figure 2.16. The 'need' will come from an end user. The 'analysis of the problem' will involve detailed communication between the engineer and end user to establish and specify a set of engineering objectives. The 'statement of design objectives' will distil these objectives into design constraints. The 'conceptual design' will explore broad solutions and this phase provides opportunity for innovation. The 'selected schemes' are a shortlist that the end user finds acceptable. The 'embodiment of schemes' explores these designs in detail and selects a preferred solution. This solution is then moved to 'detailing' a final design.

With many designs, the system interactions are conflicting, and so to maximise one aspect would severely limit another aspect. This leads to a balancing act of finding a compromise of these aspects to find a solution that fulfils all three (Burcher and Rydill 1994 pp. 1 - 4).

Within the design process the satisfaction of different requests and constraints will lead to conflict regarding the direction of design. Optimising one aspect can limit others. Consequently the final design is a compromise in terms of fulfilling all the requirements.

The challenge of this thesis is to turn Figure 2.16 into a design methodology to produce a scientific tool that meets the requirements of completely different mission scenarios.

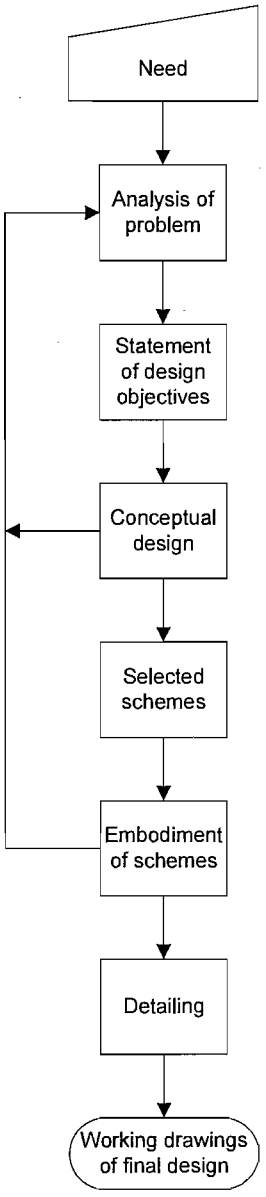

Figure 2.16 Steps of the design process.

To create a new AUV design the engineer is presented with the option of building a new concept vehicle or to modify an existing vehicle. A new design offers the opportunity to explore new technologies and techniques, but 'blue sky' options must be tempered with recognition of implementation difficulties and development costs. Modifying an existing vehicle is another iteration of its design cycle, and necessary to keep it up to date with improved technology. Both approaches have a degree of uncertainty that must be examined to provide new benefits and compromises.

The design process of an AUV is heavily influenced by existing systems, procedures and the experience of the engineer. Rarely is the design free from external influences. As a scientific tool the development of an AUV can be seen as a three tier system. At the top is the support vessel, next the AUV itself and then the sensors and equipment mounted on the AUV (Griffiths 2000). The AUV must meet the requirements from the top tier whilst imposing constraints on the bottom tier. For example, the commercial AUVs produced by Bluefin have diameters of 9 inches, 12 inches and 21 inches, to match existing torpedo launch systems.

Most AUVs, as discussed in section 2.1, exhibit long cylindrical forms, which can trace its roots back to manned submarines and the need for a single large pressure vessel (Burcher and Rydill 1994 pp. 11 - 24). The sphere is the strongest pressure vessel (and mathematically highest volume to surface area ratio), and it can be most easily extended into a cylinder (Benham, *et al.* 1996). In AUV design the pressure vessel is still required to protect pressure sensitive computer components.

Given the surface area influences hydrodynamic drag and that cylindrical pressure vessel have larger volume to surface area ratios, the smaller the proportion of AUV volume occupied by the pressure vessel the easier the challenge of adopting AUV envelope shapes with hydrodynamic advantages.

The Autosub hull shape has not changed greatly since its creation, maintaining a bow, parallel middle section and stern. For the Autosub 6000 the initial designs illustrated a very different vehicle, with a laminar flow hull and spherical pressure vessels, designed specifically for deep depths and low propulsion power (Figure 2.17*i*). This hinged on a pressure tolerant energy source being utilised.

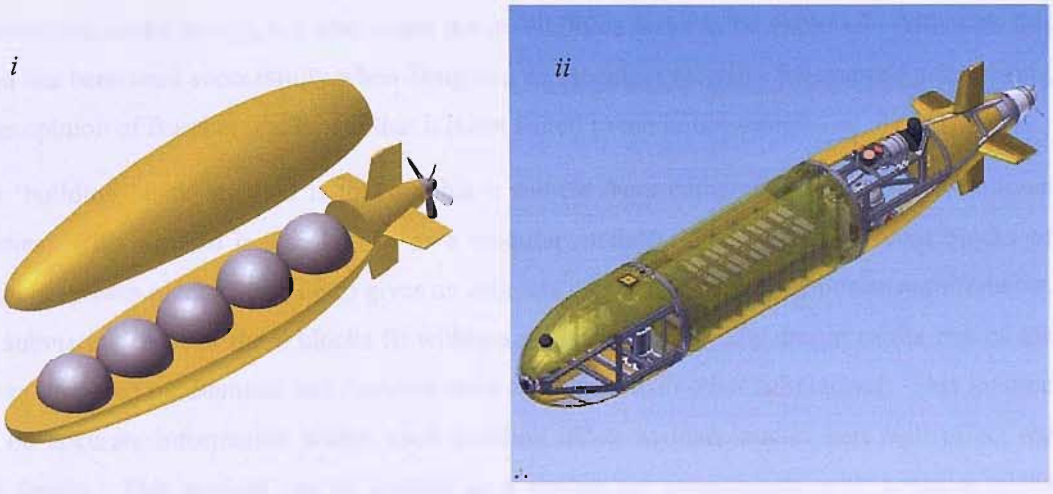

Figure 2.17 *i*) Concept sketch of Autosub 6000 and *ii*) Autosub 6000 as built.

When the lithium polymer batteries were shown to work at pressure, Chapter 4, the concept of Autosub 6000 became possible from an energy standpoint. The batteries would still be placed within the vehicle, though their positioning would depend on the sizing of the spheres and overall vehicle. However during the design cycle, the more real practicalities of economic cost and development time meant that this design option had to be pushed aside in favour of a design more similar to Autosub 2's original design (Figure 2.17*ii*). The operational Autosub 6000 design (trialled in September 2007) has instead maintained Autosub 2's bow and stern but has a new shortened middle body length. Therefore Autosub 6000 is constrained to have the same radius as Autosub, and will have the same fluid flow over the bow.

External variations of outer AUV form hide much of the associated design decisions concerning interior arrangement and content. With the literature AUV hull shape, different subsystems and AUV technological needs are discussed in isolation. A procedure to integrate these aspects into AUV design remains a challenge that is relatively unpublished.

Just as submarine design has drawn from the more established surface ship design procedures, so AUV design (with its lesser constraints) might draw from submarine design.

Burcher and Rydill give a summary of submarine related design methods. Three methods of vehicle design cited are designated, 'type ship', 'building block' and 'graphical methods'

(Burcher and Rydill 1994 pp. 247 - 251). 'Type ship' involves selecting an existing ship whose deficiencies are known and using this form as a base design. If a system is to be replaced, then it must not deviate much from the original systems mass or volume, if outside the pressure hull, and must still make all physical and electrical connections. This limits the replacement system improvements to those that do not require modifications throughout the vehicle. This can be the least intensive methodology, but also limits the possibilities that can be explored. Although this method has been used successfully when designing replacement modules for manned submarines, it is the opinion of Burcher and Rydill that it is not suited to the initial design.

The 'building block' method is to assemble a vehicle from component volumes with known properties. This method is also known as a modular method. The sum of selected blocks of equipment (power plant, sensors etc) gives an estimate of volume, mass and power requirements. For a submarine most of these blocks fit within a pressure vessel. The design of the rest of the boat can be based on diameter and fineness ratio compared with other submarines. This method relies on accurate information within each building block as inaccuracies here will affect the whole design. This method can be applied as a simple list unconcerned with position of the systems, or graphically with a simplified diagram of the vehicle (3D computational models help here) or as a spreadsheet, with mass, volume and mass moments.

A similar system called the "weight displacement centres summary" gives a table listing the weight centre of gravity (*CoG*) and the displacement centre of buoyancy (*CoB*) for each system (Allmendinger 1990). Listing each subsystem will add detail, which is required in later design stages, but can slow the initial concept design. For a small system this may not be a problem, but for large complex structures with many subsystems initial design may be hindered. Autosub uses a similar method for documenting stored equipment and its position within the vehicle. However this was only applied after the vehicle was built, and is used for varying the payload or sensors.

'Graphical methods' might be compared to the keystone within a bridge, designing a detailed solution for the key part of the system and then scaling the rest of the vehicle based on this. Experienced submarine designers know that the bow of the vehicle leads on to scale the whole vehicle (Burcher and Rydill 1994 p. 250). Is the key subsystem of an AUV as identifiable? US Navy AUVs can be characterised by their diameter, which is based upon torpedo diameters to facilitate integration with existing systems. An 8 " diameter cylinders ~100 lbs 21 " diameter cylinder ~2800 lbs, and greater than 21 " diameter weigh 5-10 tonnes (Saint-Amour 2007).

This procedure can lead to creating a number designs for consideration, which can be detailed, but equally the most time intensive. Advocacy for this method can be a result of design

experience or when improving an existing vehicle, as the majority of the vehicle may already be established. Submarines can also benefit from known proportions, e.g. the payload volume is 30% of the pressure hull volume (Burcher and Rydill 1994 p. 253). Whilst such a relationship may exist within an AUV, it is not as definite and probably varies for each system. The mass ratio for an AUV in section 2.2.1 supports that there is a trend, but also shows the variation that exists.

2.4.2 AUV internal arrangement.

An AUV has more options available for its internal construction and less rigid guidelines than a military submarine, in part due to its lack of human passengers. To address internal arrangement of AUVs 'packing' methods are considered as a tool to assist design.

Dowsland and Dowsland present a nesting method for tackling the problem of packing irregular shapes (Dowsland and Dowsland 1995). This method seeks to pack a number of irregular shapes into a simple polygon or rectangle (Figure 2.18*i*). The Dowslands comment each industry has developed its own approach, meaning there are many possible solution approaches. Each method has its own strengths and weaknesses, but there is no single overall preferred method. In conclusion, whilst there is much published work available, more is required and a purely automated system cannot reliably outperform a human expert.

Nesting is a method of approximating complex items into rectangles, making rectangular packing methods more applicable. Nesting will be used in this research to simplify more complex subsystems into more manageable shapes. To represent a subsystem the 'nested shape' will have to enclose the physical subsystem and allow volume for any required connections and mountings (Figure 2.18*ii*). Using packing methods for the nested shapes still relies on provision of a rectangular boundary and the subsystems could be only packed into a box.

Research exists into the packing of rectangles into larger rectangles. Common industrial examples are the packing of containers, cutting sheets of metal, cloth, paper from rolls of material, and stamping shapes from a sheet of material. Additionally the packing of circles and irregular shapes into set boundaries has been considered, although the irregular packing problem is "less well studied than the rectangular version of the problem" (Dowsland and Dowsland 1995).

i

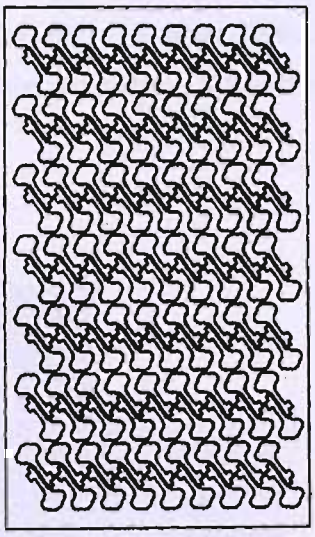

ii

Figure 2.18. i) Nesting of keys within a rectangle with 83.84 % utilisation ratio and *ii*) example nesting of ADCP within polygons.

Lodi describes a number of existing techniques for packing different size rectangles within another rectangle (Lodi, *et al.* 2002). These techniques are restricted to a 2D problem requiring all the rectangles to have an axis parallel to the horizontal and do not allow rotation of the rectangles. Techniques employed include integer linear programs involving non-polynomial forms of variables and those named; *Next-Fit Decreasing Height*, *First-Fit Decreasing Height*, *Bottom left* and associated hybrids (Berkley and Wang 1987). Figure 2.19*i* shows a bottom left system, where the rectangles are sorted by decreasing height then packed into the bottom left of the boundary first. Figure 2.19*ii* shows a first fit decreasing height packing algorithm, where a new level is only created if the next piece cannot fit into the current level. These "bin allocation" packing methods are suited to rectangular items placed within a rectangular boundary.

AUV subsystems are rarely rectangular. The pressure vessel required to protect pressure sensitive components enforces spherical or cylindrical shapes. The possibility of splitting a transversal AUV cross-section into quadrants provides perpendicular straight lines. One might consider adopting a rectangular packing method as illustrated in Figure 2.19*i*. A lengthwise cross-section of a parallel middle body might also be considered a rectangular area suitable for packing. For other hull forms and associated boundary shapes, other approaches are required.

The inverse problem of packing rectangles into circular boundaries is found in the challenge of maximising the number of rectangular semi-conductor chips produced from a circular silicon wafer (Fukagawa, *et al.* 2005). The adopted approach is graphical. Since all the chips are identical rectangles, Fukagawa considers the wafer centre to be located at some point within a

central chip's boundary. A wafer centre location is then found that maximises the number of rectangles with the wafer circle. Applications vary from 4 to 10,000 rectangles within a circle.

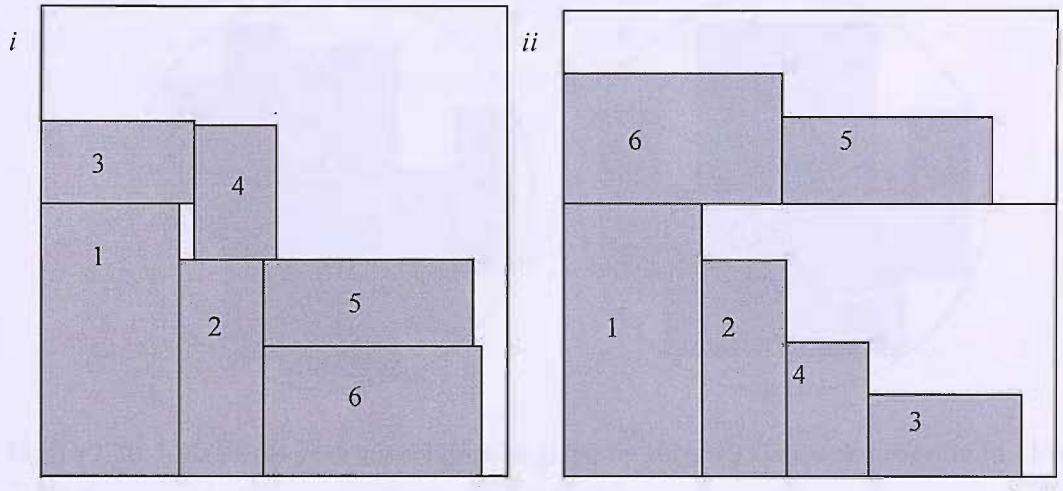

Figure 2.19. Two bottom left packing methods *i*) level packing and *ii*) normalised level packing.

This large number of rectangles is outside what a human expert could produce and so suited to an automated solution. The computer automation is only described for solving the networking problem that is derived graphically. No detail is presented on how the networking problem is generated using computational methods. This approach might be applicable to packing batteries within a pressure vessel.

Perhaps most directly suitable to AUV packing is a non-linear method of packing identical rectangles within an irregular convex shape (Birgin, *et al.* 2005). Individual rectangles must remain parallel or at 90 ° to the horizontal. The algorithm is provided as a Fortran 77 file (www16). The method leaves gaps between rectangles (e.g. batteries), but these can be removed manually or by using an 'annealing' based packing algorithm.

The complex packing produced by Birgin's method would not help battery access or maintenance, as the engineer would need to remove most batteries to get to one battery, and then remember where to replace all the batteries. This code would still be useful where the loss of one battery would not significantly affect overall pack performance, or within a disposable AUV. Figure 2.20*i* illustrates an application of this program. Nine Autosub 6000 Lithium-polymer battery packs are packed within the Autosub parallel middle body cross section. These batteries are not aligned with each other and have gaps between them. Increasing the search time did not modify this packing arrangement. It is possible for the human engineer to improve on this

alignment, removing spaces and making the cross-section more hydrostatically balanced, Figure 2.20*ii*.

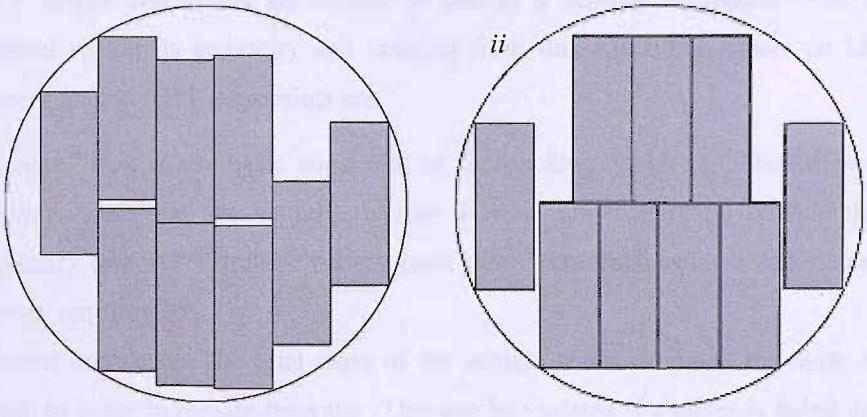

Figure 2.20. *i*) Example packing solution as given by Birgin's Genpack program in 11 trials and 0.4 seconds and *ii*) annealed solution by Author

The packing methods described and applied are essentially 2D and not immediately applicable to AUV internal volume design. Transverse or longitudinal slices might be used, but would be constrained to minimise wasted space and the third dimension (stacking 2D slices) would require consideration. AUVs require the centre of buoyancy and the centre of gravity to occur in the same vertical plane, so packing must reflect both shape and mass of each subsystem.

Batteries generally have a greater density than water and may be placed at the bottom of a vehicle, whilst positively buoyant pressure vessels and foam placed near the top. Pressure tolerant batteries and reduction of pressure vessel volume increase the packing options and hydrostatic / roll stability of an AUV.

The location and orientation of some subsystems are constrained, e.g. the motor must be at the AUV stern with the drive shaft parallel to the centreline. Permitting subsystems to be restricted to preferred locations requires the packing method to accommodate such requirements.

The packing boundary might not be defined or might vary with the design iterations. E.g. the hull shape might not be selected and might vary with design evolution. Therefore a packing boundary identification method is required.

This review of the packing methods suggests that there are as many methods as there are applications, and none have been found that cover all the needs of AUV design. Development of an AUV design methodology will loosely follow the adopted submarine design methods, to fulfil

the indicated AUV constraints. The nesting concept will be applied to identify subsystems within the AUV.

The AUV design constraints are similar to that of a manned submarine. The AUV has a pressure vessel within its geometry and drawing from this and other papers on technical and practical requirements AUV constraints are:

1. Volume. This is the basic constraint of the packing problem. The shapes all have a volume, such that the batteries cannot overlap, and cannot go outside the geometry boundary (e.g. AUV hull or battery pack side). The final volume and shape will affect energy requirement.
2. Neutral buoyancy. The total mass of the vehicle needs to match the mass of displaced water in order to remain buoyant. This can be violated if a glider is being designed, but this is a major design decision to create an alternative solution.
3. Energy. The AUV must carry its own energy source to complete its design mission. The energy required is based on many subsystems and on an unknown propulsion power, such that it is hard to initially size the energy source. Minimal hydrodynamic drag assists endurance.
4. Mass and moments. The mass of each subsystem will need to be considered, such that the *CoG* is suitably positioned around the *CoB*. A difference between these two will cause a force moment, and are important for aligning the AUV within 3D space.
5. Payload. The payload will have its own constraints on where it is mounted, and this may impact the packing of the energy source. Some items will require mounting in the bow, others will require mounting with water interaction or with contact with the outer surface of the AUV hull. Some will require pipe connections to each other, and these pipes will have a minimum bend radius, restricting placement of the two payload systems.
6. Nesting. Subsystems are rarely a simple geometric shape and come in all shapes and sizes with connectors, bolts etc all protruding. To simplify the packing problem and design process, these subsystems will be assumed to be the shape of the minimum simple geometry
7. Control. The AUV needs to be controllable by on-board systems. This is a large computational and programming challenge, but it is outside the scope of this research.
8. Damage protection. The AUV will suffer from damage though its working life, sometimes from collision with the ship during launch and recovery. The subsystems inside should be protected from this. For instruments that need to be mounted on the hull surface this is not possible. For the energy source, it should be possible to mount the

batteries sufficiently deep within the AUV hull to protect from any damage. To give a space between the hull shape and delicate subsystems, the hull shape boundary can be set smaller than the actual hull shape.

2.5 Conclusions.

Current AUVs, energy source options, the proportion of energy mass and the creation of pressure vessels have been discussed. Most AUVs use a pressure sensitive energy source. This is housed within a pressure vessel that provides buoyancy at shallow depths, but can become very heavy when operating at deep depths. The pressure vessel also tends to be a large cylinder, and likely to be the main cause for most AUVs having a parallel middle body "torpedo" shape. There are very few pressure tolerant energy sources, the most understood being Pb-acid but these have low energy density. There is no pressure tolerant high energy battery available. Fuel cells are possible, although as an emergent technology they would require research outside the scope of this thesis. A pressure tolerant energy source is an identified need.

The public domain design methods are either very general or specific to their application. No specific AUV design method has been found in literature. Such a design method will be created in this research. No automated packing methods have been found that might be readily applied to 3D AUV packing. The concept of nesting subsystems for representation within a packing method will be utilised.

Being free to alter the hull shape is only of use if there is understanding of how various shapes perform in terms of drag. Also of benefit is knowledge of how to increase the volume or dimensions of an AUV without significantly increasing the hull drag force.

The next Chapter presents the analytical equations used to estimate AUV endurance, and considers the design logic. This will illustrate the effect of increasing the energy source and hull shape drag on AUV range.

Chapter 3
AUV endurance and design.

This Chapter explores the parameters that control AUV endurance focussing on drag and the interplay of propulsion and hotel power. The interactions between the parameters are illustrated and iterative design logic is explored. Analytical equations are useful for the initial conceptual design assessments. A quantified example of these equations will be generated.

The purpose of this investigation is to narrow down the research areas of energy and hull shape as identified in Chapter 2. The energy source capacity may need to be increased, but in what manner and can this increase be quantified? The hull shape needs to be controlled, how will this affect the endurance? Following the information flow through these analytic equations there will be increased understanding of the priorities and conflicts within AUV design. This process has lead to the creation of logic flow charts that help communicate the iterative nature of AUV design.

3.1 Hydrodynamic drag equations.

Hydrodynamic drag force can be separated into pressure (form) drag and friction (viscous) drag. Pressure drag is caused by the resultant of pressures acting over the hull as it moves through the fluid. Frictional drag is caused by the fluid shear stress acting tangentially over the body surface. Pressure drag is a function of volume, and frictional drag is a function of surface area. Although volume and area are linked, they vary for each shape and so the drag will potentially vary for each shape. As the viscous drag acts over the hull surface this drag component is influenced by the state of the fluid boundary layer closest to the hull. The resulting force can be reduced by minimizing the surface area of the hull. The boundary layer and the computation approximation are more complicated and will be discussed in Chapter 5. An ideal shape would have the maximum internal useful volume for a minimal surface area. The theoretical best shape for this is a sphere, but this has a high pressure drag, boundary layer wake and practical issues with manoeuvring and manual handling.

The aim of minimizing surface area to volume ratio is the basis for classical submarine and airship design (Burcher and Rydill 1994 p. 105). Airships started with this philosophy, becoming the shape shown in Figure 3.1*i*. Submarines had practical issues to overcome, initially they were designed more like surface ships due to the amount of time spent on the surface. Later they were able to be shaped suitably to their underwater operation.

The continually changing diameter of the airship form was fine for a flexible hull, but leads to high construction costs for a pressure vessel. A cylindrical parallel body is introduced to lower production costs making the submarine shape of Figure 3.1*ii*. The shape of most rotationally symmetric AUVs is the progression from the design of manned submarines and unmanned torpedoes.

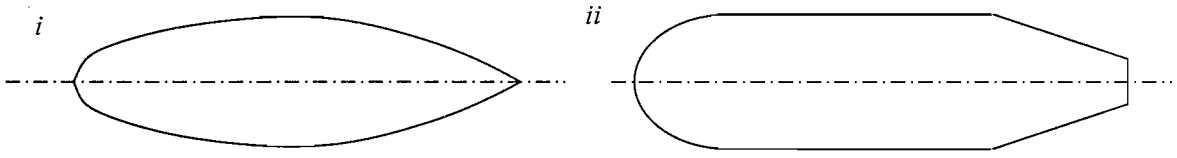

Figure 3.1 *i*) Ideal airship profile shape, with parabolic stern and elliptical bow and *ii*) common torpedo / submarine profile shape with parallel middle body.

Given these effects, there will exist optimum shapes for desired drag forces at a specific speed. The performance of shapes at different velocities will be explored in Chapter 6. The equations explaining the effect on drag are presented in section 3.2, after definition of related non-dimensional coefficients.

3.1.1 Non-dimensional coefficients.

Defined here are three non - dimensional coefficients that will be used within this thesis.

3.1.1.1 Coefficient of drag.

$C_{D\nabla}$ is required to estimate drag and propulsion power. $C_{D\nabla}$ satisfies equation 3.1.

$$C_{D\nabla} = \frac{2 \times Drag\ Force}{\rho_W \nabla_S^{2/3} U_\infty{}^2} \qquad 3.1$$

U_∞ is the free stream fluid velocity. ∇_S is the hull shape volume and the $\nabla_S^{2/3}$ variable is used in place of hull shape surface area as can any other variable with dimensions of m^2. It is important to be aware of which input value is used when comparing different $C_{D\nabla}$ values. In this thesis a subscript will indicate which input has been used. $C_{D\nabla}$ used $\nabla_S^{2/3}$ and C_{DSa} uses surface area.

The drag force is also affected by the shape of the AUV, and can vary for shapes with the same comparable volume. ∇_S does not describe the shape of the AUV, hence the $C_{D\nabla}$ value will model the shape influence. $C_{D\nabla}$ values are non-dimensionalised by ∇_S and allow the AUV volume to be scaled in size whilst maintaining a hull shape $C_{D\nabla}$. ∇_S is easier to estimate than the surface area of a complex hull form, so $C_{D\nabla}$ is perhaps the most useful coefficient of drag to an engineer.

This coefficient can express the efficiency of the body. A lower C_{D_∇} does not immediately mean a lower drag, rather more volume is carried for a specific drag. Conversely a very small complex body may have a lower overall drag than a large simple body, but the C_{D_∇} may be higher as too much volume has been sacrificed to achieve a lower drag.

The boundary layer affects the drag of the vehicle, and this coefficient can begin to approximate the effect on the total drag. As with the overall drag force (Chapter 2), the non-dimensional coefficients can be separated into component parts, see equation 3.2.

$$C_{D\nabla} = C_P + C_F \tag{3.2}$$

Where C_P is the component of drag due to pressure effects and C_F is the component of drag due to viscous friction.

3.1.1.2 Cylindrical coefficient.

The cylindrical coefficient (C_Θ) is a measure of the bluffness of a rotational shape. It is the fraction of the volume of a comparable cylinder with the same diameter as the rotational shape. It is comparable to a ship's Block coefficient, which is an expression of the bluffness of the ship hull (Rawson and Tupper 2001 p. 12).

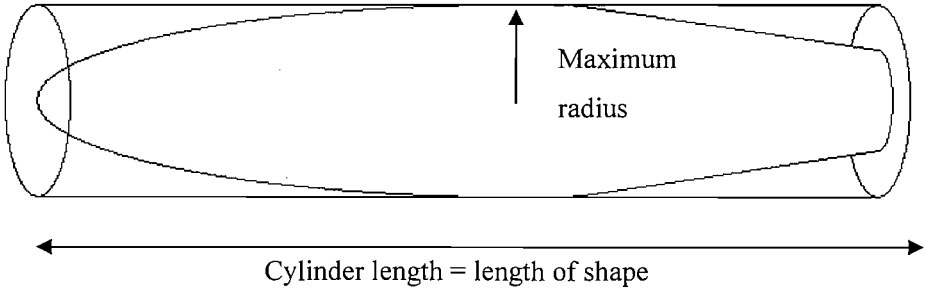

Figure 3.2 Cylindrical coefficient, the proportion of a cylinder filled by rotational shape.

The surrounding cylinder has the same length as the shape, and the cylinder radius is the same as the shape maximum radius. Cylindrical coefficient (C_Θ) is defined by equation 3.3.

$$C_\Theta = \frac{\nabla_S}{\pi R_{Max}^2 L_{AUV}} \tag{3.3}$$

A high value of C_Θ will mean the shape fills an encircling cylinder of the same length and radius, perhaps having a very bluff bow. A vehicle with a parallel middle body section will tend to have a high C_Θ. This coefficient is used to separate the drag predictions made by the computational models in Chapter 6.

3.1.1.3 Fineness ratio.

The fineness ratio of a shape is the ratio of the length to diameter and is defined in equation 3.4. This provides a numerical measure of shape slenderness. A high fineness ratio value will imply that the shape is long and slender, and a low value implies the opposite. A fineness ratio of 1.0 could imply either a short cylinder or a sphere.

$$Fineness\ Ratio = \frac{L_{AUV}}{2R_{MAx}} \tag{3.4}$$

A high fineness ratio body will not necessarily give a high C_{Θ} value, as the bow and stern might be very curved and the shape have no parallel middle body section.

3.2 Mathematical analysis of AUV parameters.

A primary limitation on AUV operation is its endurance and range. The improvement of both can be an important objective for AUV designers. It is possible to express AUV range as an equation based upon velocity, energy and drag. This section will explore this relationship.

The endurance of an AUV is dependant on the energy available and power draw. An AUV generally uses power in two ways, propulsion (P_{Prop}) and powering the onboard systems and payload (P_{Hotel} and $P_{Payload}$). The P_{Hotel} and $P_{Payload}$ can be constant over the mission duration or fluctuate with subsystem operation (Alers 1981). The energy carried onboard the AUV can be found from the specific energy and mass of the energy source as shown in equation 3.5.

The units of specific energy (Spe) of the battery chemistry are Wh kg^{-1} so the energy will be measured in Wh. The energy gravimetric density (ρ_E) denotes the battery mass per unit volume and ∇_E the volume of energy.

$$\begin{aligned} Energy &= Specific\ energy_{Batteries} \times \rho_E \times \nabla_E \\ &= Specific\ energy_{Batteries} \times Mass_{Batteries} = SpeM_E \end{aligned} \tag{3.5}$$

ρ_E can be found using equation 3.6 and the variables for each battery chemistry were presented in Table 2.1.

$$\rho_E = \frac{Spe}{Energy\ Volumetric\ Density} \tag{3.6}$$

P_{Prop} is the power required to overcome the drag force at the operational velocity accounting for propulsion inefficiencies. Drag increases with velocity squared from equation 3.1, rearranged to give equation 3.7

$$Drag\ Force = \frac{1}{2} C_{D\nabla} \rho_W \nabla_S^{2/3} U_\infty^{\ 2} \tag{3.7}$$

Power is the rate of doing work, so the required propulsion power is equation 3.8.

$$P_{Prop} = \frac{Drag \times Velocity}{Efficiency} = \frac{C_{D\nabla} \rho_W \nabla_S^{\frac{2}{3}} U_\infty^{\ 3}}{2\eta_{PT}} \tag{3.8}$$

Where η_{PT} is the non-dimensional efficiency of the power train from the energy source to the water. This includes the motor and propeller inefficiencies.

If a designer knows the desired volume, the operating speed and the $C_{D\nabla}$ of the AUV, then AUV drag can be estimated. The challenge comes when these inputs are not known, and the designer has only specified AUV endurance.

For constant U_∞ and $C_{D\nabla}$ decreasing AUV ∇_S reduces the drag resistance, hence P_{Prop}, will decrease according to $\nabla_S^{2/3}$. In contrast the displaced mass and the energy capacity will decrease proportionally with ∇_S. This implies that the energy decreases by a greater amount than is saved by reducing drag forces.

Knowing the energy source capacity and the required total power the endurance is given by equation 3.9.

$$Endurance = \frac{Energy}{Total\ power} = \frac{SpeM_E}{\frac{C_{D\nabla} \rho_W \nabla_S^{\frac{2}{3}} U_\infty^{\ 3}}{2\eta_{PT}} + P_{Hotel} + P_{Payload}} \tag{3.9}$$

Assuming constant AUV velocity, the range of the AUV is simply equation 3.10.

$$Range = \frac{SpeM_E U_\infty}{\frac{C_{D\nabla} \rho_W \nabla_S^{\frac{2}{3}} U_\infty^{\ 3}}{2\eta_{PT}} + P_{Hotel} + P_{Payload}} \tag{3.10}$$

Using the quotient rule the derivative of range with respect to velocity is equation 3.11.

$$\frac{dRange}{dU_\infty} = SpeM_E \frac{P_{Hotel} + P_{Payload} - \frac{C_D \rho_W \nabla_S^{\frac{2}{3}} U_\infty^{\ 3}}{\eta_{PT}}}{\left(P_{Hotel} + P_{Payload} + \frac{C_D \rho_W \nabla_S^{\frac{2}{3}} U_\infty^{\ 3}}{2\eta_{PT}} \right)^2} \tag{3.11}$$

Range will be a maximum when $dRange / dU_\infty = 0$. One can ignore *Spe* of $M_E = 0$ as this would imply zero endurance (equation 3.9). Hence the required U_∞ to achieve this range is given by rearranging the numerator of equation 3.11 to give equation 3.12.

$$U_\infty = \sqrt[3]{\frac{\left(P_{Hotel} + P_{Payload}\right)\eta_{PT}}{C_{D\nabla}\rho_W \nabla_S^{\frac{2}{3}}}} \qquad 3.12$$

This shows that optimum speed for maximum range is dependant on P_{Hotel}, $P_{Payload}$, η_{PT}, $C_{D\nabla}$ and ∇_S. For a mission where speed is a design parameter, equation 3.12 indicates the parameters to be controlled. Alternatively for an existing AUV with a known range and drag, the optimum U_∞ to achieve this range can be found. The hull shape could then be modified for this velocity.

Rearranging equation 3.10 to appreciate sensitivity of ∇_S, gives equation 3.13.

$$\nabla_S = \left(\left(\frac{SpeM_E U_\infty}{Range} - P_{Hotel} - P_{Payload}\right)\frac{2\eta_{PT}}{C_{D\nabla}\rho_W U_\infty^{\,3}}\right)^{\frac{3}{2}} \qquad 3.13$$

This equation permits determination of ∇_S before any other subsystems other than energy source have been sized. Prior knowledge of $P_{Payload}$ and P_{Hotel} requires some anticipation of maximum expected power draws. Estimates of M_B and $C_{D\nabla}$ are still required.

3.2.1 Worked example.

The AUV range is plotted in Figure 3.3 with varying velocity. The data values assumed are based on Autosub 2, such that the power draw is 1 kW (Griffiths, *et al.* 2004) and the balance between P_{Prop} and P_{Hotel} is split: 500 W P_{Prop} and 500 W for P_{Hotel} and $P_{Payload}$. The energy source will consist of 550 kg of batteries with a specific energy of 110 Wh kg^{-1}. That is 60500 Wh or 2.178×10^8 joules of energy. The assumed efficiency of energy transfer from the energy source to the water, η_{PT} = 52.5 % based upon a similar analysis of Autosub by Fallows (2005). Assuming a value of $C_{D\nabla}$ = 0.02648 (Kimber and Scrimshaw 1994), a hull shape volume of 3.6 m^3 and seawater density ρ_W = 1025 kgm^{-3}, U_∞ can be varied to produce a 'range' curve. The peak of the range curve is the optimal velocity (equation 3.12) and for this example base model corresponds to a range of 468 km at an optimum speed of 1.62 ms^{-1}. This assumes that the $C_{D\nabla}$ is independent of U_∞, although this is not the case and is explored in Figure 3.5*ii*.

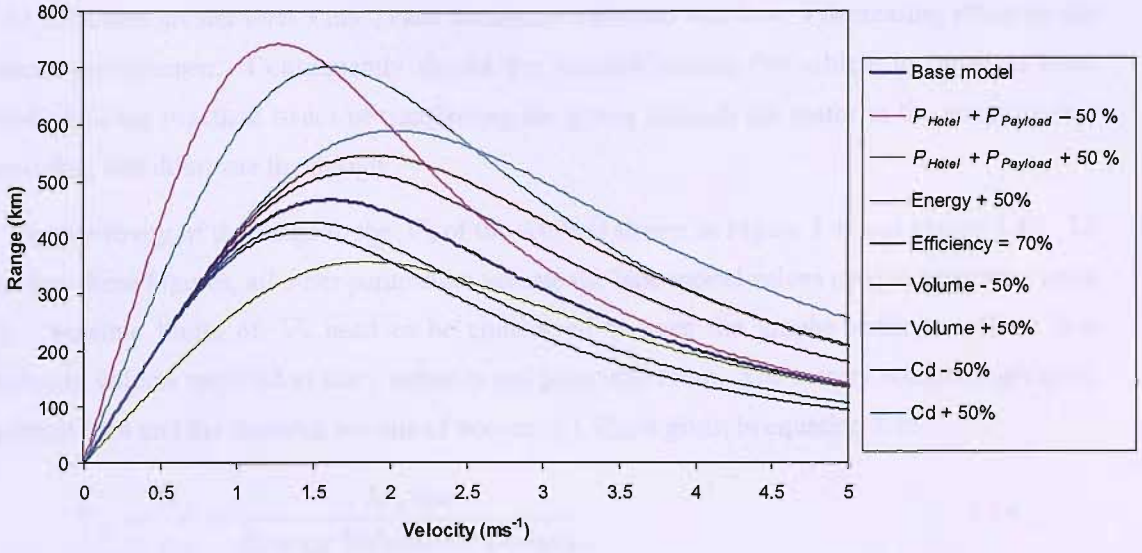

Figure 3.3 Range of the AUV whilst varying velocity and different input parameters.

The greatest range peak (743 km) in Figure 3.3 is achieved by decreasing $P_{Hotel} + P_{Payload}$ by 50%, and the lowest range peak (357 km) is caused by having a high $P_{Hotel} + P_{Payload}$ draw (increase of 50 %). The energy that is used by the hotel and payload affects the range, but also affects the optimum velocity. With a low $P_{Hotel} + P_{Payload}$ the AUV has a lower optimal speed (1ms^{-1} compared to 1.44 ms^{-1}) than with a high $P_{Hotel} + P_{Payload}$, but a greater range (743 km compared to 357 km). The two curves for the $P_{Hotel} + P_{Payload}$ in Figure 3.3 do not cross so lowering $P_{Hotel} + P_{Payload}$ draw will always improve range.

At speeds greater than 5 ms^{-1}, the improvement gained by altering the $P_{Hotel} + P_{Payload}$ draw will be insignificant, making this adjustment very velocity dependant.

The next highest range (703 km) is the result of increasing the amount of energy stored by 50%. The implicit assumption here is that this can be done without increasing the AUV volume. This can be achieved by increasing the specific energy or the mass of the energy source, although this will not alter the optimal speed of the vehicle. The energy source is the only variant that does not alter the optimum velocity of the AUV, as it does not alter any of the power draws.

The fastest optimal speed is the lowest C_{D_∇} value, which also has the third highest range (590km). This supports the desire for a low C_{D_∇} shape when operating at high velocity. None of the curves cross the base model curve, so any change improves the range, regardless of velocity, but the amount that the range is improved is sensitive to the velocity.

At velocities greater than 5 ms^{-1}, each parameter variation will have a decreasing effect on the vehicle performance. Consequently should the mission require the vehicle to travel at these speeds then the practical issues of transferring the power through the motor to the water to over come drag will dominate the design.

The sensitivity of the range to the ∇_S of the AUV is shown in Figure 3.4*i* and Figure 3.4*ii*. To generate these Figures, all other parameters assume the base model values used to generate Figure 3.3. Sensible limits of ∇_S need to be considered to keep the graphs realistic. There is a minimum volume required to carry batteries and buoyancy foam. The battery volume is given by equation 3.14 and the required volume of buoyancy (∇_B) is given in equation 3.15.

$$\nabla_E = \frac{M_E}{\rho_E} = \frac{M_E Spe}{Energy\ Volumetric\ Density} \qquad 3.14$$

$$\nabla_B = \frac{Buoyancy}{(\rho_W - \rho_B)} \qquad 3.15$$

550 kg of batteries with *Spe* = 110 Wh kg^{-1} and an assumed *Energy Volumetric Density* = 316Wh dm^{-3}, will give $\nabla_E = 0.19\ m^3$. This would require 0.495 m^3 of foam with ρ_B= 308 kgm^{-3}, the lightest foam in Figure 2.15. Therefore a suggested minimum volume for this example is 0.7 m^3. Similarly there will be a practical minimum when varying $C_{D\nabla}$. $C_{D\nabla} = 0.004$ is the lowest value for a laminar flow hull shape with no control surfaces (Parsons, *et al.* 1974) and will be used as the minimum in this example.

In each part of Figure 3.4 range sensitivity is provided for velocities at 1, 2 and 3 ms^{-1}. For constant $C_{D\nabla}$, increasing the volume of the shape will decrease the range due to increased drag, see Figure 3.4*i*. This effect is more pronounced when operating small AUVs at higher speeds. For the highest velocity (3 ms^{-1}) the curve gradient indicates that range is most sensitive to low ∇_S. At the slowest velocity (1 ms^{-1}) the range is relatively insensitive to ∇_S.

In Figure 3.4*ii* the battery mass is assumed to be 20 % of the AUV displaced mass. Consequently the range increases with increasing ∇_S. At low velocities the range increases are almost linear, but increasing speed reduces the influence of ∇_S on range. Clearly scaling the energy source with an AUV size is beneficial to the AUV range. If the increased volume is allocated to payload with a fixed energy volume, AUV range decreases with volume as per Figure 3.4*i*.

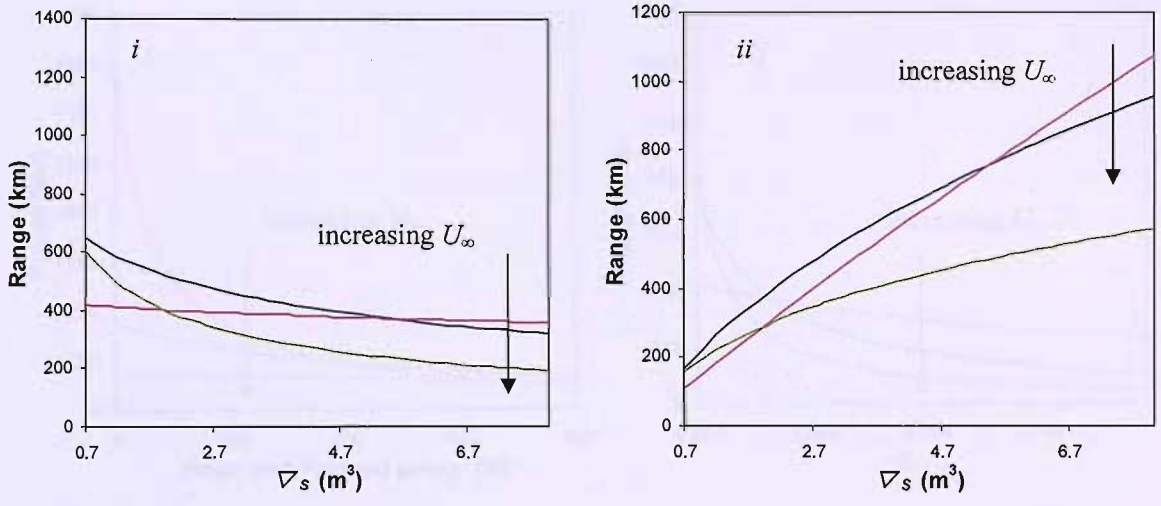

Figure 3.4 Sensitivity of AUV range with *i)* ∇_S variation with fixed energy source volume and *ii)* ∇_S with M_E equal to 20% ($\rho_W \nabla_S$).

Figure 3.4*ii* assumes a constant *Mass Ratio* for the AUV, implying that the payload has increased along with total volume. If the increased volume were allocated purely to the energy source, then the range increase would be greater than in Figure 3.4*ii*. With an appreciation of how ∇_S influences range, the hull shapes can be compared using $C_{D\nabla}$.

Figure 3.5*i* shows the affect of increasing $P_{Payload} + P_{Hotel}$. Of note is that range decreases as more energy is diverted away from P_{Prop}. Should the power be required for only propulsion, i.e. no hotel and payload, then the AUV becomes an unguided torpedo and has the maximum possible range. With increasing speed the range becomes less sensitive to the power distribution, and so becomes less of a design driver. This is unlike the volume and $C_{D\nabla}$, of Figure 3.4*i* and Figure 3.4*ii*, as both components influence P_{Prop}.

Range in Figure 3.5*ii* becomes more sensitive with increasing speed. At higher values of $C_{D\nabla}$ the range is less sensitive to varying $C_{D\nabla}$. Therefore a shape with a high $C_{D\nabla}$ may be able to increase volume and $C_{D\nabla}$ without sacrificing a significant amount of range. If the design was constrained to a bluff, high $C_{D\nabla}$ body, then operating at low velocity would give a greater range. At large velocities, $C_{D\nabla}$ becomes very important in determining vehicle range.

P_{Prop}, $P_{Payload}$ and P_{Hotel} may vary over a mission thus making an accurate range prediction more difficult. For example a sprinting AUV is unlikely to operate all instruments during a sprint to a location. A slight modification to equation 3.9 could introduce a duty cycle, to reflect the proportion of time spent at different values of P_{Prop} and $P_{Hotel} + P_{Prop}$.

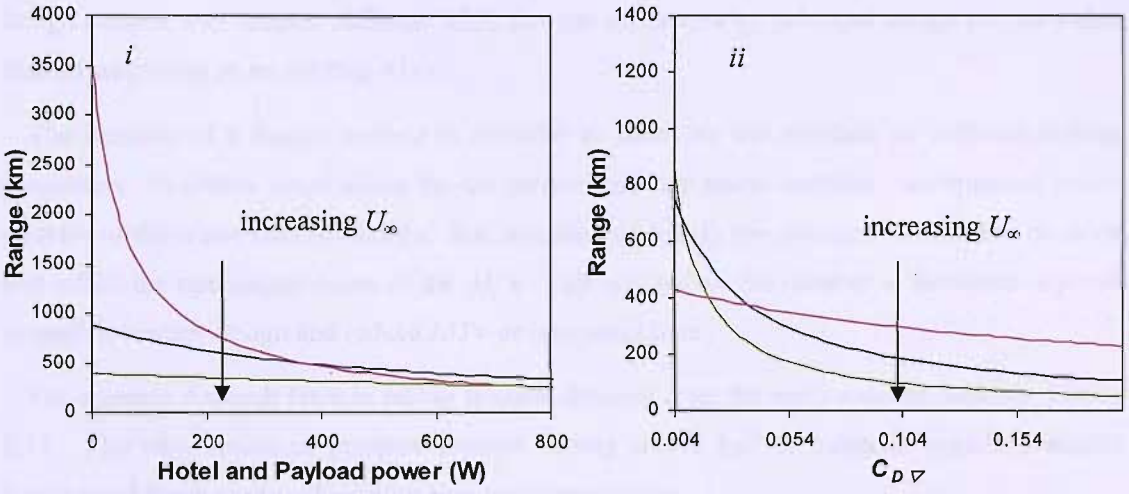

Figure 3.5 Sensitivity of AUV range with *i*) hotel and payload power and *ii*) C_{D_∇}.

Additionally the energy source will have to provide a higher P_{Prop} at high velocity. Consequently there may be changes in energy source efficiency during periods of high power demand.

Most variables required to establish power, endurance and range can be quantified at an early design stage. The principal exception to this is C_{D_∇} since this requires definition of a hull form. Chapter 6 will provide computational estimates and propose a method of using geometric parameters to define the hull shape. Displacement volume can be problematic, as its estimation requires sizing of other subsystems, such as energy capacity. Both of these parameters must be estimated and then refined through iteration. A good initial estimate will reduce the number of iterations required.

Calculations presented indicate the conflict between C_{D_∇} and ∇_S. The value of each is clearly dependant on, and constrains, the other's values. This conflict is explored further in the next section.

3.3 Iterative concept design.

The design of a system is as unique as the system. Chapter 2 discussed existing approaches to design for similar systems, such as manned submarines. Each structure has its own nuances and the design methodology should capture them. These design methods can be generalized and applied to AUVs but doing so might lose details that may be crucial for AUV design.

Whilst there is much to be said for adopting tried and testing approaches there is also a need to avoid stagnation of AUV evolution and to provide opportunities for innovation. A structured

design method may support different AUV designs influenced by principal design drivers rather than an adaptation of an existing AUV.

The iteration of a design method is essential to resolving the conflicts of different driving parameters. Feedback loops within the design methodology assess decision consequences before creation of the whole concept design. It is essential to identify the concerns of each key decision that reflect the operational needs of the AUV This will reduce the number of iterations required to reach a concept design and reduce AUV development time.

For example Autosub 6000 in reality is quite different from the early concept sketches, Figure 2.17. The new option of pressure tolerant battery source had to balanced against available funding and functionality of existing bow and stern sections.

Figure 3.6 provides a general 'top most' design process relevant to AUV design. Increasing detail, structure and refinement of this conceptual methodology is required to create a realistic design method.

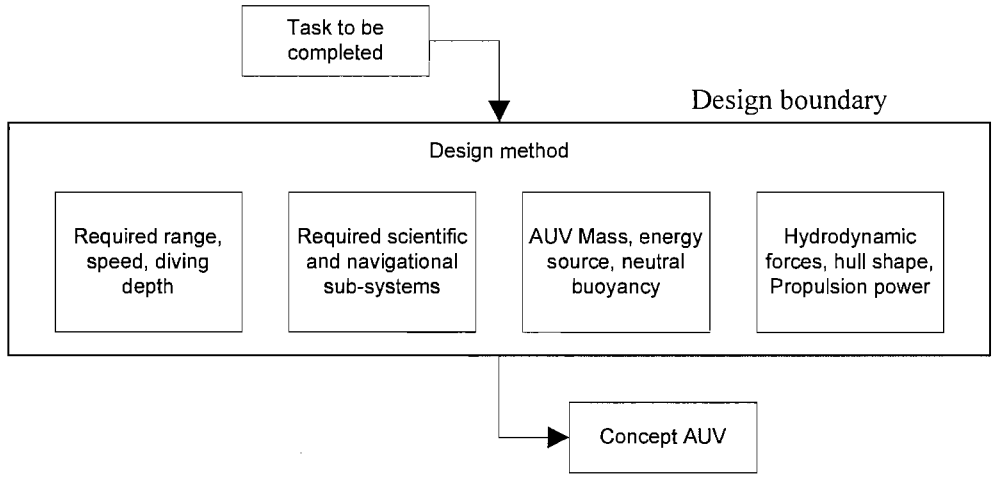

Figure 3.6 Top level design process.

Outside the 'design boundary' there may exist surface vessels or other manned vehicles that are capable of undertaking the work, but such non-AUV alternatives are not to be considered in the design method. Figure 3.7 and Figure 3.8 provide two alternative approaches to AUV design. Each design approach uses different design drivers, different feedback loops and interdependencies, although some relationships remain invariant. The influence of the 'starting point' on the design is considered next.

3.3.1 Design start points.

The design boundary of Figure 3.6 can be defined as a set of mission objectives and AUV specifications. The specifications to fulfil the mission need to be detailed and comprehensive. Greater detail present in the mission specifications will reduce the number of design iterations caused by unknown design parameters. The flow charts of Figure 3.7 and Figure 3.8 have distinct starting points. Initially, simple concept AUVs were attempted and the resulting conflicts and information flow were noted. Figure 3.7 starts with the energy requirement specification as the primary driver.

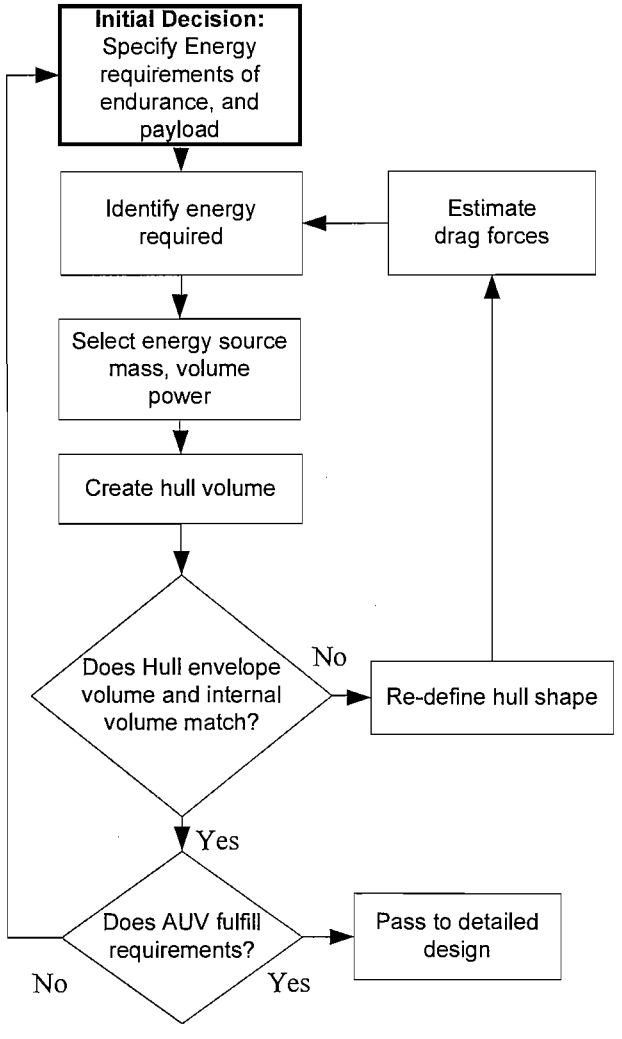

Figure 3.7 The design method from an endurance and energy initial decision.

The energy capacity required implicitly needs answers to the questions: For how long has the AUV to operate? What power draw is required by navigational sub-systems, payload sub-systems and the required propulsion? These two questions become critical decisions. Specification of the navigational and payload sub-systems may be possible, assuming the equipment has been selected previously. Specifying how long the vehicle is to operate will depend upon the propulsion power. For this an estimate of $C_{D\nabla}$, ∇_S and U_∞ is required. These estimates of power draw and drag resistance will impact the whole design as they form the start point of the first estimate.

The first feedback loop in Figure 3.7, iterates any imbalance between required volume and hull shape volume and the second feedback loop verifies AUV capability to fulfil mission objectives.

The first internal loop verifies that the volume estimate of internal sub-systems will fit within the hull envelope, and that the energy source is able to provide total required propulsion power. An estimate of the energy required to achieve the mission endurance is very dependant on the estimated power draws. The start point does not consider the size of the AUV. Arbitrarily increasing the AUV mass and volume to fit an over-sized energy source might create an AUV larger than necessary. The final feedback loop (required in most design methods) can be the most time intensive iteration loop as it re-evaluates all the intermediate steps. It is necessary to verify that the AUV is capable of the mission once all subsystems have been created.

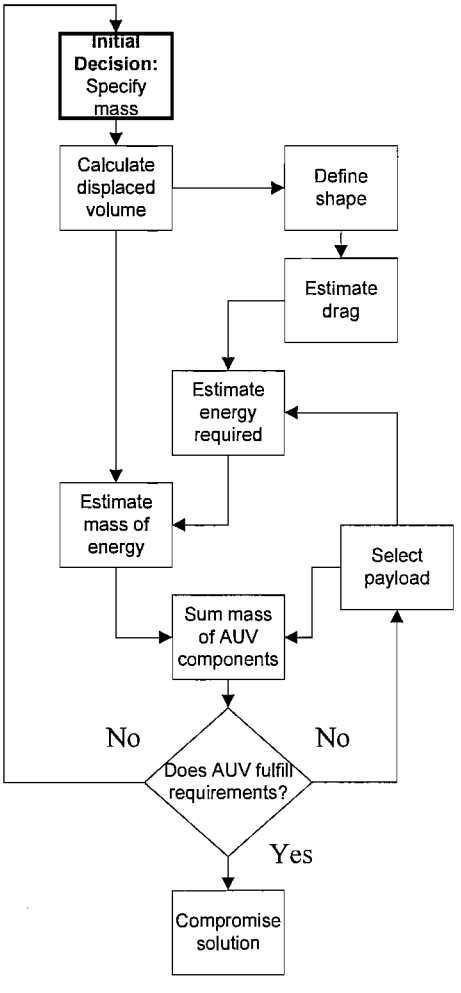

Figure 3.8 The design methodology with a mass initial decision.

Figure 3.8 illustrates a design method resulting from AUV mass being the primary driver. This approach could arise from specifying an AUV that is to be carried by personnel, by helicopter or operated from an existing launch gantry. There are three feedback loops in this method, an energy loop, a payload loop and an overall loop.

The payload carried will affect the mass budget of the vehicle and the payload power draw. The initial estimate of the energy required will control the mass of the energy source. The overall loop checks the mission requirements and modifies AUV mass accordingly. The shortcoming of this approach is that the energy has no feedback to the AUV hull shape. Consequently each stage in the design method must be re-considered and any imbalance between energy available and energy required is only identified at the last stage.

An alternative method would be to specify AUV volume. This would imply a displaced mass (ignoring free flooding sections). An example of volume driven design would be the desire to launch the AUV through a hole of specified maximum diameter. This is the likely initial design start point for the diameter controlled Bluefin vehicles (Chapter 2). This would stipulate a

maximum volume with a need to fit all sub-systems within this volume whilst fulfilling AUV mission requirements.

From discussions with industrialists at the annual UUVS conferences (Unmanned Underwater Vehicle Showcase) it is possible to gain a commercial view from marine companies who manufacture ROVs, AUVs and sensor equipment. Whilst increased vehicle endurance is desired, the focus is concerned with ensuring the quality of work done within that endurance. A vehicle that produces 6 hours of detailed, accurate and reliable survey results is often of greater commercial value than a vehicle with an endurance of 24 hours and returns low detail or misleading data. This implies that designing an AUV to end users specifications, to ensure that the AUV delivers the desired information, would be most productive. A design methodology that adopts the mission specification as the start point will be presented in Chapter 7.

The presented design methodology uses the mission as the start point, to ensure that the AUV design focuses on the required operation, and not a preset mass or energy constraint. These different start points show how the presented methodology was initially found. Decisions common to each method, such as the initial estimate of energy source volume, form the key AUV design decisions. Examples of how such decisions might be solved are presented in Chapter 8.

3.4 Chapter conclusion.

The Chapter has introduced and defined the non - dimensional terms C_{D_∇}, fineness ratio and C_Θ to quantify the hull shape independently of volume. These parameters will be used in later chapters to compare AUV shapes.

This Chapter has presented or derived the analytical equations that show the effect of volume and velocity on the range of the AUV. The energy source capacity directly affects range and endurance assuming all other parameters are held constant. This can be achieved by increasing energy density or volume of the energy source. Increasing the energy source volume will increase range, but will require an increase in AUV volume, which increases drag and reduces range. This presents challenge for the design engineer to overcome. One option is to control the C_{D_∇} of the shape and reduce the drag of an AUV of specific volume. This motivates understanding of how AUV hull shape affects the drag of the vehicle, addressed in Chapter 6.

Flow charts of design logic have been presented. They are the result of brainstorming sessions used to appreciate how following the information required for each design decision. The conflict of design parameters within the flow charts provide motivation for creating a structured method to aid key decisions and reducing the "unknowns" within a design.

The next Chapter investigates one approach to increasing specific energy for deep diving AUVs without increasing volume. This is by showing that lithium polymer batteries are a pressure tolerant energy source. This will enable the pressure vessel to be reduced and either the energy source mass to be increased or the AUV volume reduced.

Chapter 4
Lithium polymer batteries.

The need to increase the energy source capacity has been identified. One option to permit increased energy source is the reduction of pressure vessel size through the use of pressure tolerant energy sources.

The energy source must provide the required instantaneous power and provide sufficient storage to power all subsystems. Different energy sources have different power characteristics. Some provide high power and low capacity, others provide high capacity and low power. Both energy capacity and power draw must be considered when selecting an energy source. Lithium polymer cells can operate at high power whilst retaining energy capacity, so the experiments will include monitoring current variation.

This Chapter described the research completed to demonstrate that Kokam SLPB526495 lithium polymer batteries are pressure tolerant. These batteries are shown to operate at 6000 m equivalent pressure (60 MPa). Batteries in deep or Arctic water will experience cold temperatures and higher temperatures in warm tropical water. Therefore physical tests will include performance variation with pressure and temperature variation.

The methodology, physical validation and results of this case study formed a published paper presented to the Unmanned Untethered Submersible Technology (UUST) symposium. This paper is the second paper in Appendix A. Operation at high hydrostatic pressure is a new application for these batteries, and as a result of this work they have become the energy source for Autosub 6000.

4.1 Lithium polymer batteries.

Autosub 6000 is designed to dive to 6000 m and so either needs a very heavy pressure vessel or a pressure compensated energy source. Lithium polymer batteries present a rechargeable high specific energy choice for an energy source, and their performance is still an active research area. Lithium ion batteries are used in small portable devices (<10Wh), but a need for higher power or large energy capacitance energy source was recognised (Kobayashi, *et al.* 2005). More recently technology has improved such that 1kWh of lithium ion batteries are used in Gavia (Yeo 2007) and the Remus AUVs (www4).

The high specific energy of lithium polymer batteries (195 Wh kg^{-1} for Kokam SLPB526495 batteries) makes them more attractive than other secondary batteries, and their solid internal

components makes them a candidate for operation at hydrostatic pressure. At the beginning of this research there were no published literature references on lithium polymer battery performance at hydrostatic pressure. Apart from one brief mention of lithium polymer batteries at pressure (Hasvold and Storkerson 2001) the Rutherford presentation at UUST was the first time the performance of lithium polymer batteries at pressure was publicised. The earlier reported pressure test on a lithium polymer battery did not survive being brought back to atmospheric pressure. This failure was not thought to be due to the battery chemistry at pressure, but further tests were not reported.

Bluefin Robotics (www3) treated their testing of pressure compensated lithium polymer batteries, and the resultant battery pack performance, as a trade secret until 2006. This information has since become available and concurs with the results found in this thesis (Wilson and Bales 2006). Very recent developments show that the US Navy is using pressure tolerant lithium ion batteries in eight vehicles. This presents more than 1300 hours of use with a proportion of operation at 3680 m depth (Saint-Amour 2007).

The NOCS supplied batteries tested in this research are commercial lithium polymer batteries produced by Eaglepicher – Kokam (www11). They use a patented (Hong 2002) manufacture method of double folding the polymer separator sheet and then using an adhesive with no heat treating of the batteries. The polymer sheet is made of polyethylene or polypropylene and contains the lithium salt electrolyte. The anode comprises of a copper foil and the cathode plate comprises of an aluminium foil. Laminate layers are adhered together rather than heat treated to give better safety in case of electrical fire. An added benefit is that this process should not leave any compressible voids between layers. Thus having examined the battery's physical structure (Hong 2002), it was anticipated that the majority will survive the pressure testing.

Prior to the research described, the combined effect of temperature and pressure on the batteries was not known. The effect of temperature on a lithium polymer battery was observed by Shukla (Shukla, *et al.* 2001), but it was not known if this would be more noticeable than the affect of pressure. If lithium batteries are noticeably sensitive to temperature, thermal management of the energy source will be important.

A similar battery chemistry, lithium ion, generates thermal heat due to three factors: chemical reaction heat, polarization heat and ohmic heat (Sato 2001). During discharge the ohmic resistance adds to the exothermic chemical reaction. At high temperatures the battery longevity is decreased. At low temperatures the electrolyte conductivity decreases. The primary cause of degradation is either a surface film of electrolyte over the anode or cathode, or electrolyte

degradation. Physical testing and chemical reaction balances show that the molar degradation of electrodes increases with discharge current (Sato 2001). At low temperatures the drop in electrolyte conductivity is measured as an increase in ohmic resistance, and so less useful energy is removed from the battery. Although thermal modelling is not within the scope of this thesis, it is a concern with secondary battery performance in both tropical climates and cold waters.

Other issues that should be considered include battery disposal: Some battery chemistries are harmful to the environment or may release harmful chemicals during disposal. For example both nickel and cadmium (found in Ni-Cd batteries) are limited (European Union Directive 76/464/EEC 1976). Lithium batteries have safety concerns over the prospect of lithium fire. The primary cause is overcharging the battery and this is preventable by using a controlled battery charging method. Secondary concerns are the transport of lithium polymer batteries and exposure to thermal conditions and physical impact (www11).

Most practical concerns are not specific to lithium batteries. The problems of access and battery pack creation are common. The battery pack should be practically sized to permit maintenance and replacement. The batteries within the pack should be restrained to not move, break contacts or suffer damage during AUV operation.

4.2 Battery state of charge.

The battery state of charge (*SoC*), expressed as a percentage, is a measure of how much energy remains in the battery. A battery at 50 % *SoC* is considered to have expent half its energy. This is a non - dimensional comparison method so there can be direct comparison between different battery operating conditions.

Two methods of battery *SoC* estimation are the direct application of equation 4.1 or computing the battery open circuit voltage (OCV) (Chiasson and Vairamohan 2003 pp. 2863 - 2868). The OCV is the voltage at the battery terminals when the battery is not in use and has recovered to equilibrium.

$$SoC(t) = \frac{\int_0 I_D(\tau)d\tau}{Q_0} \times 100 \qquad 4.1$$

With I_D the discharging current at time t and Q_0 is the total charge the battery can hold. However this formulation does not allow the Q_0 to vary with temperature, charge current or battery life. Without extensive lists of battery charge capacities under all possible conditions, this *SoC* will not accurately predict the battery *SoC*. However the impact of adverse conditions could

be assessed by comparing capacity drawn under selected conditions with capacity drawn under ideal conditions.

For this investigation, a simple method was used to calculate *SoC*. This assumes each battery was fully charged before the start of each test, and that subsequent cycles charged to the same point. For the Kokam batteries tested, Q_0 is assumed to be the nominal battery capacity of 3.27Ah. The amount of energy removed then estimated using equation 4.1.

4.3 Battery model creation.

In order to analyse the performance of a battery, a comparison method is required. An equivalent circuit approach allows the battery internal resistance to be modelled and quantified. The change in battery performance is reflected in the equivalent circuit component's values.

Doerffel and Abu Sharkh describe the creation of an equivalent circuit model (Doerffel and Abu Sharkh 2004). The 100 Ah lithium ion batteries tested by Doerffel are not solid state and would vent gas during operation, making them unsuitable for underwater work. The method applied implements improvements mentioned in Doerffel's paper, and then the timings and values have been adjusted for a smaller capacity Kokam battery.

A simple model of a battery would be a perfect voltage source in series with a resistance, but this model would not represent the dynamic voltage behaviour of the battery. Using a resistor (R) and a capacitor (C) in a parallel pair, known as Randle's configuration, would approximate the dynamic voltage response. More RC pairs will give a more complex model but not necessarily increase the accuracy. Doerffel used a large commercial 100 Ah battery that took approximately 24 hours to reach steady state voltage after use. Consequently it would take 20 days to determine the battery OCV. Given the approximations made, Doerffel's rapid method would create a model of the 100 Ah battery in 19 hours. This is a significant time saving for the larger batteries.

The important task is to model battery voltage behaviour during a pause in charge or discharge. Doerffel conducted tests with a 1 minute pause. This was insufficient time for the battery to recover. Doerffel's described the lithium ion battery voltage response to being loaded and unloaded as slow. It was anticipated that for smaller 3.27 Ah Kokam batteries, the response would be much quicker and so the test methodology was adjusted. The pause duration was increased to 15 minutes for these tests. The result of increasing the pause time was to increase the duration of the test methodology. For the Kokam cells the whole test cycle took 14 hours.

During a pause, the voltage rises if discharging, or drops when charging, and this dynamic behaviour is modelled in the equivalent circuit. Figure 4.1 shows the form of the voltage rise

when the load is removed. The rise from V_0 to V_1 is instantaneous, and the rise from V_1 to V_2 is gradual. Given sufficient time the voltage would rise to the OCV, and be indicative of the battery *SoC*. This time can be in the order of days and is too slow for practical experiments.

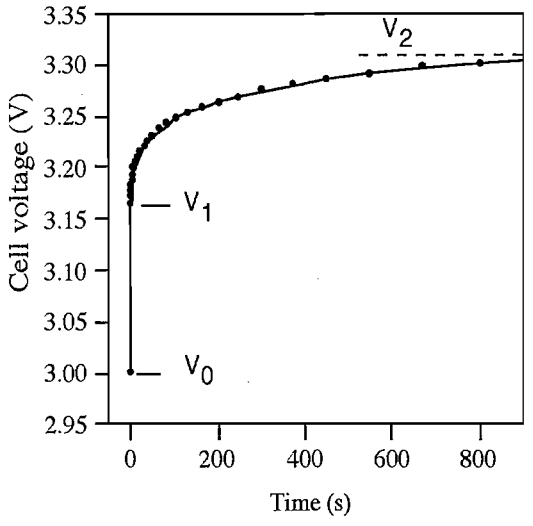

Figure 4.1 Voltage-time graph over 15 minutes of the reference battery with load of 1 A removed at T=0 showing the voltage points used to estimate the equivalent circuit parameters.

In Figure 4.2 R_{01} is the immediate ohmic resistance found in all batteries. This represents an immediate voltage rise when load is removed, V_0 to V_1 in Figure 4.1.

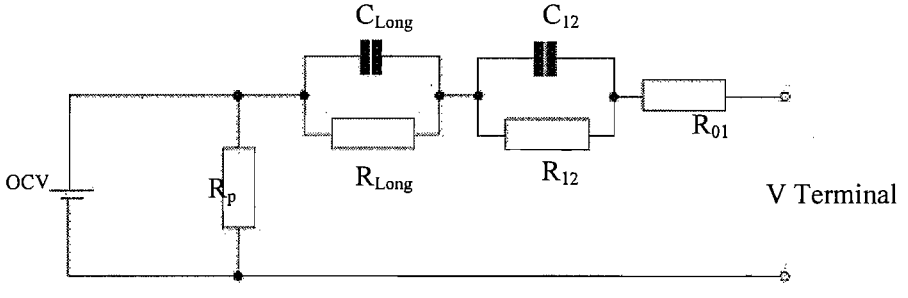

Figure 4.2 Equivalent circuit model for a solid Lithium - Ion battery as proposed by Doerffel.

The two RC combinations model the gradual increase in voltage, V_1 to V_2. R_{12} and C_{12} model the double layer capacitance and chemical reaction kinetics which occur after the load is removed. This is the most significant dynamic part of the model, and would be the recovery found for a single RC model. R_{Long} and C_{Long} model a constant voltage rise which will take the

longest to recover during the pause (for the 100 Ah battery, it was in the order of hours). For the Kokam battery this was estimated using a least squares method over the 15 minute pause, detailed in Appendix C. These effects can also be observed in the voltage drop when the battery is loaded. R_p measures the self discharge rate and was not approximated in this method. The self discharge rate of the lithium polymer battery was considered sufficiently long to not be a factor. The voltage rise when load is removed is modelled by the equivalent circuit of Figure 4.2. The dynamic voltage response is described by a pair of exponentials, equation 4.2.

$$V(t) = V_1 + iR_{12}(1 - e^{-\frac{t}{R_{12}C_{12}}}) + iR_{Long}(1 - e^{-\frac{t}{R_{Long}C_{Long}}}) \qquad 4.2$$

The of two pairs of RC values were estimated from the data using a least squares fit to minimise the difference between V as modelled using equation 4.2 and the actual data.

The values of resistance and capacitance were found to vary at each SoC pause during the test, gradually increasing as SoC decreased. For a representative model, the V function equation 4.2 requires modification. The consequences for SoC are discussed further in section 4.4.1.

The objective of a battery model is to model the performance of the battery under various conditions. This can then be used to predict the battery performance over a future mission. A greater challenge is to estimate the SoC of a battery whilst still loaded, and in effect become a fuel gauge for the battery pack. An accurate model of the battery internal resistances will allow the OCV to be estimated from a terminal voltage under known conditions.

4.3.1 Fuel gauge.

S. Abu Sharkh gives a fuel gauge model in the book "Technology and Applications of Autonomous Underwater Vehicles" (Abu Sharkh, *et al.* 2003 pp. 19 - 35). The model considers the chemical reaction of the alkaline manganese battery reaction and predicts the terminal voltage of an alkaline manganese battery. This fuel gauge model is expressed in equation 4.3.

$$V_t = V_h - \frac{\phi RT}{F}\ln\left(\frac{Q_t}{Q_r}\right) + \Delta\eta_c - \Delta\eta_a \qquad 4.3$$

Where V_h is the battery voltage at half useful life, ϕ is a constant, R is the universal gas constant, T is the absolute temperature, F is Faraday's constant, Q_t is the useful energy extracted, Q_r is the energy remaining in the battery, and η_a and η_c are the anodic and cathodic overpotentials respectively. This model was investigated for a Rayovac industrial alkaline 'D' battery at three temperatures and nine power draws. This allowed η_a and η_c to be found as a function of current

and temperature, and so become the basis of a fuel gauge. Testing against real mission data from Autosub, the predicted V_t is within 5 % of the measured data V.

The fuel gauge will still require consideration when in use, as voltage drops or sudden changes in environmental conditions can affect the energy source. Having energy for several hours operation is not a guarantee that there is sufficient energy to power up, dive, run all sensors, surface and retain energy for emergency recovery conditions.

Furthermore Stevenson observed that after an AUV mission the fuel gauge predicted six hours of available energy (Stevenson, *et al.* 2002). However, at the start of the mission there is an increased power draw due to AUV acceleration, which would lower the voltage and render the energy source useless to the vehicle.

Creation of a fuel gauge for a lithium polymer battery, is more difficult as it is not known how best to represent the effect of pressure either within an equation or within a circuit model. The circuit model of Figure 4.2 was selected and component values found by physical testing.

4.3.2 Experimental method.

Testing of the 3.27 Ah Kokam SLPB526495 lithium polymer pouch batteries was undertaken at both 0.1 MPa and 60 MPa (6000 m equivalent depth). The measurements were used to compare and analyse any differences in performance. The effects of low temperature (4°C) and high current draw (3 C or 9.75 A) were also tested and compared. Testing was split into four stages:

I. Survival test. Batteries were pressurised to 60 MPa for 30 minutes, then inspected for signs of physical failure. A 1 ohm load was put across the battery terminals to test for electrical failure.
II. Charge and discharge cycles at 0.1 MPa with varying temperature and current draw up to 9.5 A.
III. Charge and discharge cycle at 60 MPa and constant temperature and varying current draw up to 9.5 A.
IV. Data from steps II and III used to create an equivalent circuit model.

Pressure tests were done in the water based pressure vessel at NOCS. The batteries had to be insulated from the water to prevent electrical short circuit. Insulation was in the form of oil filled deformable plastic bags. Oil is electrically non-conductive, and likely to be the medium used in a battery pack produced for an AUV. It was not possible to vary the temperature of the water within the pressure vessel.

Stage I tests gave confidence that the batteries were not likely to fail at pressure, and that the insulation prevented any contact with water. 350 batteries were tested overall, with each battery undergoing up to 5 pressurisations of 30 minutes length, for a total of 2800 battery hours of testing. The maximum off load voltage change for any battery after testing was 0.003 V (1 % of nominal voltage). This is not considered large enough to signal an internal short circuit, therefore zero failures were found after testing. This stage provided confidence for the next stage of testing, but it was not possible to create survival statistics.

Stage II investigated the performance of the battery at atmospheric pressure whilst varying current draw and temperature. Stage III placed the battery at 60 MPa, and then tested the battery at currents from 1 A to 9.5 A. The battery was charged at 60 MPa to give the full cycle at pressure. The option of charging at pressure may become a future option with a docking station, so it was useful to verify charge performance at pressure.

The electrical test cycle consisted of a discharge at test current, and then a charge at a constant current. During discharge the current was held at a constant value when on load, and zero during a pause. During discharge pauses of 15 minutes at 0.327Ah (10 % of Q_0) intervals allowed the battery voltage to recover and the voltage rise to be measured. The battery was considered to be discharged when the on - load voltage reached 3V. This limit is based on the battery safe working conditions (www11).

The battery was charged with a current of 1 A, until the terminal voltage reached 4.2 V. Charging then continued at this voltage until the current fell below 0.327 A. At this point the battery was considered to be fully charged, 100 % *SoC*. During charging, pauses for 15 minutes were inserted after each 0.327 Ah of charge, representing 10 % *SoC* increase. The battery was allowed to rest for 2 hours after a discharge, and at least 4 hours after a charge, to allow the battery to reach close to equilibrium state. By inserting pauses at each 10 % *SoC* in both charge and discharge cycle, the voltage peaks during a pause occur at the same *SoC*. Lining up the voltage peaks in this fashion aids the estimation of OCV. Assuming the voltage recovery is the same after a charge or a discharge, then the OCV will occur midway between the voltage peaks.

Figure 4.3 shows the results of one charge and discharge cycle at 0.1 MPa, 23°C, with a 1 A discharge current. Key features are labelled. The voltage change during pauses and the approximate OCV are shown.

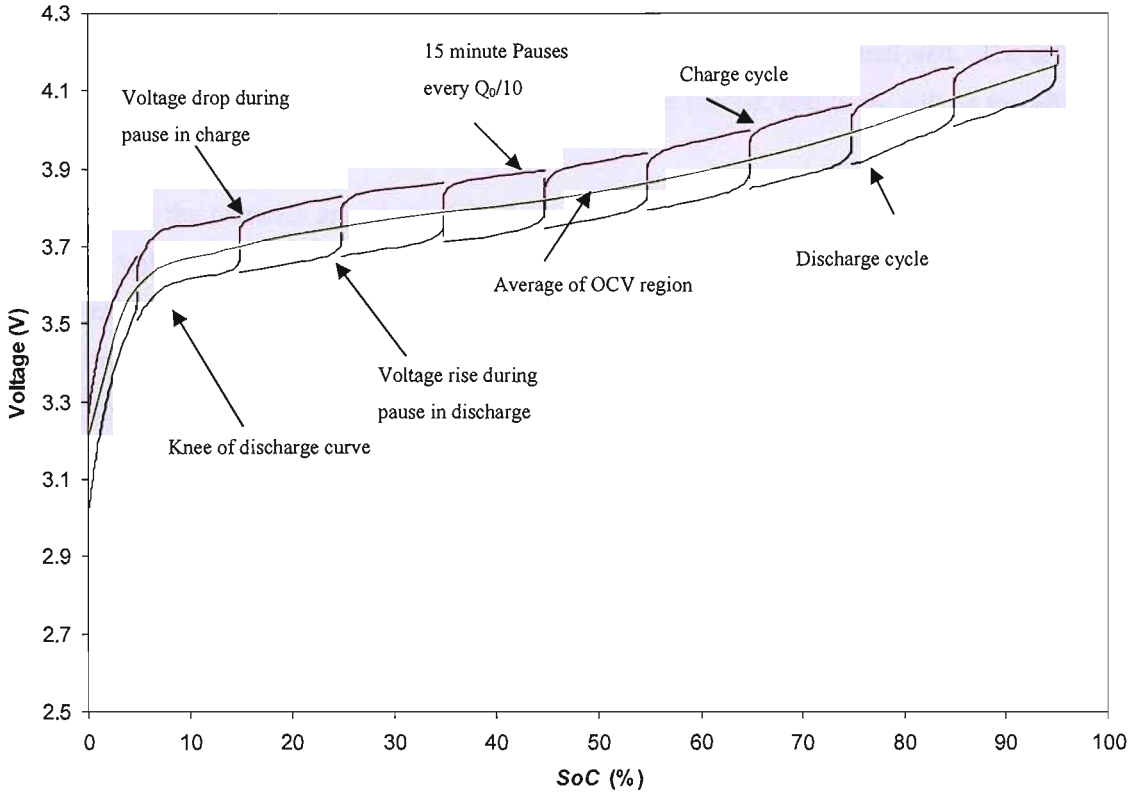

Figure 4.3. Battery voltage with state of charge during charge and discharge at 1 A at a mean temperature of 28 °C at 0.1 MPa.

At low *SoC*, less than 20 %, concentrations of lithium ions can build-up at the surface of the laminates, restricting electron flow at the end of the discharge. This is likely to be from the discharge cycle, when concentration gradients of lithium ions can form at the anode or cathode. The subsequent charging process then has to reverse this build-up. At low *SoC* these gradients have accumulated over the whole discharge, and so the time to offset them and recover to equilibrium is increased. The end of discharge of a lithium-ion battery is determined by reaction partners being locally depleted and/or reaction products being locally saturated, which - according to the Nernst equation (Ehrlich 2002 pp. 35.26) - leads to a sharp decrease in the equilibrium potential (or OCV) of the battery. This decrease is observed as the knee in the discharge curve of Figure 4.3. Due to these electrochemical effects voltage comparisons in this thesis are only conducted above 25 % *SoC*.

4.4 Experiment results.

The effect of current draw at room temperature will be the first experiment analysed. The affect of low temperature (4 °C) at different discharge rates will be second, and lastly will be the affect of 60 MPa pressure at various discharge rates.

In Figure 4.4 the batteries are adversely affected by the current drawn. High current (greater than 6.5 A) will remove energy at a greater rate and proportionally reduce the terminal voltage. This will cause the voltage to drop below the minimum 3 V sooner than at lower current draw. By definition this would mean the battery is empty of energy. The battery may not be completely depleted, and a lower current (e.g. 1 A) may yet extract more energy, but internal battery losses would mean that the total energy extracted is less than that extracted from a battery operating at a constant low current.

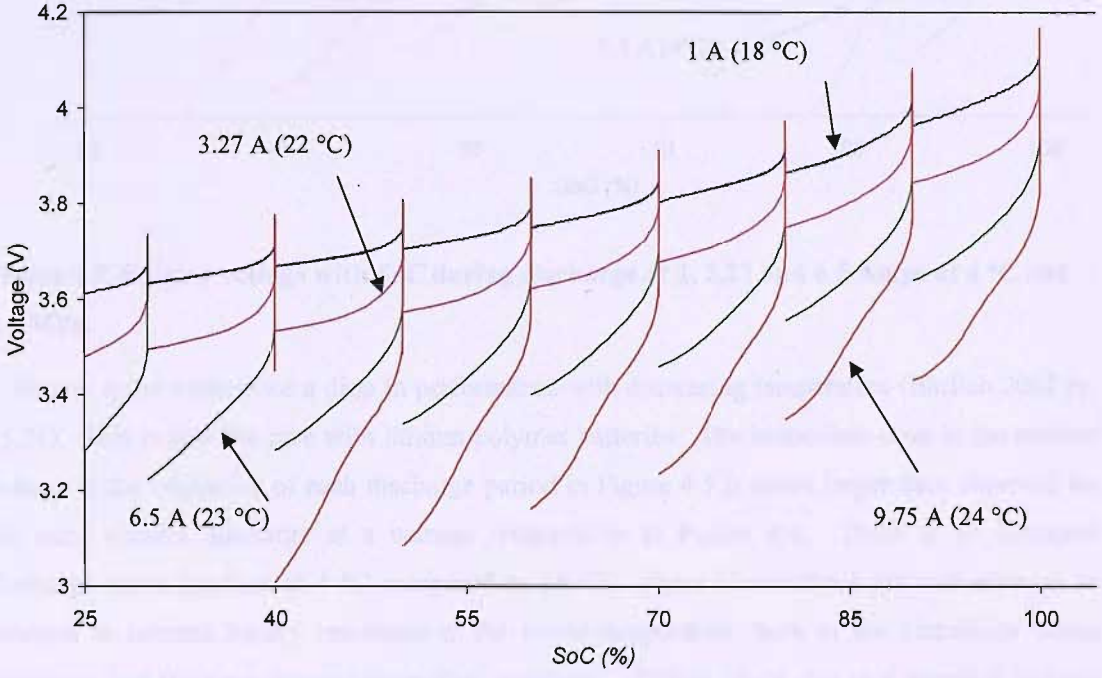

Figure 4.4. Battery voltage with *SoC* at 1, 3.27, 6.5 and 9.75 Amp discharge between 18 and 24 °C and at 0.1 MPa.

Figure 4.4 and Figure 4.5 illustrate the affect of temperature when drawing currents of 1 A, 3.27 A, 6.5 A, and 9.75 A. The effect on the voltage of increasing current draw is an increasing gradient of each line. Discharge at 1 A provided at least 90 % of nominal battery capacity at 18 °C and at 4 °C. Discharge at 3.27 A provided 90 % nominal capacity at 22 °C yet only 65 % at 4 °C. A discharge at 6.5 A and 23 °C still produced 85 % nominal capacity, yet only 17 % at 3 °C.

The voltage drop at 9.75 A and 3 °C was great enough to reach cut-off almost immediately due to internal resistance and produced no useful results.

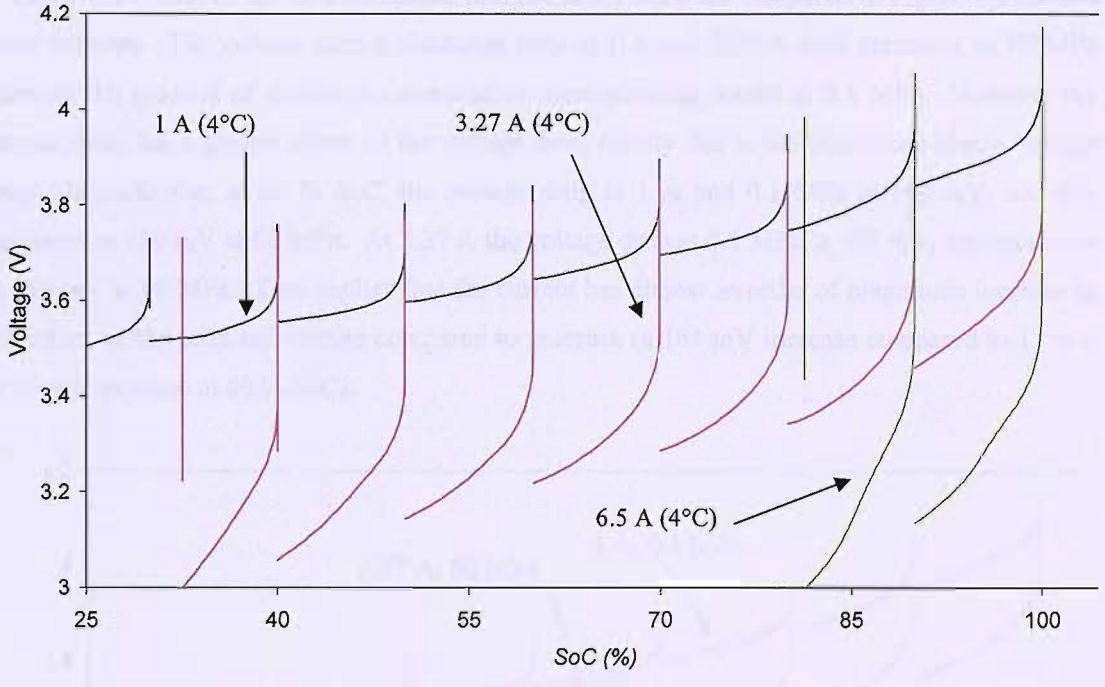

Figure 4.5. Battery voltage with *SoC* during discharge at 1, 3.27 and 6.5 Amps at 4 °C and 0.1 MPa.

Battery types experience a drop in performance with decreasing temperature (Ehrlich 2002 pp. 35.26). This is also the case with lithium polymer batteries. The immediate drop in the on-load voltage at the beginning of each discharge period in Figure 4.5 is much larger than observed for the same current discharge at a warmer temperature in Figure 4.4. There is an increased discharge curve gradient at 4 °C compared to 24 °C. These observations are indicative of an increase in internal battery resistance at the lower temperature, both in the immediate ohmic resistance and the time delayed capacitive resistance. This is likely due to a decrease in ionic conductivity in the polymer electrolyte. To quantify this, at 60 % *SoC*, the total voltage drop at 3.27 A and 22 °C is 327 mV, while at 4 °C and 3.27 A the voltage drop increases to 636 mV.

At low temperatures Figure 4.5 indicates that increased internal resistance causes a larger voltage drop and a smaller margin between on load voltage and the cut-off point. Thus at 9.75 A and 4 °C the voltage drop reaches the cut-off point prematurely, before the knee of the curve. This implies that although the battery cannot produce energy at a useful voltage even though

there may still be energy inside the battery. This energy can only be removed at a lower discharge rate or at a warmer temperature.

Lastly the effects of 60 MPa compared to those at 0.1 MPa are compared in Figure 4.6 for two draw currents. The voltage during discharge tests at 1 A and 3.27 A load pressures of 60 MPa increase the gradient of discharge compared to corresponding results at 0.1 MPa. However the current draw has a greater effect on the voltage drop, mostly due to the immediate ohmic voltage drop. In particular, at 60 % *SoC*, the voltage drop at 1 A and 0.1 MPa is 143 mV, and this increases to 160 mV at 60 MPa. At 3.27 A the voltage drop at 0.1 MPa is 327 mV, and increases to 366 mV at 60 MPa. This implies that the current has almost an order of magnitude increase in the effect on the terminal voltage compared to pressure (a 184 mV increase compared to 17 mV or 39 mV increase at 60 % *SoC*).

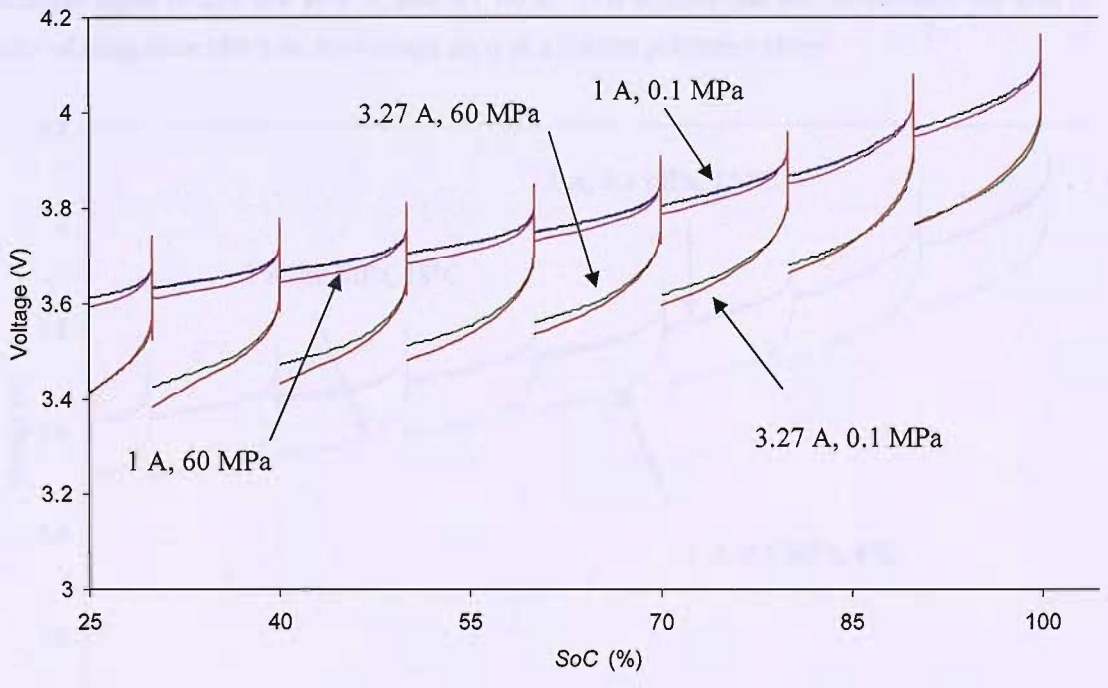

Figure 4.6 Curves of discharges at 1 A and 3.27 A, at 0.1 MPa and 60 MPa, and at 18 °C.

At 1 A load, the capacity of the battery at 60 MPa is 91 %, comparable to 90 % at 0.1 MPa as an error of ± 1 % is likely. At 3.27 A the 60 MPa capacity is 92 %, 6 % higher than the 0.1 MPa. This change is due to the knee of the discharge curve occurring earlier for the discharge at 0.1 MPa. The reason for this is probably an anomaly, as the internal resistances for the discharge at 60 MPa are slightly greater. There is anecdotal evidence of pressure squeezing laminates and

improving conductivity between layers, but this is not possible to verify without extensive pressure testing of battery internals.

The point at which this knee occurs is very dependant on slight changes in chemistry so to provide more accurate results these tests would have to be repeated. This would take many weeks of work, during which the problem of the test battery performance decaying over its lifetime would become an issue.

Figure 4.7 summarises the effect of pressure and temperature on the battery at a constant 1 A discharge. The effect of current draw has been removed to illustrate the effect of temperature and pressure. The initial ohmic drop has increased with decreasing temperature, though the gradient of voltage decrease is very similar. At 60 % *SoC* the drop in voltage at 1 Amp, 0.1 MPa and 18°C is 143 mV, this increases to 160 mV when increasing pressure to 60 MPa, and then increases again to 252 mV at 4 °C and 0.1 MPa. This implies that the temperature has also an order of magnitude effect on the voltage drop of a lithium polymer battery.

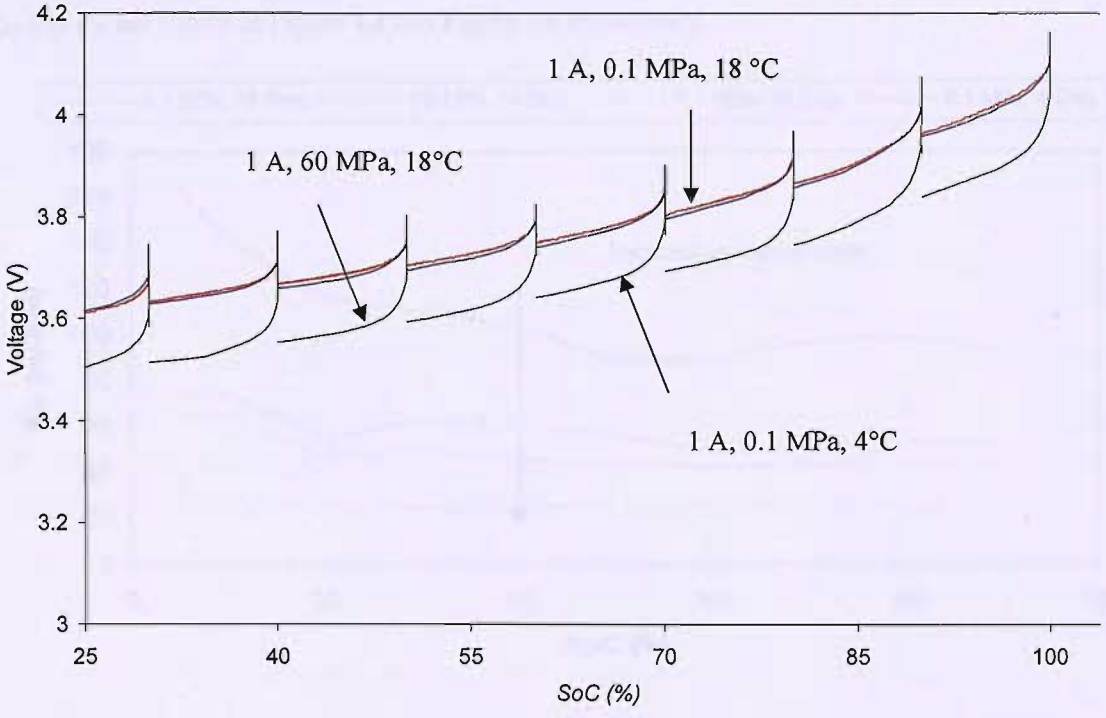

Figure 4.7 Comparison of discharges at 1 A, 0.1 MPa and 60 MPa, and 18 °C and 4 °C.

Battery charge capacity has been estimated as a function of temperature and current load at atmospheric pressure, and then compared to capacity at 60 MPa. There was no statistical difference in capacity at 18 °C and 1 A load between tests at atmospheric pressure and at 60 MPa.

However, at 3.27 A the capacity at 60 MPa was ~5 % above that at atmospheric pressure. This increase may be the result of charging the battery at a slightly different temperature.

These results form the data set that allows the calculation of equivalent circuit parameters.

4.4.1 Creating the equivalent circuit.

The batteries tested by Doerffel were large capacity lithium ion batteries, and it was found that the one minute pause was not long enough to allow the battery parameters to be sufficiently accurately derived. By allowing longer pauses of 15 minutes, and using smaller capacity batteries, the tests conducted should provide more accurate parameters.

In section 4.3 Figure 4.3 illustrated that the voltage came very close to the OCV (0.01 V or 0.5% of maximum voltage. However it was noted that the parameters of the model in equation 4.2 were variable with each pause in the test cycle. A 2 hour pause made no improvement on the voltage rise than a 15 minute pause. It is suggested that R_{01} and C_{12} R_{12}, dominate the internal resistance and hence C_{Long} R_{Long} has a very long time constant and small resistance. The values of R_{01} and R_{12} are shown in Figure 4.8 and Figure 4.9 respectively.

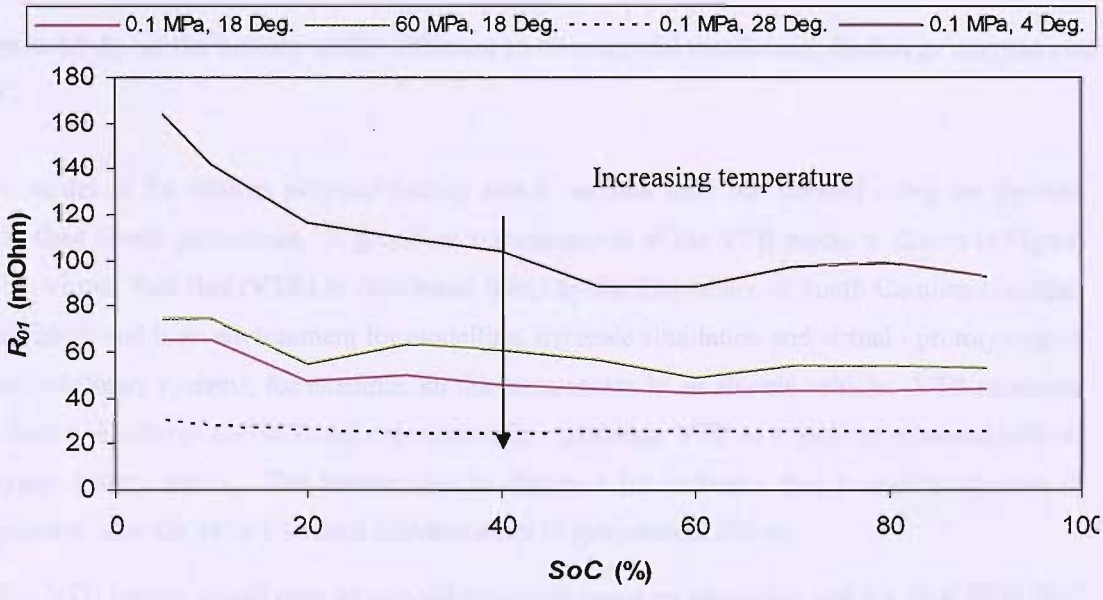

Figure 4.8 R_{01} of the battery under different environmental conditions, discharge current and SoC.

Temperature exhibits a greater effect than pressure on the equivalent circuit parameter values. Comparing these to a base battery at 18 °C and 0.1 MPa, on average, the values of R_{01} and R_{12} at 60 MPa were respectively 5 mΩ (10 %) and 11 mΩ (20 %) higher, than at atmospheric pressure

at the same temperature. Cooling the batteries from 18 °C to 4 °C increased R_{01} by 60 mΩ (120%) and R_{12} by 40 mΩ (100 %). When operating at 1 A, this increase in internal resistance would create a 0.016 V change at 60 MPa, compared to a 0.1 V change at 4 °C.

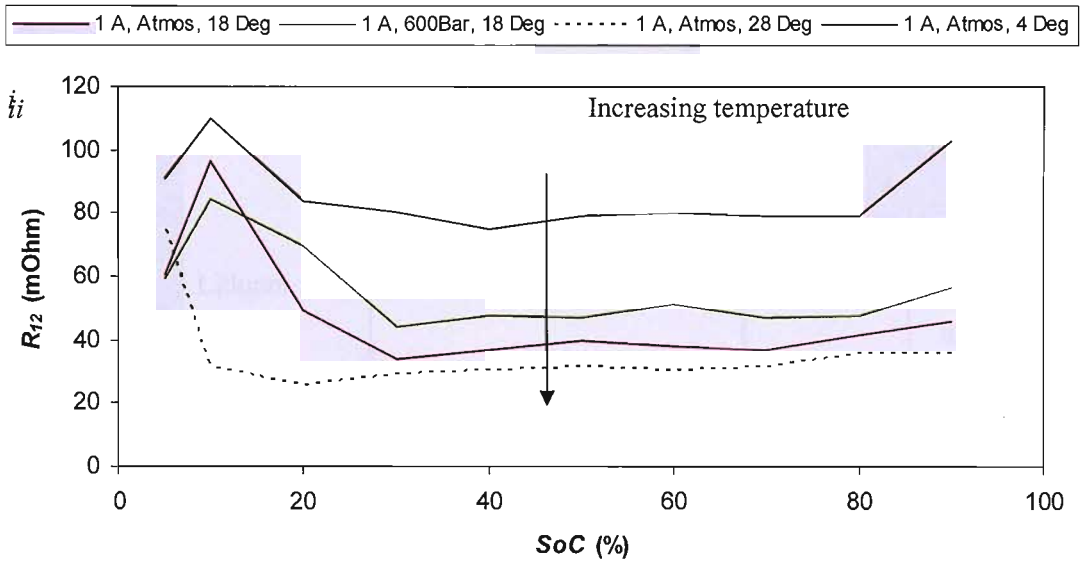

Figure 4.9 R_{12} of the battery under different environmental conditions, discharge current and *SoC*.

A model of the lithium polymer battery and a variable load was created using the derived equivalent circuit parameters. A graphical representation of the VTB model is shown in Figure 4.10. Virtual Test Bed (VTB) is distributed freely by the University of South Carolina (Dougal, *et al.* 2002) and is an environment for modelling, dynamic simulation and virtual - prototyping of interdisciplinary systems, for example, all the components in an electric vehicle. VTB recreated the battery discharge curves found experimentally, validating VTB as a medium to model lithium polymer battery packs. The broken line in Figure 4.10*i* indicates that human interaction is required to alter the battery internal resistance due to temperature effects.

The VTB battery model uses an equivalent circuit based on parameter sets for each 10 % *SoC* increment and then automatically fits a polynomial between these points. The default battery in VTB is shown in Figure 4.10*ii* and the Kokam lithium battery fitted model is shown in Figure 4.10*iii*. The VTB polynomial fitted to the Kokam results creates a 'hump' after 2.5 Ah, causing error below 20% *SoC* in Figure 4.11. As the experimental results were unpredictable below 20 % *SoC* this was not considered a major problem.

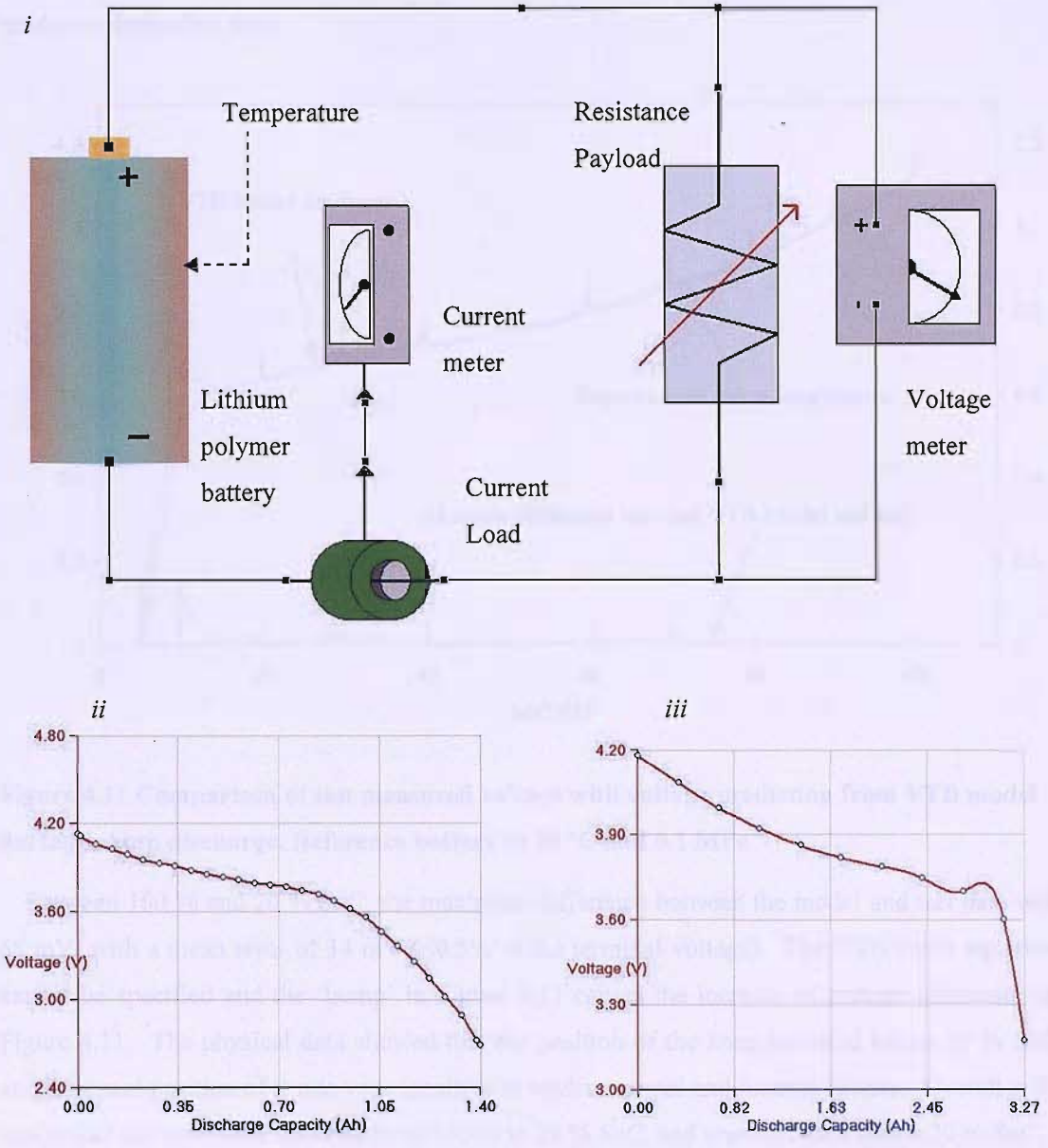

Figure 4.10 i) Kokam representation of the lithium polymer battery and discharge load. *ii*) The default OCV curve used by VTB and *iii*) the OCV curve defined by test results.

Figure 4.11 shows the results of the VTB model run under the same charge / discharge cycle as the physical lithium polymer tests at 28 °C. The equivalent circuit parameters were altered at each 10 % *SoC*, to reflect the changing values shown in Figure 4.9*i*) and Figure 4.9 *ii*). R_{Long} had not been calculated previously as a larger timescale than 15 minutes (or even 2 hours) is required to reach equilibrium. The value of C_{Long} was found from the voltage after the 2 hour pause. This

assumes that the capacitors C_{12} and C_{Long} will have ceased to provide charge hence the voltage is resistance dependant only.

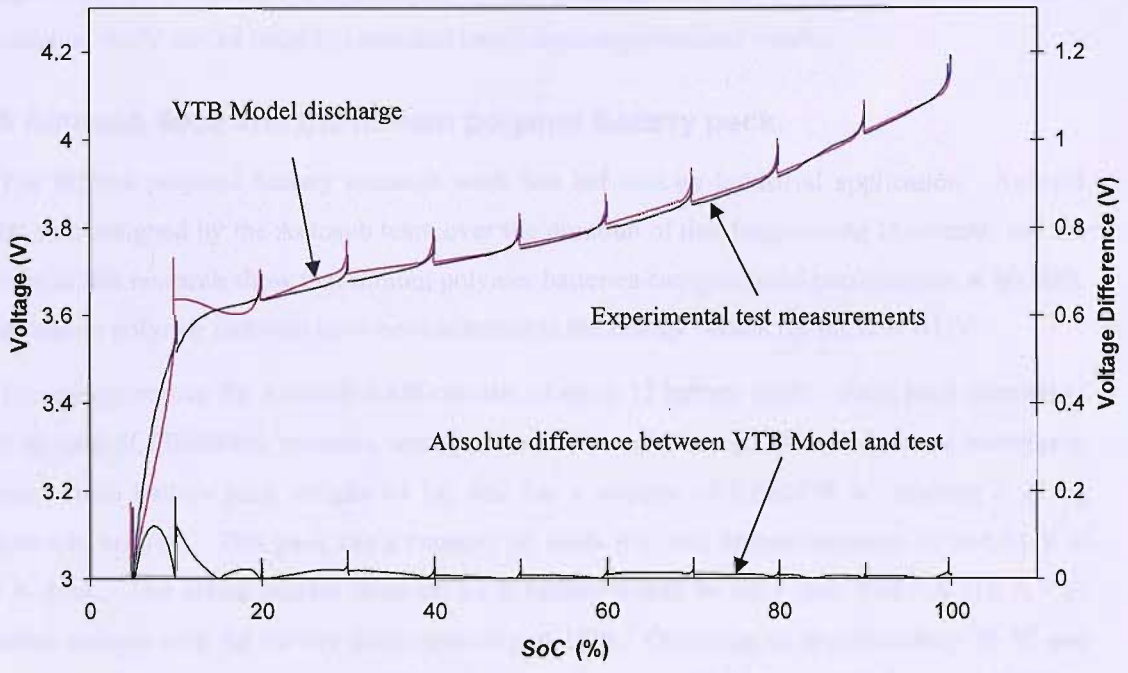

Figure 4.11 Comparison of test measured voltage with voltage prediction from VTB model during 1 Amp discharge. Reference battery at 28 °C and 0.1 MPa

Between 100 % and 20 % *SoC*, the maximum difference between the model and test data was 65 mV, with a mean error of 14 mV (<0.5% of the terminal voltage). The VTB curve equation cannot be specified and the 'hump' in Figure 4.11 causes the increase of voltage difference in Figure 4.11. The physical data showed that the position of the knee occurred below 20 % *SoC* and the exact position of it was very sensitive to environmental and internal factors. Overall with this model the results are accurate from 100 % to 20 % *SoC*, and unpredictable below 20 % *SoC*.

As designers seek to obtain greater performance from the vehicle, each parameter in the design cycle needs to be characterised as per operation rather than as per conception. The understanding of the model lithium polymer battery will provide designers with an estimate of the battery behaviour in operation. VTB is a multidisciplinary test bed, so future work might input hydrodynamic models of AUV hulls, and combine this with lithium polymer battery models, to provide a model for the AUV system. Such a model would predict effect of electrical loading and hence the behaviour of the energy source over the mission.

For the design of a concept AUV, the Kokam SLPB526495 battery can be added to an available technology database. The effects of the power available at operating pressure and temperature on the energy available have been investigated. So the energy available for a conceptual AUV can be reliably estimated based upon experimental results.

4.5 Autosub 6000 and the lithium polymer battery pack.

The lithium polymer battery research work has led into an industrial application. Autosub 6000 was designed by the Autosub team over the duration of this Engineering Doctorate, and the results of this research show that lithium polymer batteries can give good performance at 60 MPa. The lithium polymer batteries have been selected as the energy source for the new AUV.

The energy source for Autosub 6000 consists of up to 12 battery packs. Each pack consists of 405 Kokam SLPB526495 batteries, arranged into 27 parallel strings of 15 individual batteries in series. Each battery pack weighs 44 kg, and has a volume of 0.022439 m^3, making it 21 kg negatively buoyant. This pack has a capacity of 4800 Wh, and operate between 61 and 51 V at 18 A draw. The actual current draw on each battery would be very low, 0.667 A (18 A / 27 parallel strings) with the battery pack operating at 18 A. Operating at approximately 20 °C and 1000 W this battery pack is expected to give an endurance of 4.5 hours. Operating at 4 °C the resistance of each battery increases by 100 mΩ. This resistance increase would mean more energy is expended on overcoming resistance, and it is likely that the voltage drop would cause the terminal voltage to reach cut-off prematurely. Overall the battery duration time would be reduced to 3.76 hours operation. Knowing this, the mission would best be planned for 3.76 hours operation per battery pack when cold temperatures are expected.

Each battery pack has a large diaphragm to allow for the pack volume to change during operation. The battery packs are overfilled with oil to replace any air pockets to reduce volume change of the structure around the batteries. The diaphragm is fitted with a hall sensor to give a measure of diaphragm displacement over the mission and hence give an estimate of pack volume change. Four battery packs have been constructed and used as the energy source and, depending on the actual expansion of the packs, up to twelve packs may be placed within Autosub 6000's parallel middle body.

The final battery pack has an energy density of 102.3 Wh kg^{-1}, which is less than the Bluefin battery density of 116 Wh kg^{-1} (Chapter 2). This is most likely due to the titanium casing and could be reduced by using another material such as aluminium. The volume of the battery pack is 0.022439 m^3 giving it a mass density of 1961 kg m^{-3}. These values will be useful for sizing the energy source in Chapter 7 and Chapter 8.

4.5.1 Trials results.

Autosub 6000 has been for sea trials, and the results from the battery performance are very encouraging. The vehicle dived to 4556 m and remained there for 100 minutes, for a mission duration of over 7 hours 30 minutes (Furlong 2007). This was powered by four 4800 Wh battery packs. The depth, pack voltage, current draw and internal pack temperature is plotted over time in Figure 4.12.

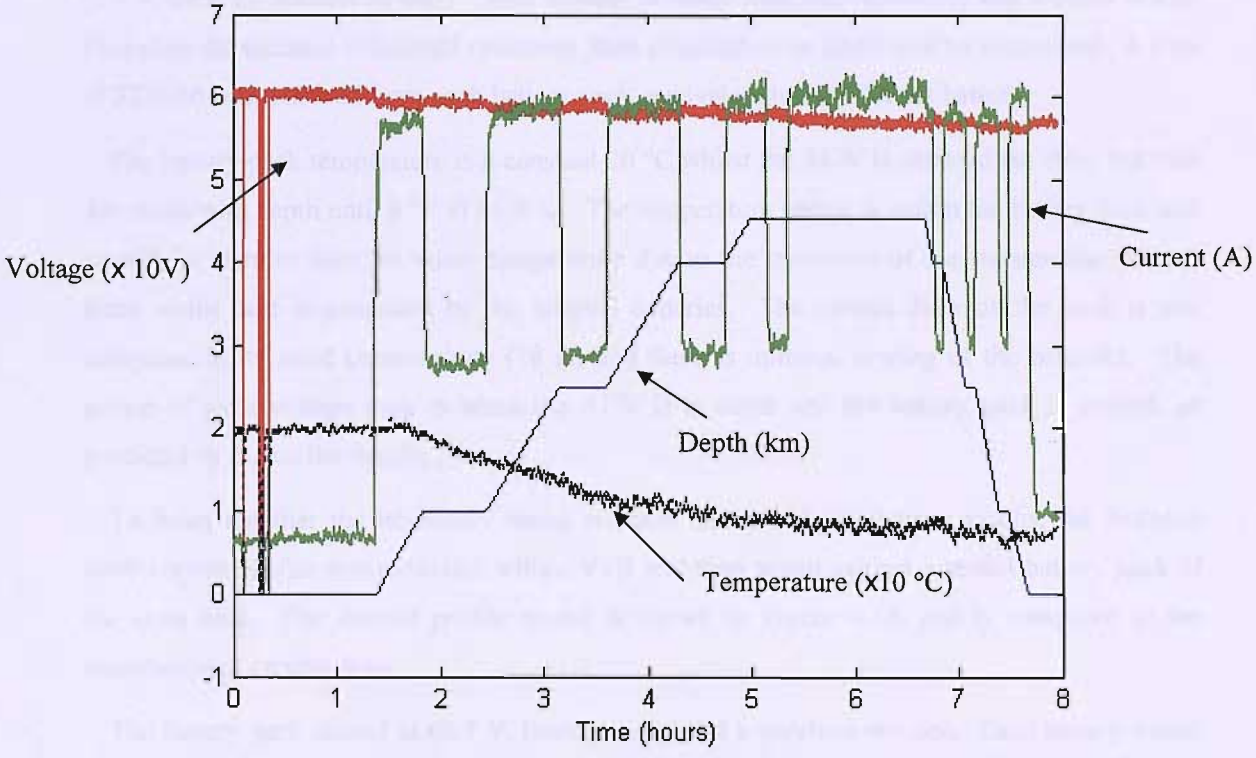

Figure 4.12 Battery voltage (V), pack current draw (A) and temperature (x10 °C) with diving depth (m) for Autosub 6000 trials mission 2.

The data logs were started whilst the AUV was onboard the support boat. The voltage spikes which drop to almost 0.0 V occurred during system reboots and pre-mission checks. Thereafter the voltage linearly decreases over the mission, showing a slight reduction with current peaks and slight recovery at lower current draws. Since the AUV is being tested, the power draw from the energy source is limited and lower than normal operational power draw, giving each battery pack an endurance of longer than 4.5 hours. There is a lot of noise in the voltage, current and temperature readings. This is perhaps caused by sensors and data logging rather than an actual voltage, current and temperature variation.

The current draw over the mission can be defined into two periods, high draw when the vehicle is diving, and low draw when maintaining a mission specified depth. Whilst maintaining a depth the vehicle is still circling, but is set to operate at 150 W, compared to 400 W when diving. The battery pack power draw is approximately 342 W (59 V, 5.8 A @ 1.75 hours, Figure 4.12) at high current, and 157 W at low current (58 V, 2.7 A @ 2.0 hours, Figure 4.12). For an individual battery the current draw is 0.215 A (5.8 A over 27 parallel strings) and for low power this is 0.1 A (2.7 A over 27 parallel strings). This current is lower than the laboratory test current draws. Therefore the increase in internal resistance from temperature or depth will be minimized. A total of 32.6 Ah was removed from each battery pack, equivalent to 1.21 Ah per battery.

The battery pack temperature is a constant 20 °C whilst the AUV is onboard the ship, but then decreases with depth until 8 °C at 4500 m. The temperature sensor is within the battery pack and so will be warmer than the water temperature due to the insulation of the surrounding oil and foam whilst heat is generated by the internal batteries. The current draw on the pack is low compared to its rated current draw (18 A) and there is minimal heating of the batteries. The period of most voltage drop is when the AUV is at depth and the battery pack is coldest, as predicted by the earlier results.

To bring together the laboratory based research and the physical trials results, the Autosub 6000 current profile was modelled within VTB and then tested against a model battery pack of the same size. The current profile model is shown in Figure 4.13, and is compared to the recorded pack current draw.

The battery pack started at 60.7 V, having completed a previous mission. Each battery would therefore have an OCV of 4.05 V (assuming the pack having been left for a few hours to stabilise), which interpolates to being at 85 % *SoC* Figure 4.3. Therefore the battery model will start at 85% *SoC*.

The temperature reduction from 20 °C to 8 °C is within the laboratory temperatures tested in section 4.4. A fuel gauge providing a conservative estimate of remaining power is preferred, so the cold 4 °C average resistance values (Figure 4.9 over 100 % to 20 % *SoC*) will be used over the mission. This is to treat the fuel gauge as if it were being used prior to the mission. To make this more accurate a temperature dependant input to the model should be created and the model run in stages with pauses to alter battery values with *SoC*.

32.6 Ah was removed from the available 89 Ah, approximately a third of the maximum possible energy. So the terminal voltage is likely to indicate that the battery is above 50% *SoC*. Although the trail results are known, and the voltage does not decrease significantly, were the

VTB model used prior to the mission this energy draw may not be so well known. Therefore the equivalent circuit values would not be as easy to predict over the mission as they vary with *SoC*. The values used to generate the battery pack voltage do not vary over the mission time.

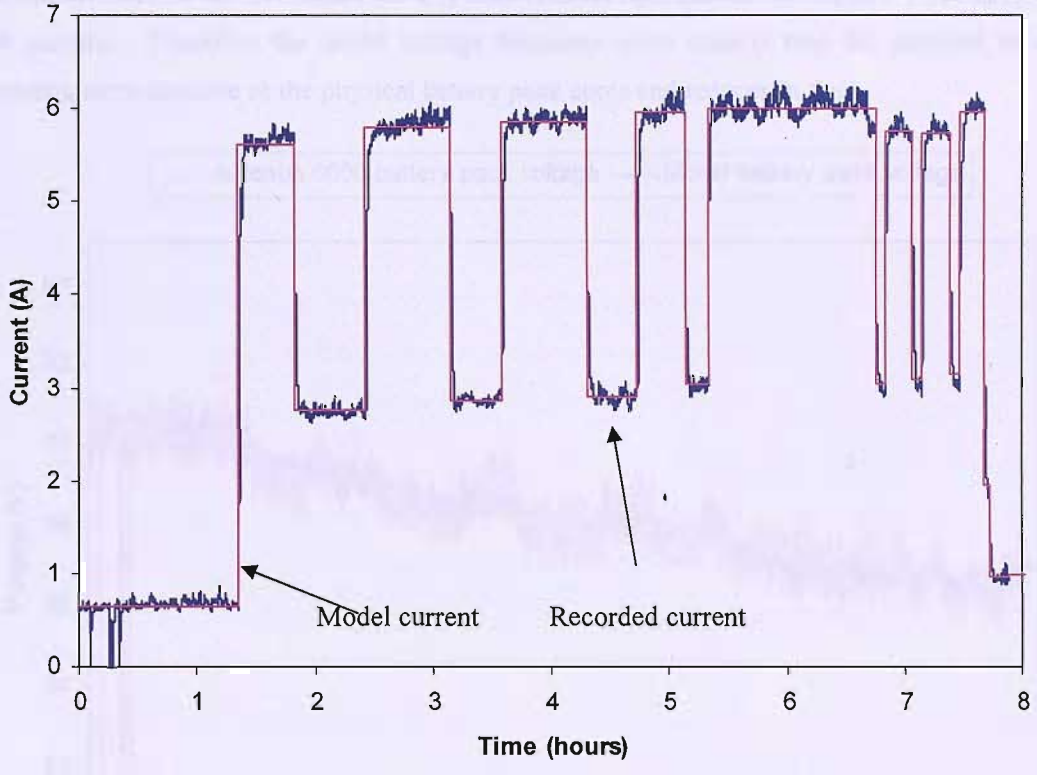

Figure 4.13 Current draw from trials and the representative model in VTB.

Figure 4.14 shows the results of using the lithium polymer battery model corresponding to the recorded current draw profile compared with the measured voltage from Autosub 6000's battery pack. The model results do not have the noise of the measured results, as it is a computational model with a smooth current draw. The different current draw states are reflected as a voltage change in both sets of data.

The noise in the trial measurements makes any quantified voltage comparison very difficult. The differences would be obscured by the noise, and a filtering algorithm is likely to increase error. The VTB model does overestimate the voltage from 5000 to 10000 seconds and is more accurate after 18000 seconds.

The model internal resistance was based on a 1 A current draw, the lowest tested, so the model voltage will decrease more quickly than the actual data. At the start of the mission there are two additional factors, temperature and internal resistance at the initial *SoC*. The equivalent circuit

parameters were those found at 4 °C and averaged over the *SoC* range. The physical battery is warmer than this at the start of the mission resulting in a lower internal battery resistance. The internal resistance of the battery has also been shown to be lower than the average at high *SoC*. The overall affect is that the model has a greater internal resistance as anticipated when the worst case scenario. Therefore the model voltage decreases more quickly than the physical results, becoming more accurate as the physical battery pack cools and reduces in *SoC*.

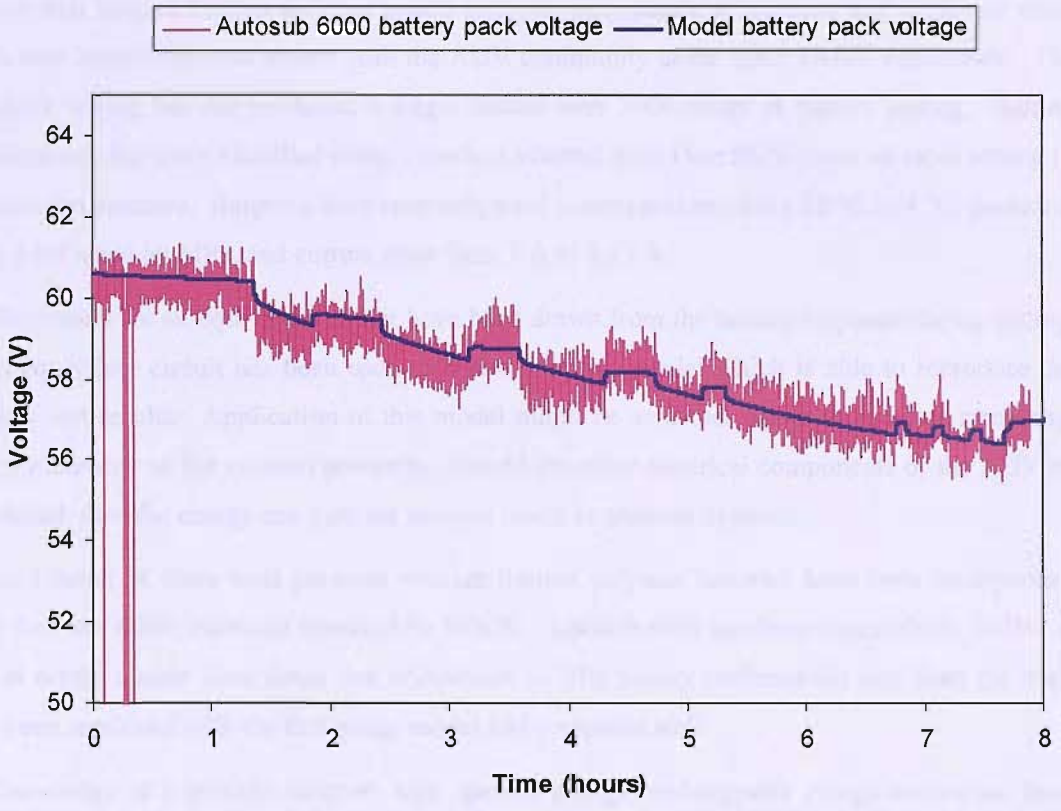

Figure 4.14 Comparison of Autosub 6000 battery pack voltage and model battery pack voltage over mission duration.

The model represents purely the batteries and a programmable load, and does not represent the battery management system or circuit board and external connections. Thus it will not account for any of the associated losses of these components.

For an AUV designer this tool would allow a detailed investigation of the energy source performance over a mission. With more physical tests a formula or look-up table of internal resistance variation with temperature could be created and so the battery resistance tailored to the expected temperature of the water.

A complete electrical model of the AUV could then be made, depending on the detail of the subsystems that would draw power from the AUV. This would permit tentative verification of AUV in terms of its design endurance during the conceptual design stages.

4.6 Conclusions.

Previous chapters provided motivation for a pressure tolerant energy source. This Chapter has shown that Kokam lithium polymer pouch batteries can operate at pressure and fulfil that need. This new knowledge was shared with the AUV community at the 2005 UUST conference. The pressure testing has not produced a single failure over 2800 hours of battery testing. Battery performance has been modelled using a method adapted from Doerffel's paper on rapid testing of lithium ion batteries. Batteries have been subjected to temperatures from 28 °C to 4 °C, pressures of 0.1 MPa and 60 MPa, and current draw from 1 A to 9.75 A.

Parameters for an equivalent circuit have been drawn from the battery response during testing. This equivalent circuit has been used to create a battery model which is able to reproduce the battery test results. Application of this model might be as a fuel gauge to estimate remaining battery capacity as the mission proceeds. Should the other electrical components of the AUV be modelled, then the energy use over the mission could be planned in detail.

As a result of these tests pressure tolerant lithium polymer batteries have been incorporated into Autosub 6000, built and operated by NOCS. Autosub 6000 has been successfully trialled at sea at depths almost three times that of Autosub 2. The battery performance data from the trials has been combined with the fuel gauge model and compares well.

Knowledge of a pressure tolerant, high specific energy, rechargeable energy source has been improved by this research and the fuel gauge developed could be a tool to help concept AUV design.

Chapter 5
Hydrodynamic investigation methodology and reviews.

There is a need to understand the effect of hull shape on the drag of an AUV because of the effect of the volumetric drag coefficient, C_{D_∇}, on AUV endurance.

To create physical AUV models and carry out testing would be too time intensive. Therefore the option of applying computational fluid dynamics (CFD) was adopted. Computational models are created and tested over a shorter time period and with less economic cost.

This Chapter discusses the hydrodynamic approach adopted to create the test results of Chapter 6. A summary of potential method theory precedes then laminar and turbulent boundary layer modelling methods. The prediction of boundary layer transition is explored due to its importance to the performance of laminar boundary layer hull shapes.

Three hull shapes are to be modelled. Relevant literature will be reviewed and used to verify the computational results. The parallel middle body is common to many AUVs including Autosub. The two laminar flow hull shapes rely on maintaining a laminar boundary layer over the majority of the body surface, so reducing the hull shape dependant C_{D_∇}. This presents an attractive option for increasing AUV endurance. The laminar flow hull shape described by Parsons (Chapter 2) will be modelled together with a second simplified laminar hull shape.

5.1 Hydrodynamic theory.

A 3D coupled potential method (Palisupan) is used for this research. The Palisupan panel code, originally created at Southampton (Turnock 1997), permits the modelling of a variety of hull shapes. The availability of the Author for discussion was also considered an advantage.

Other types of CFD modelling are available and are well described in the published literature. The theory underpinning potential flow methods has been described by other authors, and will not be repeated here. Further reading should include Anderson (2001), Katz and Plotkin (2001) and Houghten and Carpenter (2003).

Potential, panel or boundary element methods represent body surfaces as discrete panels to find the velocity and pressure of the local fluid flow.

Many theoretical fluid flow investigations exploit the concept of an irrotational, incompressible and inviscid potential fluid. This produces acceptable models for many applications, even though viscous drag influences on a body are ignored. D'Alembert's paradox is observed e.g. a spherical

body moving at a constant velocity through an infinite fluid experiences no drag force (Anderson 2001 p 269). This is a consequence of the pressure acting on the front of the body equalling the pressure acting on the rear of the body. Viscid flow produces a boundary layer and decreases the pressure acting on the stern. The balance of normal forces is the pressure drag of the shape.

The modelling is limited to flow close to the surface and cannot easily model shed vorticity or separated flow. Predictions for flow separation can be made and the effect of small separations can be estimated and included in the results. The use of a trailing wake sheet behind a sharp trailing edge captures the generation of lift. Viscous fluid effects can be modelled using a boundary layer coupled with the potential flow method.

The process of a coupled potential method can be summarised in four steps:

- Define body surface mesh and find influence coefficients for each panel. Find surface velocity and pressure coefficient across each panel.
- Integration of the pressure coefficients will produce the pressure force on the body. The surface velocity and distance from leading edge can be used to estimate the viscous force contribution, based on a local Reynolds number for each panel.
- Using the outer velocity distribution, obtain the boundary layer displacement thickness and skin friction based on solution of the momentum integral equations.
- Modify the surface velocity and pressure coefficients based upon the boundary layer behaviour. In Palisupan a normal velocity component is imposed at the centre of each panel to represent the momentum decline associated with the boundary layer.

An inviscid method would only use the first two steps. A coupled potential method iterates all four steps.

5.1.1 Boundary layer theory.

The boundary layer is a very thin region of flow at the surface of a solid body. The viscous drag of a body is dominated by the behaviour of the boundary layer and the size of the body's surface area. Further reading should be directed at published literature; for example in Curle (1962), Hoerner (1965), Schlichting (1968), Cebeci and Bradshaw (1977).

In general a laminar flow regime will have a lower skin friction than a turbulent regime. Thus, controlling the boundary layer so that transition from laminar to turbulent flow occurs further along the body can help reduce the body drag. This is the principle motivation for examining the laminar flow hull shape, Chapter 6.

When viscosity is included in the fluid model, the fluid velocity u varies from zero at the wall, (no slip condition), to the free stream velocity (U). Figure 5.1 illustrates different boundary layer velocity profiles over a surface for different flow conditions. The boundary layer thickness (δ) is defined as the point where the local velocity has reached 99 % of U.

Separation is a phenomenon where the tangential boundary layer velocity at the surface decreases to zero. The fluid streamline then separates from the body and creates an area of recirculation.

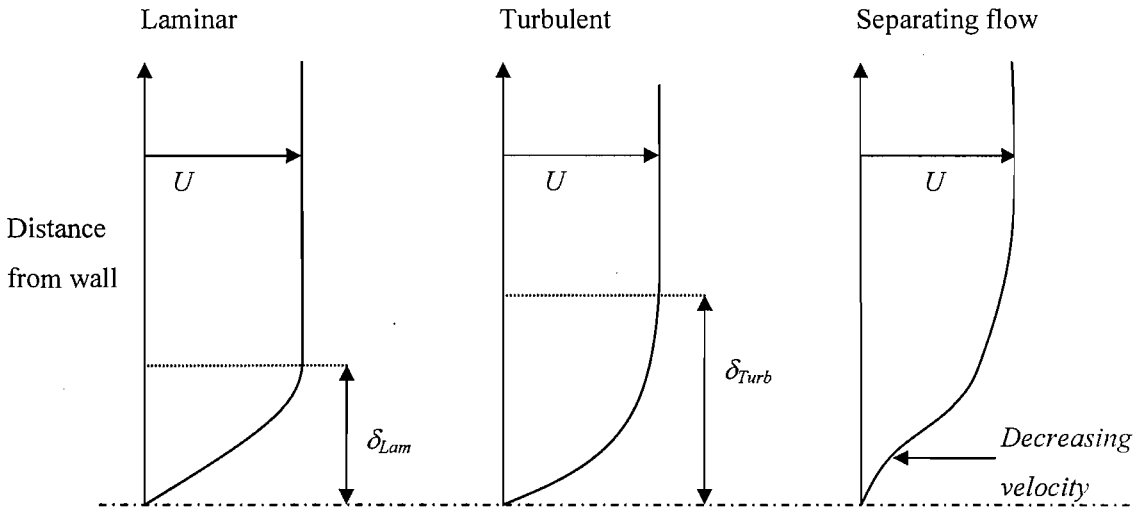

Figure 5.1 Velocity profile of a boundary layer progressing through laminar, turbulent and separating flow.

The boundary layer displacement thickness (δ^*) is the distance the inviscid model body surface would be moved normal to itself in order to represent the physical volumetric flow. The boundary layer momentum thickness (θ) results from the momentum within the boundary layer and has a similar form to the boundary layer displacement thickness. θ is defined by the distance the inviscid model body surface would have to be moved normal to itself to approximate the physical momentum. Equations 5.1 and 5.2 define δ^* and θ respectively (Houghten and Carpenter 2003 pp 385 - 387).

$$\delta^* = \int_0^\infty \left(1 - \frac{u}{U}\right) dy \qquad 5.1$$

$$\theta = \int_0^\infty \frac{u}{U}\left(1 - \frac{u}{U}\right) dy \qquad 5.2$$

The boundary layer shape factor (H) is given by $H = \delta^* / \theta$.

Palisupan has two approximations of boundary layer friction; Schlichting's skin friction approximation and the Thwaites-Head method. The Thwaites – Head method is found in Appendix F of another Ph.D thesis (Hughes 2000). A summary of the Thwaites – Head method is given in Appendix D.

Schlichting gives a simple approximation for C_F in terms of local Reynolds number, Table 5.1 (Schlichting 1968 p. 39, Turnock 1997). This approach is the default C_F approximation for the boundary layer in Palisupan where s is the distance from the leading edge of the shape to the given position along the surface, and υ is the kinematic viscosity of the fluid.

Table 5.1 C_F calculation based on Schlichting skin friction approximation.

$Re_S = \frac{\lvert U_\infty \rvert}{\upsilon} s$	$Re_S < 3 \times 10^5$	$C_F = 0.664 Re_S^{-0.5}$
	$3 \times 10^5 \leq Re_S < 1 \times 10^7$	$C_F = 0.074\, Re_S^{-0.2} - 1050 Re_S^{-1}$

This method has the advantage of requiring no knowledge of the boundary layer properties, and assumes laminar to turbulent flow transition takes place at $Re_S = 3 \times 10^5$. Schlichting's approximation is most valid when there is something to cause transition to occur at $Re_S = 3 \times 10^5$.

Thwaites's method first calculates θ for a specific U and then the boundary layer parameters H and C_F. Thwaites boundary layer approximation has been shown to give a 5 % error in θ and up to 10% error in δ (Hughes 2000). Hughes considers this to be acceptable, and the approximation has been used to model real systems. The method is considered applicable provided the universal function λ remains within the range of -0.1 and 0.1. Appendix D defines λ. Outside these limits the laminar boundary layer becomes unstable. Pashias (2001) considered this problem and it is discussed further in section 5.1.2.1.

5.1.2 Transition prediction.

Transition is the phenomenon where the boundary layer changes from laminar to turbulent flow. The first significant investigation into the conditions that maintain a laminar flow and those which cause turbulent flow was conducted by O.Reynold (Schlichting 1968 p. 3). Reynolds observed flow effects using a dye stream within water flowing through a straight pipe.

The simulation of transition is arguably the most challenging problem in CFD (Houghten and Carpenter 2003 pp. 431 - 437). Additionally Lutz and Wagner write "The determination of the transition region by empirical criteria is the weakest link in Aerodynamic analysis" (Lutz and Wagner 1998). A complete theoretical analysis of transition requires solution of the complete Navier Stokes equations, a computationally monumental task. Computational estimates in practice use theoretical and empirical results.

Transition does not occur at a point, but within a region of unstable laminar flow. Hence a transition 'point' is a relatively vague but extensively used concept. For this computational method the transition point is the first point where the boundary layer changes from laminar to turbulent flow.

The Reynolds number of the flow at the point of transition is called the critical Reynolds number, Re_{crit}. The Re_{crit} range of a flat plate with no pressure gradient is defined from the flow velocity, viscosity and the distance from the leading edge, as shown in equation 5.3 (Schlichting 1968 p. 39).

$$\mathrm{Re}_{crit} = \frac{U_\infty}{\nu} x_{crit} = 3.5 \times 10^5 \text{ to } 1 \times 10^6 \qquad 5.3$$

The laminar boundary layer becomes unstable at a distance x_{Crit} from the leading edge and transition follows. The C_F estimate in Table 5.1 is based on this value of Re_{crit}. Factors such as a pressure gradient, surface roughness or turbulence intensity of the fluid can change the value of Re_S at which transition occurs. Over a curved surface, such as the bow of an AUV, there will be a varying pressure gradient and so a boundary layer approximation capable of predicting the transition point would be preferred. In this research wall roughness is not modelled as the surface is assumed to be smooth mathematical function.

A negative pressure gradient along a body favours extending a laminar boundary layer by suppressing instability. A negative pressure gradient corresponds to decreasing pressure and increasing U. A positive pressure gradient is considered unfavourable for supporting a laminar boundary layer (Anderson 2001 pp. 715 - 722, Hoerner 1965 p. 2-11, Schlichting 1968 pp. 324 - 346, p. 366, pp. 467 - 476). Negative pressure gradients are found where the geometry radius increases, such as at the AUV bow. A positive pressure gradient is generally found at the AUV stern. Hoerner gives a graph showing the effect of pressure gradient on the Re_{crit} of the boundary layer, Figure 5.2.

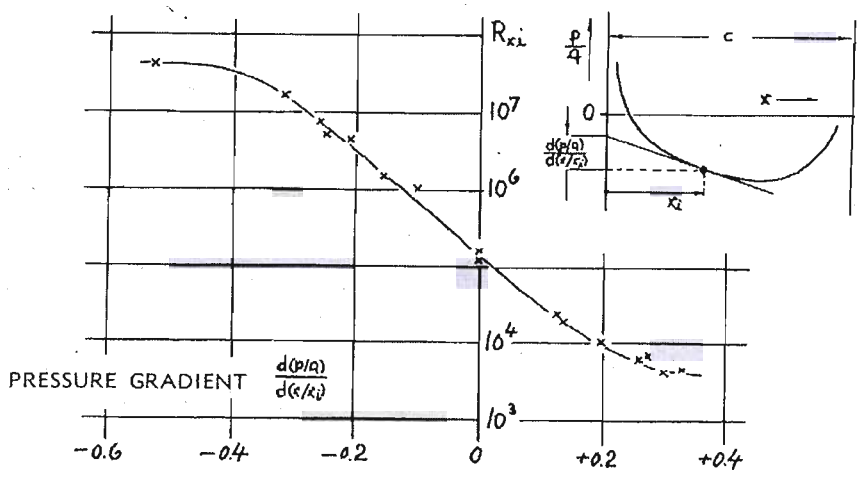

Figure 5.2 Prediction of Re_{crit} with boundary layer pressure gradient (Hoerner 1965 p. 2-11).

Figure 5.2 suggests that Re_{crit} can be increased to over 10^7 before instability occurs in the velocity profile, assuming a large pressure gradient.

Houghton and Carpenter give some rough guidelines to transition prediction within a pressure gradient (Houghten and Carpenter 2003 pp. 431 - 437). These are most applicable to wing sections and streamlined bodies.

I. If $10^5 < Re < 10^7$, then transition will occur just after the point of minimum pressure. The point of minimum pressure will often occur at the point of maximum diameter.

II. Increasing Re when the body is at a constant angle of incidence will move the point of transition forward.

III. For $Re > 10^7$ the transition point may precede the point of minimum pressure.

For computational models approximations have to be made. H can indicate boundary layer state depending on boundary layer thickness. On a flat plate, typical steady state shape factor values are H ~2.6 for a laminar boundary layer and H ~1.4 for a turbulent boundary layer (Schlichting 1968 p. 436).

Thwaites gives a minimum H value of 2.8 as a transition point during which H decreases rapidly until the boundary layer becomes turbulent (Thwaites 1960 p. 65). Laminar separation is very sensitive to pressure changes, and can occur before boundary layer transition. A H value of 3.0 would occur prior to boundary layer separation and would indicate that the velocity profile is linear, similar to the laminar velocity profile in Figure 5.1 and $H = 4.0$ is indicative of laminar flow separation (Cebeci and Bradshaw 1977 pp. 13 -19, p. 100). Palisupan triggers transition

when H is greater than 3.0. The behaviour of H before the threshold is used to determine whether the boundary layer is separating or transitioning to turbulent.

Once the boundary layer is turbulent H has to increase to between 1.8 and 2.4 to indicate separation (Cebeci and Bradshaw 1977 p. 194, Schlichting 1968 p. 645). The actual H value is not the only indicator. The rate of change of H (dH/dx) becomes very large at separation.

Numerical methods that predict boundary layer transition are generally based upon empirical correlation. Cebeci & Smith's transition criterion is based upon matching a curve to empirical transition data and e^9 instability theory (Cebeci and Smith 1974 pp. 332 - 333). Another method used by Murphy in conjunction with Palisupan for modelling a flat plate (Murphy 2005) is the *H-Re* method (Wazzan, *et al.* 1981). Both methods will be briefly described next.

The e^9 method combines stability theory with empirical results, correlating the distance from boundary layer instability to the beginning of transition. The criterion for transition is that a small disturbance introduced at the Re_{crit} has been amplified by a factor of e^9 or about 8000. Such transition prediction requires knowledge of the disturbance amplitude at each station along the body and is a level of detail not modelled by Palisupan.

An empirical approach was first used by Michel, and then by Cebeci & Smith (Cebeci and Smith 1974 pp. 332 – 333, Cebeci and Bradshaw 1977 p. 153). Michel's work correlates Re_θ with Re_x at transition for incompressible flow using empirical results for two dimensional flow with constant properties. Cebeci & Smith fit an alternative curve to the same data set to produce equation 5.4. Transition is predicted when equation 5.4 is satisfied.

$$\mathrm{Re}_{\theta tr} = 1.174\left(1+\frac{22400}{\mathrm{Re}_x}\right)\mathrm{Re}_x^{0.46}$$
$$\mathrm{Re}_\theta = \frac{u\theta}{\nu}, \mathrm{Re}_x = \frac{ux}{\nu} \qquad 5.4$$

Plotting $Re_{\theta tr}$ using equation 5.4, $f(Re_x)$, and Re_θ along the body will produce the two curves of Figure 5.3.

Figure 5.3 corresponds to the Parsons hull shape and transition should occur when these curves cross as Re_θ has exceeded $Re_{\theta tr}$. The two curves cross at a point 3.3 m from the leading edge, 41 % of total body length.

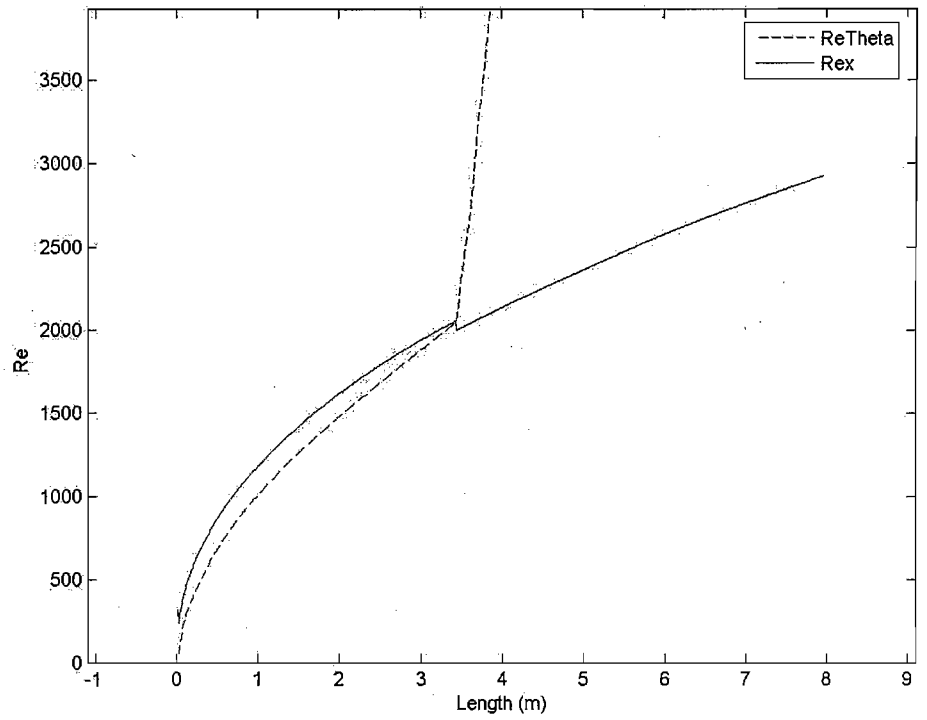

Figure 5.3 Prediction of transition plotting Re_x and R_θ for the Parsons hull shape at 3.5 ms^{-1}.

The Cebeci & Smith theory is based upon empirical tests and does not claim to support pressure effects. The parameters required for equation 5.4 can all be calculated from the Palisupan results and this method will be compared against other transition prediction methods.

This research will include pressure changes so another method is considered that claims to account for pressure effects.

Wazzan, *et al.* claim that H is the best measure of stability, therefore the transition prediction should use H and not have to rely on other parameters. H reflects the influence of pressure gradient, fluid heating and surface suction. This assumption is based upon the correlation of Re_{crit} over a variety of wedge shape and flat plate results. All the results fall on a single curve and Wazzan *et al.* state that H is therefore the immediate determinant of stability. The proposed polynomial is shown in equation 5.5.

$$\log\left[\mathrm{Re}_S\left(e^9\right)\right] = -40.4557 + 64.8066H - 26.7538H^2 + 3.3819H^3 \qquad 5.5$$

$$\text{for } 2.1 < H < 2.8.$$

Beyond the limits of H in equation 5.5 the plot will become unstable. However if H is below 2.1 then the boundary layer is considered to be laminar, and above 2.8 then the boundary layer shape is starting to indicate laminar separation.

Figure 5.4 provides the lengthwise variation of the left hand side ($log(Re_S)$) and right hand side ($f(H)$) of equation 5.5. When the curves intersect equation 5.5 is satisfied and predicts boundary layer transition. The intersection at nearly 2 m indicates the onset of boundary layer transition.

This method is suggested for 2D models, as 3D models have more complex boundary layer solutions. Palisupan models the boundary layer along streamlines along the body, and so does not consider 3D boundary layer effects. Therefore a 2D transition prediction method is applicable.

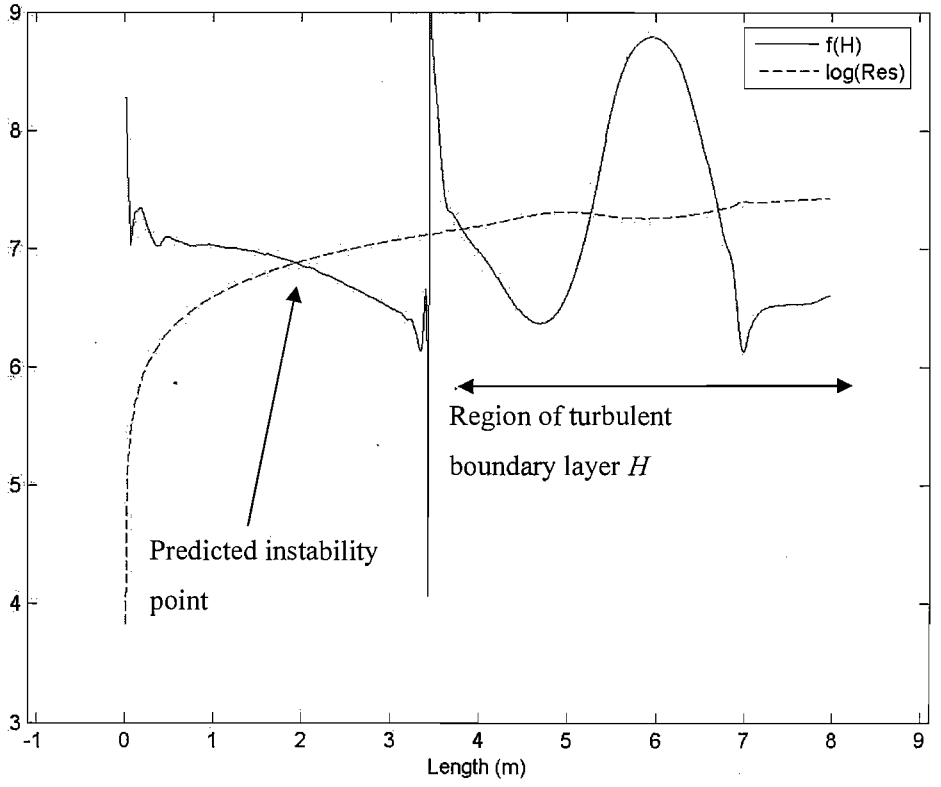

Figure 5.4 Left and right hand sides of equation 5.4 plotted against length to predict boundary layer transition for the Parsons hull shape at 3.5 ms^{-1}.

This approach was used by Chettleborough and Murphy to estimate transition for Autosub 2. Thereafter the Palisupan model was rerun with specified transition at the predicted transition point (Chettleborough 2002). The Wazzan *et al.* method will be applied in Chapter 6 and to

compare the transition prediction based on the Cebeci & Smith procedure and the Schlichting skin friction estimate.

5.1.2.1 Palisupan transition prediction method.

The Thwaites - Head approximation in Fortran code was originally written by Holt (Holt 1997) and rewritten by Hughes (Hughes 2000). It has since been rewritten into C++. This method initially estimates the laminar boundary layer from Thwaites' laminar boundary layer approximation (Cebeci and Bradshaw 1977 pg. 108 - pg.110), and then estimates the turbulent boundary layer using Head's turbulent boundary layer approximation (Cebeci and Bradshaw 1977 pg. 192 - pg.194). In the Palisupan boundary layer approximation the Thwaites' approximation is run initially. Transition criteria are checked at every panel and when these are met, Head's approximation for turbulent flow initiates and continues over the body.

Pashias worked to improve the Palisupan code to facilitate modelling of Autosub (Pashias 2001). The boundary layer initially would fluctuate between completely laminar and completely turbulent and not converge to a solution. This situation was considered attributable to two possibilities; either the geometric form of the aft body or boundary layer model was causing instability. The aft body was not investigated and so became a section of work within this Thesis, 5.1.2.2. Palisupan would not come to a solution when modelling geometries with very bluff sterns where separation is almost guaranteed, so a workable solution was required.

Work on the boundary layer model found that λ, used for the Thwaites approach, would become unstable outside of the valid -0.1 to 0.1 region. Pashias fitted an alternate function to the same data used by Thwaites to produce his function between λ = -0.1 and λ = 0.1 so that the function was no longer unstable outside this region. No results are given of this version with the Autosub model. Pashias thereafter moved on to a Polhausen boundary layer methodology. This improvement to the boundary layer estimation method has not been implemented in the code. Palisupan uses a pragmatic method whereby when λ is beyond its valid region, the value of H is held constant until λ decreases in magnitude.

Palisupan uses three criteria for transition prediction.

I. C_F decreases to 0.0.

II. H exceeds 3.0.

III. Cebeci & Smith transition prediction of equation 5.4.

These three predictors will be checked in Chapter 6. Depending upon the transition criterion met, the cause of boundary layer transition can be identified and interpreted.

5.1.2.2 Palisupan stern modelling assumptions.

An issue was found when modelling the transom stern of Autosub by Pashias and initial tests in this research. The streamline separation and wake was not captured and gave incorrect drag estimates. Figure 5.5 shows a profile of an AUV transom stern and artificial tail. The tail was sized to continue the stern gradient to a point, and so not require modelling of a separated streamline.

For a completely inviscid model the unseparated streamlines would follow the geometry around the transom stern and produce a pressure force. This is the same effect noticed by D'Alembert. For a coupled potential model the theoretical boundary layer model would often not come to a solution around such a geometry change. A practical work around was required, hence the addition of an artificial tail. Example C_P plots with and without the tail are discussed in Appendix D.

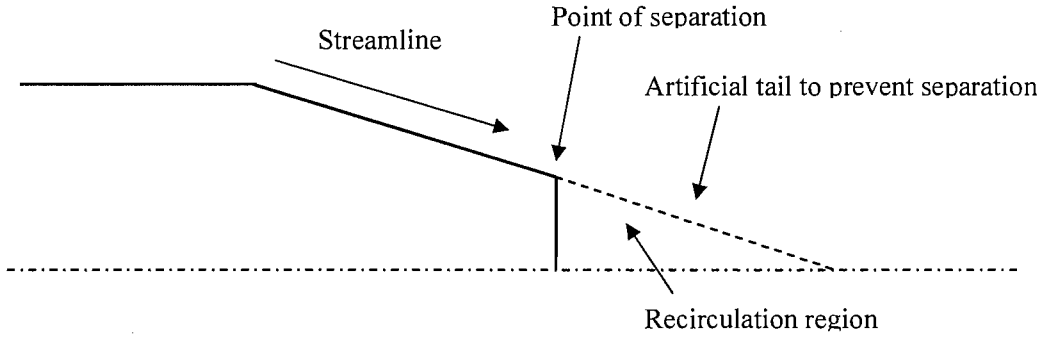

Figure 5.5 Profile of an AUV transom stern showing artificial tail.

5.1.3 Hydrodynamic theory summary.

Having summarised the basic hydrodynamic theory of potential methods special attention has been given to the likely causes (real and artificial) of laminar to turbulent boundary layer transition. The artificial treatment of separation as transition within Palisupan will require careful attention when examining the AUV hull forms investigated in Chapter 6.

5.2 Literature on hydrodynamic shape.

5.2.1 Autosub.

The evolution of Autosub was introduced in Chapter 2. This section now reviews the published research concerning the hydrodynamic characteristics of Autosub.

Kimber and Scrimshaw conducted physical hydrodynamic testing of Autosub (Kimber and Scrimshaw 1994). This used a 0.74 scale model with a cruciform arrangement of control surfaces (NACA 0015 aerofoil sections of varying length) and a freewheeling propeller. The drag results of the bare body were not published. For the full scale Autosub vehicle with the smallest tested control surfaces the drag was estimated at 127.5 N at a design speed of 2 ms^{-1}, for a form displacement of 3.512 m^3, C_{D_∇} = 0.02648. The middle sized appendage set increases drag to 129.0 N and the largest sizes gives a drag of 137.8 N, corresponding to C_{D_∇} = 0.02724 and C_{D_∇}=0.02909. This does not include a volume increase resulting from increasing appendage size.

Autosub's hull shape was examined by Pashias utilising an earlier version of Palisupan (Pashias 2001). The body is modelled both as a bare model and with control surfaces included. The predominant focus of the report is the modelling and stabilisation of the boundary layer. The numerical stabilisation of Thwaites – Head boundary layer model within Palisupan was discussed in section 5.1.3.1. The modelling results at 2 ms^{-1} estimated the bare hull drag at 105.04 N. The cruciform control surface arrangement increased drag by 23.92 N for a total drag of 128.96 N. Given a form displacement of 3.208 m^3, this would result in C_{D_∇} = 0.02356 for the bare hull and C_{D_∇} = 0.02892 for the appendage set (not including increased volume from appendages). This compares very well to the Kimber and Scrimshaw results, and provides encouragement that the Palisupan program can model the Autosub hull. The boundary layer used a Polhausen approximation and indicated that the boundary layer could separate at 1.08 m (15.4 % of body length) as C_F reached zero, but did not actually undergo transition until 2.08 m (29.7 % of body length). No insight is shown regarding what triggers boundary layer transition but this is a first investigation of the boundary layer transition point for Autosub. The current version of Palisupan does not use the Polhausen model.

Further tests by Pashias then covered some variant bare hulls at 2.0 ms^{-1}, which were defined by simple parabola profiles with four coordinates. It was found that if the point of maximum diameter occurred far along the body length, giving a bluff stern, then the drag estimate would suddenly decrease. This is considered an error by Pashias but is not explored. This highlights a problem with inviscid flows and modelling separation around such a large geometry change.

Chettleborough followed Pashias's work of modelling Autosub in Palisupan (Chettleborough 2002). The bare hull and cruciform control surfaces are both modelled. The boundary layer model theory was not discussed, but the identification of transition points was considered. The bare hull drag prediction with transition manually set at 0.977 m is 95.78 N (C_{D_∇} = 0.0198), of which 89.97 N is due to friction. Hoerner gives a drag relationship for rudders accounting for 4% of the surface area results in a 6 % increase in drag (Hoerner 1965). Chettleborough comments that a 6 % increase gives a drag increase of 5.75 N, which will not give a total drag that compares with Kimber and Scrimshaw. The control surfaces are then assumed to have C_{DSa} = 0.02 and surface area of 0.94 m^2 to give an increase of 38.54N. This gives a total drag estimate of 134.32N (C_{D_∇} = 0.0278). This compares well with Kimber and Scrimshaw for a medium sized appendage set. The bow is evaluated as a single body without the middle body or stern, and the boundary layer transition occurs at 0.629 m (9 % of total body length). When considering the whole body the boundary layer transition is found to occur at 0.806 m (11 % of body length) along the bow when using the *H-Re* method. Transition is forced at this point within Palisupan and the drag estimates generated based upon this transition prediction.

The aspect ratio of the bow was varied, by increasing the length of the whole vehicle. The results show the transition moving backwards with increasing bow length, and hence a decreased C_{D_∇} due to longer laminar boundary layers. Chettleborough does not examine the Palisupan code but comments that Palisupan would often not solve the boundary layer problem. These transition prediction results are expected from previous work, but may be accidental. The improvements of modelling the stern made in this research (adding a tail) stabilise the results and encourage successful solution of the boundary layer code.

Fallows produced towing tank data of a scale model of Autosub (Fallows 2005). The primary aim was to assess the influence of appendages upon the bare hull drag at different angles of attack (Aoa, Figure 5.6). The appendages represented payload subsystems that protruded beyond the hull shape and into the flow. The towing tank results were checked against theory and computational methods to establish the true drag force of the bare hull. The C_{D_∇} results from physical testing of the bare hull are shown in Figure 5.6.

Due to the length restrictions of the Southampton Solent University tank used by Fallows it was not possible to investigate the model at higher *Re*. The presented results indicate that there is a cubic polynomial formula to describe the drag of Autosub, with a local minimum C_{D_∇} = 0.012 at *Re* 6 x 10^6. Deceleration tests of the actual Autosub were conducted at sea and their results analysed and compared by Fallows. The C_{D_∇} at sea was found in the *Re* range of 5 x 10^6 to 9 x 10^6.

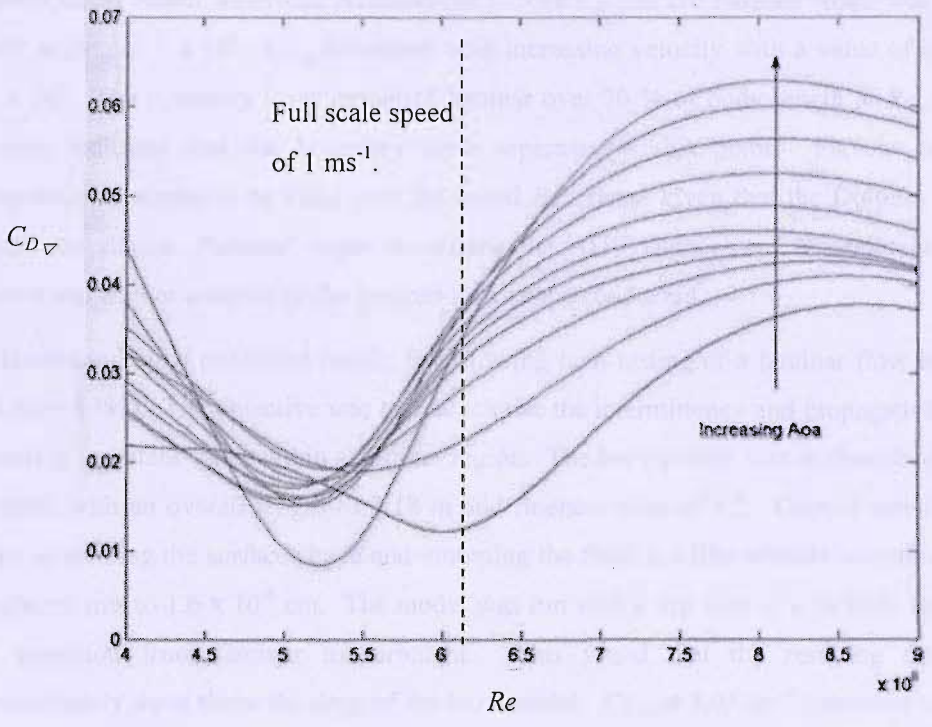

Figure 5.6 Drag prediction and $C_{D\nabla}$ of the Autosub model including control surfaces at various *Re* and angles of attack (Fallows 2005 pp. 180 -181).

Fallows's results gave a quadratic polynomial, with a local $C_{D\nabla}$ maximum of 0.07 to 0.085 between $Re = 7 \times 10^6$ and $Re = 7.5 \times 10^6$.

One towing tank data point is corrected for the angle of attack (2.5 °), payload fit, nose modifications, and gives a predicted drag of 168 N at 1.4 ms^{-1}. Fallows considers this to be a good fit with the deceleration results and considers the towing tank data to be true.

Overall, Fallows's experiments give additional physical results with which to compare predicted drag found from Palisupan models. Figure 5.6 demonstrate that the velocity is important to the $C_{D\nabla}$ predictions. A single $C_{D\nabla}$ value for a particular shape may vary with velocity, and this will considered in later in Chapter 6.

5.2.2 Laminar flow body.

The laminar flow shape was introduced in Chapter 2. Parsons provided predictions for the model operating at a Re_{∇} range of 1×10^6 to 1.6×10^7. The analysis combined a potential method with an empirical boundary layer approximation.

The predicted theoretical results are compared against physical testing of the Dolphin AUV (developed by North American Aviation Inc.). The $C_{D\nabla}$ of the Parsons shape was estimated at 0.009 at Re_{∇} of 1 x 10^6. $C_{D\nabla}$ decreased with increasing velocity with a value of 0.004 at Re = 1.6 x 10^7. The boundary layer remained laminar over 70 % of body length at Re_{∇} = 1.0 x 10^7. Parsons indicates that the boundary layer separates at this point. Parsons considers the computational model to be valid over the tested Re_{∇} range given that the Dolphin physical test results are similar. Parsons' paper describing the AUV shape has been referenced by other authors and further analysis of the laminar flow shape conducted.

Hansen and Hoyt published results from towing tank testing of a laminar flow body (Hansen and Hoyt 1984). The objective was to characterise the intermittency and propagation of naturally occurring turbulent spots within a laminar region. The body profile was as described by Parsons, however with an overall length of 3.18 m and fineness ratio of 4.5. Careful consideration was given to creating the surface shape and mounting the flush hot film sensors to reduce the surface roughness rms to 1.6 x 10^{-6} cm. The model was run with a trip wire at 6 % body length to force the transition from laminar to turbulent. This found that the resulting drag that was approximately three times the drag of the base model. $C_{D\nabla}$ at 3.05 ms^{-1} increased to 0.021 from $C_{D\nabla}$ = 0.007. Without the trip wire the boundary layer transition was observed to occur up to 0.67 % to 0.72 % of the body length. Hansen compares physical test results with computational results and shows the results are similar for Re_{∇} between 1.0 x 10^6 and 3.0 x 10^6. At greater values of Re the $C_{D\nabla}$ of the physical model increases, suggesting forward movement of the transition point. Below this velocity, the $C_{D\nabla}$ of the physical model sharply increases, suggesting that the laminar boundary layer is separating and forming a bubble, which reattaches as a turbulent layer further downstream. This is illustrated in Figure 5.7.

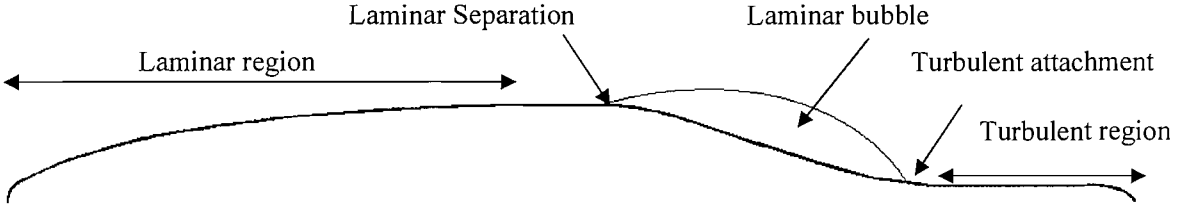

Figure 5.7 Laminar separation bubble formation and position on the profile of a laminar flow body.

Figure 5.7 shows the laminar separation bubble occurring just after the point of maximum diameter. Hansen and Hoyt estimate the separation point to occur at 68 % of body length from computational results. The laminar bubble grows larger with decreasing speed, but it is not

discussed whether the separation point moves forward, or the turbulent attachment moves backward.

Hot films on the body gave local fluid flow velocities in order to measure the intermittency of the boundary layer. The results showed that the instability of the boundary layer increased with speed and indicated higher intermittency values on the stations forward of the point of maximum diameter. The measurement technique was able to detect turbulent "droplets" within the otherwise laminar boundary layer. The droplets' leading edge has a velocity of 84 % of the freestream velocity and their trailing edge has a velocity 39 % of the freestream velocity. The droplets move along the bow getting smaller as they progress along the body. Hansen and Hoyt also show that longitudinal pairs of roughness elements are very effective at tripping the boundary layer and consequently expressed concern about the physical realisation of a laminar boundary layer body due to this sensitivity. Once the vehicle is in use, and fouling occurs (from collision or organic build-up) then Hansen and Hoyt claim that the body will not maintain the laminar boundary layer.

Babb provides physical results of a laminar flow hull shape operating in the open ocean (Babb 1994). A half scale model (3 m long, design speed of 5 ms^{-1}) was made buoyant and a drop weight attached. The test shape was then dropped in 1000 m of water, such that the weight would be released and the hull would accelerate towards the surface. On the ascent the vehicle travelled at 3.5 – 4.0 ms^{-1}. This translates to a C_{D_∇} of 0.015 (at $Re = 1 \times 10^7$), twice that of an identical model tested in a wind tunnel. This C_{D_∇} estimate is still half that of a fat torpedo and Babb suggests that this value could be lowered at depth.

This observed C_{D_∇} increase is either due to an inferior surface quality or the existence of particulates and turbulence within the water column having a measurable affect on the laminar boundary layer. Only one dive was completed successfully, and entrained water from the surface would have cooled during the test, resulting in varying buoyancy force (estimated at 1 kg net buoyancy change). Ideally more test runs with a greater understanding of the buoyancy force would give more confidence in the results. This remains important to this work as it represents ocean testing of the laminar flow body and shows that a reduction in drag exists at this *Re* when operated in the ocean and the bow exposed to fouling.

Dress undertook physical testing of a Parsons laminar flow body in a wind tunnel and within an oil filled tank (Dress 1989). A small model was used, 0.305 m in length and half the AUV diameter of the Parsons model giving a fineness ratio of 7.5. The results must be compared using non-dimensional *Re* and C_{DSA}. The model was run at $Re = 3 \times 10^5$ to 1.2×10^6 and C_{DSA} is

observed to decrease with increasing *Re*. The drag curve is not linear but is almost sinusoidal (0 ° to 120 °). As the *Re* number is approximately doubled one finds that C_{DSA} = 0.0125 at *Re* = 3.5 x 10^5, C_{DSA} = 0.01 at *Re* = 7.0 x 10^5, and C_{DSA} = 0.0045 at *Re* = 1.2 x 10^6. The reason for high drag found at lower *Re* is the separation of the laminar boundary layer as reported by Hansen and Hoyt. This is illustrated in Figure 5.7. The separation is estimated to originate at 50 % of the body length, before the point of maximum diameter at 59 % of body length. The laminar separation was observed to move forward with decreasing *Re*. The laminar bubble reattaches near the tail of the body and reattachment will move forward with increasing *Re*. Hence, the laminar bubble decreases in size with increasing *Re* and the C_{DSA} decreases. Tests were also completed with transition triggered at 50 % of body length. This showed a consistent low C_{DSA}= 0.005 to 0.0045 over the *Re* range 0.3 x 10^6 to 1.4 x 10^6. The turbulent boundary layer is less likely to separate from the body and causes less drag than the laminar separation bubble.

Both Hansen and Dress show that the Parsons body is inappropriate for slow speed applications as the pressure gradient is insufficient to prevent laminar separation. If the laminar flow is only held over 50 % of the body and transition is forced, rather than letting laminar separation occur, then the body could be used for lower speed applications. The key aim is to prevent laminar separation by tripping turbulent flow before separation and decreasing drag compared to a laminar separation bubble.

The Parsons shape has been investigated further by both Huggins and Packwood, in a series of papers: The first paper considers an airship, a torpedo and a laminar flow body for a long range 7000 km, 30 day AUV resulting in a minimum velocity of 2.5 ms^{-1} (Huggins and Packwood 1994). The C_{D_∇} for each is found and *Re* based polynomial curves fitted to experimental results from other authors. The control surfaces, appendages and propulsion of the AUV are not discussed and so would have to be similar for each shape to remain comparable.

Using the same analytic process for estimating range, as presented in Chapter 3, the torpedo shape is shown to be able to store the most volume, but the drag penalty makes it unable to maintain the required speed. To maintain the required speed would require more battery volume making the AUV too large. The chosen AUV hull form is the laminar hull shape as this has the lowest overall drag when operating at the required velocity. Huggins does increase the volume of the AUV by an arbitrary 15 % to account for inefficiencies in the power train or energy source.

This review of Huggins and Packwood's paper suggests that the research in this Thesis represents a move to another level of hydrodynamic detail, perhaps as a second iteration of

Huggins and Packwood's first estimate. The hydrodynamic research in Chapter 6 is not limited to three hull forms allowing more freedom in the shape.

The second paper by Packwood and Huggins examines the afterbody shaping and transition prediction of the Parsons shape with the aim of incorporating a single propeller and cruciform control surfaces whilst not adversely affecting drag (Packwood and Huggins 1994). Results conducted at Re = 9.16 x 10^6 show that $C_{D\nabla}$ can be refined by shaping the tail ($C_{D\nabla}$=$\pm$ 0.0004) but then acknowledge that practical concerns of mounting control surfaces and propeller will determine the stern shape. Most of the paper is then concerned with the numerical modelling of the transition of the boundary layer. The program is a potential flow model, although it can include boundary layer effects and wake flow. The turbulent portion of the boundary layer is based on the Head approach (Curle 1962). The transition was initially forced at 67 % body length, but was later determined numerically using the Cebeci & Smith method (Cebeci and Smith 1974). The Cebeci – Smith method used here is the same as Parsons used in the original paper defining the body. Unsurprisingly the transition prediction is very similar. Transition was estimated at 51 % of body length using the Cebeci-Smith method adapted for 3D flow by Packwood and Huggins. The pure 2D version of the Cebeci-Smith method predicted transition at 67 %, though Packwood indicated that there is little to commend the 2D application on a 3D model.

Drag estimates are made, and the 2D model gave $C_{D\nabla}$ = 0.0062 (transition at 67 % body length) and the 3D adaptation model gave $C_{D\nabla}$ = 0.0107 (transition at 51 % body length). The estimated transition lengths are considered to match Hansen and Hoyt and Parsons allowing for the challenges of modelling a boundary layer. Finally within this paper Packwood and Huggins conclude that whilst the potential flow method can model a laminar flow over the bow of the AUV, more work on transition prediction is required.

The third paper presents the results of wind tunnel testing of a fully appended Parsons laminar flow vehicle (Huggins and Packwood 1995). The model is 6 m long, ∇_S is 4.4 m^3, and the AUV has a Parsons hull shape bow and middle body with a modified tail resulting from Packwood and Huggins's work (Packwood and Huggins 1994). The hull is a conventional glass fibre lay-up and, unlike the Hansen and Hoyt model, no special attention was paid to smoothness or waviness of the surface. At Re_{∇} = 2.5 x 10^6 the $C_{D\nabla}$ was found to have a local minimum of 0.00527. The drag increases with decreasing or increasing velocity. The air flow carrying china clay particles over the body showed that a laminar boundary layer was held to 70 % of the body length at Re_{∇} = 2.5 x 10^6 and that this was quite resilient to changes of incidence up to 4 °. This is different to the Hansen and Hoyt's results showing that $C_{D\nabla}$ increased by 25 % at 2 ° and at the

same Re_{∇}. Along with Babb's work, these results support the idea that the body surface need not be very specially treated to maintain the laminar boundary layer and that the laminar flow vehicle would maintain laminar flow in operational use.

Physical testing by Huggins and Packwood show the $C_{D\nabla}$ minimum at $Re_{\nabla} = 2.5 \times 10^6$, 25 % of Parsons' design speed of $Re_{\nabla} = 1 \times 10^7$. This suggests that the physical models will not support a laminar boundary layer at a high Re_{∇}.

Lutz and Wagner present a completely computational study using a potential method (Lutz and Wagner 1998). Each body is simplified and represented by a low order panel distribution and then a spline fit through the surface source strength distributions. A first order integral procedure is used to calculate the boundary layer development, and transition is based upon linear stability theory and the Cebeci & Smith version of the e^9 criterion.

As shown by previous authors (Hansen and Hoyt, Huggins & Packwood), the laminar hull shape is best suited to a specific design velocity, and so five *Re* regions were set up each covering a small Re_{∇} range. The design of the 1st regime shape originated from an ellipsoid, and the following shapes were based upon the previous regimes shape. The results of this study are reproduced here in Figure 5.8. The AUV shapes are shown at the bottom of Figure 5.8*ii* and the progression of the design with increasing velocity can be seen.

Figure 5.8*i* shows that the estimate of $C_{D\nabla}$ stays below 0.01 and decreases over each design regime until $Re_{\nabla} = 2 \times 10^7$. Above this threshold the $C_{D\nabla}$ of each shape increases within the Re_{∇} range 2×10^7 to 1×10^8, and is almost constant for Re_{∇} above 1×10^8. Below $Re_{\nabla} = 1 \times 10^6$ laminar separation without reattachment is predicted and so the results are not shown. Such a large laminar bubble would contribute to a very large $C_{D\nabla}$ prediction.

With increasing Re_{∇} a greater pressure gradient is required to maintain the laminar boundary layer, hence the radius increases or the point of maximum diameter moves forward. Enlarging the radius increases the chance of turbulent separation and creation of a recirculation region along the stern. Therefore for high Re_{∇} values (greater than 1×10^8) it may be preferable to adopt a more slender body with a greater turbulent boundary layer but without any separation. The regime III model is singled out for further investigation, as this has the longest laminar boundary layer prediction with instability occurring at 9 % of the body length, although transition is suppressed over 45 % of the body. This observation illustrates how fragile the laminar boundary layer can be.

Lutz and Wagner's results will provide a useful comparison for the laminar flow variants discussed in Chapter 6. When the boundary layer transition prediction is corrected, comparisons

could be made between the two sets of models for verification of trends. The suspected error found within Palisupan's boundary layer transition is identified and discussed in Chapter 6.

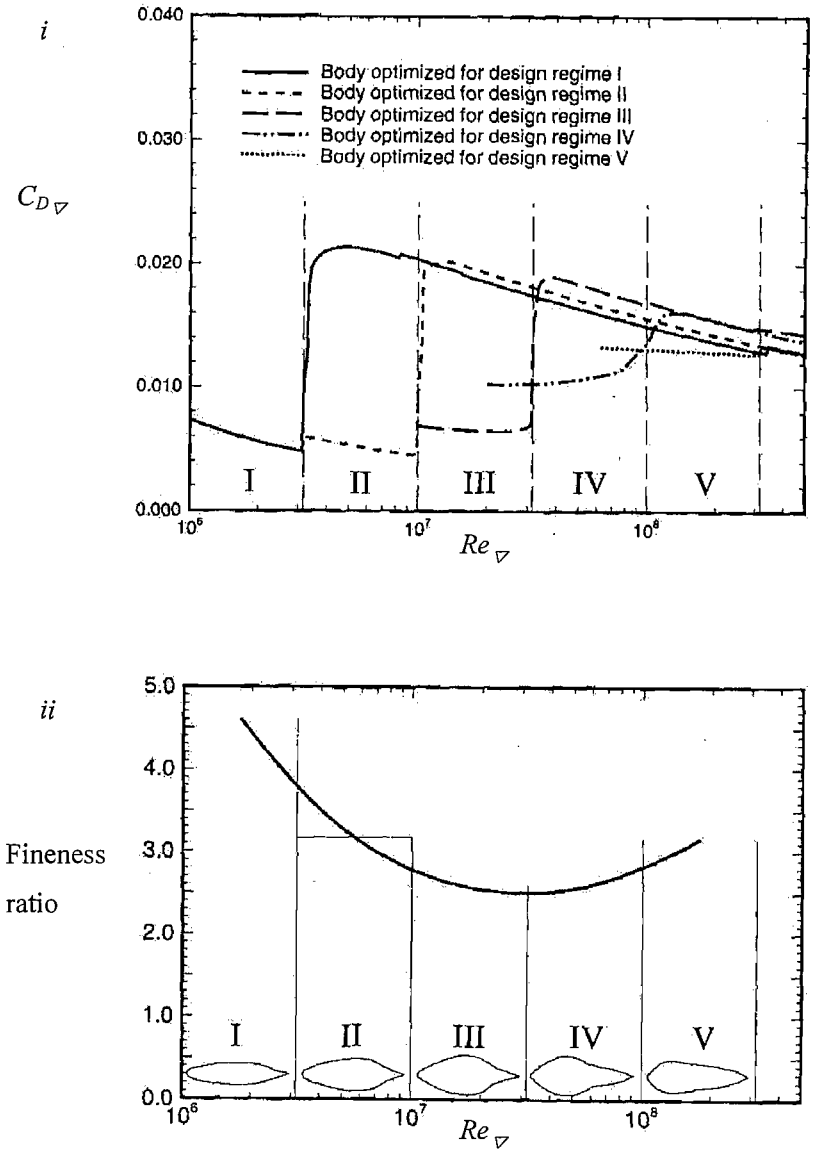

Figure 5.8 *i)* $C_{D\nabla}$ and *ii)* fineness ratio of a shape optimised across increasing *Re* regimes.

Overall the laminar flow body presents a low drag shape when operating at an optimal velocity. Parsons' original hull shape design operated at $Re_\nabla = 1 \times 10^7$, and other papers have shown that this represents the upper limit of the low drag region of a laminar hull shape. Operating above this velocity range will lead to increased drag due to the hull shape wake. At lower velocities the boundary layer will undergo laminar separation and reattachment. This separation bubble is larger at lower velocities and will cause a sharp rise in $C_{D\nabla}$. This observation has been confirmed

in physical tests undertaken by Dress, and the boundary layer instability reported by Hansen and Hoyt. Computational modelling by Parsons, Packwood and Huggins supports the low drag concept, but the prediction of the laminar boundary layer separation or transition is sensitive to the boundary layer model utilised.

5.3 Conclusions.

This Chapter has summarised the methodology of different hydrodynamic testing and reviewed literature on the hydrodynamic characteristics of the chosen hull shapes. These tools are needed to move from Chapter 3, where the sensitivity of range to C_{D_∇} is investigated, to Chapter 6 where hull shape options are investigated.

The literature concerning Autosub describes the design progression of the vehicle, and the in service modifications as challenges arise. The drag predictions have been covered by four Authors, two by physical testing and two by computational testing. 2 ms^{-1} is the common velocity and drag predictions range from 95.78 N to 105 N for the bare model, $C_{D_\nabla} = 0.02356$ to $C_{D_\nabla} = 0.0198$. This work is mostly done retrospectively to better understand the operation of Autosub. This Thesis will consider this a base hull shape and then move forward to creating a design method that aids in predicting C_{D_∇} in the initial design stages.

Laminar flow literature suggests that the Parsons hull shape offers a low C_{D_∇} compared to parallel middle body forms. The laminar boundary layer is maintained by a pressure gradient over the bow, and this is sensitive to AUV velocity. Theoretically a laminar flow AUV should operate at $Re = 1 \times 10^7$, giving $C_{D_\nabla} = 0.005$. If the Re is too high, the transition point moves forward along the body, and if Re is too low, then the laminar boundary layer will begin to separate, forming a laminar bubble, and the C_{D_∇} will quickly rise. The point of separation moves forward with decreasing Re. Beyond the optimum velocity range the C_{D_∇} increase gives the laminar flow body no advantage over a parallel middle body shape. The laminar flow shape at $Re = 1 \times 10^7$ can maintain a laminar boundary layer to over 50 % of the body length, but physical tests show that there are unstable patches over most of the bow. Computational modelling of this body shape will be dominated by the transition prediction method.

The reasoning behind the selection of hull shapes should be considered. Whilst a shape might be ideal for a specific cruising velocity, it might be impractical to mount the subsystems or energy source required by the mission. A design method that considers both the arrangement and size of subsystems in conjunction with the hull shape would be of use to an AUV designer. The presented design method in Chapter 7 is a first attempt to bring these concerns within a design cycle.

The next Chapter presents the results of the Palisupan CFD models. Both Schlichting's skin friction estimate and coupled Thwaites - Head boundary layer models are applied and their results discussed. Equations of C_{D_∇} are generated based upon simple input design parameters to facilitate the design method presented in Chapter 7.

Chapter 6
Theoretical study of AUV hull shape hydrodynamic characteristics.

The prediction of hydrodynamic characteristics using Palisupan for three families of AUV hull form is reported.

The Parsons model with the Thwaites - Head boundary layer will be examined to gauge the effect of the boundary layer on the drag estimates. The boundary layer state will have an effect on the drag. This is controlled by velocity, as the changing *Re* will affect boundary layer initial conditions, transition point and thickness.

The models with the Schlichting skin friction estimate will be considered using non dimensional techniques. This will identify an analytically expressed relationship between drag and the input profile geometry variables. The intention is to integrate such a relationship into a design method given appropriate assumptions and limitations.

Chapter 2 indicated that the Autosub body will have a turbulent boundary layer for most of its length, transition occurring at a point 11 % to 15 % of the body length. For a laminar flow AUV shape, the boundary layer model will be more important to its drag prediction, as the estimated position of transition from laminar to turbulent flow occurs at 70 % of body length.

The principal task is to explore the effect of hull shape on $C_{D\nabla}$. Varying $C_{D\nabla}$ represents a change in shape, so that the AUV volume can be scaled to suit. The shapes investigated will have a base model, so that the effect on drag of individual geometric parameter changes from the base model can be investigated.

6.1 Shape 1: The Parsons body.

Parsons defined a hull shape profile that when modelled in a potential flow computational program, would support a laminar boundary layer over 70 % of the body length at $Re_{\nabla} = 1 \times 10^7$ (Parsons, *et al.* 1974). The shape introduced in Chapter 2 was reviewed in terms of hydrodynamic characteristics predicted by other researchers presented in Chapter 5. This section will provide the geometric definition required for use with Palisupan and discuss the resulting hydrodynamic drag results and associated boundary layer modelling.

6.1.1 Geometry definition.

Figure 6.1 shows the base profile of the Parsons body. To match the Autosub and the later Rutherford models, the base Parsons model is scaled to 8 m length, keeping a fineness ratio of 4.8 to match Parsons' paper. The base model has a volume of 7.82684 m^3 and surface area of 25.260 m^2. As shown in Appendix D, the presence of a tail stabilises the C_P at the stern.

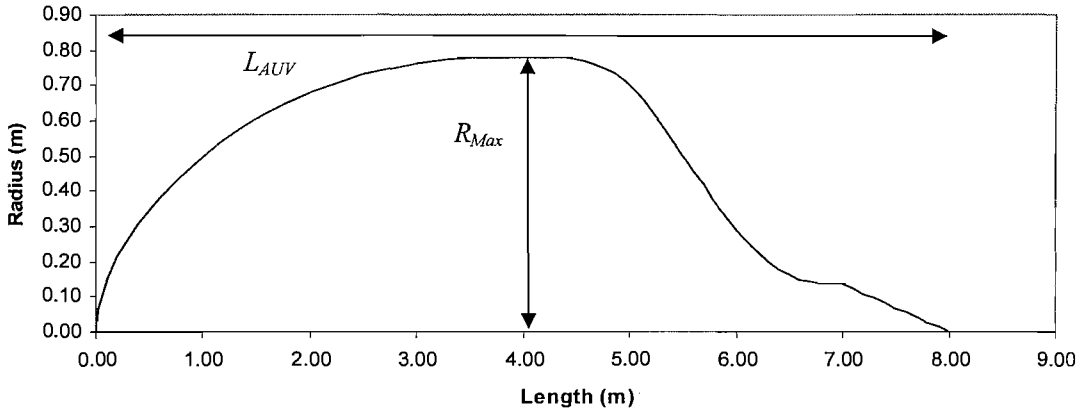

Figure 6.1 Profile for the Parsons body modelled for the same length as the Autosub model.

The model has been examined for velocities of 0.5 ms^{-1} to 12 ms^{-1} using Palisupan with a Schlichting skin friction estimation. Figure 6.2*i* and Figure 6.2*ii* provide the predicted drag force and C_{D_∇} of the Parsons model plotted against increasing speed based upon the results from the Schlichting skin friction estimation.

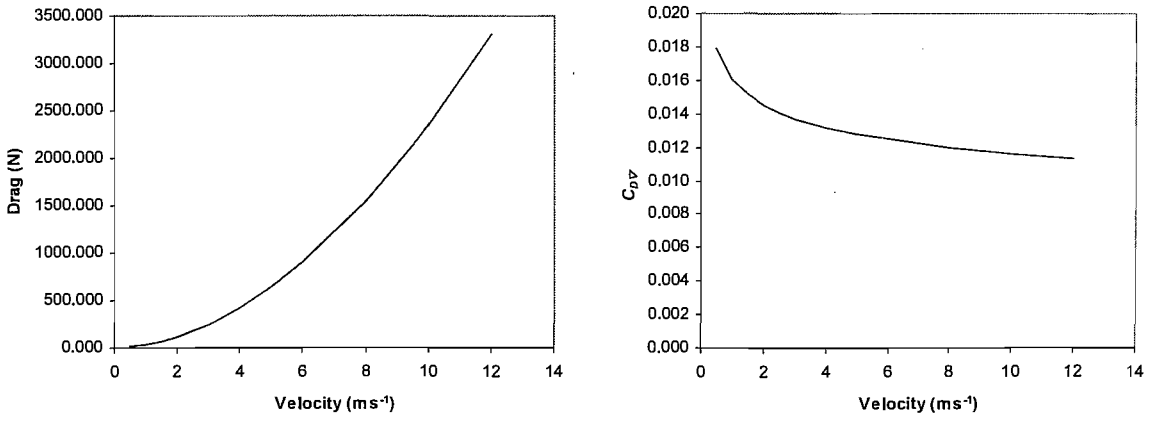

Figure 6.2*i* Predicted drag force and *ii*) C_{D_∇} of the Parsons model with increasing speed using the Sclichting skin friction approximation.

The drag of the Parsons body increases with increasing speed (u^2) as anticipated from Chapter 3. The Schlichting skin friction estimation does not model the effect of pressure on the boundary layer, so transition is assumed to occur at $Re_x = 3 \times 10^5$. The C_{D_∇} is greater at lower speeds as the boundary layer is thicker (greater δ) and so absorbs more energy from the flow. The model captures this effect through C_{D_∇}.

Although the Schlichting skin friction approximation forced transition at $Re_S = 3 \times 10^5$, hull shapes with a gently sloping bow can have a lower C_{D_∇} than those with a bluff bow. A bluff bow will have a greater s, surface area and velocity variation over a shorter fraction of the total body length. Therefore a bluff bow will exceed $Re_S = 3 \times 10^5$ at an earlier x position. A laminar flow model has a curve length s similar to x and so transition will appear to occur further along the body. With transition occurring at a greater x position, combined with a small surface area over the bow, the laminar flow model will have a lower overall C_{D_∇} estimate.

The Thwaites – Head model will allow the laminar boundary layer to continue along the Parsons hull shape profile, and according to literature (Chapter 2), should reduce the predicted C_F and so improve the drag efficiency of the Parsons hull shape. The next section applies the Thwaites – Head boundary layer approximation to the Parsons body.

6.1.2 Thwaites-Head boundary layer model.

The boundary layer approximation has been shown to effectively estimate boundary layer laminar to turbulent transition on flat plates (Murphy 2005). The AUV curved surfaces and pressure gradients test the limits of this methodology. The Parsons hull shape relies on maintaining a laminar boundary layer over the majority of its bow.

The first model attempts to recreate the results presented by Parsons. The velocity was set to 6.0 ms^{-1} so that the Re_∇ value based upon total displaced volume is the same as given in the original paper by Parsons, $R_{e_\nabla}=1 \times 10^7$.

Figure 6.3*i* shows the C_P variation along the length of the Parsons hull shape with transition predicted by Palisupan using one of the three criteria based on C_F, H, and Cebeci & Smith as discussed in Chapter 5. Figure 6.3*i* indicates stagnation at the tip of the bow by a high C_P. Thereafter C_P decreases over the bow with a peak at the point of maximum width. Here C_P increases over the stern with another peak at the geometric transition from stern to tail. Inspecting the C_F values in Figure 6.3*ii* along the boundary layer shows a jump at 4.73 m (59.1 % of 8 m body, 67.6 % of 7 m body without tail), indicating a change from a laminar skin friction to a turbulent skin friction. This was then be verified by inspecting δ and H.

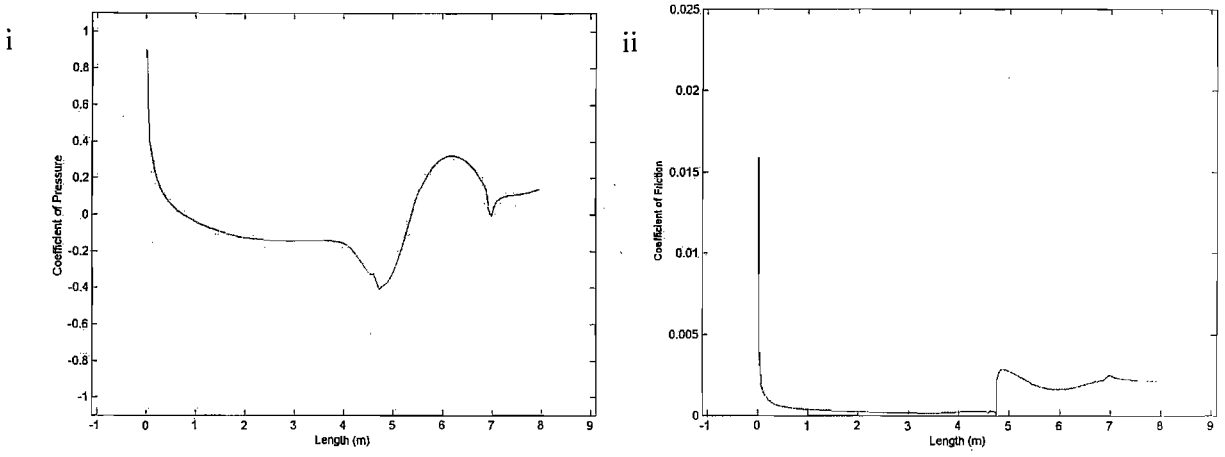

Figure 6.3 C_P and C_F variation with length along the base Parsons profile with transition predicted by Palisupan at R_{e_∇}=1 x 10^7.

Figure 6.4*i* shows δ and Figure 6.4*ii* shows H of the base Parsons model at 6.0 ms^{-1}. The increase of C_F in Figure 6.3*ii* is caused by a jump in δ in Figure 6.4*i* which is a consequence of H exceeding 3.0. The hull shape radius at 4.73 m (59.1 % of body length) is reducing and is after the point of maximum radius and just after the minimum C_P. After the minimum C_P there is an unfavourable pressure gradient for the boundary layer, consequently any boundary layer instability will cause transition or separation. As H is greater than 3.0, it might indicate laminar boundary layer separation. However, the decreasing H trend at 4.0 m, as discussed in Chapter 5, is indicative of boundary layer transition occurring before separation.

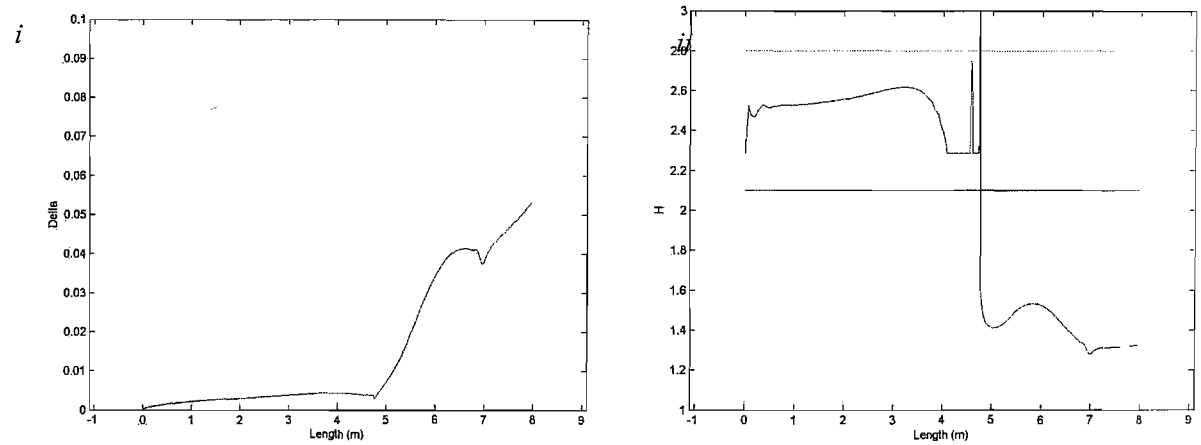

Figure 6.4*i*) δ and *ii*) H of the base Parsons model at R_{e_∇}=1 x 10^7.

The H value remains constant from 4.0 m to 4.5 m. This is an effect of the boundary layer modelling method used and not representative of a physical boundary layer. The calculation of

the laminar boundary layer would become very unstable should the parameter λ exceed the valid range -0.1 to 0.1. The model approach by Pashias holds λ at a constant level until it returns to within its valid range and then H would be re-evaluated, in this case exceeding 3.0.

At $R_e = 4 \times 10^7$ ($R_{e\,\nabla}=1 \times 10^7$) the transition location should be slightly forward of the point of minimum pressure (Houghten and Carpenter 2003 pp. 398 - 399). The point of minimum pressure, 4.6 m from the bow, is as observed in Figure 6.18*i*, occurs just after the point of maximum diameter at 4.0 m from the bow in Figure 6.15*i*. From these rough guidelines the transition location should occur before the point of maximum pressure and before 4.6 m.

Figure 6.5*i* shows the application of the Cebeci & Smith method as implemented by Palisupan ($Re_{\theta Palisupan}$) and by a version found in Cebeci and Bradshaw (Re_θ) (Cebeci and Bradshaw 1977 p. 153). The generation of the two values of $Re_{\theta Palisupan}$ and Re_θ are discussed further in section 6.1.3. At 6.0 ms^{-1} boundary layer transition is caused by H exceeding 3.0 and not the value of $Re_{\theta Palisupan}$. This was not the case at lower velocities as explained in section 6.1.3. Were Re_θ used, then transition would have occurred when Re_θ intersects the Re curve at 3.2 m (40 % of body length). This location matches the beginning of the downwards H trend in Figure 6.3*ii*, also indicating transition.

Figure 6.5*ii* shows the *H-Re* transition method (Wazzan, *et al.* 1981). In this example the transition should have occurred earlier at 1.5 m (18.8 % of body length) and not at 4.73 m (59.1 % of body length) as modelled by Palisupan.

i

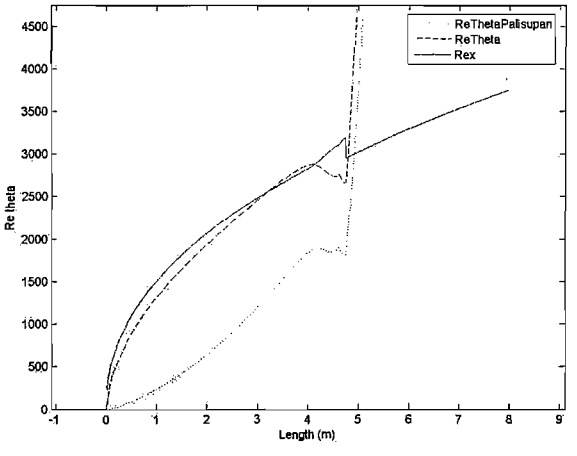

ii

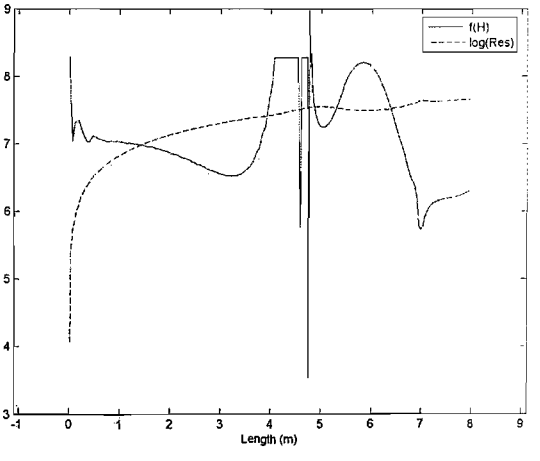

Figure 6.5*i*) Transition predicted using the method suggested by Cebeci & Smith and *ii*) by *H-Re* method at $R_{e\,\nabla}=1 \times 10^7$.

6.1.2.1 Comparison with literature.

Table 6.1 gives a summary of results from different sources for the Parsons hull shape. Care must be taken when comparing the Reynolds number and coefficient of drag, as different non-dimensional values have been used. Dress and Packwood & Huggins use length to define Re, Babb, Hansen and Hoyt, and Parsons use $\nabla_S^{1/3}$ to define Re_∇. Dress uses surface area to non-dimensionalise C_{DSa} and the other sources listed use $\nabla_S^{2/3}$ to find $C_{D\nabla}$. The Palisupan results from model testing are presented in both formats. In Table 1.6 the generated Palisupan results are based upon the whole body drag and total displaced volume or surface area.

It was anticipated that the Schlichting skin friction estimation would not represent the laminar flow hull. At $Re_\nabla = 1.0 \times 10^7$ the Schlichting approach overestimates $C_{D\nabla}$ compared to Parsons' approach, and at $Re = 1.3 \times 10^7$ Schlichting overestimates $C_{D\nabla}$ compared to Packwood & Huggins. This overestimation of drag is due to the Schlichting approach assuming a boundary layer transition point occurring early along the bow. Dress's paper shows that the C_{DSa} will rise after Re increases above 1.0×10^7. The results presented here do not show an increasing trend in C_{DSa} after this $Re = 1.0 \times 10^7$. The increase could be due to flow separation and wake behind the body.

The Thwaites – Head boundary layer model was anticipated to better represent the laminar flow hull. At Parsons' design value of Re_∇ the $C_{D\nabla}$ results compare very well, despite two different mathematical models being used, both predict $C_{D\nabla} = 0.005$ at $Re_\nabla = 1.0 \times 10^7$. A 1 m tail was added to the Parsons shape to generate the model, without the tail gives transition at 0.68 at $Re_\nabla = 1.0 \times 10^7$, which compares well with Parsons' estimate of 0.7.

Packwood & Huggins uses the same 2D boundary layer transition method as used by Palisupan, and generate similar results, but reported at different Re values. Packwood & Huggins claim to generate comparable $C_{D\nabla}$ to Hansen and Hoyt and at the same design Re. However, the reference Re_∇ differs from the Re_∇ used by Parsons. At $Re = 9.6 \times 10^6$ Packwood & Huggins estimate $C_{D\nabla} = 0.0062$. Assuming that $Re_\nabla = Re/4$ for the Parsons hull shape, Packwood & Huggins results occur at $Re_\nabla = 2.3 \times 10^6$. Hansen and Hoyt estimate $C_{D\nabla} = 0.007$ at $Re_\nabla = 2.5 \times 10^6$, so Packwood and Huggins results do compare to Hansen and Hoyt.

Dress operates at a lower Re than the other sources and this was deliberate to allow visualisation of laminar boundary layer separation. Below $Re_\nabla = 2.5 \times 10^6$ the Palisupan results are not considered to be accurate as the transition is triggered by a suspect transition criteria, (discussed in section 6.1.3) and cannot be compared to Dress results.

Table 6.1 Summary of $C_{D\nabla}$ and transition location of the Parsons hull shape from different sources.

Source	Reynolds number $[Re_{\nabla}]$	Reynolds number $[Re]$	$C_{D\nabla}$	C_{DSa}	Transition location $[x/Length]$	Notes
Babb (1994)	2.3×10^7		0.0150		-	Single test in the open ocean.
Dress (1989)		3.5×10^5		0.0125	-	Fineness ratio 7.5, oil based flow tunnel results. At low Re laminar separation occurs at 0.5 body length
		7.0×10^5		0.0100	-	
		1.2×10^6		0.0045	0.678	
Hansen and Hoyt (1984)	6.0×10^5		0.0167			Shows from hot film analysis that the $C_{D\nabla}$ rise at high velocities is due to intermittency of the laminar boundary layer.
	1.0×10^6		0.0110			
	2.5×10^6		0.007		0.70	
	3.5×10^6		0.008			
Huggins & Packwood (1995)	2.5×10^6		0.0053		0.70	Wind tunnel test
Packwood & Huggins (1994)		9.2×10^6	0.0107		0.514	Cebeci & Smith and 3D transformation
		9.2×10^6	0.0062		0.671	Cebeci & Smith 2D.
		9.2×10^6	0.0062		0.67	Artificially fixed
Parsons (1974)	1.0×10^7		0.0050		0.70	Transition based on Cebeci & Smith
Parsons hull shape from Palisupan model	3.3×10^6	1.3×10^7	0.0145	0.0023	0.02	Schlichting
	1.0×10^7	4.0×10^7	0.0125	0.0019	0.007	Schlichting
	1.6×10^7	6.4×10^7	0.0117	0.0018	0.005	Schlichting
	3.3×10^6	1.3×10^7	0.0142[&]	0.0022[&]	0.278*	Thwaites – Head
	1.0×10^7	4.0×10^7	0.0049	0.0008	0.593	Thwaites – Head
	1.6×10^7	6.4×10^7	0.0038	0.0006	0.606	Thwaites – Head

* This value is believed to be incorrect and will be discussed in section 6.2.3.

[&] This value is questionable as a consequence of incorrect predicted boundary layer transition point

The Thwaites – Head model can model the laminar boundary layer with a variable transition point. This was not possible with the Schlichting skin friction estimation. The results agree with Parsons' results at $Re_{\nabla} = 1 \times 10^5$ for both transition length (considering a 7 m model) and $C_{D\nabla}$. The results do not agree with the physical test results available, although this can often be

expected with computational models. Improvement of the model will improve the results compared to physical testing.

There is some debate to the validity of the published computational models. Physical tests do not show the decrease in drag from the laminar boundary layer at the high *Re* modelled. Huggins & Packwood have comparable C_{D_∇} results to the Parsons and Palisupan results from the computational model. For the physical model, the local C_{D_∇} minimum is at $Re_\nabla = 1 \times 10^6$ and C_{D_∇} increases with velocity. Hansen and Hoyt also show a minimum C_{D_∇} at $Re_\nabla = 1 \times 10^6$, and increasing C_{D_∇} with increasing velocity.

The next stage is to model the Parsons body at different velocities. These models did not give expected results and an issue regarding Palisupan transition prediction was found.

6.1.3 The effect of velocity on Palisupan transition prediction.

From the earlier hydrodynamic theory the boundary layer transition is sensitive to the fluid velocity. Over a flat plate laminar flow can only be maintained at low velocities, and the transition point will move forward with increasing velocity. The pressure gradient over the bow of the laminar flow shape can be used to delay the transition point, but transition will still move forward when the velocity increases.

From the physical results presented by Hansen & Hoyt and Huggins & Packwood, it is expected that C_{D_∇} will increase when operating above the laminar flow optimal range. This is partly due to the transition point moving forward. However, as shown by Dress and Hansen & Hoyt the C_{D_∇} value of the laminar flow hull shape will also increase at decreasing velocity. This is due to the formation of a laminar separation bubble and the leading edge of the bubble moves forward with decreasing velocity.

The Palisupan results do not show decreasing transition length with increasing velocity and are considered to be incorrect. The compiled C_F for the Parsons shape at multiple velocities is shown in Figure 6.6*i*. The transition lengths are summarised in Figure 6.6*ii*. This work has identified a coding error as discussed next.

Transition can be identified by C_F suddenly increasing. The point at which this occurs in Figure 6.6 is seen to move forward with decreasing velocity. If the boundary layer were separating then C_F would approach zero at the point of transition and H would be greater than 3.0. These conditions are not met at low velocities by the Palisupan model.

Dress and Hansen & Hoyt identify a laminar separation bubble occurring further upstream with decreasing velocity, but do not provide specifics about where this separation occurs. Dress

comments that it has been observed at 50 % of body length and that this occurs below a *Re* of 1 x 10^6. As can be seen in Table 6.1, the Palisupan models are operating at a higher *Re*, and Figure 6.6 indicates that transition is occurring much further forward than 50 % of body length.

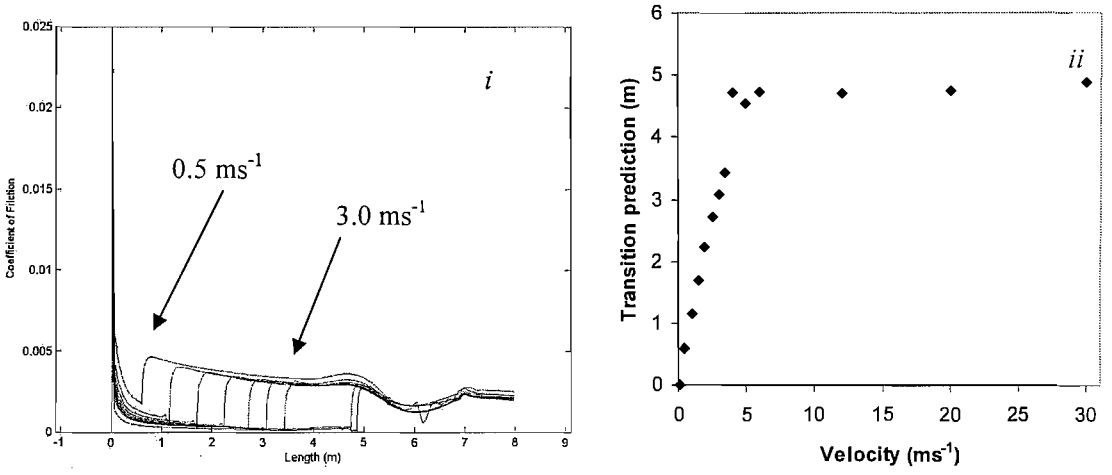

Decreasing transition length with decreasing velocity indicates an error in the computer coding

Figure 6.6 Compiled C_F for the Parsons shape with decreasing velocity as modelled by Palisupan.

After investigation, Palisupan's estimation of Re_θ within the Cebeci & Smith transition prediction was found to be suspect. The calculation of $Re_{\theta Palisupan}$ and Re_θ are shown in equation 6.1 and equation 6.2. Re_θ as presented in equation 6.1 can be found in Cebeci and Bradshaw's discussion of the Cebeci & Smith method (Cebeci and Bradshaw 1977) in Houghten and Carpenter and in Schlichting (Houghten and Carpenter 2003 pp. 398 - 399, Schlichting 1968).

$$\mathrm{Re}_{\theta Palisupan} = \frac{s\theta}{v} \qquad 6.1$$

$$\mathrm{Re}_\theta = \frac{U\theta}{v} \qquad 6.2$$

The difference between the two equations is that velocity, used by Re_θ results in a non - dimensional Reynolds number, whereas the distance s in $Re_{\theta Palisupan}$ results in dimensions, inconsistent with the non-dimensional Reynolds number. s is a constant for a given hull shape, so $Re_{\theta Palisupan}$ will be a function of θ. At low velocities θ is large and will trigger transition early. Two examples at 0.5 ms^{-1} and 12 ms^{-1} illustrate this point.

Figure 6.7 shows the Parsons shape at 0.5 ms^{-1} subject to a model Re= 3.36 x 10^6 and a Re_{∇} = 8.34 x 10^5.

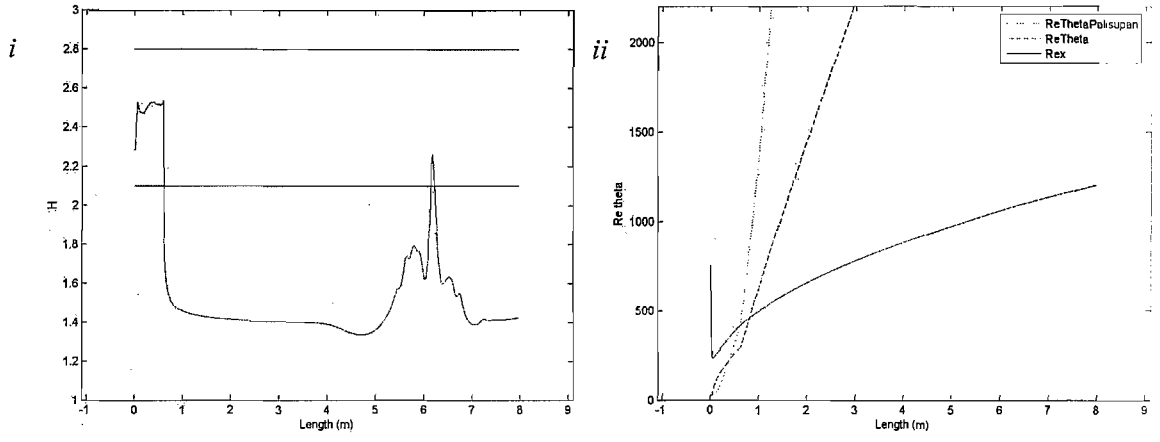

Figure 6.7 *i*) *H* and *ii*) the Cebeci & Smith method of transition prediction at 0.5 ms^{-1}, showing suspect $Re_{\theta Palisupan}$ causing early transition prediction

Figure 6.7*i* shows H at an initial average value of 2.5, as expected for a laminar boundary layer. Transition is not caused by H exceeding 3.0. Figure 6.7*ii* shows the curves for a Cebeci & Smith transition method, with both Re_θ and $Re_{\theta Palisupan}$ calculations. $Re_{\theta Palisupan}$ intersects the Re curve at 0.60 m (7.5 % of body length), triggering transition within Palisupan. Re_θ does not intersect at this point, and the trend is for it to continue below the Re curve. As θ changes at transition, affecting Re_θ, it is not possible to say what transition location would be predicted by the corrected Re_θ.

For the model at 0.5 ms^{-1}, this implies that transition has occurred earlier than expected. The boundary layer was expected to continue further along the body and the hull shape drag prediction would decrease.

A model with $C_F \simeq 0.0$ has not yet been found, but it may be possible with more complex hull shape geometries. Therefore if H is the only correct transition criterion, Palisupan will only trigger transition when the laminar boundary layer model starts to separate ($H > 3.0$). Earlier transition from increasing Reynolds number will not be shown, as $Re_{\theta Palisupan}$ decreases with increasing speed. This is illustrated by modelling the Parsons hull shape at the higher velocity of 12 ms^{-1}. This equates to $Re = 8.1 \times 10^7$ and $Re_\nabla = 2.0 \times 10^7$ and transition is expected earlier than the point of minimum pressure.

Figure 6.8*i* shows that H at 12.0 ms^{-1} is very similar to H at 6.0 ms^{-1}, Figure 6.3*ii*. Although there is a decreasing trend in H after 3.5 m, transition does not occur until 4.77 m, when H exceeds 3.0. Constant H between 4.0 m and 4.5 m is a result of Palisupan approximation when λ exceeds its limits. Figure 6.8*ii* shows the Cebeci & Smith transition prediction method.

$Re_{\theta Palisupan}$ does not intersect at all and is less than $Re_{\theta Palisupan}$ in Figure 6.4*i* as θ has decreased. Re_{θ} intersects Re at 2.1 m, earlier than 3.2 m, Figure 6.4*i*. This would give the Parsons hull shape at 12.0 ms^{-1} a shorter laminar boundary layer and a higher $C_{D\nabla}$ value than at 6.0 ms^{-1}.

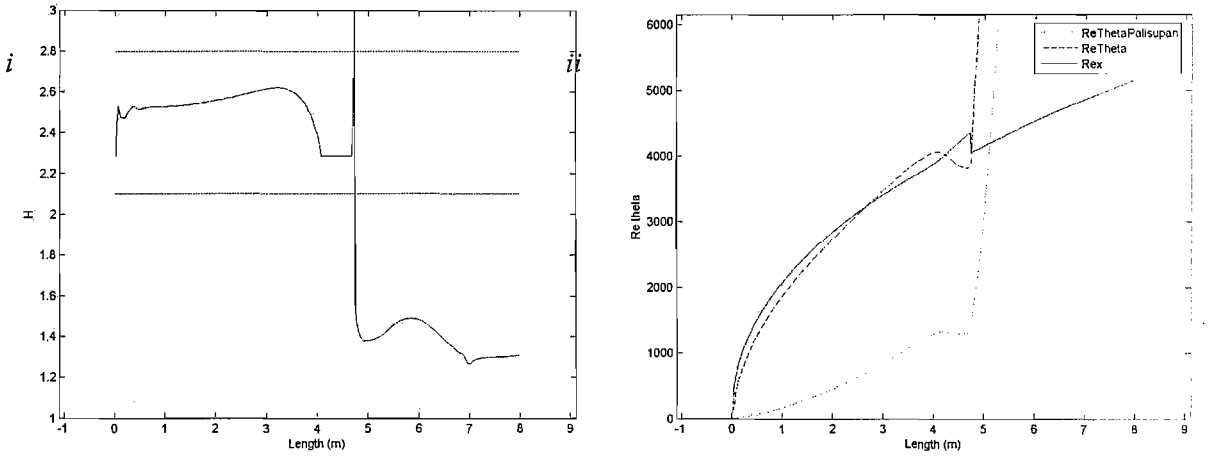

Figure 6.8 *i*) *H* and *ii*) the Cebeci & Smith method of transition prediction at 12.0 ms^{-1}.

6.1.4 Summary of the Parsons hull shape.

Compared to the source of the Parsons hull shape literature (Parsons, *et al.* 1974) at the same Re_{∇} Palisupan predicts transition at 68 % of length, a comparable position along the profile shape and predicts the same $C_{D\nabla}$. This occurs just after the point of maximum diameter at 67.8 % of a 7 m body (not including 1 m tail). This is itself encouraging, as the Thwaites – Head model models a pressure gradient at high *Re*.

However the transition prediction is based on an incorrect value of $Re_{\theta Palisupan}$ which predicts transition on the parameters θ and s, and not θ and U. Although the Parsons model run at the same Re_{∇} replicates Parsons' results. This is due to transition at this *Re* being driven by *H* exceeding 3.0 at the point of maximum diameter and is correct in Palisupan, yet causes transition too early at lower velocities.

For the design method, the Parsons body could represent a low drag shape. Modelling the base shape has been successful, and results from literature may be used to guide the range of velocities that the AUV might operate. A similar model will be made from simply defined curves for parametric variation. This improves the intuitiveness of the hull shape parameters and aids the generation of a smooth hull profile. This shape is modelled in Palisupan and discussed in section 6.3.

6.2 Shape 2: Parallel middle body.

The parallel middle body hull shape is common to many AUVs and was therefore selected for computational modelling. The Autosub hull shape is used as the base model. The Schlichting skin friction approximation is used for these models.

The Thwaites – Head boundary layer model was only considered accurate at a specific velocity. The Schlichting skin friction estimation enabled drag predictions at lower speed velocities (2 ms^{-1}) representative of AUV velocities.

6.2.1 Geometry definition and variants.

The geometric profile of a family of parallel middle body AUV hull shape is illustrated in Figure 6.9.

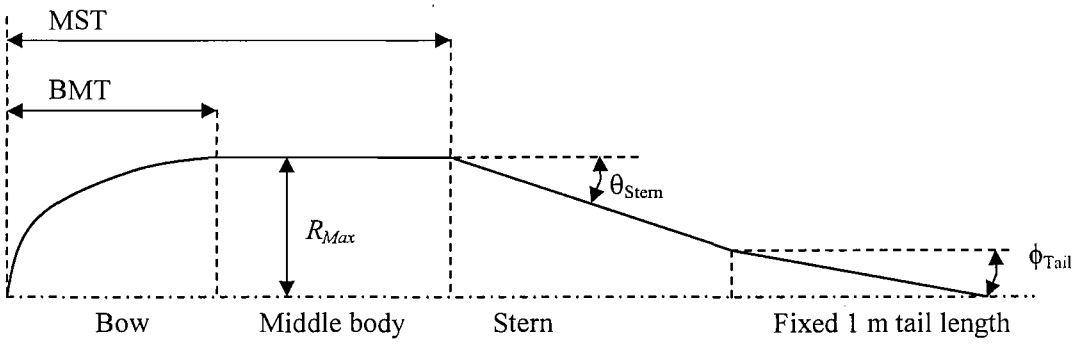

Figure 6.9 Parallel middle body hull shape profile definition including tail.

The inputs to be varied during modelling are BMT length, MST length and R_{Max} which will control the bow aspect ratio. The stern length will control θ_{Stern} but ϕ_{Tail} needs to be separately constrained. The bow aspect ratio is defined by equation 6.3.

$$Bow\ AR = \frac{R_{Max}}{BMT} \qquad 6.3$$

R_{Max} is the radius of the hull at the bow to middle body transition (BMT), and for the parallel middle body R_{Max} will be the maximum radius.

The profile of each variant of parallel middle body geometry is shown in Figure 6.10a and Figure 6.10b. Table 6.2 gives a list of the geometric parameters used for each hull shape variant.

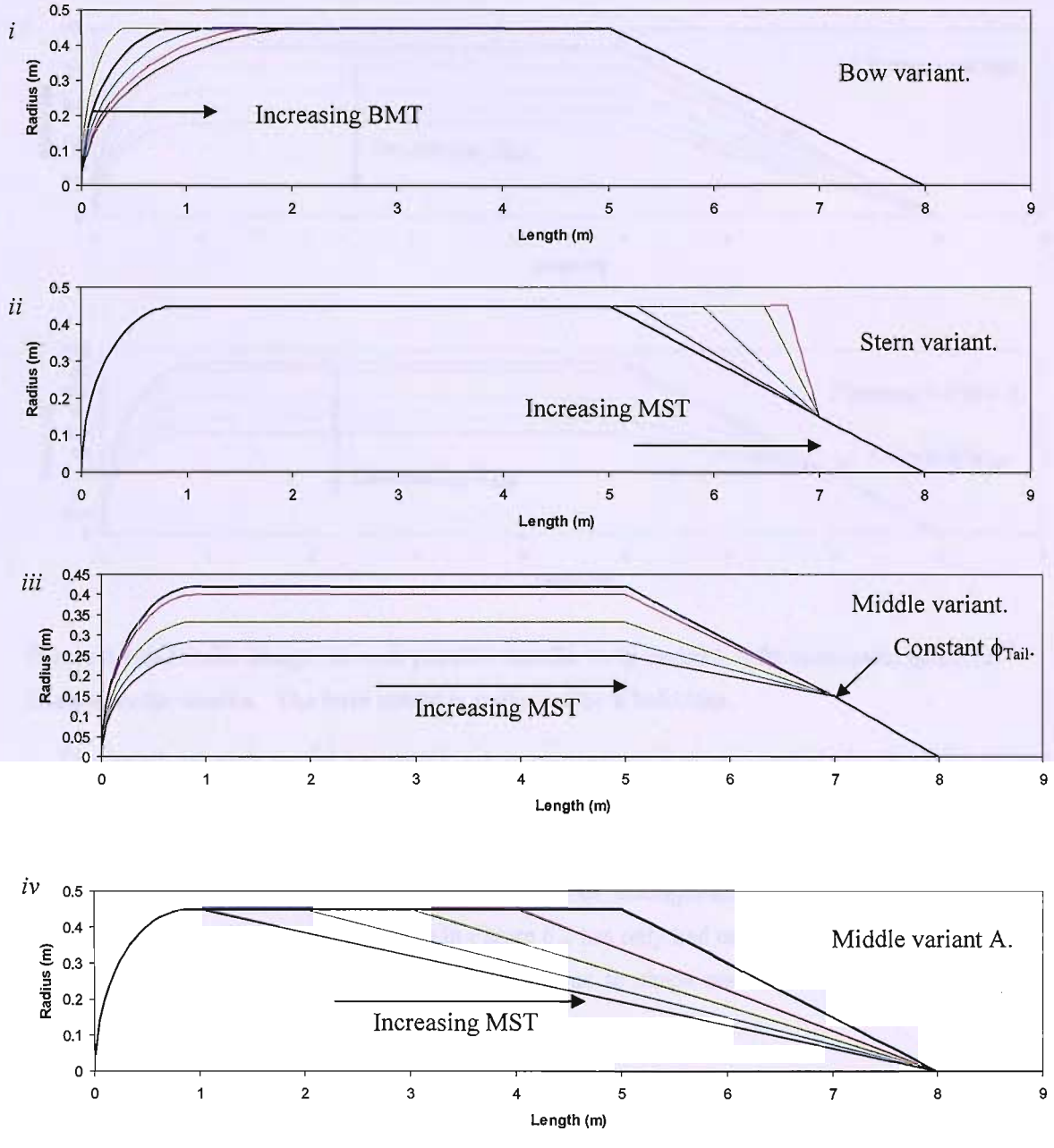

Figure 6.10a Profile images of each parallel middle body variant. *i*) bow, *ii*) stern *iii*) middle, *iv*) 2nd middle version. The base model is indicated by a bold line.

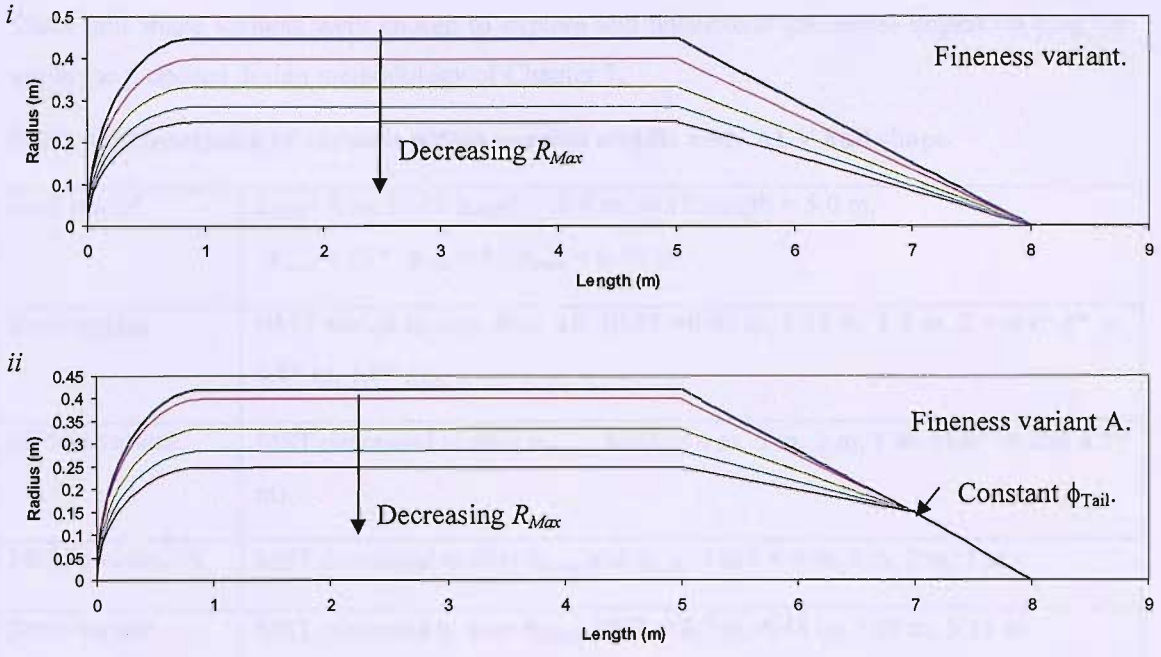

Figure 6.10b Profile images of each parallel middle body variant. *i*) fineness ratio and *ii*) 2nd fineness ratio version. The base model is indicated by a bold line.

The length of each model variant (L_{AUV}) is constant at 8 m so constant Re ($L_{AUV}U$ / υ) is maintained for constant velocity. Keeping the volume constant was considered, as this would enable direct comparison between shapes. However, this would require simultaneous variation of all input parameters and so increase the difficulty of distinguishing the influence of a single parameter change. Each of the variants in Figure 6.2 has only had one input altered from the base model. It will be possible to compare the drag due to shape and not volume by using non-dimensional coefficients, such as $C_{D\nabla}$.

There are two versions of the middle body variant groups, termed middle body and middle body with an affix A. These have the same MST length, but ϕ_{Tail} is constant for the first middle body variant group. In the second group, with an affix A, $\phi_{Tail} = \theta_{Stern}$. Likewise, there are two versions of the fineness ratio variant groups, termed fineness and fineness A. For the fineness model, $\phi_{Tail} = \theta_{Stern}$ to give a constant gradient stern and tail. The fineness A group have a constant ϕ_{Tail}, and θ_{Stern} will alter with maximum radius.

It is expected that the bow variants will have the greatest impact on body drag as pressure drag and boundary layer length are influenced by the bow. Increasing the hull shape fineness ratio will decrease the drag acting on the body and significantly decrease volume. The shape of the stern was not expected to have a large effect on drag whilst the boundary layer does not separate.

These hull shape variants were chosen to explore and understand geometric impact on drag for use in the proposed design methodology of Chapter 7.

Table 6.2 Generation of variants within parallel middle body AUV hull shape.

Base model	L_{AUV}= 8 m, BMT length = 0.9 m, MST length = 5.0 m, θ_{Stern} = 15 °, ϕ_{Tail} = 15 R_{Max} = 0.45 m
Bow variant	BMT varied to alter *Bow AR*. BMT =0.45 m, 1.35 m, 1.8 m, 2.4 m (0.6* m, 0.8* m, 1.0* m).
Middle variant	MST decreased to alter θ_{Stern}. MST = 4 m, 3 m, 2 m, 1 m. (4.9* m and 4.5* m).
Middle variant A	MST decreased to alter θ_{Stern} and ϕ_{Tail}. MST = 4 m, 3 m, 2 m, 1 m.
Stern variant	MST increased to alter θ_{Stern}. MST = 6.7 m, 6.48 m, 5.88 m, 5.15 m.
Fineness variant	R_{Max} varied to alter AUV fineness ratio (L_{AUV} / 2 R_{Max}). R_{Max} = 0.25 m, 0.286 m, 0.333 m, 0.4 m. (0.421* m, 0.444* m, 0.5* m, 0.667* m, 1.0* m).
Fineness variant A	R_{Max} varied to alter AUV fineness ratio, ϕ_{Tail} held constant. (L_{AUV} / 2 R_{Max}). R_{Max} = 0.25 m, 0.286 m, 0.333 m, 0.4 m. (0.421* m, 0.444* m, 0.5* m, 0.667* m).
* These variants also modelled and are not included in Figure 6.2 as they were not tested over the full velocity range (0.5 ms^{-1} to 12 ms^{-1}).	

The effect of velocity changes from 0.5 ms^{-1} to 12.0 ms^{-1} upon the $C_{D\nabla}$ of the base model and variants were examined. The predicted $C_{D\nabla}$ of these hull shapes using the Schlichting skin friction estimation is shown in Figure 6.11. It was not expected that a change in shape would alter the effect of speed on the $C_{D\nabla}$ prediction of the shape. The differences in $C_{D\nabla}$ caused by shape can be found at a set speed, and changes in speed would exacerbate any differences. The models were created as quarterbodies and the drag estimates, volumes and surface areas provided for the whole body.

For variations of form over the variant hull shapes $\nabla_S^{2/3}$ varies and so $C_{D\nabla}$ will vary. This variation in $\nabla_S^{2/3}$ at a set speed will result in changes in drag whereas for a fixed drag variations in form will limit achievable speed. The $C_{D\nabla}$ curves do not intersect and any advantage (or disadvantage) a particular hull shape variant has over other similar variants is exhibited at all velocities.

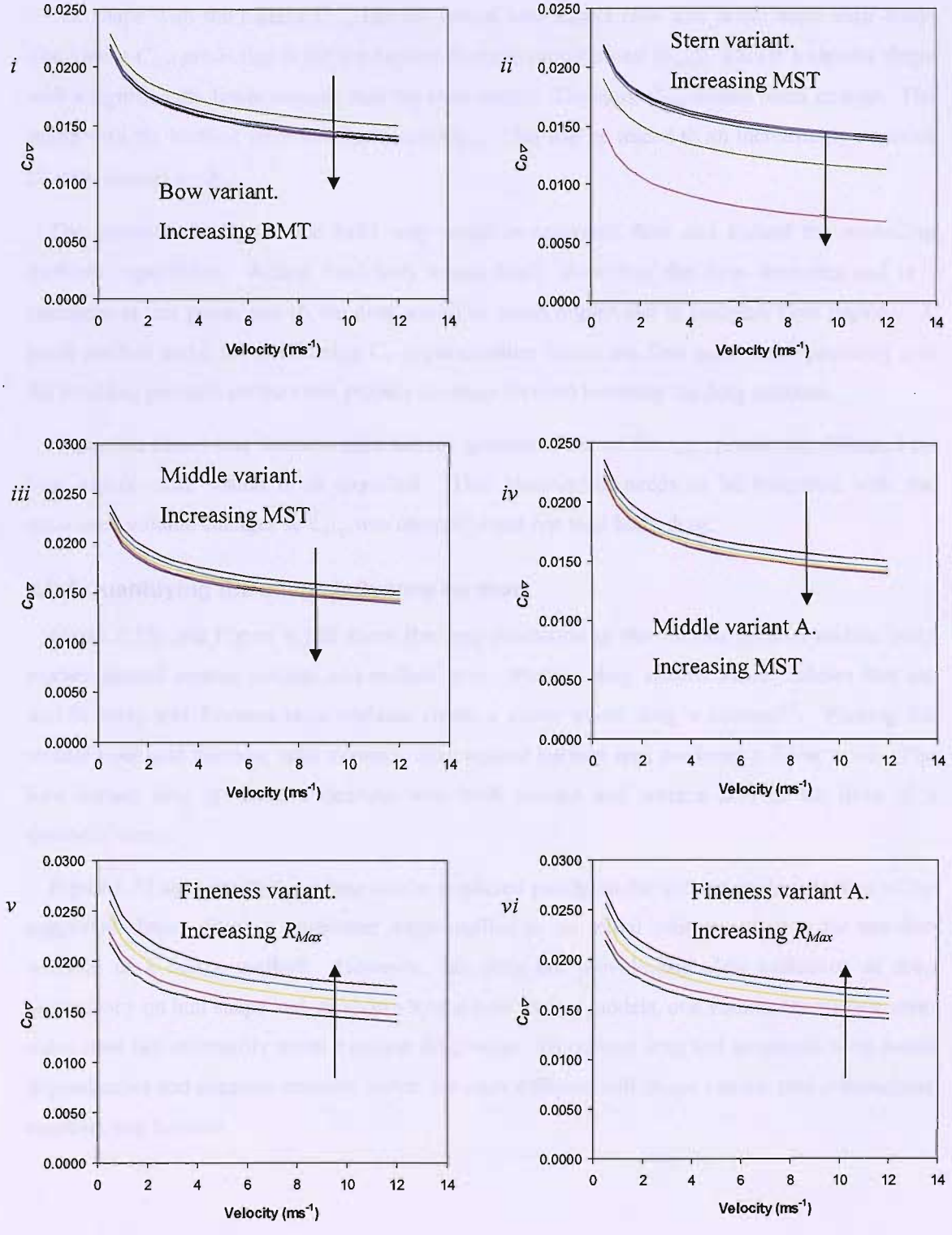

Figure 6.11 $C_{D\nabla}$ with increasing velocity for parallel middle body variants *i*) bow *ii*) stern *iii*) middle *iv*) middle A *v*) fineness ratio and *vi*) fineness ratio A. Base model indicated by bold line.

The shape with the highest C_{D_∇} has the lowest bow aspect ratio and is the most bluff body. The lowest C_{D_∇} prediction is for the highest fineness ratio (lowest R_{Max}). This is a slender shape with a significantly lower volume than the base model. The stern C_{D_∇} results seem strange. The shape with the bluffest stern has the lowest C_{D_∇}. This can be traced to an increasingly negative C_P with increasing θ_{Stern}.

The geometry change at the MST may result in separated flow and exceed the modelling methods capabilities. Actual fluid tests would likely show that the flow separates and re - circulates at this point, and so the drag would be much higher due to complex flow regions. A panel method using the Schlichting C_F approximation forces the flow around the geometry and the resulting pressure on the stern propels the body forward lowering the drag estimate.

Inspection shows that fineness ratio has the greatest effect on the C_{D_∇} prediction, followed by bow aspect ratio, which is as expected. This observation needs to be tempered with the associated volume changes so C_{D_∇} was compared and not total body drag.

6.2.2 Quantifying the shape influence on drag.

Figure 6.12*i* and Figure 6.12*ii* show the drag prediction of the various parallel middle body models plotted against volume and surface area. Plotting drag against volume shows that the middle body and fineness ratio variants create a curve where drag α volume$^{2/3}$. Plotting the middle body and fineness ratio variants' drag against surface area produces a linear trend. The bow variant drag predictions increase with both volume and surface area in the form of a parabolic curve.

Figure 6.12 suggests that the drag can be predicted purely on the volume or surface area of the suggested shape. Such a prediction might suffice as an initial estimate of drag for the first iteration of a design method. However, this does not provide any clear indication of drag dependency on hull shape and, as shown by the bow variant models, one volume (or surface area) value does not necessarily mean a unique drag value. To unravel drag and geometric form based dependencies and generate separate curves for each different hull shape variant, non-dimensional numbers will be used.

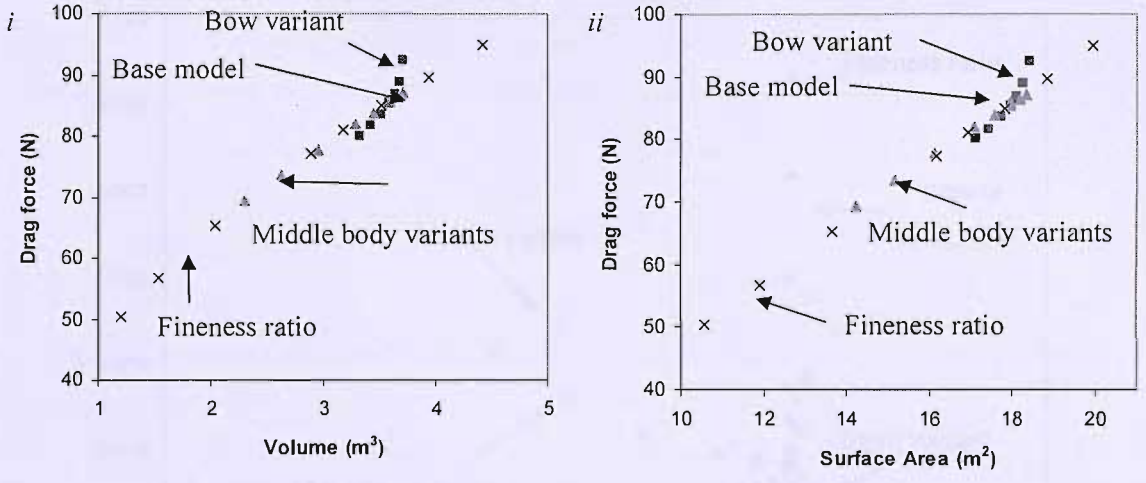

Figure 6.12 Drag force prediction with *i*) volume and *ii*) surface area for the parallel middle body. The base model is the Autosub model.

As discussed in section 3.1.1.2, C_Θ (∇_S / $\pi R_{Max}^2 L_{AUV}$) can illustrate the fullness of a shape. $C_{D\nabla}$ can rate the drag of the body irrespective of volume. The objective of this exercise is to use the geometric profile inputs to describe the shape and the corresponding C_Θ value. The change in C_Θ particular to the altered input parameter is then used to predict the $C_{D\nabla}$ of the shape.

The affect of each separate hull parameter can be seen as a distinct $C_{D\nabla}$ path in Figure 6.13.

The bow variant shows that decreasing the bow aspect ratio will increase the C_Θ of the shape. This increases the $C_{D\nabla}$ values in an exponential manner.

The fineness ratio variants (L_{AUV} / 2 R_{Max}) actually have no effect on C_Θ and so the $C_{D\nabla}$ plot against C_Θ is a vertical line.

The fineness ratio A variants (with the constant radius tail) do affect C_Θ and $C_{D\nabla}$. These hull shape variants will be used for the input geometric parameter analyses.

The middle body variants and stern variants are both consequences of moving the MST point, and so can be considered to be the same path. This path shows decreasing $C_{D\nabla}$ with increasing C_Θ. This might only be true for values of C_Θ where the boundary layer does not separate from the stern.

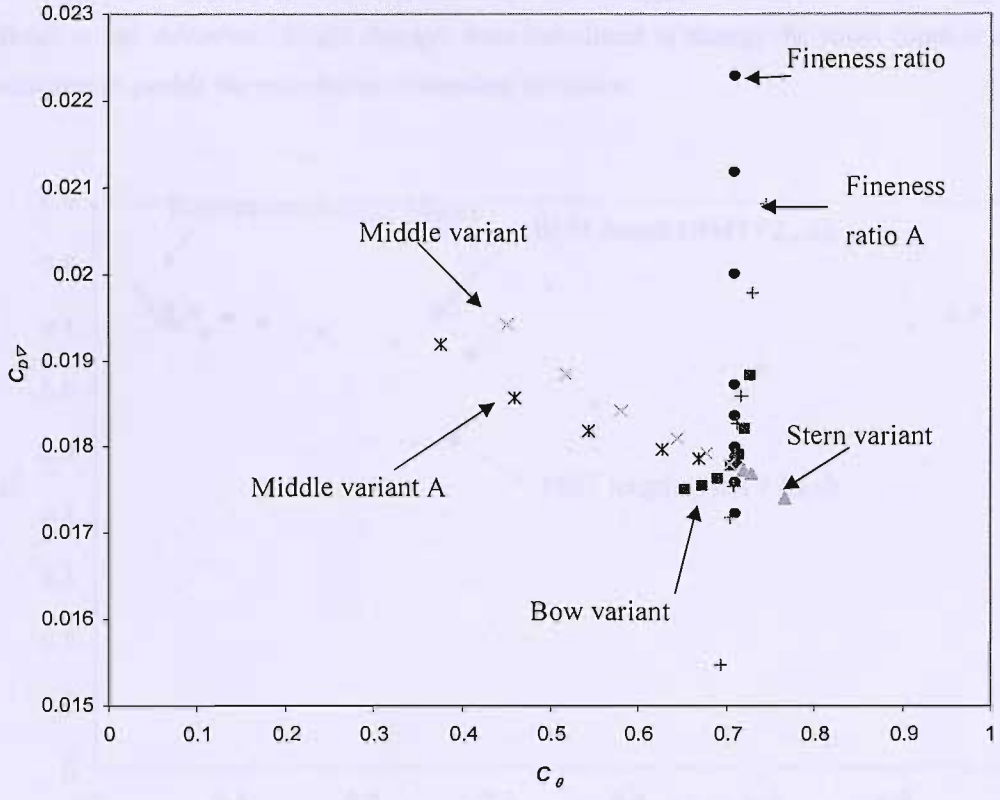

Figure 6.13 $C_{D\nabla}$ variation with C_Θ for each parallel middle body variant with the Schlichting skin friction estimation.

Figure 6.14 shows how the input variables affect the C_Θ of the body shape.

The non-dimensional bow length (BST / L_{AUV}) and MST (MST / L_{AUV}) have a linear affect on the hull shape C_Θ. The gradient of the stern, caused by varying MST has the greatest affect on the shape C_Θ and appears to be a linear curve. The minimum C_Θ (0.452) occurs when MST / L_{AUV} is located at 0.125 (1.0 m of an 8 m body). The fineness ratio A variants with constant $\phi_{Tail} = \theta_{Stern}$ show a decrease in C_Θ with increasing R_{Max}. The affect of hull shape fineness ratio on C_Θ decays with increasing radius.

The effect of each variant curve on $C_{D\nabla}$ will be to be captured within a single function to predict $C_{D\nabla}$. A consequence of quoting $C_{D\nabla}$ to four decimal places is the assumption that errors within the fluid modelling are less than 0.5×10^{-4}. This is not always true and explains why not all the curves intersect one point corresponding to the base model in Figure 6.15.

The statistical variance of the models were tested, running the exact model repeatedly would not result in any deviation. Slight changes were introduced to change the panel count or critical co-ordinates to permit the calculation of standard deviation.

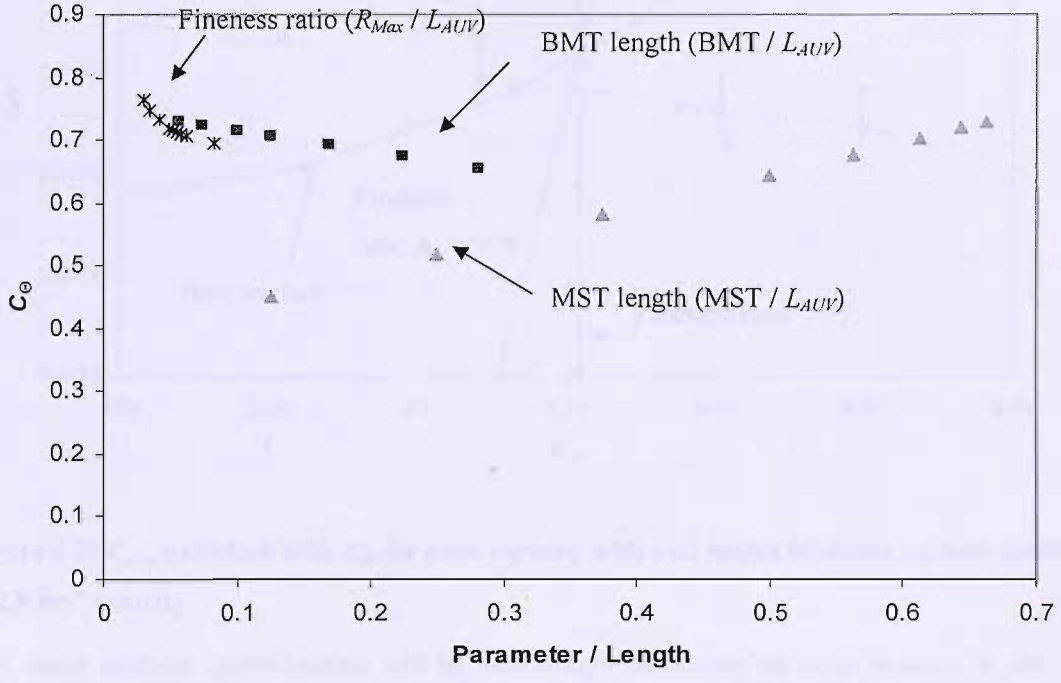

Figure 6.14 C_Θ variation of the parallel middle body model, each geometric parameter non-dimensionalised by body length.

The $C_{D\nabla}$ estimate was found to be sensitive to the location of the first two coordinate points defining the nose of the hull shape bow. This variation is shown in Figure 6.15 using error bars set at twice the estimated standard deviation. The $C_{D\nabla}$ error had a standard deviation of 3.4×10^{5}. This variation represents less than 0.5 % of the estimated $C_{D\nabla}$ and hence does not reduce the significance of the trends displayed in Figure 6.13.

Using a linear approximation method between two points that straddle the base model on any given curve, it is possible to find the gradient of that curve at the base model. From this it will be possible to estimate the change in $C_{D\nabla}$ from a change in input parameters along that curve. This approach will be used to observe how the drag of the body will change with small changes in profile parameters.

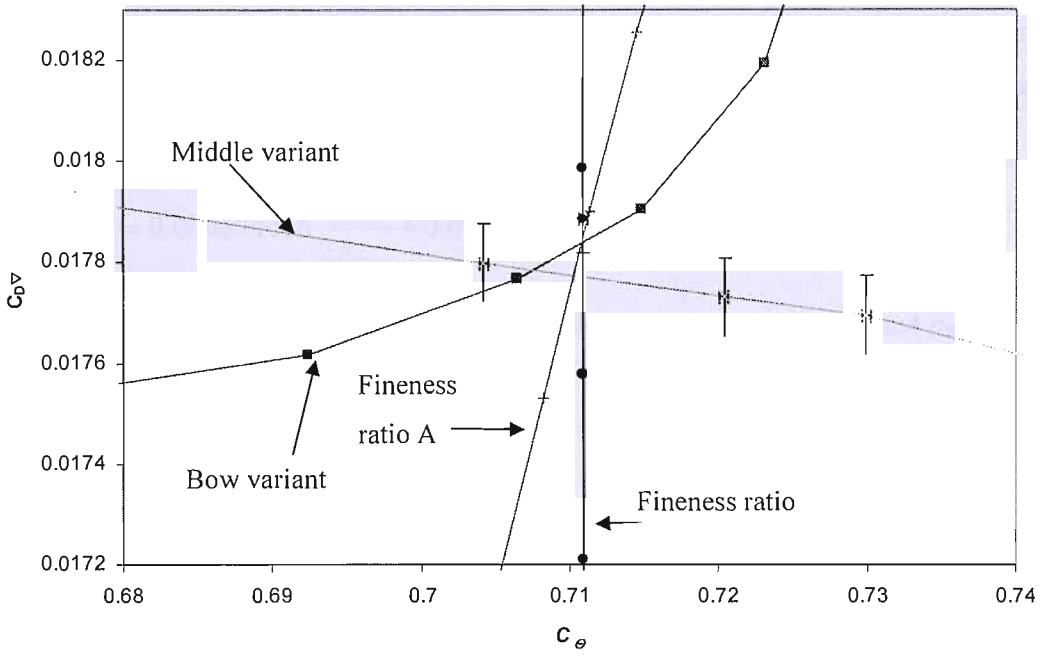

Figure 6.15 $C_{D\nabla}$ variation with C_Θ for each variant, with axis scaled to centre on base model at 2.0 ms^{-1} velocity.

A linear gradient approximation will be increasingly inaccurate for large changes in profile parameters as the curves are nonlinear, especially true of the bow curve. More complex polynomials should be created when a drag prediction that includes boundary layer state is used to generate $C_{D\nabla}$ estimates.

The variation of $C_{D\nabla}$ for different input model parameters is shown in equation 6.4, given that $\Delta m = m_i - m_{Base}$, $\Delta n = n_i - n_{Base}$ and $\Delta p = p_i - p_{Base}$.

$$C_{D\nabla} = C_{D\nabla}\big|_{Base\ model} + \left.\frac{\partial C_{D\nabla}}{\partial C_\Theta}\frac{\partial C_\Theta}{\partial m}\right|_{Base\ model} \Delta m + \left.\frac{\partial C_{D\nabla}}{\partial C_\Theta}\frac{\partial C_\Theta}{\partial n}\right|_{Base\ model} \Delta n + \left.\frac{\partial C_{D\nabla}}{\partial C_\Theta}\frac{\partial C_\Theta}{\partial p}\right|_{Base\ model} \Delta p \qquad 6.4$$

Here m, n and p are non - dimensional input parameters for the shape profile and the subscript i indicates a particular model variant. In order to make the estimate applicable to any length of AUV hull shape, the input parameters of m, n and p are non-dimensionalised by total AUV length. This assumes that a hull profile will have the same $C_{D\nabla}$ when all parameters are scaled, although the AUV's *Re* value might be affected.

For the parallel middle body model m is BMT length / L_{AUV}, n is MST length / L_{AUV} and p is R_{Max} / L_{AUV}. The fineness ratio variant with a constant ϕ_{Tail} is used for this evaluation. When ϕ_{Tail} = θ_{Stern} the $C_{D\nabla}$ trend is a vertical line with an infinite gradient. The vertical line is useful as $C_{D\nabla}$ can be represented as a function of AUV fineness ratio as given in equation 6.5.

$$C_{D\nabla} = 0.000694416\frac{L_{AUV}}{2R_{Max}} + 0.01117433 \qquad 6.5$$

For the specific velocity of 2.0 ms^{-1}, the base model parameters m_{Base}, n_{Base} and p_{Base} (0.1125, 0.625 and 0.05625) and $C_{D\nabla}$ (0.17887) are known. The gradient of each variant trend at the base model has been found:

$$\left.\frac{\partial C_{D\nabla}}{\partial C_\Theta}\frac{\partial C_\Theta}{\partial m}\right|_{Base\ model} = -0.005510583, \left.\frac{\partial C_{D\nabla}}{\partial C_\Theta}\frac{\partial C_\Theta}{\partial n}\right|_{Base\ model} = -0.004190950,$$

$$\left.\frac{\partial C_{D\nabla}}{\partial C_\Theta}\frac{\partial C_\Theta}{\partial p}\right|_{Base\ model} = -0.112099299.$$

Substituting the base model values into equation 6.4 will give equation 6.6, leaving an expression in terms of m_i, n_i, p_i.

$$C_{D\nabla} = 0.027432 - 0.005510583m_i - 0.004190950n_i - 0.112099299p_i \qquad 6.6$$

To replicate the base model, let m_i = m_{Base}, n_i = n_{Base} and p_i = p_{Base} and equation 6.6 will estimate $C_{D\nabla}$ = 0.01788713. This is within a standard deviation of the base model.

From the parallel middle body model results one may deduce that increasing the BMT or the MST or R_{Max} will decrease the $C_{D\nabla}$ of the resulting shape. This is reflected in equation 6.4.

The limits for which equation 6.6 is valid must be considered. The geometric input parameters are subject to 0.0 < m_i, n_i, p_i <1.0 as they must be real lengths and constrained by L_{AUV}. The minimum $C_{D\nabla}$ would occur when m_i, n_i and p_i have unity, $C_{D\nabla}$ = -0.09437. A negative $C_{D\nabla}$ is not realistic and implies that the geometric upper limits are less than 1.0. These parameter values correspond to an AUV consisting of only a bow with a radius equal to overall length. This hemisphere would have lowest $C_{D\nabla}$ in part due to its large volume to surface area ratio, however the drag force would be complicated by the complex fluid flow about the stern and flow separation.

Equation 6.6 is a linear approximation, therefore errors will increase as the shape differs from the base model. Equation 6.7 represents how far removed the 'current' design is from the base model.

$$Difference = |m_i - m_{Base}| + |n_i - n_{Base}| + |p_i - p_{Base}| \quad 6.7$$

This considers the absolute value of the difference of each input parameter. The higher the difference the further the concept hull shape is removed from the base shape. This also will give a rough comparative measure of the error in C_{D_∇} prediction. A large 'difference' will have greater C_{D_∇} error than a hull shape with a small 'difference'. This will be used in Chapter 7 to evaluate the degree of confidence in a C_{D_∇} prediction.

From the coefficients in equation 6.6 and the curves in Figure 6.12 further design implications can be suggested. The AUV fineness ratio has the greatest effect on C_{D_∇} as it has the greatest coefficient in equation 6.6. The bow has a large effect on the C_{D_∇} of the shape, especially at high C_Θ values when the curve is nonlinear and most sensitive of parameter variation from the base model. The MST length has a large effect on the C_Θ of the shape, but does not have a great effect on its C_{D_∇}

6.2.3 Summary for the parallel middle body hull shape.

The base parallel middle body model is an attempt to model the hydrodynamic behaviour of Autosub using Palisupan. The base model and twenty five variants have been run at speeds from 0.5 ms^{-1} to 12 ms^{-1}. The results have been compared with those produced from published sources, and have been found to underestimate the overall drag. The addition of control surfaces is required to compare against physical testing.

The parametric analysis generated an equation for C_{D_∇} based on hull shape variation. The inputs are intuitive hull shape profile dimensions. The equation is valid at 2 ms^{-1} given the Schlichting C_F approximation and the process can be repeated at alternative velocities. Error in calculating C_{D_∇} is increased as the hull shape profile varies from the base model. This parametric analysis will be conducted on the simplified laminar flow hull shape.

6.3 Shape 3: Rutherford body.

The Rutherford shape is inspired by the Parsons hull shape. The Parsons hull shape required three equations: a 4^{th} degree polynomial for the bow, and two 5^{th} degree polynomials for the middle body and stern. The defining geometric equations for the Rutherford body are significantly more suitable for a design sensitivity study. The associated geometric parameters are: maximum radius, position of maximum radius and bow curvature. These parameters will be intuitively accessible to a design engineer in the early stages of the design cycle. Variants of the

shape will be created and modelled to gauge the effect of shape on the C_{D_∇} values for a laminar flow shape.

The bow is intended to provide a favourable pressure gradient similar to that found on the Parsons shape.

6.3.1 Geometry definition.

Figure 6.16 shows comparative profiles of the Parsons and Rutherford geometries.

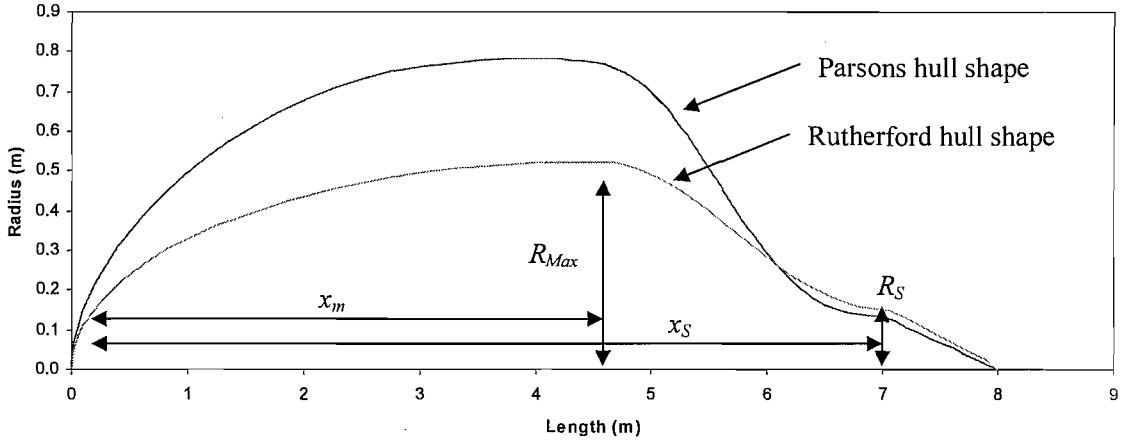

Figure 6.16 Comparison of the Parsons laminar flow and Rutherford shape hull profiles.

The analytic formulas used to create these shapes are shown in equation 6.8 and equation 6.9.

$$\text{Bow -> } y = R_{Max}\left(1-\frac{(x-x_m)^2}{x_m^2}\right)^{\frac{1}{n_{Bow}}} : 0 \le x \le x_m \qquad 6.8$$

$$\text{Stern -> } y = \left(\frac{R_{Max}-R_S}{2}\right)\cos\theta + \left(\frac{R_{Max}}{2}+\frac{R_S}{2}\right) \qquad 6.9$$

for θ at $x_m = 0.0°$, θ at $x_S = 180°$.

The profile swaps from one curve to the next at the point of maximum radius (R_{Max}). This is constrained by both bow and stern curve gradients = 0.0 at R_{Max}. R_S is the transom stern radius, x is the lengthwise station, and n_{Bow} is the power of the bow curve. For the base model 8 m in length; R_{Max} = 0.523 m, x_m = 4.5 m, R_S = 0.15 m and n_{Bow} = 2, giving the same length and volume as the parallel middle body.

The bow is an elliptical curve. The pressure gradient will be favourable for a laminar boundary layer, but this will only be advantageous when the bow to stern transition occurs far down the body. If the bow has an aspect ratio (x_m / R_{Max}) of 2, the bow will be the same curve as the parallel middle body's bow and there will only be a short laminar boundary length. Models will be created that vary the bow aspect ratio to inspect boundary layer development and compare the bow aspect ratio variants modelled for the parallel middle body discussed in section 6.2. Figure 6.17 shows the profiles of the family of variants modelled for the Rutherford body and Table 6.3 defines the illustrated variants.

Table 6.3 Generation of variants within parallel middle body AUV hull shape.

Base model.	R_{Max} = 0.523 m, x_m = 4.5 m, R_S = 0.15 m, x_S = 7 m and n_{Bow} = 2.
Bow aspect ratio variant.	x_m varies to vary aspect ratio (x_m / R_{Max}) of bow. x_m = 2.5 m, 3.0 m, 3.5 m, 4.0 m, 5.0 m, 5.5 m (4.4* m, 4.45* m, 4.55* m, 4.6* m).
Bow curvature variant.	n_{Bow} varies to alter bow curvature. n = 0.6, 0.8, 1.0, 1.5, 3, 4, 5) .
Fineness variant.	R_{Max} varies to alter hull shape fineness ratio (L_{AUV} / $2R_{Max}$). R_{Max} = 0.333 m, 0.4 m, 0.667 m, 1.0 m.
* These variants also modelled and are not included in Figure 6.2 as they were not tested over the full velocity range (0.5 ms^{-1} to 12 ms^{-1}).	

The hull shape has a higher fineness ratio than the Parsons shape, so one variant will reduce the fineness ratio to a comparable slenderness.

The Rutherford shape has the same stern radius as the Autosub model, and is modelled without any control surfaces. Making the assumption that both hull shapes would operate with cruciform control surfaces and a single propeller maintains comparison between the two bare hull models. From experience of the parallel middle body and the Parsons hull shape, a constant tail was added to stabilise the C_P results of the Rutherford body results.

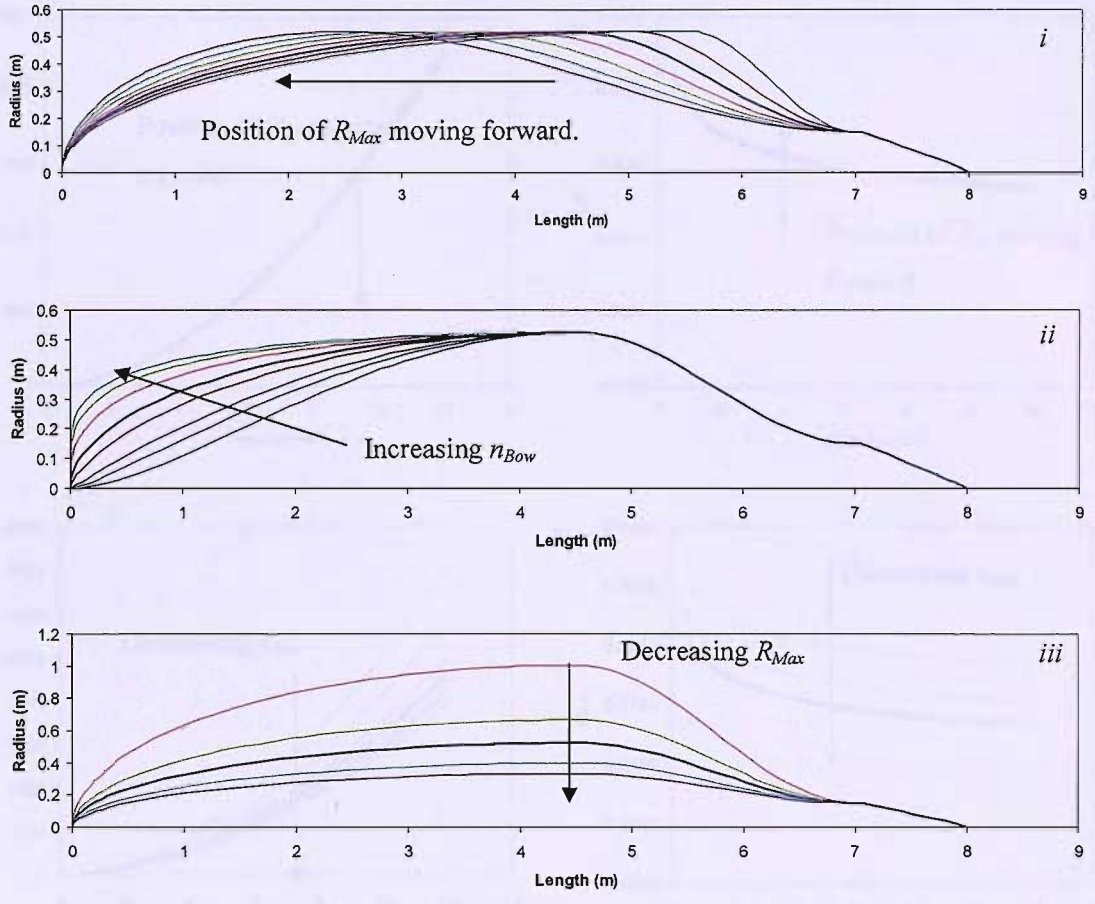

Figure 6.17 Profiles of Rutherford shape variants. *i*) Position of maximum diameter *ii*) Bow curvature *iii*) Fineness ratio.

Hydrodynamic characteristics for different geometric variants generated using the Schlichting estimate of C_F are presented in Figure 6.18. The drag predictions in Figure 6.17 are for the whole hull shape. Figure 6.18*i* and *ii* correspond with Figure 6.17*i*, Figure 6.18*iii* and *iv* correspond with Figure 6.17*ii* and Figure 6.18*v* and *vi* correspond with Figure 6.17*iii*.

Considering the Parsons hull shape, the drag estimates are comparable. The Rutherford C_{D_∇} is higher as the Parsons hull shape has a larger displaced volume. The position of R_{Max} makes little overall difference to the predicted drag and C_{D_∇} levels of the Rutherford shape. The bow curvature increases the shape volume and drag estimate, yet has little impact on C_{D_∇} except for $n_{Bow} > 3$, when C_{D_∇} increases noticeably. This is due to the increasing C_P values expected of an increasingly bluff body. Similar to other model results, the fineness ratio has a large effect on the volume and so impacts both the drag estimate and C_{D_∇}.

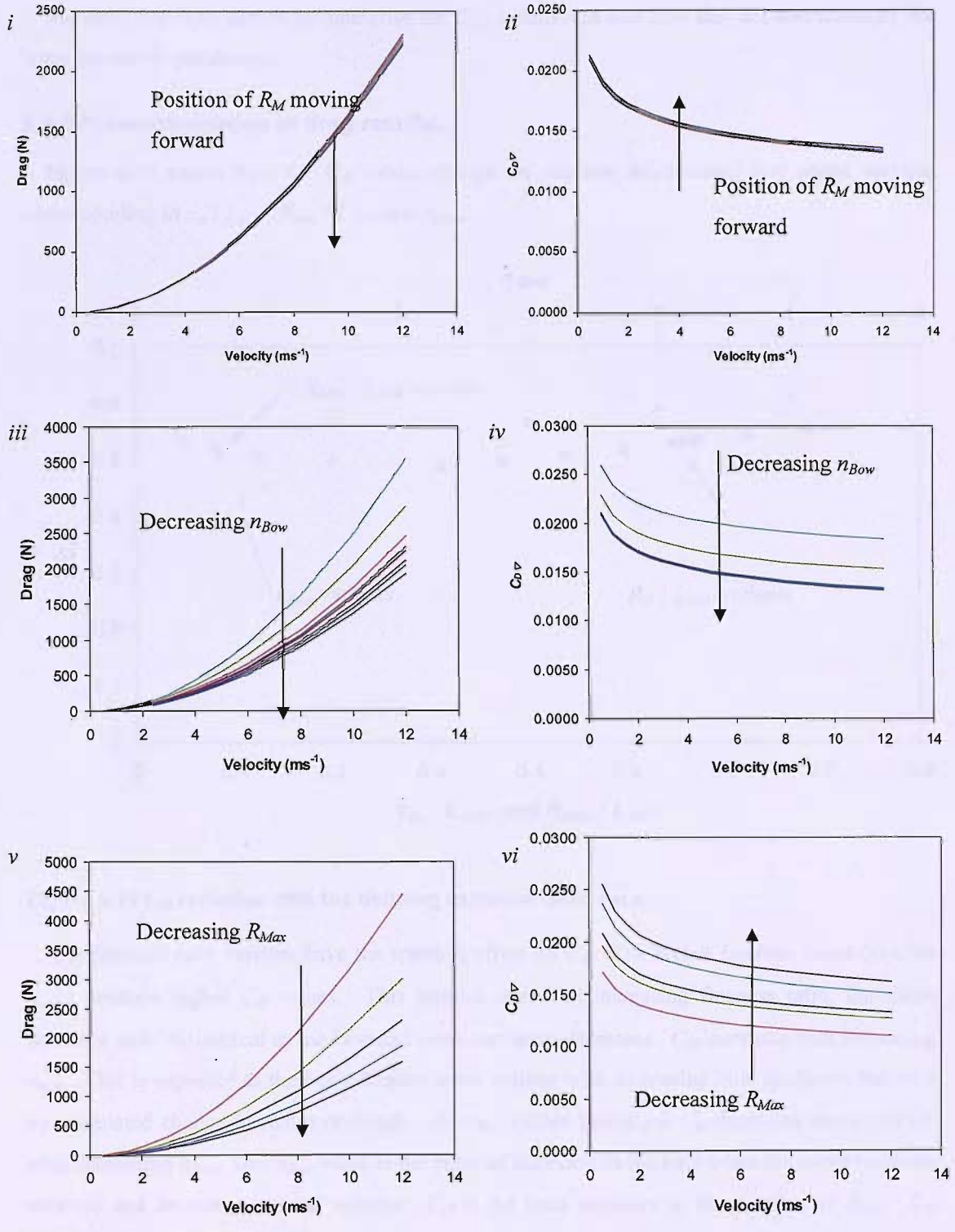

Figure 6.18 Rutherford body whilst varying position of maximum diameter *i*) drag prediction, *ii*) $C_{D\nabla}$, bow variant *iii*) drag prediction *iv*) $C_{D\nabla}$ and fineness ratio and *v*) drag prediction and *vi*) $C_{D\nabla}$

The next step is to start to parameterise the $C_{D\nabla}$ results and find how they are controlled by the input geometric parameters.

6.3.2 Parameterisation of drag results.

Figure 6.19 shows how the C_Θ values change for the non dimensional hull shape variants corresponding to x_m / L_{AUV}, R_{Max} / L_{AUV} and n_{Bow}.

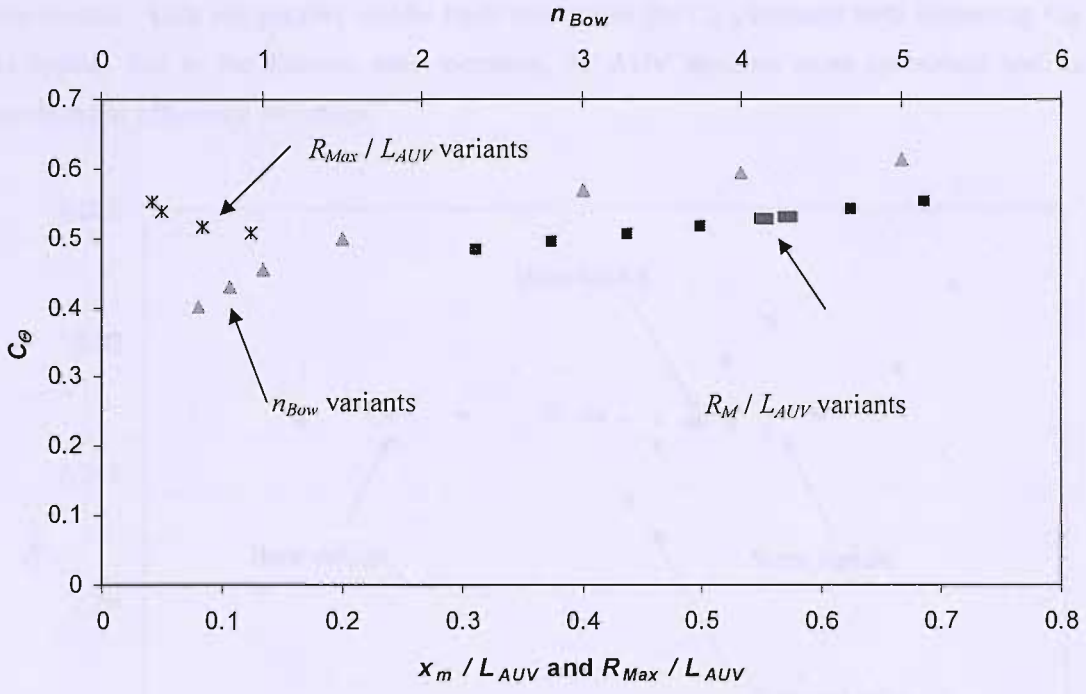

Figure 6.19 C_Θ variation with the defining variation difference.

The fineness ratio variants have the smallest effect on C_Θ. The higher fineness ratios (smaller R_{Max}) produce higher C_Θ values. This implies that with increasing fineness ratio, the shape becomes more cylindrical as the bow and stern curvature decreases. C_Θ increases with increasing n_{Bow}. This is expected as the hull occupies more volume with increasing bow bluffness, but with no associated change in radius or length. At n_{Bow} values below 1.0 C_Θ decreases more quickly with decreasing n_{Bow}. This n_{Bow} value is the point of inflexion in the bow when the curve becomes concave and decreases internal volume. C_Θ is the least sensitive to the position of R_{Max}. C_Θ increases as the bow to stern transition moves backwards along the body. The variants with a short bow and long tail have the lowest C_Θ and the bluffest leading edge. The C_Θ is not very sensitive to this variant because the volume lost from the bow is balanced by the volume gained at the stern.

Figure 6.20 illustrates the sensitivity of the C_{D_∇} values of the Rutherford model variants as a function of C_θ for an advance velocity of 2.0 ms^{-1} using the Schlichting skin friction estimation. The Schlichting results at increasing speed were investigated, and the trends for each variant remain the same. Overall C_{D_∇} estimates decrease with increasing velocity, as illustrated in Figure 6.18.

When R_S is held constant, the hull shape stern becomes more horizontal with increasing fineness ratio. Like the parallel middle body this makes the C_{D_∇} increase with increasing C_Θ. This implies that as the fineness ratio increases, the AUV becomes more cylindrical and its hydrodynamic efficiency decreases.

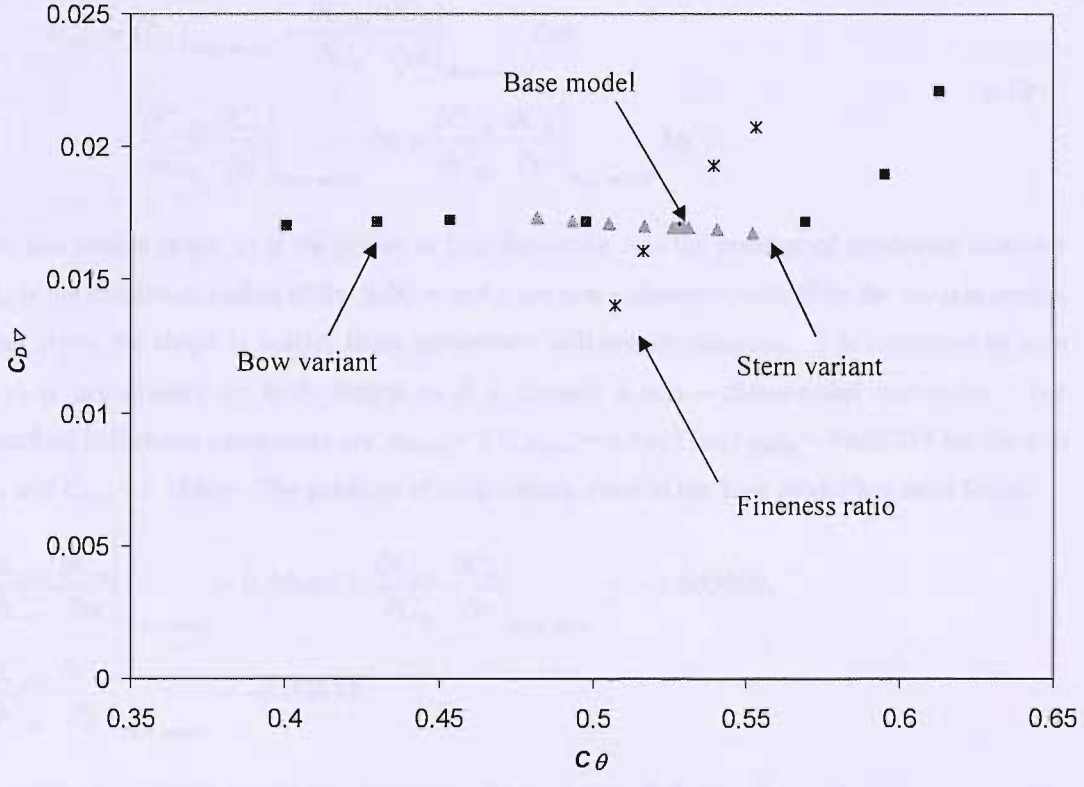

Figure 6.20 C_{D_∇} for the Rutherford variants at 2 ms^{-1} with the Schlichting skin friction estimation.

Varying the bow curvature gives a polynomial trend, with a point of inflexion at $C_\Theta = 0.53$. C_{D_∇} increases rapidly when C_Θ is greater than 0.55, and decreases slowly when C_Θ is less than 0.5. C_Θ is greater than 0.55 when n_{Bow} is greater than 2 and so gives a bluff bow. The C_{D_∇} of the shape is therefore very sensitive to the bow curvature once n_{Bow} increases beyond 2.0. At values

of n_{Bow} less than 2.0, $C_{D\nabla}$ is not as sensitive to bow curvature, increasing slightly with C_Θ, although a less severe bow curve will reduce $C_{D\nabla}$.

The stern variants tested create a linear trend that shows decreasing $C_{D\nabla}$ with increasing C_Θ. For the stern variant, the smallest C_Θ occurs when the location of R_{Max} is closest to the leading edge, creating a short, bluff bow. This is because the sinusoidal tail does not enclose as much volume per unit length as the elliptical bow. A more hydrodynamically efficient shape therefore occurs when the elliptical bow forms the majority of the shape and encloses more volume.

For the Schlichting based results a parameterised equation (equation 6.10) for $C_{D\nabla}$ based upon the input design parameters was utilised, analogous to equation 6.4.

$$C_{D\nabla} = C_{D\nabla}\Big|_{Base\ model} + \frac{\partial C_{D\nabla}}{\partial C_\Theta}\frac{\partial C_\Theta}{\partial m}\Big|_{Base\ model}\Delta m + \frac{\partial C_{D\nabla}}{\partial C_\Theta}\frac{\partial C_\Theta}{\partial n}\Big|_{Base\ model}\Delta n + \frac{\partial C_{D\nabla}}{\partial C_\Theta}\frac{\partial C_\Theta}{\partial p}\Big|_{Base\ model}\Delta p \qquad 6.10$$

For this profile shape, m is the power of bow curvature, n is the position of maximum diameter and p is the maximum radius of the hull. n and p are non – dimensionalised by the vehicle length, so that when the shape is scaled, these parameters will remain constant. It is important to note that m is not divided by body length as it is already a non – dimensional parameter. The Rutherford hull shape parameters are: $m_{Base} = 2.0$, $n_{Base} = 0.5625$, and $p_{Base} = 0.065375$ for the 8 m body and $C_{D\nabla} = 0.16969$. The gradient of each variant trend at the base model has been found:

$$\frac{\partial C_{D\nabla}}{\partial C_\Theta}\frac{\partial C_\Theta}{\partial m}\Big|_{Base\ model} = 0.000017,\quad \frac{\partial C_{D\nabla}}{\partial C_\Theta}\frac{\partial C_\Theta}{\partial n}\Big|_{Base\ model} = -0.000990,$$

$$\frac{\partial C_{D\nabla}}{\partial C_\Theta}\frac{\partial C_\Theta}{\partial p}\Big|_{Base\ model} = -0.09634.$$

Equation 6.11 shows a quantified version of equation 6.10 for the Rutherford shape using the Schlichting skin friction estimation at 2 ms^{-1}.

$$C_{D\nabla} = 0.023793 + 0.000017m_i - 0.000990n_i - 0.09634p_i \qquad 6.11$$

As with the parallel middle body model, increasing the maximum radius of the vehicle, represented by p_i in equation 6.11, will increase drag but decrease $C_{D\nabla}$. Moving the point of R_{Max} (n_i) away from the bow (increasing x_m) will decrease the $C_{D\nabla}$. Increasing the bluffness of the bow by increasing n_{Bow} (m_i) will increase $C_{D\nabla}$. As equation 6.10 is a linear approximation based upon

gradients at the base model it will not accurately capture the variations of $C_{D\nabla}$ values in Figure 6.20 for higher C_Θ values. The limits of n_i and p_i have been set at 0.0 and 1.0, although this is likely to be less if the prediction errors are to be minimised. The parameter difference equation 6.7 (section 6.1.2) will be used with the Rutherford hull shape when estimating $C_{D\nabla}$ values in the design cycle.

6.3.3 Summary for the Rutherford body.

The Rutherford body has been generated and modelled in Palisupan. The base model and its nineteen variants have been modelled at speeds from 0.5 ms^{-1} up to 12 ms^{-1}. The Schlichting results have been parameterised to give an expression for $C_{D\nabla}$ determined from input geometric parameters. This equation can then be passed to the presented design methodology, section 6.3.6.

When using the Schlichting skin friction estimation with the Rutherford body, trends similar to the parallel middle body have been found. For example, increasing the fineness ratio or bow length decreases $C_{D\nabla}$. These form hydrodynamic guidelines for AUV hull shapes. These trends might be altered if a more complex boundary layer model was applied.

Further work might be directed at the transition prediction method within Palisupan, so that the affect of the laminar boundary layer upon $C_{D\nabla}$ prediction can be found with greater confidence. This would then update the $C_{D\nabla}$ trend for each variant and the linear approximation equation for $C_{D\nabla}$. These tests would then be repeated at different velocities to explore each shape variant's boundary layer sensitivity to velocity.

6.3.4 Implications for a design methodology.

Within the design cycle, a very first estimate of $C_{D\nabla}$ might be found using an empirical formula or lookup table. Further iterations will call for another estimate to update the design. A more detailed estimation method of $C_{D\nabla}$ would be required, especially if the hull shape has only altered slightly. For example, an empirical formula might only consider operating velocity, and then only for a specific shape. There is no provision for variation of $C_{D\nabla}$ for changes in the hull shape. This would normally be solved by detailed modelling of the hull shape. The purpose of this research is to identify some of the hull shape trends so as to enable a second approximation of $C_{D\nabla}$ before committing to expensive modelling.

Working from these results some guidelines and possible applications within a design cycle can be generated. For the parallel middle body and the Rutherford body the effect on drag caused by altering profile parameters has been quantified to provide an equation for $C_{D\nabla}$. These equations can be included in the design cycle to give the engineer an estimate of $C_{D\nabla}$ quickly and reduce

the overall iteration time. Guidelines are to be considered for designing an AUV, together with an indication of the effect of changing the AUV shape.

The guidelines are as follows:

- The hull shape before the point of maximum diameter (normally the bow) has the most affect on C_{D_∇} prediction.
- Increasing AUV fineness ratio generally decreases drag but increases C_{D_∇} except for high valued fineness ratio laminar hull shapes where C_P is no longer able to suppress boundary layer instability.
- At very low speeds of less than 1 ms^{-1}, there is little difference between the drag force of the AUV hull shapes tested.
- For a body with a very short, or very stable, transition length, increasing velocity will increase drag force but decrease C_{D_∇} and make the shape more efficient at transporting a specific volume.
- The Parsons body and Rutherford body are most efficient for AUVs within a range of operating speeds that maintain a laminar boundary layer over the majority of the body.
- Moving the point of maximum diameter towards the stern, by either increasing bow length or increasing parallel middle body length will increase volume and decrease C_{D_∇}. This may cause boundary layer separation at the stern which has not been captured within this work.

A parameterised equation that gives a C_{D_∇} value based upon input design geometry parameters can be directly applied within a design methodology. Should a design have a specific hull shape at the start, then a parameterised equation can give an estimate of C_{D_∇}. Any changes to the shape to alter volume can also be evaluated to find a new estimate of C_{D_∇}.

In a design method where the hull shape is fitted around a known set of internal subsystems, then the parameterised equation can give an estimate of C_{D_∇} quickly. Normally the shape would have to be modelled, either computationally or physically, and its C_{D_∇} value determined. A parameterised equation will offer time savings and indicate what changes should be made to the internal components at an earlier stage of the design cycle.

As an example, fitting a hull shape about known internal components is shown in Figure 6.21. In this example, the length of bow of the Rutherford shape and increased radius would be hydrodynamically advantageous. However the increased volume may not be filled by buoyancy

and so represent wasted space. Alternatively the *CoB* required may require more available volume in the bow or stern than is enclosed by the hull shape.

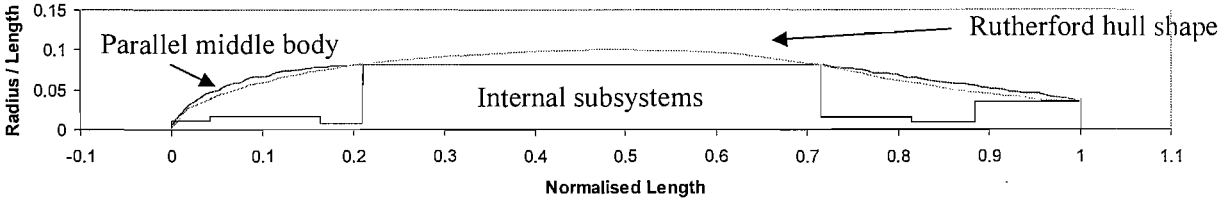

Figure 6.21 Fitting a hull shape about known components and finding hull shape parameters.

The geometric profile parameters were selected in order to be determined by the arrangement of internal components. The hull radius can be determined by the maximum radius of the internal component. For the parallel middle body the BMT position and MST position can be set such that the hull shape completely envelopes the internal components. The creation of the design cycle, including the derived guidelines and the parameterised equations is described in Chapter 7.

6.4 Conclusions.

Three different base hull shapes have been described and then altered to create a total 48 different models. The drag predictions for these models have been determined and discussed. The C_{D_∇} results have been analysed to identify trends for each hull shape variant. The causes of each observed trend have been explained in terms of each design parameter.

The laminar flow hull shape defined by Parsons and modelled in Palisupan has been successful in recreating Parsons' results. Results indicate that it does present a hull shape with greater volume yet reduced drag force coefficient compared to a parallel middle body hull shape and so would be an advantageous shape for an AUV.

An error has been found within boundary layer transition criteria utilised by Palisupan. This has meant that the drag prediction using Thwaites – Head for hull shapes reliant on maintaining a laminar boundary layer over a large proportion of length is likely to be incorrect. The Schlichting skin friction estimation method has been used and is expected to overestimate C_{D_∇} for the laminar flow hull shapes.

The parallel middle body shape representative of Autosub has been compared to the work found in literature. For a bare body with no control surfaces, the drag estimates have been found to be similar, although with a tendency to under predict overall drag.

The intention of this Chapter was to find a fast method of estimating the hydrodynamic drag of a large variety of shapes. The hull shapes are based on existing AUV shapes, which are then altered to produce families of shapes which might be considered by an AUV designer. An appreciation of the affect the hull shape has on the drag will aid the design method. Guidelines have been created for the design of different hull shapes along with two parameterised equations of C_{D_∇} based on Schlichting at a constant *Re*.

The application for the equations of C_{D_∇} will be to estimate drag force for hull shapes during design iteration. Such estimates would remove the need to completely model a shape after each alteration and present a time saving. The inclusion of these estimates into a design methodology has been introduced in this Chapter, and is discussed more fully in Chapter 7.

Chapter 7
Creating the design method.

This Chapter describes the proposed design methodology and the logic of its creation.

Chapter 2 discussed how design is specific to the application, and that manned submarines are constrained by the large pressure vessel which occupies most of the hull. Chapter 4 has successfully tested a pressure tolerant energy source enabling the pressure vessel to be removed or reduced in volume. Consequently AUV design options are increased as the hull shape is less constrained.

Chapter 3 provided two 'design logic' flow charts, based on a different start point. The selected start point often defines the first critical decision to be made and justified. The proposed structured method focuses the design on the mission requirements and what the AUV needs to achieve.

The mission objectives and a list of required subsystems are drawn from the mission description and form the design 'start point'. Subsystems that are not specified will be approximated and such decisions made can be influential to the AUV design.

The design method uses the specified subsystems to generate multiple AUV internal design options. These options are filtered for neutral buoyancy and hydrostatic stability. A hull shape is then fitted around these subsystems hence hull form is influenced by subsystem placement not an existing AUV design. The design method then utilises the parameterised equations of $C_{D_{\nabla}}$ described in Chapter 6 to predict drag force predictions. Overall AUV performance is then evaluated against mission objectives.

Chapter 8 tests the design method on two example AUV case studies to fulfil described missions.

7.1 The design cycle flow chart.

Figure 7.1 illustrates the proposed design methodology. In order to automate certain steps the method is more detailed and structured than the examples presented in Chapter 3.

There are feedback loops within each level and information can pass from one level to another. Level I gathers information into required subsystems. This information includes mass, dimensions, volume and power draw. Known subsystem characteristics will be drawn from the mission specification, i.e. AUV payload. The unspecified subsystems such as the energy source

and pressure vessel size are not defined in the mission specification. These have to be assigned based on experience or calculated to meet known requirements. In many cases as the design is refined so iteration will indicate final characteristics of initially unspecified subsystems. Key decisions are made when defining the unspecified subsystems and the consequences of differing key decisions made are illustrated in Chapter 8.

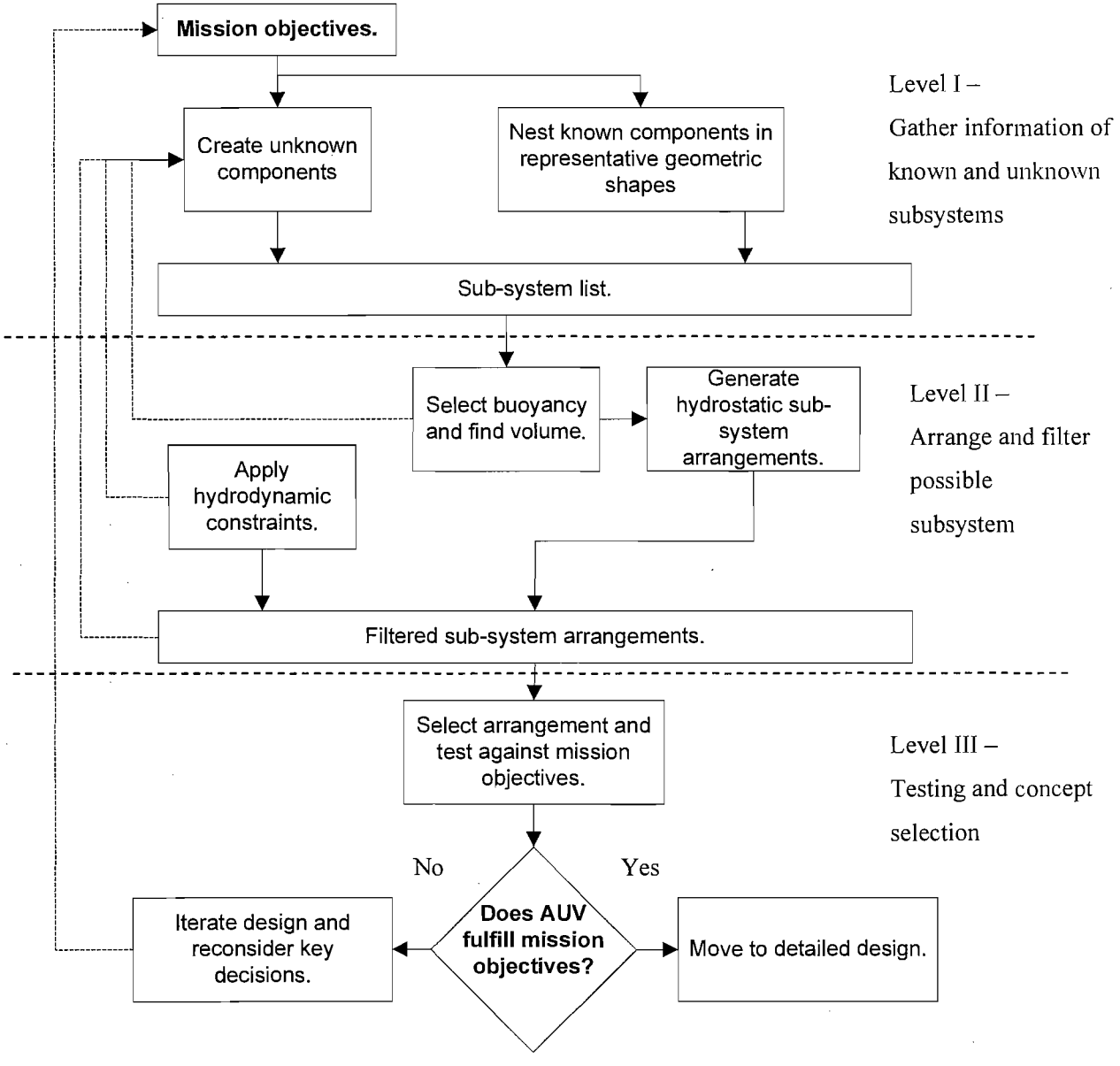

Figure 7.1 Design method with key decisions identified.

Level II arranges and filters defined subsystems to provide a list of possible arrangements that are neutrally buoyant, hydrostatically stable and faired by a hull shape. The first stage determines the amount of buoyancy required and those arrangements compliant with neutral buoyancy. The

first feedback loop occurs here. If the sum of subsystems is positively buoyant then the definition of unspecified subsystems in level I should be reconsidered or mass added.

The arrangements are made hydrostatically stable and filtered by finding the lengthwise position of added buoyancy. The parameters for the hull shape are quantified for the remaining arrangements and C_{D_∇} predicted. All subsystems must be enveloped by the hull shape. This is the second main feedback loop. From the estimated C_{D_∇} and volume the propulsion power is estimated and compared to energy capacity and required AUV endurance. Should the AUV carry insufficient energy, then the energy source needs to be reconsidered. The selection of AUV hull shape type, parallel middle body or laminar flow body, forms a key decision.

Level III selects a candidate design and checks that the concept AUV fulfils the mission requirements. If successful the AUV can be moved to detail design. If unsuccessful then the design is iterated.

Each level of this design method will be discussed and justified in sections 7.3 to 7.5. Section 7.2 discusses the overall objectives and constraints for the design methodology.

7.2 Design objectives and constraints.

Design objectives are properties the AUV should exhibit but are difficult to quantify. These objectives should be allowed to influence decisions made and selection of different options. A number of design options and the choices that might arise are considered.

A common first objective is to increase AUV endurance. If an AUV fulfils all its design criteria, and a decision has to be made between candidate designs, then the greatest endurance will be chosen.

A second objective is that the AUV will be as compact as possible. This is twofold, as minimising volume to reduce drag force and wasted space. Minimising volume will also minimise AUV mass (assuming neutral buoyancy) easing handling when out of the water. Wasted space is often free-flooding, and serves no purpose for the AUV operation.

A third objective is that the AUV should be capable of operating at deep depths. This would increase the capability and safety factor of depth measurement. This objective will likely conflict with the second objective and so may be given less priority.

Other objectives that might be included could be economic viability in terms of capital and operational costs, practical manufacture and repair, and compatibility with existing systems. These are valid, but are not currently considered in the design methodology. These objectives lead to the creation of design constraints.

Constraints are defined rules of requirements the design method must fulfil. These structure the first design attempt and aid automation. After the first iteration, or during feed back loops, these constraints might be broken by the design engineer to manually move towards an improved design.

The first constraint is that the AUV is neutrally buoyant. This is common to most existing AUVs described in Chapter 2. Neutral buoyancy aids control and manoeuvring, as the vehicle does not require power to maintain its depth. A positively buoyant AUV is to be reconsidered and its mass increased, but preferably not by increasing dead weight. Dead weight is mass added that does not have any 'real' purpose, e.g. lead weights. Dead weight is often unavoidable in practise, but should not be used during conceptual design. Negative buoyancy is resolved with the addition of foam or increases in buoyant pressure vessel size.

The second constraint is the AUV should be hydrostatically stable in the water and be able to maintain level travel without use of control surfaces. This means that the moments of all the subsystems need to be balanced.

For a rotationally symmetric shape, each subsystem will initially be assumed to lie on a central axis. This arrangement will be viewed as a 2D longitudinal slice. The length of the AUV will be the combined length of all the subsystems sequentially arranged without gaps. The radius of the vehicle will be the radius of the largest subsystem.

The five constraints of the design process are thus:

- The AUV must be neutrally buoyant.
- The AUV must be hydrostatically stable.
- All subsystems are arranged on the central axis.
- Total length = Sum of lengths of the subsystems.
- Maximum radius = Radius of largest subsystem.

Each level of the proposed design method is now described.

7.3 Level I of method.

The volume and mass of the energy source can be found by either a direct estimation of mass or by estimating required energy capacity.

Estimation of the required energy source capacity is a function of the energy density of the energy supply, the required range, speed of AUV operation and the power demands of the

payload. The design method can either ignore the energy source or make an initial estimate of propulsion power. By ignoring the energy source, it is possible to generate a minimum volume AUV that is then refined to include an energy source from the power demands of the previous iteration. Such an approach will require at least two iterations before finding a concept AUV. The energy source is considered an unknown in the method of Figure 7.1 and energy source capacity is initially estimated.

An initial estimate of propulsion power might be generated by selecting a hull shape volume and estimating C_{D_∇} using an empirical approach or by defining a motor with a known power requirement. The accuracy of these estimates will influence the number of iterations required to produce a concept AUV.

An alternative approach would consider the mass of the AUV, especially as some missions might constrain AUV mass. A maximum AUV mass will create an upper limit for the energy source mass. Without an AUV mass limit the energy source mass can be found if the mass of all other subsystems known. The AUV *Mass Ratio* (from Chapter 2) can guide the proportion of energy source mass by estimating total AUV mass. This is derived from the sum of component masses, shown in equation 7.1.

$$\begin{aligned} M_{AUV} &= M_{Structure} + M_{Payload} + M_{Hotel} + M_{\mathrm{Prop}} + M_{PV} + M_E + M_B \\ &= M_{SS} + M_E + M_B \end{aligned} \tag{7.1}$$

M_{SS} is shorthand notation for the mass of all subsystems apart from M_E and M_B which are unknown. To determine M_{AUV} it is necessary to eliminate M_E and M_B explicitly from equation 7.1. The 'buoyancy mass' (buoyancy force / gravity) is defined by equation 7.2.

$$\begin{aligned} B &= \nabla_B \rho_B - \nabla_B \rho_W \\ &= -\nabla_B (\rho_W - \rho_B) \end{aligned} \tag{7.2}$$

This quantity can also be expressed as equation 7.3.

$$B = (\nabla_{SS} + \nabla_E)\rho_W - (M_{SS} + M_E) \tag{7.3}$$

From $M_B = \nabla_B \rho_B$ then M_B can be found by rearranging equation 7.2 for B and substituting this into equation 7.3 to give equation 7.4.

$$M_B = \frac{-\rho_B}{(\rho_W - \rho_B)}\left((\nabla_{SS} + \nabla_E)\rho_W - (M_{SS} + M_E)\right) \tag{7.4}$$

So it follows that M_{AUV} can be expressed as equation 7.5.

$$M_{AUV} = M_{SS} + M_E - \frac{\rho_B}{(\rho_W - \rho_B)}\left((\nabla_{SS} + \nabla_E)\rho_W - (M_{SS} + M_E)\right) \tag{7.5}$$

Noting that $M_E = \rho_E \nabla_E$ and M_E = *Mass Ratio* x M_{AUV} (from definition in Chapter 2) rearrangement of equation 7.5 leads to equation 7.6.

$$M_{AUV}\left(1 - Mass\ Ratio - \frac{\rho_B Mass\ Ratio}{\rho_W - \rho_B} + \frac{\rho_W \rho_B Mass\ Ratio}{\rho_E(\rho_W - \rho_B)}\right) = M_{SS} + \frac{\rho_B M_{SS}}{(\rho_W - \rho_B)} - \frac{\rho_W \rho_B \nabla_{SS}}{(\rho_W - \rho_B)} \tag{7.6}$$

Since *Mass Ratio* is a quantity that can specified, equation 7.6 permits estimation of M_{AUV} without explicitly knowing M_B or M_E at the initial stages of the design.

This will give a value of the AUV total mass, including buoyancy and energy source. M_E can be estimated, thereafter the energy source mass multiplied by the chosen battery energy density gives an estimate of total energy capacity.

A pressure sensitive energy source could also be found provided the mass of the pressure vessel is included in M_E. In this case the actual energy source mass becomes dependant on the operational depth of the AUV.

The dimensions of the energy source have not been set, and this becomes another key decision. To estimate the physical dimensions of the energy source, the size of the largest subsystem might be compared to the size of a single battery of the chosen energy source chemistry.

If the batteries are many times smaller than the largest subsystem, a large battery pack is created and added to the subsystem list. If the batteries are of a similar scale to the largest payload, then each energy battery can be considered as an individual subsystem. It might be possible to pack the batteries around other subsystems at a later stage, although this would be very difficult to model, build and physically maintain. The presented design methodology assumes that the batteries define a single battery pack subsystem.

Dimensioning the length and radius of the energy source will be discussed further in Chapter 8 when examining different design scenarios. This decision remains unanswered initially but is solved by iterating the design and comparing the fitted hull shape.

7.4 Level II of method.

Once the list of subsystems has been completed Level II finds the volume of buoyancy to make the AUV neutrally buoyant. The subsystems are arranged to form a hydrostatically stable AUV internal structure. The hull shape is fitted around the subsystem arrangement.

A first stage is to estimate the volume of foam required to make the AUV neutrally buoyant. With knowledge of AUV subsystems, ρ_B and ρ_W, then the volume of foam, ∇_B, required for neutral buoyancy can be found from equation 7.4. A positively buoyant AUV is considered as inefficient, as it can potentially carry more mass than its current load. A negatively buoyant AUV can be made neutrally buoyant with the addition of foam or buoyant pressure vessel.

The volume of foam is required for the hydrostatic balancing of the AUV. The hydrostatic balancing of the subsystem arrangements is the next stage in the design process.

The overriding constraint for the AUV hydrostatic balance is that the longitudinal position of *CoG* is the same as that of *CoB*. *CoG* must be below *CoB* in the same vertical plane for roll stability. The *CoG* and *CoB* can be found using moments of mass and cross-sectional area. Moving subsystems to adjust the *CoG* also affects the *CoB* location. A solution commonly used in ship design (Rawson and Tupper 2001 pp. 121 - 123) is to pick an arbitrary co-ordinate around which the subsystems are manually balanced. This approach is valid for ship design as there is usually a candidate hull form of known displacement and *CoB*, with small changes in the latter when the design is altered. The complication for an AUV is that there is no predefined hull and no prior *CoB* location, so the process has to be iterative.

Equations 7.7 and 7.8 indicate how the longitudinal position (x) of *CoB* and *CoG* are determined (Rawson and Tupper 1994 pp. 15 - 18)

$$CoB = \frac{Moment_x}{Volume_{AUV}} = \frac{\int_0^{Length} A_{Slice}\, x dx}{\int_0^{Length} A_{Slice}\, dx} \qquad 7.7$$

$$CoG = \frac{Mass_x}{Mass_{AUV}} = \frac{\int_0^{Length} x dM_x}{M_{AUV}} \qquad 7.8$$

A_{Slice} is the area of a cross-sectional slice (yz plane), and dM_x is the elemental mass at a point x. The moments are calculated about the origin, $x = 0$, and the first subsystem is placed at the origin. For the other axes, x needs to be replaced with y or z, and the limits suitably altered. In the design constraints all subsystem masses are initially assumed to lie on the longitudinal axis.

When the foam buoyancy is added to the subsystem arrangement, its placement is determined by the required moments to balance the whole subsystem arrangement (Figure 7.2). The foam has no set shape, so can be moulded around existing components. The arrangement will be discounted if the foam lever arm (L_{Foam}) is less than zero or greater than the AUV arrangement length, L_{AUV}. Figure 7.2 shows L_{Foam} greater than L_{AUV} so the arrangement would be discarded.

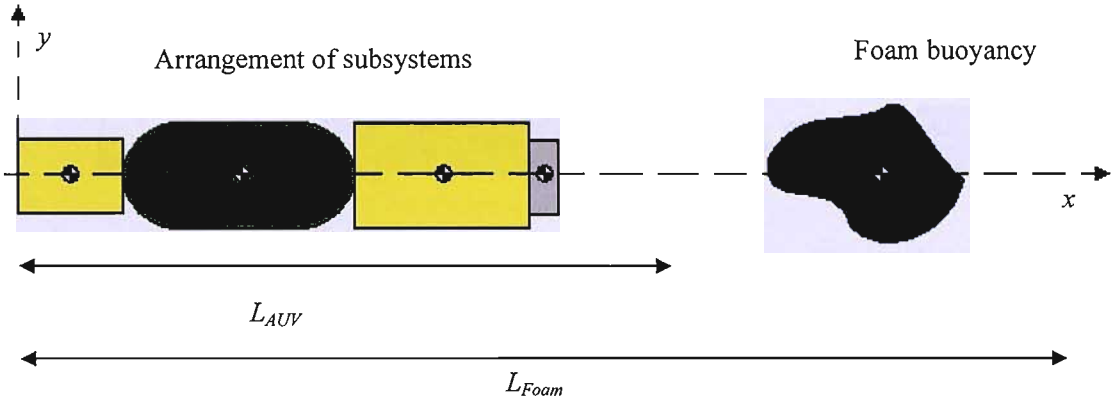

Figure 7.2 Illustrating the addition of foam to a subsystem arrangement.

Having identified the foam position, the subsystem arrangement is now neutrally buoyant and hydrostatically balanced. The next challenge is to define the hull shape such that it encloses the subsystems and defines the shape of the foam. This hull envelope should follow similar lines as the internal subsystems and so enclose as little water as possible. In this methodology the position of the subsystems will determine the hull shape.

In Chapter 6 the assessed hull shapes were defined using dimensions of appropriate geometric parameters. These parameters are identified from the subsystem arrangement to create a hull shape. For example, for the parallel middle body hull shape, the geometric parameters were length, radius, BMT length and MST length. The arrangement of the subsystems and their dimensions lead to a hull shape as illustrated in Figure 7.3. The hull shape fairing will have a physical thickness depending on the construction material, but is represented by a single line in this method.

The subsystem with the largest radius is selected as the largest subsystem. This defines the hull shape maximum radius. The length of the subsystem arrangement defines the length of the hull. For the parallel middle body hull shape, the BMT can be defined by the forward interface of the largest subsystem and the MST defined by the rear interface. Fitting linear lines between these transition points and the outermost edge of the subsystem at the bow and stern will give a first estimate of available volume and identify any subsystems not enclosed by these lines. The parallel middle body stern is linear and so already defined. The bow curvature requires balancing

of the amount of volume available at the bow for buoyancy and the radius of any subsystems within, against the hydrodynamic drag a bluff bow will produce.

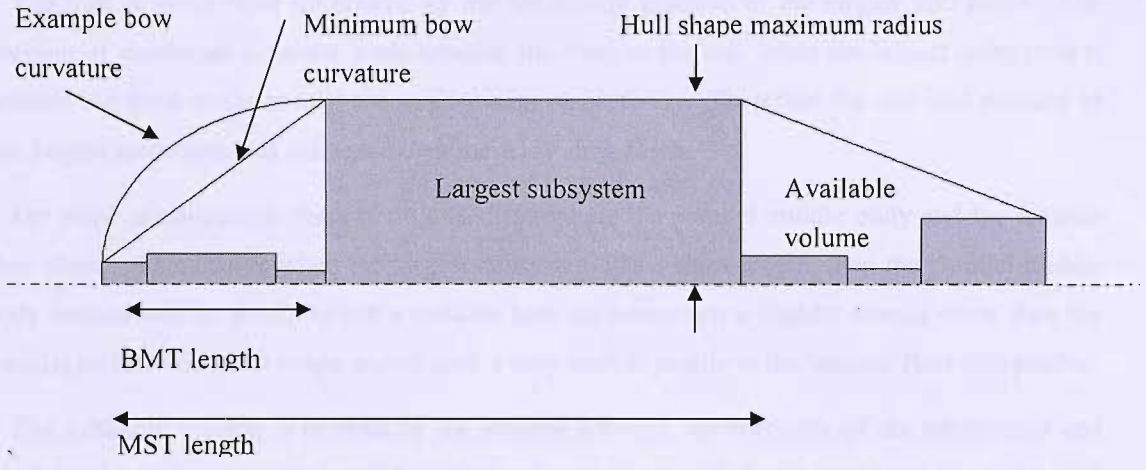

Figure 7.3 Example parallel middle body hull shape defined by subsystems.

A laminar flow shape is defined by its maximum diameter and position of maximum diameter (Figure 7.4). These are not as strictly defined by the subsystem arrangement as for the parallel middle body hull shape.

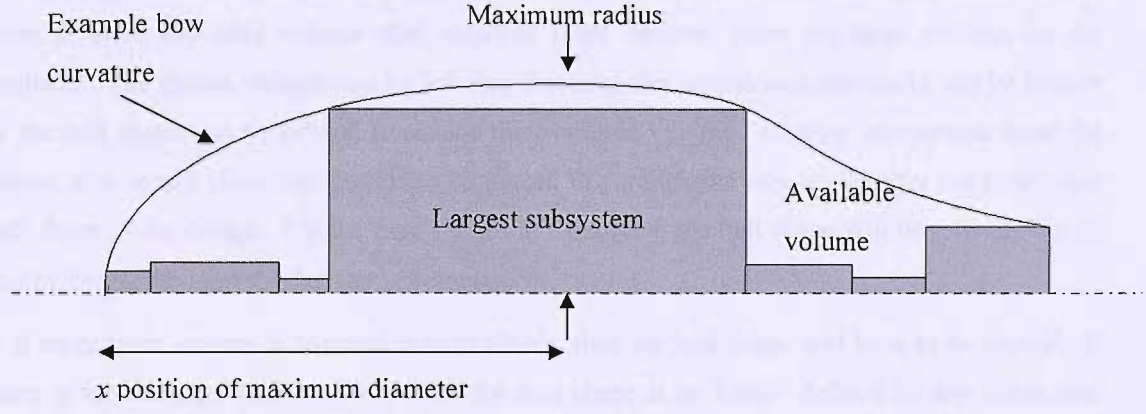

Figure 7.4 Example laminar flow hull shape defined by subsystems.

Similar to the parallel middle body, the length of the subsystem arrangement defines the length of the laminar hull shape. The largest subsystem still defines the maximum radius of the hull, but not as directly as for the parallel middle body. The forward and rear interfaces of the largest subsystem must be enveloped by the laminar hull shape, so the maximum radius will be greater than the radius of the largest subsystem. The position of the maximum radius can occur over the length of the largest subsystem. This gives an area in which the hull defining parameters may

occur and is solved by the engineer. The exact position of maximum radius balances these positional constraints.

The hull shape is most influenced by the lengthwise position of the largest subsystem. The position of maximum diameter tends towards the front or the rear when the largest subsystem is towards the front or the rear of the arrangement respectively. Therefore the size and position of this largest subsystem has influence over the AUV drag force.

For some arrangements there is little to differentiate the parallel middle body and the laminar flow shape. This occurs when the largest subsystem has a short length, then the parallel middle body section will be short. Given a suitable bow curvature and a slightly altered stern, then the parallel middle body hull shape would have a very similar profile to the laminar flow hull profile.

The available volume is defined by the volume between the boundary of the subsystems and the desired hull shape. If the available volume is completely filled with buoyancy foam, the *CoB* of this buoyancy foam can be compared to the *CoB* lever arm required to hydrostatically balance the shape. In Figure 7.3 and Figure 7.4 the available volume falls to either side of the largest subsystem. The foam can be formed into a ring, surrounding the subsystems, and cut into sections to allow physical access.

The foam volume within each void will be determined by the neutral buoyancy condition. If there is more available volume than required foam volume, there are three options for the engineer. The excess volume can be left free flooding, the central axis constraint can be broken or the hull shape can be refined to reduce the available volume. Moving subsystems from the central axis would allow subsystems to be placed in parallel, but this would alter the length and hull shape of the design. For the case studies in Chapter 8, the hull shape will be refined first by reconsidering the largest subsystem geometry.

If more foam volume is required than available, then the hull shape will have to be altered. If there is such a large excess of foam that the hull shape is no longer defined by any subsystem then there will be no obvious geometric constraint on the hull shape. The hull shape becomes a more critical decision for the engineer. The hull shape should be selected arbitrarily, the arrangement reconsidered, or the arrangement constraints relaxed.

A comparison of foam volume and available volume will filter out impractical subsystem arrangements. The hull shape can be refined slightly to give a concept design or the design steps repeated iteratively to refine the design.

Once the hull shape has been defined, the hydrodynamic properties are evaluated and the propulsion power found using the parameterised equations for C_{D_∇} from Chapter 6. This can then be compared to any initial P_{Prop} estimates. Those hull shapes that require a higher propulsion power than provided by the energy source can be eliminated from the design options.

If the propulsion power was not estimated in Level I, then the endurance of the vehicle will need to be found and all shapes carried over to Level III.

7.5 Level III of method.

Level III selects a candidate AUV for iteration. The candidate AUVs have been sized, all subsystems defined and hull shapes fitted. These AUVs must be checked to examine if all of the mission specifications and objectives are satisfied. Those that cannot fulfil the specifications are removed from consideration. Should more than one candidate fulfil all specifications, then the objectives of minimum volume and mass, maximum diving depth and endurance are considered. This selection requires decisions by the engineer. At this stage other design aspects such as economic cost and physical maintenance not covered by this design process should be investigated.

The key decisions that might be reconsidered are the size and dimensions of the energy source, the hull shape selection, and the selection of the concept AUV. Which of these is selected is dependant on the required design alteration. The first choice made in the design method can have the most affect on the outcome, but require greater iteration. In this methodology the subsystem that defines the radius is often the most crucial. The radius and position of this largest subsystem has a great affect on the shape of the hull and the volume available for packing. If major changes of the concept design are required, it is suggested that the largest subsystem be considered for the next iteration.

This design methodology including hydrostatic balancing and hydrodynamic hull shape fitting can be automated. This is discussed in the next section.

7.6 Automating the design method.

Level II of the design methodology described was automated using a Matlab code (Mathworks 1994). The code is given in Appendix E. The code requires a complete subsystem list with associated volume, mass and dimensions (as shown in Chapter 8). The code outputs a list of possible subsystem arrangements and the lever arm of the buoyancy foam. Table 7.1 shows the developed logic of the Matlab code. This code creates a finite list of possible subsystem arrangements.

The Matlab code input requires a list of all subsystems. They are nested within representative geometric shapes to constrain the external dimensions. The subsystem mass and displaced volume are consistent with the physical system, not the 'nested shape'. The engineer specifies any constraints on subsystem placement or orientation at this point. The method will not rotate subsystems to interchange their length and radius, though subsystems can be flagged in order to fix a position in their ordering. For example, the motor might be the last subsystem at the stern and will only be placed with its driving axis long the AUV centreline.

Table 7.1 List of logic process of automated section of design method.

Input.	List of subsystems and their positional constraints.
Code logic	Create finite list of possible subsystem arrangements. Find length, maximum radius and longitudinal position of maximum radius. Find required foam volume Calculate *CoB* and *CoG* of each arrangement. Find the foam lever arm to make arrangement balanced. Filter arrangement list for lever arm < 0 m and lever arm > AUV Length. Fit parallel middle body hull shape and compare available volume (only done for case study B)
Outputs	Complete list of subsystem arrangements.

There will be a factorial number of unique combinations of subsystems. The advantage of automating the system is that all arrangements can be checked and filtered to provide a more manageable number. For example, in Figures 7.3 or 7.4 there are 7 subsystems, and there are theoretically 5040 (7!) ways to arrange them. If the motor is then fixed as the final subsystem, there would be only 720 (6!) arrangements.

The output will give a list of arrangements and the required volume and position of foam buoyancy. An arrangement with a foam lever arm greater than the arrangement length, or less than zero, is flagged to be filtered out. The remaining arrangements have a foam lever arm in the range of zero to length of arrangement.

Hull shapes have to be fitted and the available volume checked against the required foam volume. This process is discussed in Chapter 8 when the design method is applied to example case studies.

At the end of this process there will be one or more possible arrangements of subsystems that, when faired within a suggested hull shape, will fulfil the mission specifications. If the methodology does not produce any possible subsystem arrangements then either the mission specifications or the design constraints need relaxing and the design iterated. The human mind is remarkably apt at arranging irregular shapes, and so it is likely that a result from the automated system can be improved manually (Dowsland and Dowsland 1995).

It is very important to understand what the design method is capable of and its limitations.

7.7 Capabilities and limitations of the design method.

By considering the 2D profile, the design methodology is intended for rotationally symmetric AUVs. It is most easily applied to AUVs with a single propeller at the stern, but with consideration of the hydrostatic balance in 3D, propellers could be mounted elsewhere.

By including every arrangement the design may move away from more traditional arrangements. Creating the AUV in a structured method, where each decision is highlighted and understood, will give confidence in a new arrangement.

The hull shape is defined by the subsystems within the AUV. This removes the initial hull shape selection, as this can be very easily influenced by previous AUVs. If a hull shape is defined early on, the task would be to fit the subsystems within the hull shape. This might force an energy source size, and only at the end of iteration would the mission specifications be verified. The presented design method will encourage innovation in the hull shape by removing the need to select an initial hull shape.

The hydrodynamic equations that predict C_{D_∇} are geometry driven, and show how the different arrangements of the hull shape can affect the propulsion power. This pre-empts the modelling of the concept hull shape once all the other decisions have been made and influences the design methodology earlier in the process. This is clearly dependant on the relevance and accuracy of the C_{D_∇} equation.

One intention for a structured design methodology is to improve design time. A structured design will give purpose and direction to the method and so reduce the time from stage to stage. The key decisions take the most time, for example the creation of the energy source shape. Accurate initial estimates of energy source size and dimensions will reduce the number of iterations required to identify a practical workable candidate design.

The automated section will explore every possible arrangement of the input subsystems and find the required foam volume and the lever arm required for hydrostatic balance. This then

produces a list of arrangements that can be hydrostatically balanced by buoyancy placement within the length of the AUV. Increasing the number of subsystems will increase the computational time, but this is the least time consuming part of the process and the code is not optimised for speed.

The automated method currently does not yet aid in creating the hull shape. It will fit a parallel middle body hull shape, but the laminar hull shape requires human interaction.

7.8 Conclusions.

This Chapter has discussed the creation of an AUV design methodology. Previous work has suggested that a pressure tolerant energy source will allow the size of pressure vessel to be reduced and for more AUV shapes and arrangements to be made available. Hydrodynamic work has presented a method to estimate the drag forces from hull shape profile geometry.

The design method generates all the required subsystems and then considers all possible arrangements. As the pressure vessel should no longer dominate the hull shape, a novel arrangement might be found by a thorough search. This is different to a design method that establishes a single large subsystem (for example the pressure vessel) and scales the design off this, or selects a hull shape and attempts to fit all subsystems within.

The approach for the placement of internal subsystems to control the hull shape profile is discussed. The buoyancy foam is packed within the hull shape to give a high packing efficiency and reduced wasted space. The parameterised equations of $C_{D\nabla}$ from Chapter 6 are then applied to estimate AUV drag. This moves the hydrodynamic analysis forward in the concept design, and allows design iteration to continue without extensive modelling of each candidate AUV hull shape at each iteration.

Key decisions of energy source capacity and dimensions are required by the design engineer. These decisions might be considered in further work to increase understanding of their consequences and generate more guidelines.

This Thesis presents this design methodology as a structured approach for AUV design and an aid for innovation.

The next Chapter takes this design methodology and applies it to two example AUV missions as design case studies. The key decisions made and their implications will be discussed. This provides an opportunity to observe the capabilities and limitations of the design method.

Chapter 8
Case studies.

This Chapter applies the design methodology created in Chapter 7 to two case studies. The missions were selected to test different aspects of the design methodology, speed, range and diving depth. These applications will illustrate the process and highlight the key decisions made. The AUVs are to be designed for a single mission with specified objectives and payload. The design methodology does not copy an existing design; it will start from a 'blank sheet'.

The missions are first described and the design specifications are extracted. The size, power and constraints of the navigational and payload instruments are discussed and grouped into specific packages. The design methodology is then applied to each of these missions to give a concept design.

8.1 Mission descriptions.

Prior to applying any design method, the design objectives must be specified. Presented here are descriptions of possible AUV missions which test the AUV parameters of speed, range and depth. Quantative design boundaries for AUV design will be extracted from these mission descriptions. These constraints exercised the design cycle, highlighted any breakdowns in the logic, and revealed parameters and constraints that had not anticipated. As the design methodology is applied the stages will be explained in terms of the influence from the particular mission being considered.

8.1.1 Mission concept A.

8.1.1.1 Synopsis.

Sprint AUV- capable of getting to a work area quickly. For example; in response to an oceanographic or geological event and then conducting a low speed survey, before returning to a base point.

8.1.1.2 Reasoning behind AUV specification.

This mission would be best used in conjunction with another large scale ocean survey system. For example, a satellite might find an ocean thermal spike and, after post processing, decide that closer investigation is worthwhile. This event would activate the closest AUV that could reach the work location in a suitable time.

The different operating velocities (sprint and survey) will test the design methodology to find a concept AUV that can fulfil the mission objectives. A hull shape should be found that is efficient at the different operating velocities. The sprint velocity imposes high power requirements on the energy source power supply, which could increase energy source size.

The travel time to survey area will have to be shorter than possible by a surface vessel and at less economic cost. A response from a vessel of opportunity might take 6 days (www19) by which time monitoring the important part of the event may be missed (a series of earthquakes in the cited reference). The AUV would also have to carry enough instruments to make it preferable to sending a light surface ship to the work area.

Response time is paramount whereas the retrieval can be accomplished without the same urgency. The AUV can return slowly or be picked up by a surface vessel. A surface vessel pickup may not be the most economical option, but may save on the energy storage requirement of the AUV. This mission will assume that energy is required for the return journey.

An operational depth of 200 m would be sufficient to measure phenomena in the top surface layer of water following a sprint distance of 100 km. The AUV will travel 5 km at the survey site (an area of approximately 0.25 km^2). To put this into perspective, 100 km is half the width of the Alboran Sea (www20) so two AUVs would be able to monitor the whole of the Alboran Sea. The AUV will be required to run at 21.6 km h^{-1} (6 ms^{-1}) giving a response time of 4 hours 38 minutes, excluding initial set up time.

The essential characteristics of the AUV are summarized in Table 8.1.

Table 8.1 Mission A mission requirements.

Mission Parameter		Detail
Location	i) Area of the world	Dependant on launch system
	ii) Seafloor / water column	Surface
	iii) Required operating depth	200 m
Mission type	i) Category	Fast response survey
	ii) Description	Science platform
Mission time		Faster than current response systems.

8.1.1.3 Design constraints.

The design constraints required to fulfil mission A are drawn from Table 8.1.

- Sufficient endurance to get to work site and conduct survey.
- The AUV sprint speed will be 6 ms^{-1} and the slower survey speed will be 1 ms^{-1}.
- Energy source must be capable of maintaining high and low power draw.
- Navigational capability to find survey area and provide adequate accuracy during the survey.
- Depth is a tertiary concern, so 200 m will suffice. Collapse pressure will be 700 m (required depth plus arbitrary safety margin of 500 m)
- Scientific payload may vary on the mission being conducted, but select example payload of scientific sensors for case study.

Table 8.2, summarizes requirements of the AUV design.

Table 8.2 Mission A design boundary.

Design Constraint		Value
Depth	i) Operating depth	200 m
	ii) Collapse depth	700 m
Range		100 km @ sprint speed. 5 km @ survey speed. 100 km @ survey speed
Speed	i) Sprint speed	6 ms^{-1}
	ii) Survey speed	1 ms^{-1}
Payload	i) Required load	CTD. Wetlabs fluorimeter, Seabird transmissometer, Seabird oxygen sensor,
	ii) Maximum payload mass	60 kg
	iii) Maximum payload power	10 W

The second mission and its requirements are investigated next.

8.1.2 Mission concept B.

8.1.2.1 Synopsis.

An AUV capable of deep sea bed exploration at a lower mass and greater endurance than the American "SAMS" AUV (MacNaughten, *et al.* 2005).

8.1.2.2 Reasoning.

The US Navy use the Subsurface Autonomous Mapping System (SAMS) developed and built by WHOI (MacNaughten, *et al.* 2005). SAMS is full ocean depth capable and conducts side scan bottom mapping and physical oceanographic data collection. The AUV is powered by 8 kWh of pressure sensitive lithium ion batteries, giving 12 hours endurance at a cruise speed of 2 ms^{-1}. Operating at 6000 m depth, SAMS is able to reach 97 % of the worlds ocean sea beds.

To compete with SAMS, the concept AUV created in this case study will have to be capable of at least the same depth, and be able to achieve either a larger survey area or a faster survey time, whilst carrying a similar payload. The science payload systems carried on SAMS are: pressure sensor, CTD, acoustic Doppler current profiler (ADCP), optical backscatter and side scan sonar. The same sensors will be carried on the concept AUV.

The principal required AUV characteristics are summarized in Table 8.3.

Table 8.3 Mission B requirements.

Mission Parameter		Detail
Location	i) Area of the world	Mid ocean
	ii) Seafloor / water column	Rough floor, sea currents
	iii) Required operating depth	6000m
Mission type	i) Category	Exploration
	ii) Description	Electronic imaging to find areas of interest
Mission time		Maximum endurance and maximum range

Chapter 3 demonstrated that a slow AUV would have a longer range than a comparable AUV at higher velocity. At depth the ocean currents are generally less than the currents at the surface and since the AUV will spend most of its mission time at 6000 m, it is assumed strong currents

are rarely encountered. The AUV will have to manoeuvre at the surface (launch and recovery) so must be capable of speeds greater than surface currents. The required maximum velocity will be 2.5 ms^{-1}, to account for currents up to 0.5 ms^{-1}. The range might benefit from operating at a lower velocity. This will be investigated during the design iteration.

This example is an opportunity to use the insight gained regarding the pressure tolerant lithium polymer batteries tested in Chapter 4. The purpose is to remove the energy source from the pressure vessel. Consequently the pressure vessel volume may be reduced since not all the components are pressure tolerant. The mass saved by a smaller pressure vessel will allow the AUV to dedicate a greater proportion of the total mass to the energy source or payload.

8.1.2.3 Design constraints.

The design constraints consistent with the mission description are:

- Depth rating of 6000 m, collapse depth of 6500 m (operating depth +500 m).
- Navigational ability to follow sea bed
- Imaging of sea bed area.
- Cruising velocity of 2.0 ms^{-1}.
- Operate within adverse currents of 0.5 ms^{-1}.
- Endurance of 36 hours, three times that of SAMS.
- Mass less than 1000 kg, comparable to SAMS.

The payload is specified in Table 8.4 and covered in more detail in section 8.2.

8.1.3 Other mission scenarios.

Missions A and B provide distinct technical challenges with different design drivers. These challenges are not exclusive to the needs of future vehicles. Here some additional non-quantified missions are presented to highlight future technical goals and the need for a developing design methodology.

Mammal monitoring. An AUV capable of tracking and monitoring marine mammals without causing the mammal undue stress. This is not currently possible. Tags can be fitted to dolphins and whales, though there are animal stress issues regarding animal capture and the large energy source required for long endurance. Combine this with optical cameras, depth measurements and other sensors, and then the tag becomes very weighty. To require the AUV to be as

manoeuvrable as a dolphin and dive to the same depths as the great whales would provide a significant design challenge.

Table 8.4 Mission B design boundary.

Design Constraint		Value
Depth	i) Operating depth	6000 m
	ii) Collapse depth	6500 m
Endurance	i) Mission time	32 hours
Size	i) Mass	1000 kg
Speed	i) Cruise speed	2.0 ms^{-1},
	ii) Maximum speed	2.5 ms^{-1} (Cruise speed + 0.5 ms^{-1})
Payload	i) Specific sensors	Side scan sonar, Pressure sensor, CTD, ADCP, Optical back scatter.
	ii) Maximum payload mass	30 kg
	iii) Maximum payload power	35 W

AUV – ROV interaction operation. An AUV capable of carrying a payload from a surface vessel to a submerged ROV. This AUV would allow the ROV to continue work whilst tools and materials are carried to and from the worksite. To enable real time saving the AUV would have to conduct a return journey in less time than the ROV can be deployed, unloaded and recovered. The largest challenge is not the distance, nor the operating depth, rather the nature of a removable and variable payload. Changing the payload during each journey will change the hydrostatic balance and neutral buoyancy of the AUV. This mission seed might be best suited for an AUV capable of travel in multiple directions, or no preferred travel direction, in order to remove the need to turn around at surface and sea bed. Such an AUV is outside the capabilities of the presented design method for axis-symmetric AUVs.

Stealth AUV. A stealth AUV would require investigation and reduction of AUV sonar signature, generated magnetic fields or radiated heat. The AUV shape might have to be similar to a flat fish, where by the AUV could immerse itself in bottom sediment. This is beginning to depart from the energy and hydrodynamic aspects of this Engineering Doctorate, and introduces military requirements not covered in this thesis.

8.2 Navigation and payload packages.

8.2.1 Introduction.

Initial design estimates might approximate the power draw, volume and mass for the payload, but would not consider payload position within a hull shape. The proposed design method refines such initial estimates to include real subsystems. To create an inclusive concept design some knowledge of the subsystems beyond energy and hull envelope is required. Estimates have to be made of the mass and power requirements of navigation and payload sensors, which are then arranged into example packages to be considered when testing the design method.

In the early stages of this research, equipment was not specialised for AUV use. Consequently sensors drew more power and weighed more than an ideal sensor for an AUV. The equipment was designed for surface ships and tethered systems without the same power and mass restrictions. This situation has been changing over the course of this research with specialist orders and advancement of AUV technology. For example; Reson Offshore Ltd. have created a multi-beam sonar that is 21" in diameter, specifically to match 21" diameter AUVs (www21). For the purposes of these concept designs, the payload and navigation will be based upon Autosub payloads. It would be possible to select a preferred mass, volume and power draw and assume that equipment could be developed to fit. This approach has been rejected as it would make the research too abstract and less immediately applicable.

Some subsystems that form the base hotel of computer processors, power management systems and hard drives are required in all AUVs (the base hotel subsystems). Other subsystems are optional depending on the information to be gathered during the mission. The subsystems have been classified as either 'navigation' or 'scientific payload' and are listed in the following sections. This is an arbitrary split as some subsystems fulfil dual roles of navigation and science data collection. The next section discusses the required base hotel and navigational payload.

8.2.2 Required equipment.

The AUV needs computational ability to run control logic and navigational processes. This will also store digital data from sensors for post mission processing. Computational equipment will have to be stored at atmospheric pressure somewhere on the AUV within a small pressure vessel.

The mission requirements will dictate what navigation is required. There may not be much flexibility available in navigational subsystem requirements, so the energy source and layout must accommodate these necessary subsystems.

The AUV will need a navigation system to find AUV position relative to other objects and AUV position within the water column. At best this will avoid collisions and plan routes around obstacles. This will be considered to be a complex hotel package.

The Spray glider has a GPS system that provides a position when near the water surface. This data is used to then correct the AUV route. When submerged the glider detects its heading and attitude to steer the AUV towards the next waypoint (www22). This will be considered as a basic level of navigation, as it provides a low amount of data to the AUV.

The packages presented would have to be scaled to fit different size AUVs. The method of scaling may well change for each item of equipment. For example, the processor and hard disc would be the same size for AUVs large enough to support standard computer parts, with economics being the driving factor on the power of the processor. The scaling of each subsystem will be discussed on a case-by-case basis as required.

Table 8.5 lists the base hotel equipment that occurs on every AUV. The GPS system might be removed, but it is likely that a global position is required by all AUVs. The mass and power requirements of these subsystems are modelled on those deployed within Autosub and do not represent optimal subsystems (McPhail 2006b, Stevenson 2005). These subsystems form the base hotel for the case studies addressed in sections 8.3 and 8.4. For convenience a base hotel total mass, volume and power is given in Table 8.5.

Table 8.5 Base hotel subsystems mass, volume, power and constraints.

Base hotel subsystem	Mass kg	Volume m^3	Power W	Pressure tolerant? Y/N
Power node electronics	5.9	0.0156	2	N
Power chassis	10.0	0.0196	3	N
Motor controller chassis	10.0	0.0196	4	N
Mission module	4.5	0.0196	2	N
GPS.	7.3	0.0196	35	N
Totals				
Base hotel subsystem	37.7	0.0940	46	N

The pressure sensitive subsystems require 0.1 MPa and are placed within a pressure vessel. Some of the subsystems include the mass of an aluminium pressure vessel endcap. In Autosub this endcap forms the end of a pressure vessel, creating a water-tight electrical connection to the outside of the pressure vessel. This mass is included here as it is assumed that the subsystems will also need electrical connection outside of the pressure vessel and so a similar method (and associated mass) will be necessary.

Table 8.6 provides a summary of the navigational sensors found within Autosub. These are necessary for its navigation and collision avoidance performance. Concept vehicles could utilize some or all of these or other equipment, with an appropriate scaling in system properties.

Table 8.6 Navigational payload mass, volume, power and constraints.

Navigation subsystem	Mass kg	Volume m^3	Power W	Notes
Dumb transponder	12.8	0.0071	4	
3 ball homing beacon	2.9	0.0011	3	
Altimeter	2.9	0.0013	2	
Argos beacon and transmitter	15.7	0.0074	0	(in titanium case & independent power supply)
Emergency beacon	38.4	0.0083	3	
Phins gyro-compass (www23)	4.5	0.0078	12	
150kHz ADCP RD instruments workhorse Quartermaster. 450 m Bottom Track	56.0	0.0488	-	Titanium case. Independent power source.
300 kHz ADCP (revised small case) 200 m Bottom Track	14.5	0.0029	5	
22kHz ACCP	77.0	0.0050	100	ACCP limited to 5000m of sea floor.

The 150kHz ADCP can have a separate power source. This system has mass and volume, but requires no power from the energy source.

The AUV will require propulsion. A single propeller is assumed for these case studies. The motor in Autosub is a 1.6 kW DC brushless motor (Stevenson and Hunter 1994). It is oversized for the AUV, but allows different propellers to be mounted on the motor. The motor characteristics are given in Table 8.7.

Table 8.7 1.6 kW Autosub motor.

Structure	Volume m^3	Mass kg	Power W	Constraints
Motor	0.0096	28.0	up to 1.6 kW	Must be placed at stern with shortest dimension on x axis

8.2.3 Optional payload.

Table 8.8 summarises the payload that can found in Autosub. These sensors are primarily carried for scientific research and data acquisition. Other AUVs would carry equipment depending on mission objectives.

Some subsystems will not operate over the whole mission. The associated duty cycle of such subsystems will be expressed as a scaling factor (0.0 - 1.0) on the power draw of that subsystem. The duty cycle of each subsystem will be discussed for each mission in sections 8.3 and 8.4. Another consideration is system redundancy; carrying duplicate systems onboard as insurance should another subsystem fail. The negative impact of carrying redundant systems is that they occupy more of the mass budget of the AUV. This mass penalty is balanced against the likelihood of subsystem failure and operators' acceptable level of risk. For these case studies, no duplicate subsystems will be carried.

The next section groups the payload subsystems into sample packages and compares their capabilities.

8.2.4 Sample hotel configurations.

8.2.4.1 Simple navigation package.

A simple AUV navigation system will only acquire a GPS fix when at the surface. After diving the AUV uses an altimeter for depth until surfacing to acquire the next GPS position fix. This would mean that the AUV would be unaware of its surroundings or adverse currents. The only time it would be able to correct its course relative to the earth would be when at the surface. Some feedback can be programmed, by finding the finite difference when acquiring a waypoint and using this to estimate current velocity until the next waypoint.

Table 8.8 Optional scientific payload.

Science payload	Mass kg	Volume m^3	Power W	Notes
Edgetech Sub bottom profiler	20.9	0.00870	52.0	Transmitter and receiver which both need to be in free flooded section. Electronics need 0.1 MPa
Kongsberg swath Transceiver	19.0	0.00800	122.0	Transmitter and receiver which both need to be in free flooded section. Electronics need 0.1 MPa
Titanium CTD electronics assembly	20.7	0.00850	3.0	Requires water interaction, and if not directly in the flow, requires a pump
Aqua Monitor	31.1	0.01160	3.0	
Sea Bird fluorimeter	0.9	0.00070	Negligible	
Sea Bird Transmissometer	5.1	0.00230	Negligible	
Sea Bird Oxygen sensor	0.8	0.00040	Negligible	
Camera flash	6.6	0.00350	5.0	50 J flash, 5 W max
Turbulence probe	15.8	0.01530	3.0	As from Prof. Tom Osborne (John's Hopkins University, Baltimore)
Wetlabs fluorimeter	0.6	0.00025	0.6	
Wetlabs BB2F optical backscatter	1.3	0.00054	0.9	(www24)
Edge tech Side scan sonar 2200S	7.3	0.00244	30.0	Adapted for an AUV.

A simple navigation system is all that the Spray glider uses, so it can be useful as a navigation system for an AUV (www22). Difficulties arise for waters with obstacles such as sea ice. The error of the track would then be proportional to the time spent submerged. For oceanographic surveys far from land, a position error of up to 1 km may be acceptable (Griffiths 2000). With a GPS system, the error will be a function of the frequency of visits to the surface to acquire a fix and modifying AUV heading. An altimeter is the only other subsystem, to guide AUV depth.

The power demand of this navigational package is mainly from the GPS system. However, GPS would only be active when the AUV is at the surface. A duty cycle would be applied to account for the time when the GPS system is not active. The number of times the AUV surfaces would improve the navigational accuracy, but increase the energy requirement for the GPS. The GPS used in the simple package is not optimised, and there are much smaller systems available such as that used in the Spray glider.

8.2.4.2 Bottom track hotel package.

Table 8.9 Components of a bottom tracking navigation subsystem.

Subsystem	Mass kg	Volume m^3	Power W	Notes
300kHz ADCP	14.5	0.0029	5	self contained titanium case
Altimeter	2.6	0.0012	2	
Totals				
Bottom tracking navigation subsystem	17.1	0.0041	7	

When the ADCP is in range of the sea bed the AUV might use bottom tracking to adjust an initial position provided by the GPS system included in the base hotel. The sea bed would be required to be relatively flat as steep cliffs may not be 'seen' by a downwards looking ADCP. Careful mounting of the ADCP or multiple ADCPs could be used to track both seabed and the area in front of the AUV. Such an AUV would have an awareness of local currents and its velocity and position relative to the sea bed allowing for more accurate navigation and tracking. When the ADCP is out of range of the sea bed the AUV would not have any reference data beyond its altimeter, and so would be unaware of its surroundings.

The ADCP based navigation system would be fine for shallow water work, less than 1000 m, or when the AUV can stay near the ocean bottom for the majority of its mission. The equipment

used and system total is specified in Table 8.9. Given accurate imaging of the sea bed the bottom tracking package could give AUV position to an accuracy of a few metres. This package would benefit from a 3D mapping system such as a swath or side scan sonar, assuming that the onboard processing power was sufficient to process and navigate from the bottom images in real time. The bottom tracking navigation subsystem does not require any space at 0.1 MPa pressure. This presents a navigation system for an AUV design that can function outside of a pressure vessel.

8.2.4.3 Complex navigational package.

This would have similar capability to Autosub utilizing bottom tracking, velocity log and a homing beacon. A GPS system is included as part of the base hotel package Table 8.5. With the addition of a forward facing ADCP, this package would also be able to cope with collision avoidance. The subsystems suggested for a complex navigation package are listed in Table 8.10.

Table 8.10 Components of a complex navigation package.

Subsystem	Mass kg	Volume m^3	Power W	Notes
Dumb transponder	12.8	0.0071	4	
3 ball homing beacon	2.9	0.0011	3	
Altimeter (Short)	2.9	0.0013	2	
Argos beacon and transmitter (in titanium case &independent power supply)	15.7	0.0074	0	
Emergency beacon	38.4	0.0083	3	
Phins gyro-compass (www23)	4.5	0.0078	12	
150kHz ADCP RD instruments workhorse Quartermaster	56.0	0.0488		Titanium case. Independent power source.
300 kHz ADCP	14.5	0.0029	5	self contained titanium case
Totals				
Complex navigation package	147.7	0.0839	29	

This is a more comprehensive control package, and as such it has a larger mass than either of the other control packages. This package consumes more power than either of the alternative navigation packages discussed.

The missions and existing subsystems have been described. The next section applies the design method to produce an AUV design to complete mission A.

8.3 Case Study A - Sprint to work area AUV.

This case study applies the design methodology to produce a technically feasible AUV design capably of undertaking mission description A. This design focuses on the energy source of the AUV, as the high-speed requirement dominates the power use of the AUV. The first step is to size the subsystems that have not been explicitly specified in the design boundary. This requires crucial design decisions.

The list of key decisions to be made in this design are:

- First estimate of P_{Prop} - motor size scaled to be 50 kW.
- Selection of energy - pressure tolerant lithium polymer batteries or Panasonic batteries.
- Energy dimensions - influence radius of AUV hull shape.
- Selection of buoyancy type - foam or pressure vessel considered.
- Selection of hull shape - parallel middle body or laminar flow hull shape.

Figure 8.1 provides the design method proposed in Chapter 7 and applied to this case study. Each stage of the method will be described and specific issues highlighted as iteration proceeds through two complete design loops.

8.3.1 First design iteration.

Mission objective, payload and navigation components.

The start point is the identification of the mission objectives as described for mission A. The payload and navigation components are specified, using options from Table 8.5 and Table 8.8. The decisions are summarized in Table 8.11.

The simple hotel set is used for navigation, as the AUV is going to operate at shallow depth and is therefore able to surface and utilise a GPS system. A secondary aim would be to limit the number of times the AUV activates the GPS to reduce the power required for navigation. However, this will negatively affect navigation accuracy and so a balance must be found, dependant on the local ocean currents and magnitude of acceptable error.

By reducing the energy used by the GPS, a greater proportion of the onboard energy can be dedicated to propulsion and a longer range. However, a lower hotel load will decrease the optimal speed of the AUV (Chapter 3).

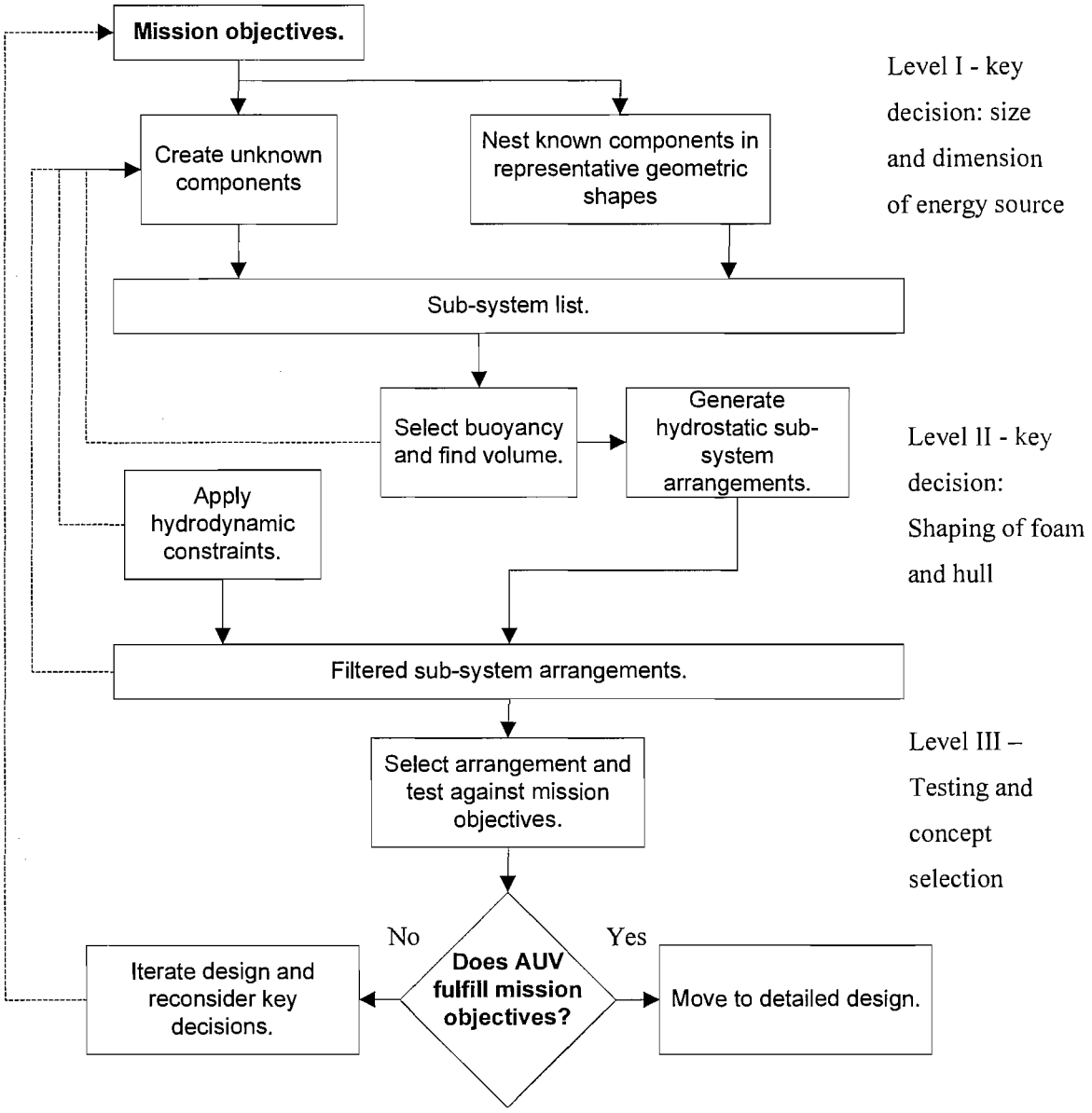

Figure 8.1 Design method to follow and key decisions identified.

As this mission has a specified velocity and range, the AUV must fulfil both of these requirements which may necessitate operation outside of an optimal velocity. The first iteration will assume the GPS is active constantly. This would represent the energy required for greatest navigational accuracy. Actual GPS operation can be refined in later cycles.

The length of a component in Table 8.11 is defined as the longest dimension. The volume and mass are accurate to the actual subsystem. The length, breadth and depth (or diameter) characteristics describe the bounding box in which the equipment is nested.

Table 8.11 Mission specified subsystem list for case study A.

Subsystem	Length m	Breadth m	Depth m	Volume m^3	Mass kg	Power W	Pressure tolerant? Y/N	Constraints
Navigation								
Base hotel package	0.955	0.354 diam	0.354 diam	0.0940	37.7	46.0	N	
Altimeter	0.180	0.096 diam	0.096 diam	0.0013	2.6	2.0	Y	
Payload								
CTD	0.520	0.140 diam	0.140 diam	0.0085	20.7	3.0	Y	Pump included
Wetlabs fluorimeter	0.202	0.063 diam	0.063 diam	0.0025	0.6	0.6	Y	
Seabird transmissometer	0.429	0.129 diam	0.129 diam	0.0023	5.1	Neg.	Y	
Seabird oxygen sensor	0.300	0.073 diam	0.073 diam	0.0004	0.8	Neg.	Y	
Totals								
			Total hotel	0.0953	40.3	48.0	N	Pressure vessel
			Total payload	0.0205	22.3	3.6	Y	
AUV minimum system	1.631	0.14	0.14	0.1160	62.6	51.6		

The AUV is assumed to be longer than its diameter (L_{AUV} / $2R_{Max}$ > 1.0) therefore all subsystems initially have the longest dimension placed along the x-axis. This can be altered by subsystem positional constraints or during the design iteration.

The base hotel subsystems will not be scaled in size. Refined models might increase the power chassis to facilitate larger power cables. The payload is specified by the mission and will not increase with AUV size.

The unknown subsystems are; the pressure hull, the energy source and the motor. The total volume of the pressure sensitive subsystems is required to size the pressure vessel. The mission operates at 200m, and so a pressure vessel would provide buoyancy and a pressure sensitive

energy source is a valid choice. However, the energy source is likely to be very large to provide sufficient energy for propulsion. Such an energy source within a pressure vessel would dominate the AUV shape. A pressure tolerant energy source would allow more hull shape variation. The energy source for the first iteration will be the pressure tolerant lithium polymer cells. The alternative case of a pressure sensitive energy source is investigated in section 8.3.2.

Create pressure vessel for sensitive components.

Using a pressure tolerant energy source means that the total volume of the pressure sensitive subsystems is known. The creation of a cylindrical pressure vessel is described in Appendix B and Chapter 2.

Specifying either the length or radius of the pressure vessel will influence the collapse method, the mass of the pressure vessel and its overall affect on the AUV design. For this design scenario the pressure vessel radius will be set by the subsystem with the largest diameter. The length will then be found from the required internal volume. This will keep the pressure vessel of the same order of size as the other subsystems. The pressure vessel minimum internal radius is 0.177 m and must contain a volume of 0.094 m^3 (see Table 8.11). The collapse depth is 700 m and has a safety factor of 20 % (arbitrary amount for metals with uniform and known characteristics)

Table 8.12 Pressure vessel properties for case study A with a pressure tolerant energy source.

Pressure vessel properties.	Designed to resist material yield	Designed to resist wall buckling
Material	Titanium IMI 318 (Ti – 6Al – 4V)	Titanium IMI 318 (Ti – 6Al – 4V)
Outer radius	0.1788 m	0.1855 m
Overall length	1.228 m	1.241 m
Wall thickness	0.0018 m	0.0085 m
Internal volume	0.09419 m^3	0.09419 m^3
Displaced volume	0.11113 m^3	0.1208 m^3
Sufficient for internal components?	Yes	Yes
Mass in air including internal components	48.6 kg	90.4 kg
Total buoyancy	65.5 kg	33.4 kg

The right hand column of Table 8.12 provides the dimensions for the pressure vessel. The first column produces a pressure vessel that will resist material yield at pressure, equation 2.8. The fineness ratio of 3.434 (centre column) is less than 10, so the full pressure vessel buckling

equation is used, as given in Appendix B, to increase the wall thickness was increased. The fineness ratio of the second pressure vessel iteration is 3.345. The pressure vessel is positively buoyant when all subsystems are packed within.

Select energy source and size.

Energy source selection contains two key decisions; capacity and dimensions. There are many ways to come to a first estimate of energy capacity. These include estimating $\nabla_S^{2/3} C_{D\nabla}$ of the hull shape and finding drag force and power, or using the *Mass Ratio* presented in Chapter 2, or directly estimating the propulsion power. Here Autosub's motor is scaled to suit the mission speed and so estimate power required by the motor.

Due to the very wide range of motors and propellers available, it will be assumed that a drive train and propeller can be found that fulfils the same efficiency of the motor given in Table 8.7. Assuming the overall value of $\nabla_S^{2/3} C_{D\nabla}$ remains constant to Autosub, there will be a cubic increase of propulsion power. Increasing velocity from 2 ms^{-1} to 6 ms^{-1} will result in 9 times the drag force and a power increase factor of 27. A second iteration (section 8.3.3) will update the estimate of $\nabla_S^{2/3} C_{D\nabla}$ and alter the required motor power.

Scaling the Autosub motor power by 27 will give a 43.2 kW motor but would result in a 756 kg motor. This is a very heavy motor which might fulfil the power requirement, but other options are investigated. Specifying a propulsion power of 43.2 kW becomes a key design decision.

Subsea Systems produce pressure compensated thrusters capable of 50 kW, and 975 kgf (www26). This thruster weighs 48 kg (32 kg in water) and has a 600 mm diameter propeller. The nested dimensions, volume, mass and power are given in Table 8.13. As for Table 8.11, the volume and mass represent the actual subsystem, the dimensions represent the bounding cylinder for the nesting approach.

Table 8.13 50 kW electric motor for case study A.

Structure	Length m	Breadth m	Depth m	Volume m^3	Mass kg	Power W	Pressure tolerant?	Constraints
Motor	0.50	0.30 diam	0.30 diam	0.0353	48.0		Y	Stern placement.

Only the hub of this motor will have to fit within the AUV, and so although the mass and buoyancy will remain constant, only a small section will be represented as a nested subsystem. This is a specific motor for this case study. There are others that are similar or that can be custom made to similar specifications. Using this motor allows the maximum propulsion power to be

estimated and the energy source to be sized. The motor and propeller efficiency will be assumed to remain constant at the different operating velocities.

Now that P_{Prop} is known, 50 kW, the capacity of the energy source can be found. Travelling for 100 km at 6 ms^{-1} and 105 km at 1 ms^{-1}, means that the AUV will spend 4 hours 37 minutes at 6 ms^{-1} and 29 hours 10 minutes at 1 ms^{-1}. Over this journey the navigation will be active all the time (100 % duty cycle) and the payload will only be active when at the survey site.

50 kW will be supplied to the motor over the sprint range, and less over the survey range. The survey speed is 1 ms^{-1}, 6 times less than sprint speed, requiring 216 times less power, 232 W. Table 8.14 shows that 240 kWh of power is required for this design concept, and that the majority of this power is put into the propulsion during the sprint section of the AUV. The efficiency of the propeller and power train is likely to vary with velocity and this has not been addressed for this energy estimate.

Table 8.14 Power usage and total power requirement estimation.

Source	Power	Duration	Energy
	W	Hours	Wh
Propulsion – Sprint	50000	4.630	231500.00
Propulsion – Survey	232	1.389	322.25
Propulsion – Return journey	232	27.78	6444.96
Hotel	48	33.769	1620.91
Payload	3.6	1.389	5.00
		Total energy usage	239893.12

It is possible to size the energy source from the known endurance and the required P_{Prop} from a specified motor. Lithium polymer batteries are to be the energy source as they are high energy density, and capable of the high power density required for P_{Prop}. The pressure balanced battery pack has an energy density of 102.3 Wh kg^{-1} and a mass density of 1960 kg m^{-3}, including protection, battery management system and structure. The energy source will have a mass of 2346 kg (volume = 1.197 m^3) and provide just under 240 kWh.

The energy source is a shapeless volume and requires dimensioning. One option is for the energy source to fit within the diameter of the motor hub (0.30 m), allowing placement along the

whole length of the AUV. This would make the energy source 26.6 m long, physically unrealistic due to structural challenges. The energy source could be cubic, resulting in each side being 1.062 m, which is physically more achievable and is used for this first iteration in Table 8.15. The volume of the energy source is the largest subsystem of the AUV design, so its dimensions will have a large impact on the shape of the AUV. The dimensioning of the energy source becomes a second key decision for the shape of this AUV.

Subsystem list.

All the subsystems have been sized (Table 8.11 and motor, pressure vessel and energy source described) and are presented in Table 8.15.

Table 8.15 List of subsystems for hydrostatic balancing.

Subsystem	Length m	Breadth m	Depth m	Volume m^3	Mass kg	Power W	Constraints
Altimeter	0.180	0.096 diam	0.096 diam	0.0013	2.6	2.0	
CTD	0.520	0.14 diam	0.14 diam	0.0085	20.7	3.0	Pump included
Wetlabs fluorimeter	0.202	0.063 diam	0.063 diam	0.0025	0.6	0.6	
Seabird transmissometer	0.429	0.129 diam	0.129 diam	0.0023	5.1	Neg.	
Seabird oxygen sensor	0.300	0.073 diam	0.073 diam	0.0004	0.8	Neg.	
Pressure vessel	1.241	0.371 diam	0.371 diam	0.1208	90.4	46.0	
Motor	0.500	0.30 diam	0.30 diam	0.0353	48.0	50000.0	Stern placement
Energy source	1.062	1.502 diam	1.502 diam	1.1970	2346.0		Nested diam,
Total							
Total subsystems	4.422	1.062 max	1.062 max	1.3681	2514.2		
				Buoyancy required (kg)	1111.9		

The pressure sensitive subsystems are included in the pressure vessel. This is now ready to be arranged for hydrostatic balancing to find a buoyancy system and hull shape.

Select buoyancy and find volume

From Table 8.15 the AUV requires 1111.9 kg of buoyancy to make it neutrally buoyant. Given the shallow depth of this mission, pressure vessels are a viable option for buoyancy provision. This will be tested in section 8.3.2. The total volume of the AUV is the sum of its parts, much like the M_{AUV} equation presented in Chapter 4. The volumetric version of this is presented in equation 8.1. From the derivation of equation 7.2 the buoyancy volume is equation 8.2.

$$\nabla_{AUV} = \nabla_{Structure} + \nabla_{Payload} + \nabla_{Hotel} + \nabla_{Prop} + \nabla_{PV} + \nabla_{Energy} + \nabla_{B} \qquad 8.1$$

$$\nabla_{B} = \frac{Buoyancy}{\rho_{W} - \rho_{B}} \qquad 8.2$$

Once the buoyancy material is selected (a foam or a pressure vessel) the additional volume can be included in ∇_{AUV}.

Trelleborg syntactic foam rated at 1000 m depth with ρ_B = 400 kgm^{-3} will be used (www25). This means that 1.779 m^3 of foam, weighing 711.6 kg, is required to make the whole AUV neutrally buoyant. The neutrally buoyant AUV will have a mass of 3225.8 kg and a volume of 3.147 m^3. 1.779 m^3 of foam is greater than the total subsystem volume meaning that 56.5 % of the total AUV volume is made of buoyancy foam. This is a large amount of the volume budget and will have implications when packing subsystems within the hull shape.

The foam required to balance the AUV is still undefined in shape. Only its volume and centre of mass location is found by hydrostatic balancing. The hull shape will constrain the shape of the foam, and this will be described later in the design process.

Generate hydrostatic subsystem arrangements.

Figure 8.2 provides the longitudinal position of the *CoG* of the required buoyancy (L_{Foam}) as a fraction of AUV length. It also shows the sequential position of the energy and the pressure vessel. The first conclusion is that none of the possible combinations result in a L_{Foam} greater than the AUV length, implying that each combination is possible without increasing AUV length.

The code in Appendix E generates the possible arrangement combinations within a matrix. Matrix rows are generated sequentially and then filtered for duplicate numbers to leave a matrix of unique arrangements. The subsystem arrangement number is the row number within the matrix.

As shown in Table 8.15 the energy source of the AUV has a mass twenty six times that of the pressure vessel, which in turn is nearly twice the mass of the motor. This causes the AUV *CoG* to occur within the energy source regardless of the arrangement of subsystems. The next greatest mass is the pressure vessel and its affect on L_{Foam} can be seen in Figure 8.2. When the pressure vessel is put aft of the energy source, L_{Foam} decreases as the relative position of the energy source moves forward. The other subsystems are much lighter than the energy source or pressure vessel, and they cause the noise in the plot of L_{Foam}

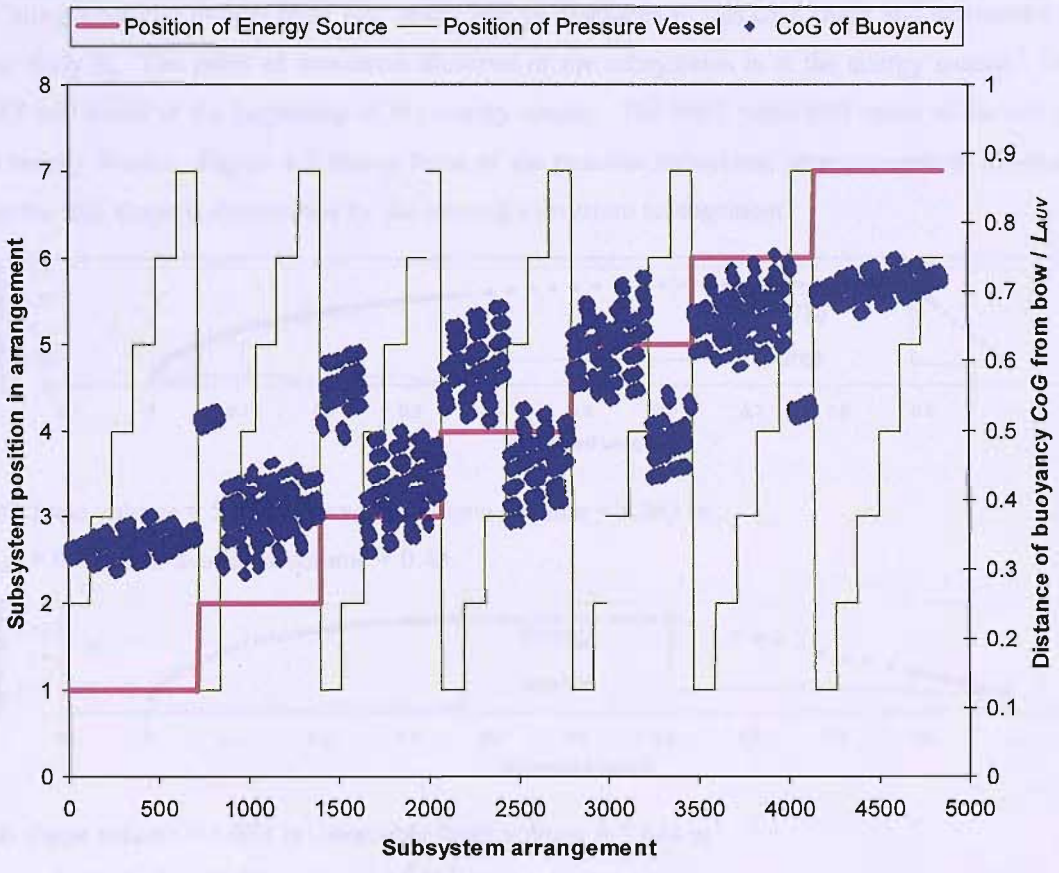

Figure 8.2 *CoG* of buoyancy (L_{Foam}) with position of energy source and pressure vessel within the subsystem arrangement for case study A with pressure tolerant energy source.

As the *CoG* is centred on the heaviest subsystem, it suggests that for this design the arrangement of the subsystems can initially be ignored, and the design iteration based upon the dimensions of the energy source.

AUV fineness ratio could provide an indication of C_{D_∇} and is used to update the energy capacity estimates. The design would still require the other subsystems to refine the shape. The

design will continue with the current energy source dimensions and the other subsystems will be included to aid determining the length of the AUV.

Apply hydrodynamic constraints.

A hull shape has to be fitted around the subsystems, to provide a C_{D_∇} value such that the required range of the AUV can be achieved. Therefore the hull shape will constrain the subsystem arrangement chosen and the shape of any buoyancy foam.

Fitting a parallel middle body hull shape will be discussed in this case study and automated in case study B. The point of maximum diameter of the subsystems is at the energy source. The BMT will occur at the beginning of the energy source. The MST point will occur at the end of the energy source. Figure 8.3 shows three of the possible subsystem arrangements to illustrate how the hull shape is determined by the internal subsystem arrangement.

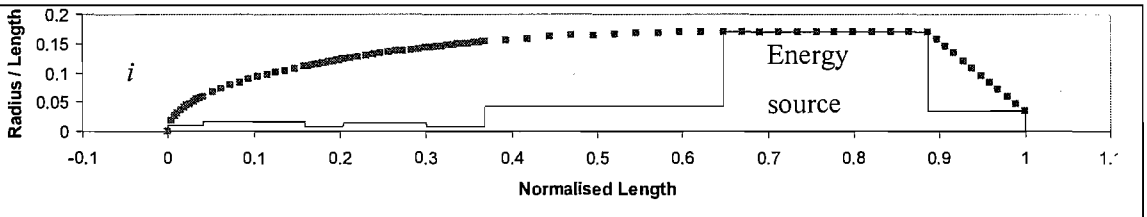

Hull shape volume = 5.639 m^3, available foam volume = 4.263 m^3.

L_{Foam} = 0.77, *CoB* available volume = 0.45.

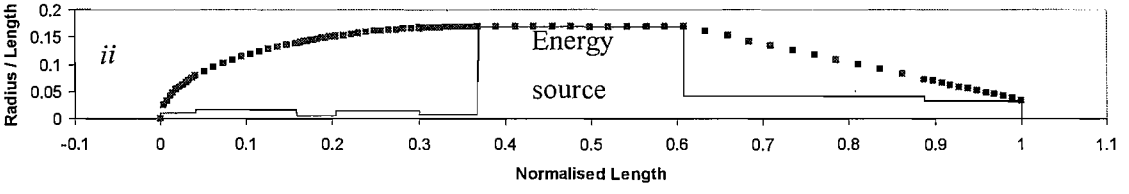

Hull shape volume = 5.083 m^3, available foam volume = 3.644 m^3.

L_{Foam} = 0.48, *CoB* available volume = 0.40.

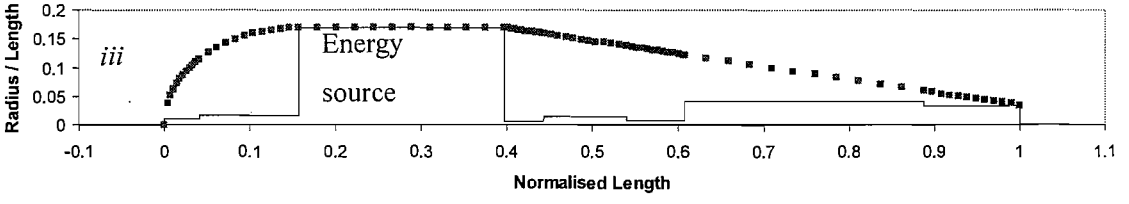

Hull shape volume = 4.666 m^3, available foam volume = 3.256 m^3.

L_{Foam} = 0.27, *CoB* available volume = 0.41.

Figure 8.3 Possible AUV subsystem arrangements with a parallel middle body hull shape for case study A with a pressure tolerant energy source.

The pressure tolerant energy source has permitted a much shorter parallel middle body length for each arrangement. However, the large energy source radius results in a large amount of available volume within the hull shape.

The volume available for foam within the hull shape is shown within Figure 8.3 and each hull shape has volume greater than the 1.779 m^3 required for buoyancy. This implies that the maximum radius is too large and the decision to make the energy source a 1.061 m cube needs refinement.

When L_{Foam} matches the available volume CoB then the foam buoyancy can be placed in the correct position to hydrostatically balance the AUV.

The arrangement and hull shape that best achieves balance is Figure 8.3*ii*, where the foam straddles the energy source. As there is greater volume than that required by the foam, it would be possible to achieve the required L_{Foam} of the other two hull shape. This is achieved by unevenly distributing the foam, packing more foam in the stern available volume and not the bow available volume.

Estimates of $C_{D\nabla}$ for these hull designs can now be made from the equations derived in Chapter 6 (equation 6.4). Table 8.16 provides the estimated $C_{D\nabla}$ and drag of the hull shapes in Figure 8.3 together with the hull shape non - dimensional parameters (m, n, and p).

Table 8.16 Estimated $C_{D\nabla}$ and drag of example parallel middle body hull forms showing non-dimensional parameters for case study A with pressure tolerant energy source.

Example	BMT m	MST m	Maximum radius of AUV, R_{Max} p	Estimated $C_{D\nabla}$	Difference from base model.	Estimated drag at 6.0 ms^{-1}. N
Figure 8.3*i*	0.6477	0.8872	0.1694	0.0012	0.9106	70.1
Figure 8.3*ii*	0.3678	0.6074	0.1694	0.0039	0.3861	212.7
Figure 8.3*iii*	0.1579	0.3974	0.1694	0.0059	0.3862	304.0

The most influential input to $C_{D\nabla}$ is the AUV radius, and the three candidates have R_{Max} defined by the largest subsystem. Figure 8.3*iii* has the bluffest bow as the BMT occurs early, and which results in a higher $C_{D\nabla}$, Table 8.16.

The hull with the lowest C_{D_∇} is Figure 8.3*i*, as this has the longest bow and shortest stern. Although Figure 8.3*iii* has the least volume it has the highest drag estimate, dominated by a high C_{D_∇}.

The primary reason for C_{D_∇} increasing for each arrangement is the decreasing BMT length. Although the hull shape volume decreases, the drag prediction increases for each arrangement. Here the highest C_{D_∇} produces the highest drag value.

It is worth noting that the lowest drag is for the largest shape, due to a very low C_{D_∇} prediction. This shape is far removed from the Autosub base model (0.9106 is the largest difference in Table 8.16) and so there is likely to be large errors in predicting the C_{D_∇}. Such a long bow and short stern would likely incur boundary layer effects and wake separation. These effects are not captured in the C_{D_∇} equation based on the Schlichting skin friction estimation results. However, this example does illustrate the design method and how the internal arrangement might determine the hull shape. An improved C_{D_∇} is necessary in future work.

The curved bow makes Figure 8.3*i* very reminiscent of the laminar flow shapes, implying that the laminar flow hull shape may be more suitable for this subsystem arrangement. These subsystem arrangements will be fitted with a laminar flow hull shape before reconsidering previous key decisions. This uses the Rutherford shape C_{D_∇} estimation. This has been applied to the same three example arrangements and is shown in Figure 8.4.

All three hull shapes have greater available volume than is required by foam buoyancy. The smallest hull shape, Figure 8.4*iii*, has the energy source closest to the bow, and the largest shape has the energy source furthest from the bow, Figure 8.4*i*. This is because the stern profile curve is concave and encloses less volume than the bow profile curve. Therefore laminar flow hull shapes with a long bow will have greater volume than those with a small bow. This is also true for the parallel middle body shapes with a curved bow and linear stern. Figure 8.4*ii* places the energy source in the middle of the arrangement and is the most hydrostatically balanced arrangement (smallest difference between the required L_{Foam} and the available volume CoB).

The point of maximum diameter is forced to occur along the largest subsystem: the energy source. The radius of the hull and the exact position of the point of maximum diameter can be adjusted within the length of the largest subsystem in order for the bow and stern to clear the energy source at the edges of the subsystem.

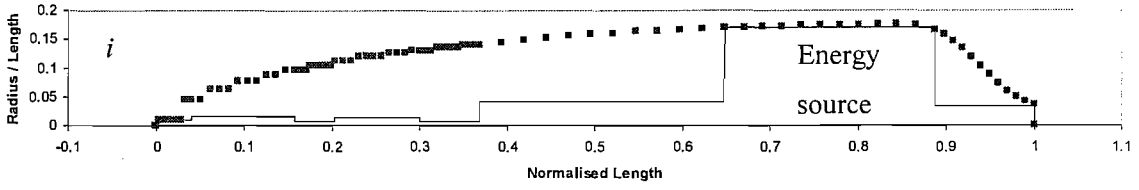

Hull shape volume = 5.398 m^3, available foam volume = 3.249 m^3.

L_{Foam} = 0.77, *CoB* available volume = 0.48.

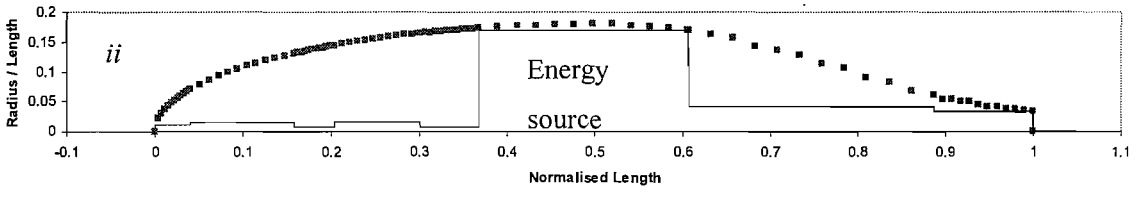

Hull shape volume = 5.027 m^3, available foam volume = 3.653 m^3.

L_{Foam} = 0.48, *CoB* available volume = 0.41.

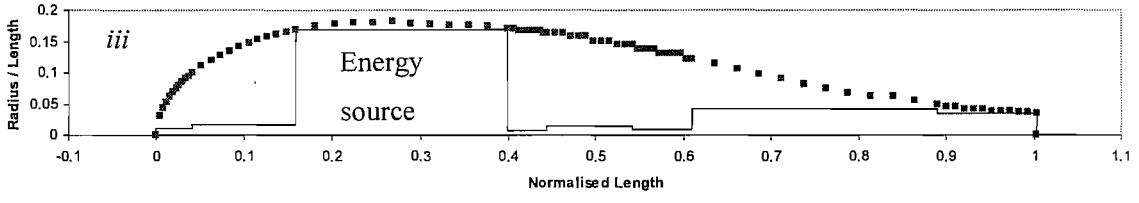

Hull shape volume = 4.537 m^3, available foam volume = 3.237 m^3.

L_{Foam} = 0.27, *CoB* available volume = 0.40.

Figure 8.4 Possible AUV subsystem arrangements with a Rutherford hull shape for case study A with pressure tolerant energy source

The hull shape input parameters, estimated $C_{D\nabla}$ and drag are reported in Table 8.17. From the Rutherford shape $C_{D\nabla}$ equation in Chapter 6 (equation 6.9), R_{Max} is the most influential parameter on hull shape $C_{D\nabla}$. However, the shape with the largest radius, Figure 8.4*iii*, has the greatest $C_{D\nabla}$ although due to a smaller volume it has the lowest estimated drag. Figure 8.4*ii* has the lowest $C_{D\nabla}$ implying that it has the most efficient overall shape, yet its volume increases the drag estimate to above that of Figure 8.4*iii*. Figure 8.4*i* has the smallest radius but the longest bow, giving it the middle $C_{D\nabla}$ value but highest drag of the three hull shapes. The estimated drag of these three concepts increases with the volume of the AUV and the lowest drag belongs to the

smallest AUV. Figure 8.4*ii* is the shape that most resembles the base hull (lowest difference in Table 8.17), so has the least error entrained within the C_{D_∇} equation.

Table 8.17 Estimated C_{D_∇} and drag of example Rutherford hull forms showing non-dimensional parameters for case study A with a pressure tolerant energy source.

Example	Bow curvature m	MST n	Maximum radius of AUV, R_{Max} p	Estimated C_{D_∇}	Difference from base model	Estimated drag at 6.0 ms^{-1} N
Figure 8.4*i*	2	0.8570	0.1759	0.0060	0.4050	340.6
Figure 8.4*ii*	2	0.5074	0.1804	0.0059	0.1701	319.4
Figure 8.4*iii*	2	0.2488	0.1809	0.0062	0.4292	313.5

The Rutherford hull shape suffers from the same packing inefficiencies as the parallel middle body shape; the volume available for foam is much larger than the 1.779 m^3 required for hydrostatic balance. The AUV radius specified when sizing the energy source forces the fairing to have a radius disproportionate to the other subsystems, and so generate too much unused space.

Contrasting the two hull shapes, the Rutherford hull shape and parallel middle body, the AUV hull shape volumes are comparable, although the parallel middle body has an overall lower drag prediction. This is mostly due to the C_{D_∇} equations, which are linear approximations of the Schlichting skin friction estimation results. Were the boundary layer transition and the wake effects included along with a more complex C_{D_∇} approximation, the resulting hull shape C_{D_∇} and drag predictions might be different.

This case study is now ready for its first iteration, having discussed the results of this first attempt. To improve packing and hydrodynamic performance, the energy source dimensions should be addressed, reducing its radius and/or splitting it into two or more subsystems. The next section looks at changing the key decision to use the pressure tolerant cells in favour of higher energy but pressure sensitive battery cells.

8.3.2 Alternative choices.

For this shallow depth mission, pressure vessels are a viable buoyancy source. This section explores the alternative decision to use a pressure sensitive energy source.

The battery pack is required to supply 240 kWh of energy with a 50048 W peak draw. Battery chemistries that supply either high energy density or high power density could include excess individual batteries to make up the required power or energy, but this would increase the mass of the energy source. A commercial battery chemistry was found that could meet both energy density and power demands.

Panasonic CR18650E secondary batteries have an energy density of 188 Wh kg^{-1}, with a density of 2620 kg m^{-3} and are formed as cylindrical cells (www27). A battery pack containing 27556 batteries (166 battery strings in parallel, 166 strings in series giving a bus peak voltage of 664 V) with a mass of 1281.354 kg, will supply 241 kWh up to 50048 W power draw. This battery pack requires 0.8136 $m^3$of volume, at approximately 60 % packing efficiency for circular shapes packed within a circular pressure vessel with wiring and structure taking volume.

The enclosing pressure vessel will act as buoyancy to support the pressure tolerant subsystems. From Table 8.15, ignoring pressure tolerant energy source and pressure vessel, the pressure tolerant subsystems have a mass of 77.8 kg and a volume of 0.0503 m^3 requiring 26.2 kg of buoyancy is required. Therefore the pressure vessel was sized to provide 26.2 kg of buoyancy including the mass of internal energy source and pressure sensitive subsystems, Table 8.18. The pressure vessel has a minimum radius of 0.177 m (defined by the base hotel subsystems). The process altered the radius of the pressure vessel for a known internal volume, until the required buoyancy is achieved whilst resisting material yield and buckling pressure.

Table 8.18 Pressure vessel properties when housing 1281.354 kg of Panasonic CR18650E lithium ion batteries for case study A.

Pressure vessel properties.	Designed to resist material yield & buckling.
Material	Titanium IMI 318
Outer radius	0.5912 m
Overall length	1.739 m
Wall thickness	0.006 m
Internal volume	0.9078 m^3
Displaced volume	1.4770 m^3
Sufficient volume for internal components?	Yes
Mass in air of pressure vessel	168.633 kg
Mass in air including internal components	1487.687 kg
Total buoyancy	26.2 kg

This pressure vessel replaces the pressure vessel in Table 8.15 and removes the energy source from the list. This is the last subsystem that needs to be specified. All the required subsystems have been defined to produce a neutrally buoyant AUV. The design progresses to the next stage of arranging the subsystems.

Hydrostatic balancing.

The AUV is neutrally buoyant and no foam is required so L_{Foam} is zero. This does not imply that the shape is hydrostatically balanced. For this example, the pressure vessel mass and displacement is much larger than the sum of all the other subsystems, and dominates the hydrostatic stability. An additional issue is that with no required foam, the available volume within the hull shape will not be filled, so must be free flooding and is effectively wasted space.

The automated Matlab code was run for this example and the *CoG* and *CoB* of the subsystems without foam determined. The *CoB* and *CoG* always occurred within the pressure vessel length. There was a maximum of -1.08 % of AUV length difference between *CoG* and *CoB*. This is plotted in Figure 8.5.

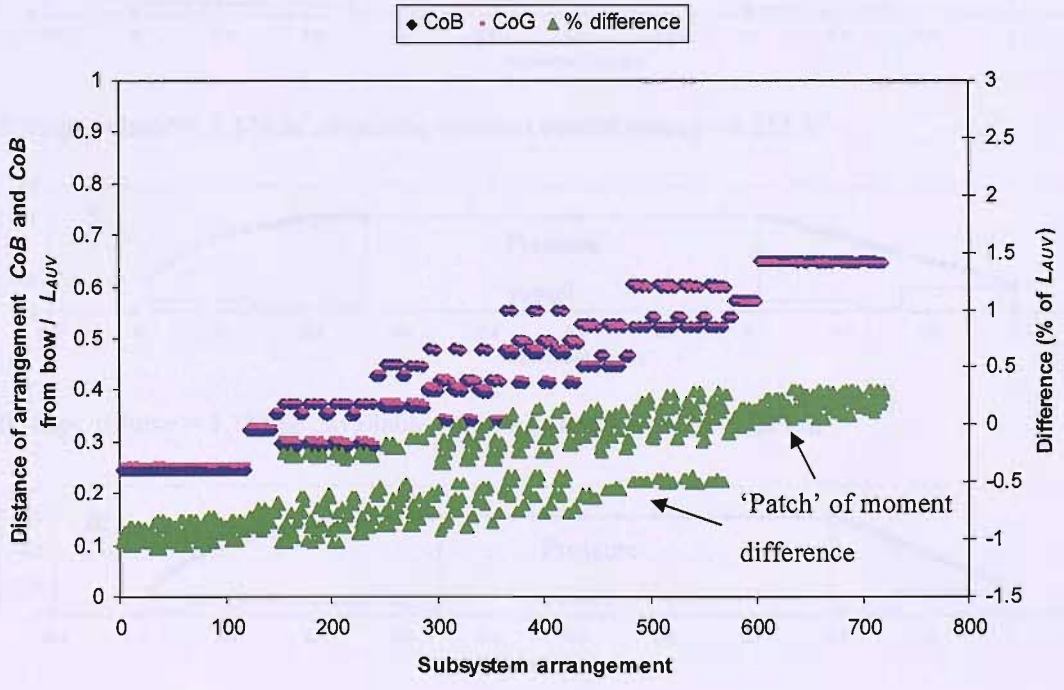

Figure 8.5 Comparison of *CoB* and *CoG* for case study A with Panasonic batteries.

All the arrangements are possible if *CoG* – *CoB* difference of 1.5 % is acceptable to the design. Resolving the difference would require the addition of mass and buoyancy within the hull shape. The addition of mass is avoided in this example, as such designs can have a tendency to

continually increase in mass (Burcher and Rydill 1994 p. 263). There are two 'patches' of moment difference, so the design can be filtered to only consider the designs with the least moment difference.

There are 6 subsystems that are not positionally constrained therefore there are 720 possible combinations. 18 of these have *CoB* and *CoG* in the same vertical plane, and 3 of these are fitted with a hull shape as potential feasible designs for the next stage of the design process.

Figure 8.6 shows 3 possible AUV subsystem arrangements with possible parallel middle body hull shape. The pressure vessel is the largest subsystem and dominates the hull shape. These shapes are hydrostatically balanced and so the available volume becomes wasted space. These arrangements would be candidates for breaking the axial constraint and moving subsystems off the centre axis.

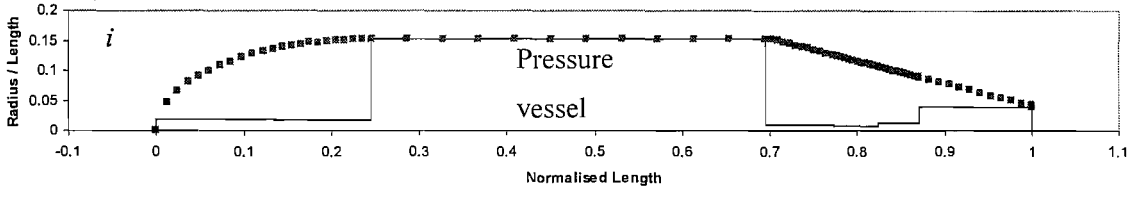

Hull shape volume = 3.174 m^3, available volume (wasted space) = 1.252 m^3

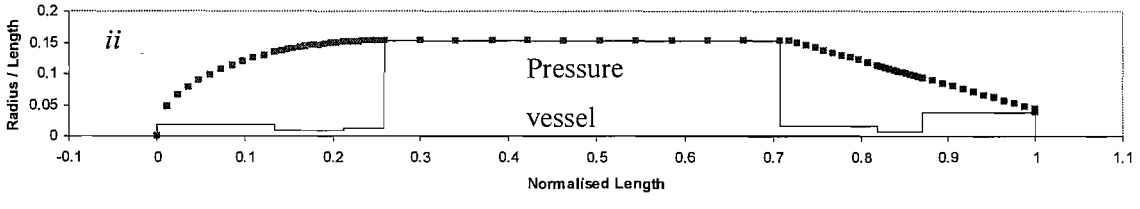

Hull shape volume = 3.187 m^3, available volume (wasted space) = 1.227 m^3

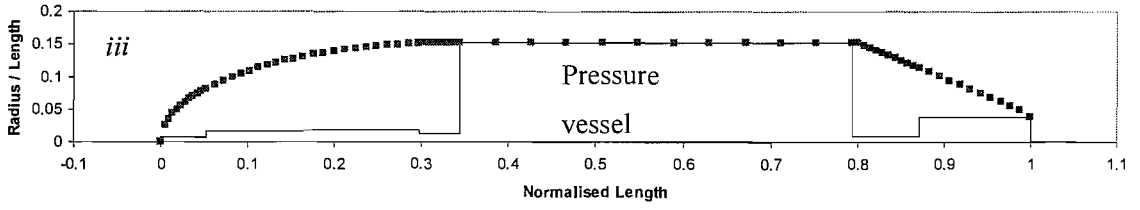

Hull shape volume = 3.267 m^3, available volume (wasted space) = 1.337 m^3

Figure 8.6 Example AUV subsystem arrangements with a parallel middle body hull shape for case study A.

The hydrodynamic performance of the hull shapes in Figure 8.6 is shown in Table 8.19. Whilst the radius is held constant the bow has the greatest effect on the drag of the shape. As such, Figure 8.6*iii* has the lowest drag and Figure 8.6*i* has the highest drag. The hull shape input parameters for Figure 8.6*iii* are furthest from the base Autosub hull shape parameters (0.4963), and will have greatest error because of the linear approximation.

Table 8.19 Estimated C_{D_∇} and drag for example parallel middle body hull forms showing non-dimensional parameters for case study A with pressure sensitive energy source.

Example	BMT m	MST n	Maximum radius of AUV, R_{Max} p	Estimated C_{D_∇}	Difference from base model	Estimated drag at 6 ms^{-1} N
Figure 8.6*i*	0.2452	0.6946	0.1528	0.0060	0.2989	239.1
Figure 8.6*ii*	0.2584	0.7078	0.1528	0.0059	0.3253	235.7
Figure 8.6*iii*	0.3439	0.7933	0.1528	0.0051	0.4963	207.2

The C_{D_∇} of the three example shapes in Table 8.19 decreases as the pressure vessel containing energy source moves backward along the shape. This decrease is caused by two hull shape changes: the BMT length and the MST length both increasing. The hull shape volume increases as the pressure vessel moves backward.

Figure 8.6*i* and Figure 8.6*ii* have similar hull shapes and give similar drag estimates (3.4 N difference). Figure 8.6*iii* has a lower drag estimate, due to a bluff stern. This might cause separation and consequentially have a higher drag force.

Figure 8.7 shows the three examples of subsystem arrangements from Figure 8.6 with the Rutherford laminar flow hull shape. The pressure vessel is a long subsystem which gives a large area for the point of maximum diameter to occur. As the pressure vessel is parallel sided, the curvature of the laminar hull shape increases the amount of wasted space. All three shapes have wasted space. Figure 8.7*i* has the lowest available volume, 1.453 m^3, resulting in 1489 kg of seawater carried within the AUV.

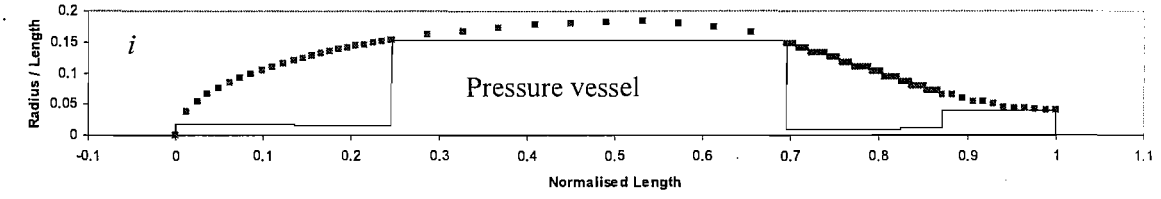

Hull shape volume = 3.431 m^3, available volume (wasted space) = 1.453 m^3

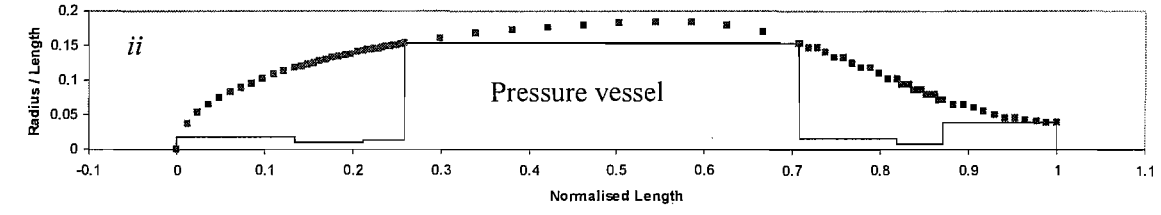

Hull shape volume = 3.478 m^3, available volume (wasted space) = 1.565 m^3

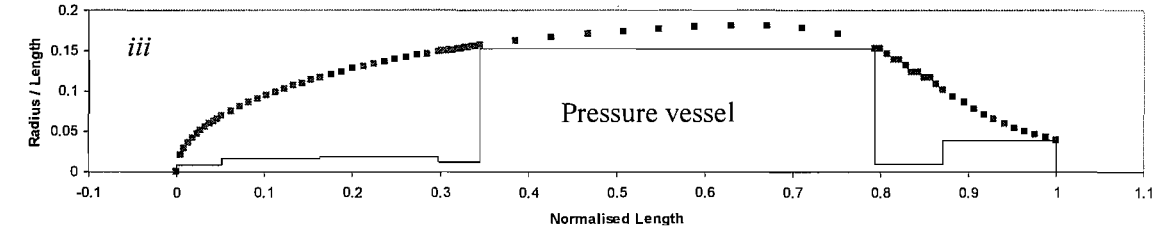

Hull shape volume = 3.608 m^3, available volume (wasted space) = 1.666 m^3

Figure 8.7 Example AUV subsystem arrangements with a Rutherford hull shape for case study A with pressure sensitive energy source.

Table 8.20 reports the C_{D_∇} and drag estimates of the shapes in Figure 8.7.

The drag estimates are very similar (difference of 12.4 N), as both the C_{D_∇} and volume of the laminar hull shapes are similar. Figure 8.7*i* has the smallest volume and lowest drag. The largest shape, Figure 8.7*iii*, has the highest C_{D_∇} and highest drag estimate. This hull shape has the longest bow and so may benefit most from a laminar boundary layer. The bow length must be balanced by the angle of the stern as streamline separation would increase drag.

The shapes in Figure 8.7 have the same problem as the parallel middle body shape, Figure 8.6; the pressure vessel radius is too large and the available volume for foam is too great. However, the pressure vessel fills the parallel middle body section of the parallel middle body hull shape giving less wasted space (lowest is Figure 8.6*ii* with 1.227 m^3). The laminar hull curves around the pressure vessel and increases wasted space (1.565 m^3 for Figure 8.7*ii*).

Table 8.20 Estimated $C_{D\nabla}$ and drag for example Rutherford hull forms showing non - dimensional parameters for case study A with pressure sensitive energy source.

Example	Bow curvature m	MST n	Maximum radius of AUV, R_{Max} p	Estimated $C_{D\nabla}$	Difference from base model	Estimated drag at 6.0 ms^{-1} N
Figure 8.7*i*	2	0.5426	0.1835	0.0056	0.1380	235.0
Figure 8.7*ii*	2	0.5814	0.1835	0.0056	0.1370	237.2
Figure 8.7*iii*	2	0.6925	0.1809	0.0057	0.2455	247.4

The drag predictions of the two hull shape families are comparable, apart from the lowest, Figure 8.6*iii* (207.2 N) and the highest Figure 8.7*iii* (247.4 N). These two hull shapes also have the greatest geometric parameter difference from the base model.

What would be the next iteration for this energy option? The pressure vessel could be redimensioned to give a different hull shape, or split into multiple pressure vessels which might enable greater flexibility regarding their position, but with associated increases in wiring and structure.

The analysis presented suggests selection of the Panasonic energy source with the parallel middle body hull shape as a candidate design, Figure 8.6*iii*. The pressure tolerant energy source arrangements will not be selected due to greater mass and volume of the concept AUV. For the Panasonic energy source the laminar flow hull shape has more wasted space (1.666 m^3, Figure 8.6*iii*, compared to 1.337 m^3 for Figure 8.6*iii*). Figure 8.6*iii* has the lowest drag prediction of the parallel middle sided hull shapes. At this diving depth the buoyancy provided by the pressure hull appears to be more important to the AUV design than flexibility of shape.

Does concept AUV fulfil mission requirements?

The concept AUV volume, energy capacity and $C_{D\nabla}$ have been determined using the proposed design method. All the parameters to estimate the range of the AUV are known, and the concept design will be tested against mission objectives. These parameters are summarised in Table 8.21.

The AUV volume is the hull shape envelope volume, not the exact displaced volume, and will be used for the $\nabla^{2/3}$ term when finding AUV drag. The disparity between the displaced volume and the AUV hull volume is caused by the excess available volume and from the 'nested' subsystems occupying more volume in the design than their respective displacement volumes.

The available volume outside of nested subsystems is considered to be empty. The volume difference between nested volume and displacement volume is assumed to be required by connections, pipes and cabling.

Table 8.21 Concept AUV after one full iteration of design methodology.

Parameter	Value
AUV volume	3.267 m^3
AUV mass	1565.487 kg
Available volume, assumed to be free-flooding	1.337 m^3 based on nested volume (1.739m^3 based on displacement volume)
Mass of energy	1281.354 kg
Energy source density	188 Wh kg^{-1}
C_{D_∇}	0.0051
Hotel Power	48 W
Payload Power	3.6 W
Total energy consumed by hotel and payload	1626 Wh
Thrust power @ 6 ms^{-1} with 56.25 % efficiency	2210 W
Thrust power @ 1 ms^{-1} with 56.25 % efficiency	10 W
Total energy consumed by propulsion	10524 Wh
@ sprint	10232 Wh
@ survey	14 Wh
@ return	278 Wh
Total energy used over mission	12150 Wh
% of stored energy used	5 %

Table 8.21 shows a thrust power of 2210 W for the concept design when considering a 56.25 % efficient power train. This power is very low as the motor was scaled to produce 50,000 W.

C_{D_∇} = 0.0051 does not include the drag of control surfaces or appendages and consequently will increase for the operational AUV. However, to require 50000 W for propulsion power with the same volume the C_{D_∇} value would have to increase to 0.205. The P_{Prop} estimate at the

beginning of the design cycle was a gross overestimate so the motor is overpowered for the design that has emerged.

Only 5 % of the total energy stored is used over the mission and this is considered overlarge and the design method will be iterated. This AUV has a *Mass Ratio* of 0.819, which is higher than any AUV presented in Chapter 4. A high *Mass Ratio* would be indicative of this AUV's prime design driver being endurance at high velocity, but might suggest that more payload should be fitted to make use of the energy available.

This concept would achieve the desired mission objectives, but it would not do so within the objectives of minimal volume and mass. A second iteration will re-evaluate the key decision of motor and energy source.

8.3.3 Second iteration.

From the results of the first iteration, P_{Prop} and the motor were over estimated. The candidate AUV P_{Prop} was 2210 W at sprint speed (6 ms^{-1}). The drag prediction is anticipated to decrease with a smaller energy source volume. Therefore a new motor will be sized that will provide a similar power. Panasonic batteries will be selected as the energy source.

Sea Max THL-404-8 thrusters from Deep Sea Systems (www28) provide up to 43 kgf, 422 N at a max power of 2500 W. This will replace the 50 kW motor in the first iteration and the revised nested dimensions are given in Table 8.22.

Table 8.22 Sea Max THL-404-8 thruster nested properties.

Structure	Length m	Breadth m	Depth m	Volume m^3	Mass kg	Power W	Pressure tolerant?	Constraints
Motor	0.466	0.114 diam	0.114 diam	0.0044	11.8	up to 2500	Y	Stern placement.

From Table 8.21, the concept AUV required 12150 Wh of energy at 2548 W. This is achieved by 1444 of Panasonic CR18650E secondary batteries with a mass of 67.146 kg (0.0427 m^3). The energy source is much smaller than the first iteration and thus requires a smaller pressure vessel.

As for the first iteration, the pressure vessel was sized to provide buoyancy to achieve neutral buoyancy when combined with the pressure tolerant subsystems. These had a total mass of 41.6kg and a displaced volume of 0.0194 m^3 requiring 21.715 kg of buoyancy. The pressure vessel has to contain 37.7 kg of base hotel subsystems and 67.146 kg of energy source. The properties of the new pressure vessel are given in Table 8.23.

Table 8.23 Pressure vessel properties when housing 67.146 kg of Panasonic CR18650E lithium ion batteries for case study A.

Pressure vessel properties.	Designed to resist material yield & buckling.
Material	Titanium IMI 318
Outer radius	0.2283 m
Overall length	1.240 m
Wall thickness	0.0073 m
Internal volume	0.1369 m^3
Displaced volume	0.1782 m^3
Sufficient volume for internal components?	Yes
Mass in air of pressure vessel	56.0 kg
Mass in air including internal components	160.9 kg
Total buoyancy	21.715 kg

The total AUV mass is sum of the mass of the pressure vessel (including associated internal subsystems) and the mass of the pressure tolerant subsystems, thus $M_{AUV} = 202.5$ kg.

This pressure vessel and motor replace those in Table 8.15 and the energy source can be removed from consideration. The other subsystems in Table 8.15 have not changed. Therefore the design proceeds to the hydrostatic balancing of the possible subsystem arrangements.

The automated process is repeated for the second iteration properties and the *CoG* and *CoB* for the difference possible arrangements are shown in Figure 8.8. The difference has increased to a maximum magnitude of -8 %. This increase is because the pressure vessel is smaller and does not dominate the mass balance of the AUV as greatly as the first iteration. Therefore mass balance is more sensitive to the position of smaller subsystems.

CoB and *CoG* occur at the same location, (difference: $(CoB - CoG) / L_{AUV} = 0.0$ %), for four subsystem arrangements. These arrangements are fitted with a parallel middle body hull shape and shown in Figure 8.9.

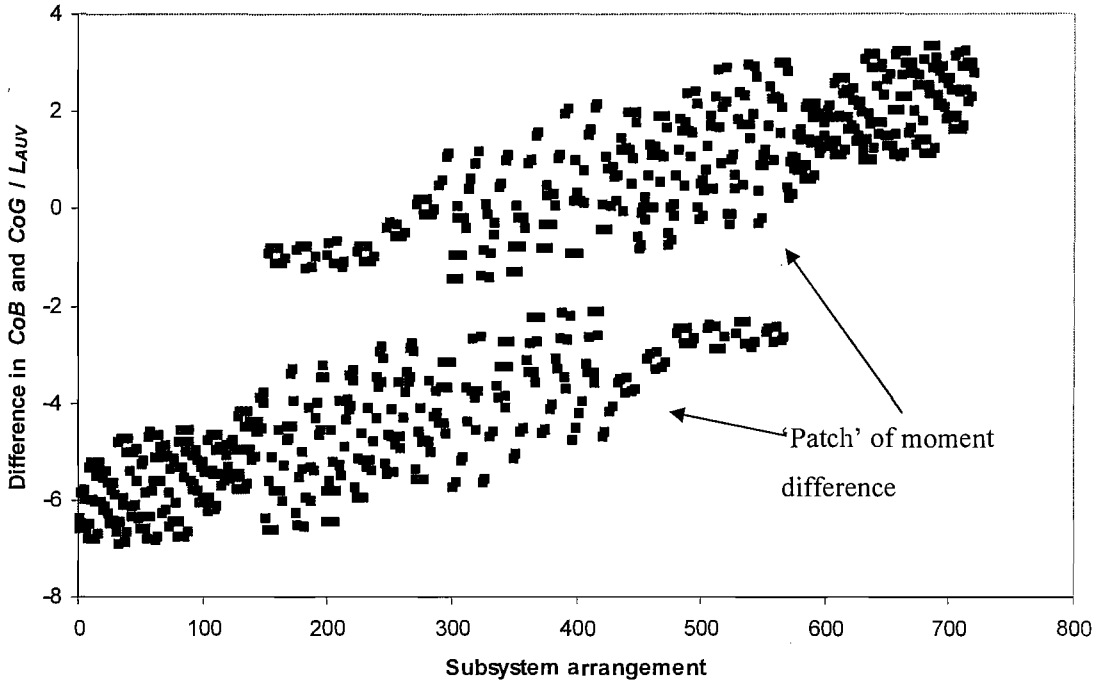

Figure 8.8 Difference between *CoB* and *CoG* as a proportion of L_{AUV} with subsystem arrangement for case study A with Panasonic batteries.

Because of the smaller energy source and required pressure vessel, the fitted hull shapes are much smaller than the first iteration, resulting in less wasted space. The pressure vessel is still the largest subsystem and dominates the hull shape.

The pressure vessel is the same distance from the bow for Figure 8.9*i* and Figure 8.9*ii*, therefore these two have identical hull shape input parameters. However, the different subsystem arrangements result in different available volume estimates (0.0011 m^3). This is an error, as there should be the same available volume for a particular hull shape irrespective of internal arrangement. The error is caused by the Simpson's integration used to find the hull shape volume within the code and the volume estimates appear to be accurate to 2 decimal places. Whilst the hull shape volume for profiles defined by algebraic expressions can be found analytically, this would have to be processed manually for each hull shape profile. The Simpson's numerical integration allows an automated estimate for any hull shape geometry.

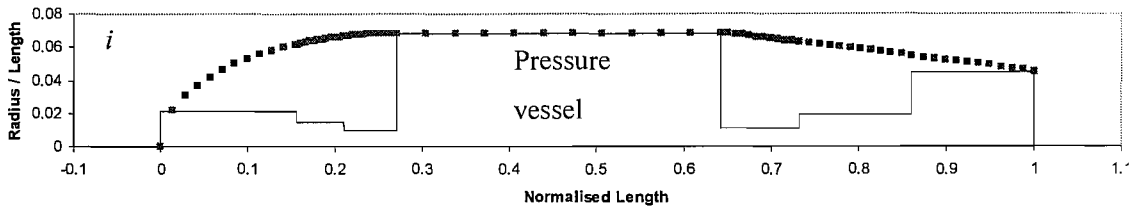

Hull shape volume = 0.4377 m^3, available volume (wasted space) = 0.1891 m^3

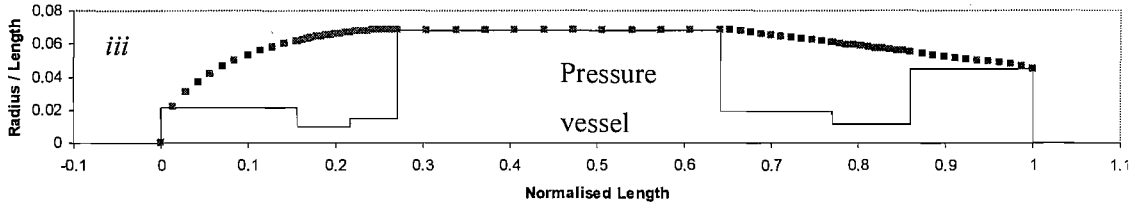

Hull shape volume = 0.4377 m^3, available volume (wasted space) = 0.1902 m^3

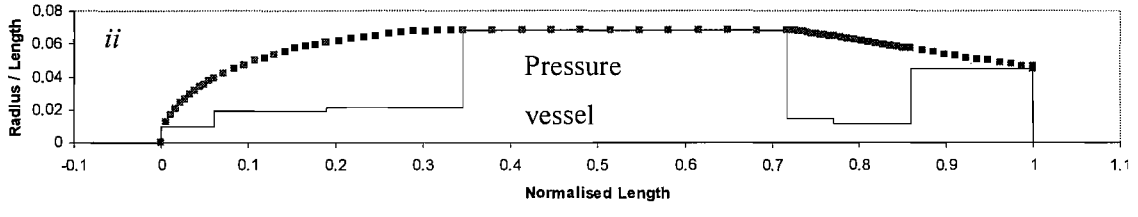

Hull shape volume = 0.4365 m^3, available volume (wasted space) = 0.1859 m^3

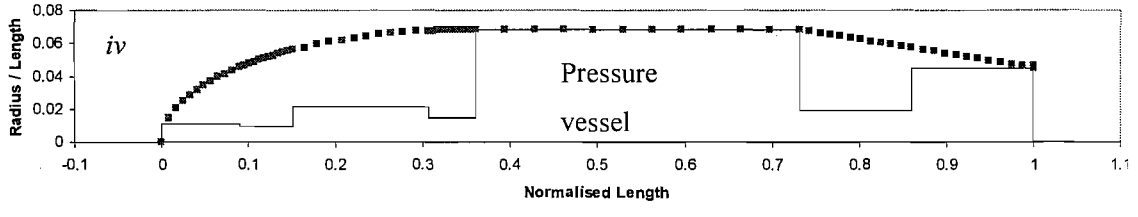

Hull shape volume = 0.4363 m^3, available volume (wasted space) = 0.1843 m^3

Figure 8.9 Example AUV subsystem arrangements with a parallel middle body hull shape for the 2nd iteration of case study A.

The hydrodynamic performance of the four hull shapes presented in Figure 8.9 is shown in Table 8.24. Figure 8.9*iv* has the lowest drag as it has the longest bow. The hull shape profile input parameters for Figure 8.9*iv* are furthest from the base Autosub hull shape parameters

(0.3667), and will have greatest drag error due to the linear approximation. Figure 8.9*i* and Figure 8.9*ii* have the same hull shape and so have the same drag prediction, 165.9 N.

The four parallel middle body hull shapes have very similar estimates of volume and wasted space. Selection of a candidate should therefore be based upon the drag estimates.

Table 8.24 Drag predictions for Panasonic batteries fitted with a parallel middle body hull shape for the 2nd iteration of case study A.

Example	BMT m	MST n	Maximum radius of AUV, R_{Max} p	Estimated C_{D_∇}	Difference from base model	Estimated drag at 6 ms^{-1} N
Figure 8.9*i*	0.2703	0.6419	0.0684	0.0156	0.1869	165.9
Figure 8.9*ii*	0.2703	0.6419	0.0684	0.0156	0.1869	165.9
Figure 8.9*iii*	0.3449	0.7165	0.0684	0.0149	0.3361	158.2
Figure 8.9*iv*	0.3602	0.7318	0.0684	0.0147	0.3667	156.0

A laminar flow hull shape is also fitted to the four arrangements, see Figure 8.10. The arrangement with the smallest parallel middle body hull shape, Figure 8.9*iv*, gives the largest laminar hull shape hull shape, Figure 8.10*iv*. However, the difference between the four laminar hull shape volumes is very small: 0.0004 m^3. This is because the pressure vessel placement does not vary greatly and so the hull shape profile is similar for each arrangement.

The transom stern radius of the shapes in Figure 8.9 and Figure 8.10 is constrained by the motor radius and is large compared to the hull shape maximum radius. This gives a very large shape change and would likely cause boundary layer separation and a large wake. Further shaping of the stern and analysis of the flow through the propeller would be important for these concept AUV designs.

Similar to the parallel middle body, the selection of a candidate laminar flow hull shape should be based upon drag estimates, Table 8.25. However as the shape does not vary much (the parallel middle body bow length varied) the drag estimates are very similar to each other. Figure 8.10*i* and Figure 8.10*ii* have the same parameters as the base model, therefore have a difference of 0.0.

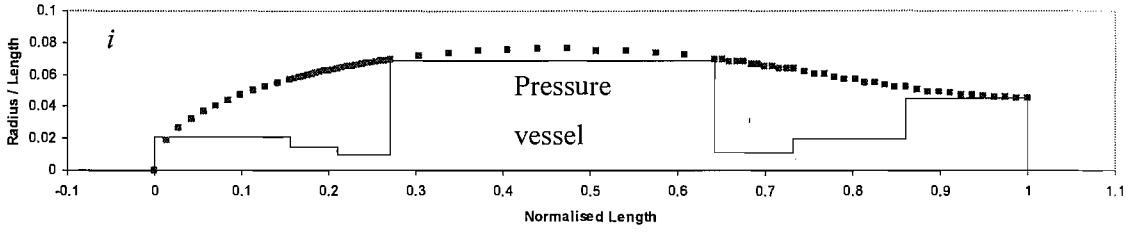

Hull shape volume = 0.4529 m^3, available volume (wasted space) = 0.2059 m^3

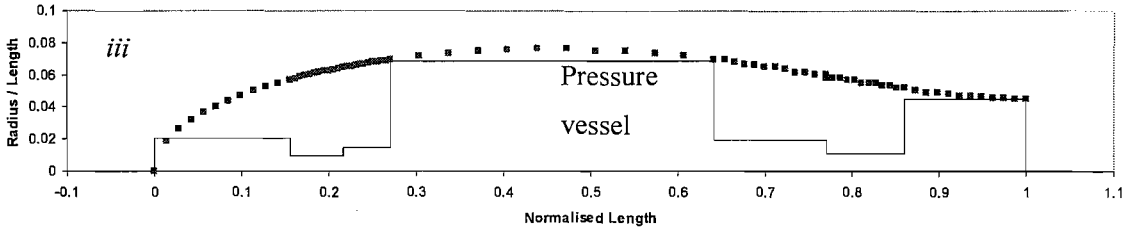

Hull shape volume = 0.4529 m^3, available volume (wasted space) = 0.2061 m^3

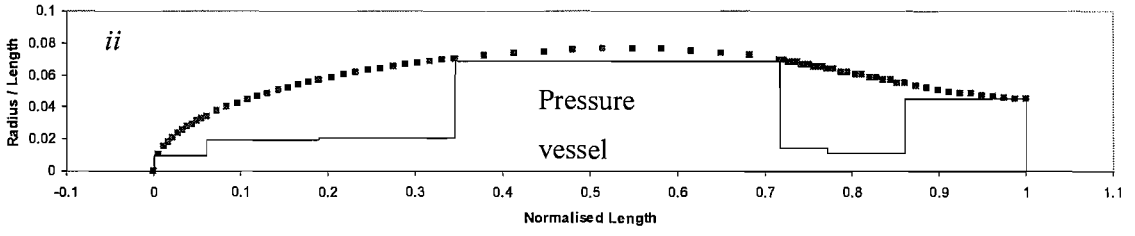

Hull shape volume = 0.4532 m^3, available volume (wasted space) = 0.2055 m^3

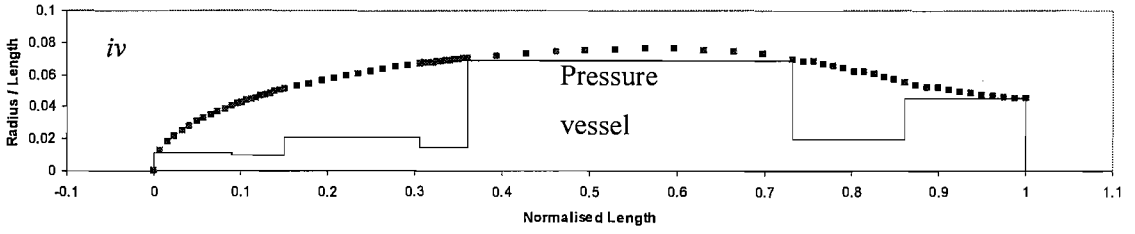

Hull shape volume = 0.4533 m^3, available volume (wasted space) = 0.2044 m^3

Figure 8.10 Example AUV subsystem arrangements with a laminar flow hull shape for the 2nd iteration of case study A.

Table 8.25 Estimated $C_{D\nabla}$ and drag for example Rutherford hull forms showing non-dimensional parameters for 2nd iteration of case study A.

Example	Bow curvature m	MST n	Maximum radius of AUV, R_{Max} p	Estimated $C_{D\nabla}$	Difference from base model	Estimated drag at 6.0 ms^{-1} N
Figure 8.10*i*	2	0.4645	0.0764	0.0160	0.0	174.1
Figure 8.10*ii*	2	0.4645	0.0764	0.0160	0.0	174.1
Figure 8.10*iii*	2	0.5694	0.0764	0.0159	0.105	173.1
Figure 8.10*iv*	2	0.5993	0.0764	0.0159	0.1358	173.1

Due to the similarities of all the laminar flow hull shape results of volume, wasted space and drag prediction, there is no defining difference between the four arrangements. The parallel middle body hull shape does offer two concepts that have a lower drag than the other options, Figure 8.9*iii* and Figure 8.9*iv*. Figure 8.9*iv* will be selected as the candidate hull design as it is slightly smaller than Figure 8.9*iii*. The current candidate hull design is compared against mission requirements next.

Does concept AUV fulfil mission requirements?

The volume, energy capacity and $C_{D\nabla}$ for the concept AUV have been found. All the parameters to evaluate AUV performance are known. The performance of the concept design, Figure 8.9*iv*, over the mission is presented in Table 8.21.

The concept AUV weighs 202.5 kg, and has a hull volume of 0.4363 m^3. This is much smaller than the 1565.487 kg, 3.267 m^3 concept vehicle from the first iteration. The free-flooding volume has decreased between iterations, from 1.337 m^3 to 0.1843 m^3. The AUV has a *Mass Ratio* of 0.33, which is higher than the AUVs reviewed in Chapter 2 and is indicative of the high speed and power requirements of this mission.

76 % of the stored energy is used by the AUV over the mission. This is an improvement over 5% of the energy used by the first AUV concept. The drag of the vehicle will increase once control surfaces and appendages are added, so more power will be used for propulsion. Improved $C_{D\nabla}$ estimates from Chapter 6 would also affect the drag force. At the end of the mission some energy is desired in case of recovery problems. Therefore, using 76 % of the energy at this stage

of the design is considered satisfactory. This concept AUV can be passed to the detailed design stage.

Table 8.26 Concept AUV after one full iteration of design methodology.

Parameter	Value
AUV volume	$0.4363m^3$
AUV mass	202.5 kg
Available volume, assumed to be free flooding.	0.1843 m^3 based on nested volume (0.2387 m^3 based on displacement volume)
Mass of energy	67.146 kg
Energy source density	188 Wh kg^{-1}
$C_{D\nabla}$	0.0147
Hotel Power	48 W
Payload Power	3.6 W
Total energy consumed by hotel and payload	1626 Wh
Thrust power @ 6 ms^{-1} with 56.25 % efficiency	1664 W
Thrust power @ 1 ms^{-1} with 56.25 % efficiency	8 W
Total energy consumed by propulsion	7937 Wh
@ sprint	7704 Wh
@ survey	11 Wh
@ return	222 Wh
Total energy used over mission	9563 Wh
% of stored energy used	76 %

8.3.4 Case study A conclusions

The design methodology has been followed through two complete iterations, with discussion at each stage of the process. Two options for the energy source have been described and the methodology applied to each. The key decision at the start of the design process has been shown to be important. In this case study the AUV energy source was oversized on the first iteration.

5040 possible combinations (8 factorial) have been tested by the automated code. For the Panasonic energy source, these arrangements were filtered down to 18 in the first iteration and down to 4 in the second iteration. Automatically considering all possible arrangements ensures that none are overlooked. 5040 combinations could not easily have been investigated by an engineer.

By showing two iterations of the design, reconsidering the energy source and pressure vessel, the advantage of rapidly estimating $C_{D_{\nabla}}$ is shown. Without this approximation each concept would have to be tested individually, increasing the time and economic cost of the design method.

The pressure tolerant energy source created the largest AUV hull shape, as it required foam buoyancy to make the AUV neutrally buoyant. The radius of the energy source created a large hull shape with excess volume above that required by the foam buoyancy. The pressure vessel containing the Panasonic energy source was sized to make the AUV neutrally buoyant so no foam was required. The disadvantage was that any available space within the hull shape becomes free flooding.

The Panasonic energy source required a large pressure vessel. This pressure vessel dominates the hull shape and fits best within a long parallel middle body. It was possible to reduce the radius of the pressure vessel to give a smaller radius AUV, but this would increase the length of the pressure vessel, making the AUV longer. Additionally the mass of the pressure vessel would increase to resist buckling failure.

The pressure tolerant energy source and small pressure vessel created a heavier AUV concept than the Panasonic energy source packed within a large pressure vessel. At this diving depth the pressure vessel provides all the buoyancy for the AUV. The next case study will operate at a greater depth, and the mass of any pressure vessels used will increase.

The hull shape provided an outer boundary for the buoyancy foam and further filtered the subsystem arrangements. The hull shape is controlled by the largest subsystem. In this case study the pressure tolerant energy source or the pressure vessel containing the pressure sensitive energy source are the largest subsystems. There are fewer options when dimensioning a pressure vessel due to the requirement of resisting pressure forcing a cylindrical shape. The pressure tolerant energy source could be almost any shape, giving more options for the initial dimensions. Further work might explore axis-asymmetric shapes with the objective to finding optimum dimensions of a pressure tolerant energy source.

Quantifying the initial decision of the design is crucial to the rest of the design. Selecting a motor gave a starting point to estimate the propulsion power, hence size the energy source and

AUV volume. The next case study will consider other options for the first estimate of energy capacity.

The final concept AUV can fulfil the mission. It is a parallel middle body hull shape, has a mass of 202.5 kg, and uses 76 % of its stored energy. The energy source consists of 67.146 kg of Panasonic CR18650E secondary batteries stored within a pressure vessel. A deep diving case study is discussed in the next section.

8.4 Case study B- Deep sea exploration AUV.

This case study applies the design methodology to mission description B for a deep diving AUV. Although the principal objective is to compete with the SAMS AUV, the design will not copy the hull shape or internal structure of SAMS.

The key decisions made in this design are:

- Energy capacity - specification of energy mass to AUV mass ratio.
- Hull shape selection
- Placement of side scan sonar outside of hull

The design methodology again follows the procedure summarized in Figure 8.1.

Payload navigation and components.

The navigational system will be based upon the bottom track model, as the AUV will need a detailed map of obstacles when nearing the work site. When in the water column, the AUV will use its altimeter to establish depth, and then ascend / descend in a spiral until GPS or ADCP contact is made. Also included is a GPS system for when the AUV is at the surface.

The design boundary specified subsystems are stated in Table 8.27. The volume and mass are accurate to the actual piece of equipment, the length, breadth and depth (or diameter) are the dimensions of the bounding box in which the equipment is nested.

The Edgetech side scan sonar has to be mounted along the length of the AUV, and so would require a parallel middle body along this length. This side scan sonar must also be mounted on the periphery of the AUV hull, not along the centreline, and so cannot be immediately included within the automated arrangement method described in Chapter 7. For this case study the side scan sonar will be mounted along the hull shape side, outside the hull, and so represented by a point mass of length 0.0 that occurs between subsystems in the arrangement. This is an approximate estimate as the sonar could be moved along the length of a subsystem, but it enabled the automated design method to arrange the subsystems.

The engineer is now tasked with finding the unknown subsystems to complete the list ready for hydrostatic arrangement. Therefore the energy source and pressure vessel need to be selected and sized.

Table 8.27 Specified hotel and navigational payload for case study B.

Item	Length m	Breadth m	Depth m	Volume m^3	Mass kg	Power W	Pressure tolerant?	Constraints
Navigation								
Base hotel package	0.955	0.354 diam	0.354 diam	0.09400	37.7	46.0	N	
300 kHz ADCP)	0.228 diam	0.228 diam	0.211 diam	0.00290	14.5	5.0	Y	
Altimeter	0.180	0.096 diam	0.096 diam	0.00130	2.6	2.0	Y	
Structure								
Motor	0.140	0.300 diam	0.300 diam	0.00960	28.0		Y	Placed at stern lengthwise
Payload								
CTD	0.520	0.140 diam	0.140 diam	0.00850	20.7	3.0	Y	Pump included
Wetlabs BB2F optical backscatter	0.256	0.063 diam	0.063 diam	0.00054	1.3	0.9	Y	(www24)
Edge tech Side scan sonar 2200S	0.0 (0.780)	0.076	0.038	0.00225	7.3	30.0	Y	Adapted for an AUV. Must go lengthwise (www29)
Totals								
Total hotel and navigation				0.11010	54.8	53.0	N	
Total payload				0.01148	29.3	33.9	Y	
Total structure				0.00960	28.0		Y	Power draw dependant on hull
AUV minimum system	1.324 m (2.104)	0.300	0.300	0.13120	112.1	86.9		

Create pressure vessel for sensitive components.

A cylindrical pressure vessel is required to house the pressure sensitive components. The collapse depth is 6500 m with a safety factor of 1.2 (20 % is an arbitrary value for metals with

uniform and known characteristics). For this case study the pressure vessel will have a minimum internal radius of 0.177 m (largest radius of internal subsystems not including length, Table 8.11). It must also provide a volume of 0.094 m^3 (Table 8.11). The radius constrains the pressure vessel length. The wall thickness can be found by considering pressure vessel yield and buckling.

The pressure vessel characteristics are given in Table 8.28.

Table 8.28 Pressure vessel properties for mission navigation and control.

Pressure vessel properties.	Designed to resist material yield	Design to resist buckling
Material	Titanium IMI 318 (Ti – 6Al – 4V)	Titanium IMI 318 (Ti – 6Al – 4V)
Outer radius	0.1937 m	0.2002 m
Overall length	1.256 m	1.271 m
Wall thickness	0.0167 m	0.0232 m
Internal volume	0.09419 m^3	0.09419 m^3
Displaced volume	0.1328 m^3	0.1431 m^3
Sufficient for internal components?	Yes	Yes
Mass in air when empty	106.704 kg	151.395
Mass in air including internal components	144.404 kg	189.095
Total buoyancy	-8.252 kg	-42.384 kg

Select energy source and size.

The deep diving depth of the AUV implies that were a pressure sensitive energy source used, the mass of the pressure vessel required to protect it would take a large proportion of the mass budget and create a heavy AUV. The pressure tolerant lithium polymer batteries were tested for this reason and their performance 60 MPa pressure (equivalent to 6000 m) is discussed in Chapter 4.

A minimum energy source size limit can be set by considering the energy required over the hotel and payload for the 32 hour duration. The GPS system will only be used at the surface, and so will only be active for a fraction of the mission duration. The active duration is determined by the time required for a surface vessel to recover the AUV. There will be a recovery location programmed within the mission, and the distance from this point will depend on navigational error from the on board subsystems. This error is a function of mission duration, so in this example the time at the surface will be assumed to be 10 % of the mission time.

The ADCP and side scan sonar will only be active when nearing the sea-bed. The mission time at the sea bed will depend on the speed of ascent and descent. If the AUV flies at 45 °, the ascent and descent speed will be 1.414 ms^{-1} when maintaining its 2 ms^{-1} cruise speed It will take the AUV 1.18 hours to travel from the surface to the sea bed, and the side scan and ADCP are assumed to be activated after 1 hour in preparation for sea bed contact.

Table 8.29 shows the expected energy usage for the AUV subsystems during the mission, excluding the demands of propulsion power. From Chapter 4, the pressure balanced lithium polymer battery pack has an energy density of 102.3 $Whkg^{-1}$ and a mass density of 1960 kgm^{-3}, including protection, battery management system and structure. 1743.8 kWh would require 17.05 kg of lithium polymer battery pack. This is smaller than the battery packs made for Autosub 6000 and so may have a different energy density. However, the propulsion power has not yet been estimated and will increase the required energy source capacity.

Table 8.29 Power usage and total power requirement estimation of hotel and payload for case study B.

Source – when active	Power	Duration	Energy
	W	Hours	Wh
Propulsion	Unknown	Unknown	Unknown
Only active at surface	35	3	105
Only active at depth	35	26.8	938
Through out mission	21.9	32	700.8
Total energy usage (Wh)			1743.8 + unknown

This first energy source capacity estimation is a key decision for the design. This estimation would benefit greatly from prior knowledge, either from a type ship design, engineer experience or many iterations of the design cycle. Without any appreciation of the hull shape or propulsion power, it is not known what energy capacity is required, and so this must be checked once a hull shape has been defined. Case study A based the energy capacity on an estimate of propulsion power. This illustrated the iterative nature of such an energy capacity estimate. This case study will base the energy source mass on a prediction of the total AUV mass.

From Chapter 2 it is known that no described AUV capable of 1500 m depth operation had a *Mass Ratio* greater than 25 %. Autosub 6000 now improves on this with 26.5 % of its mass

allocated to the M_E. For this case study, as a challenge, the *Mass Ratio* will be set to 30%. The AUV mass equation from Chapter 7 is repeated here, equation 8.3.

$$M_{AUV}\left(1 - Mass\ Ratio - \frac{\rho_B Mass\ Ratio}{\rho_W - \rho_B} + \frac{\rho_W \rho_B Mass\ Ratio}{\rho_E(\rho_W - \rho_B)}\right) = M_{SS} + \frac{\rho_B M_{SS}}{(\rho_W - \rho_B)} - \frac{\rho_W \rho_B \nabla_{SS}}{(\rho_W - \rho_B)} \quad 8.3$$

The mass of the other subsystems is known (263.495 kg including pressure vessel), so M_{AUV} can be estimated. The overall AUV mass is estimated at 744.408 kg, 257.591 kg of which is foam buoyancy requiring 0.444 m^3 of volume within the hull shape. The energy mass can be estimated as 223.322 kg (30% of the AUV), and with a density of 1960 kg m^{-3}, a lithium polymer battery energy source will have a volume of 0.114 m^3 and store 22846 Wh of energy.

For comparison, a pressure sensitive energy source might be chosen. This will be considered briefly to illustrate the potential mass saving of a pressure tolerant energy source. A second titanium cylindrical pressure vessel rated at 6500 m would store the energy source for a total mass of 223.322 kg. This pressure vessel would have to be neutrally buoyant in order that no more foam is required and the AUV mass is not increased. The pressure vessel mass would use a large amount of the 223.322 kg available, leaving very little for the energy source. With no dimensional constraint, the mass of the pressure vessel is sensitive to the length and radius. A long pressure cylinder will have a small radius (to maintain a constant volume) and require a thick pressure vessel wall to resist failure at pressure. A short pressure vessel will have a larger radius and require a thinner wall thickness to resist failure.

Creating a cylindrical pressure vessel using the same method as of Appendix B, gives a pressure vessel with mass of 166.0 kg and displacement volume of 0.2178 m^3. This would support 57.322 kg of Panasonic CR18650E secondary batteries. With an energy density of 188 Wh kg^{-1}, these batteries would store 10777 Wh of energy. This is 47 % of the energy stored by using pressure tolerant lithium polymer batteries and so will not be used in this case study. Were an alternative primary battery energy source used, it would require access into the pressure vessel for maintenance and replacement. This would increase the AUV down time between missions and increase risk of damage to the pressure vessel seals.

Dimensioning the chosen lithium polymer battery energy source is a key decision. The maximum radius of subsystems in Table 8.27 is 0.300 m and the diameter of the pressure vessel is 0.3874 m. The decision might be made to fit the energy source within the diameter of the

pressure vessel, hence forming a cuboid 0.283 m by 0.283 m and 1.421 m long. A cube was selected, each side measuring 0.485 m, giving a nested diameter of 0.686 m.

The unknown subsystems have now been sized and can be included in Table 8.27. The subsystem list has been created and is ready to be passed to the hydrostatic balancing process.

Hydrostatic arrangement

The Matlab code found all the possible arrangements and the required lever arm for foam buoyancy. Figure 8.11 shows the L_{Foam} required for the buoyancy foam to balance each of the 5040 (7!) possible arrangements.

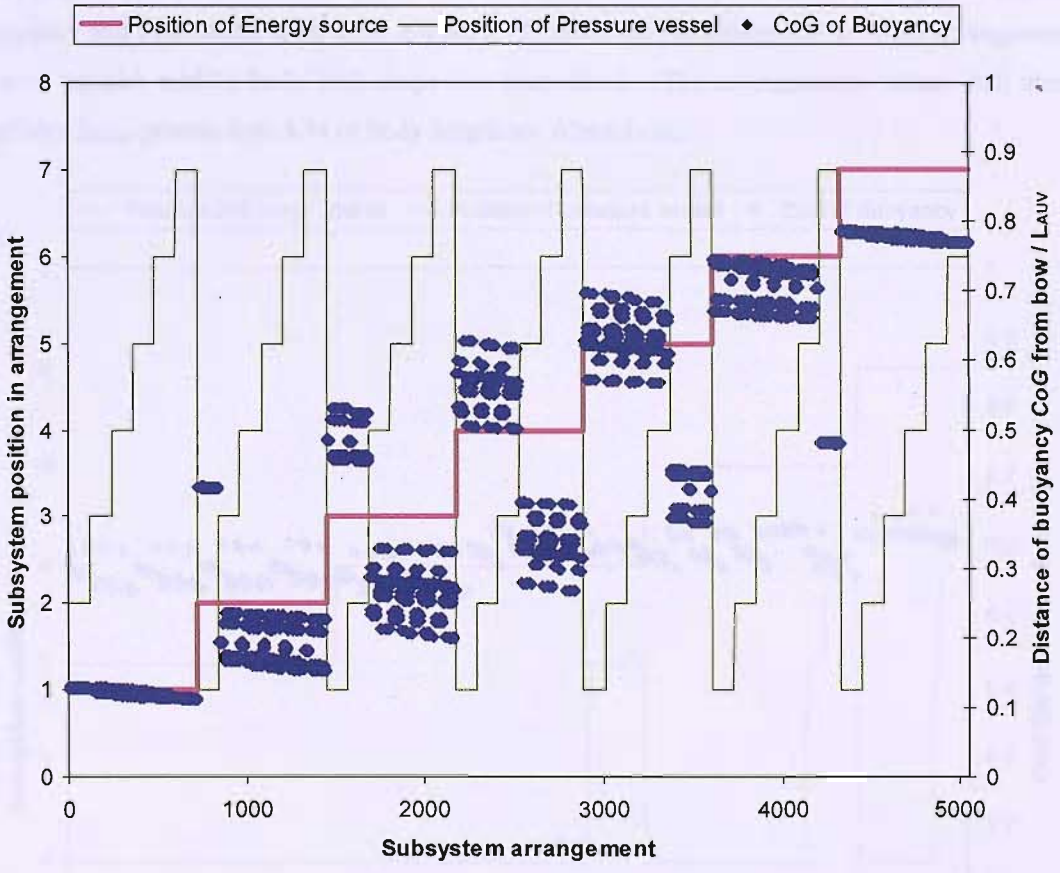

Figure 8.11 *CoG* of the buoyancy (L_{Foam}) with position of energy source and pressure vessel for case study B.

L_{Foam} occurs between 0.29 and 0.76 of the AUV length for all the arrangements, so none are filtered from consideration at this stage. Similar to section 8.3 L_{Foam} in Figure 8.11 is most sensitive to the energy source, and then the pressure vessel. The engineer can either decide where the largest subsystem is to occur, and find where the foam will be, or select L_{Foam} and find what

arrangements are possible. For example, if the energy source was the first subsystem, L_{Foam} will occur around 0.3 of the length, so whichever hull shape and arrangement is selected, the foam must be placed around this position, or split into multiple blocks.

Apply hydrodynamic constraints

A hull shape can be fitted about each arrangement in Figure 8.11 and the volume available for the foam, along with its *CoB*, can then be found. The previous case study in Section 8.3 shows the decision process when comparing hull shapes and verifying that the subsystems fitted within the hull shape. This process is automated for this case study. The parallel middle body is fitted over the subsystems to find the *CoB* of the available volume. This is checked against required buoyancy and hydrostatic lever arm. Figure 8.12 shows the remaining 325 possible arrangements after a parallel middle body hull shape has been fitted. The arrangements whose hull shape provides L_{Foam} greater than 8 % of body length are filtered out.

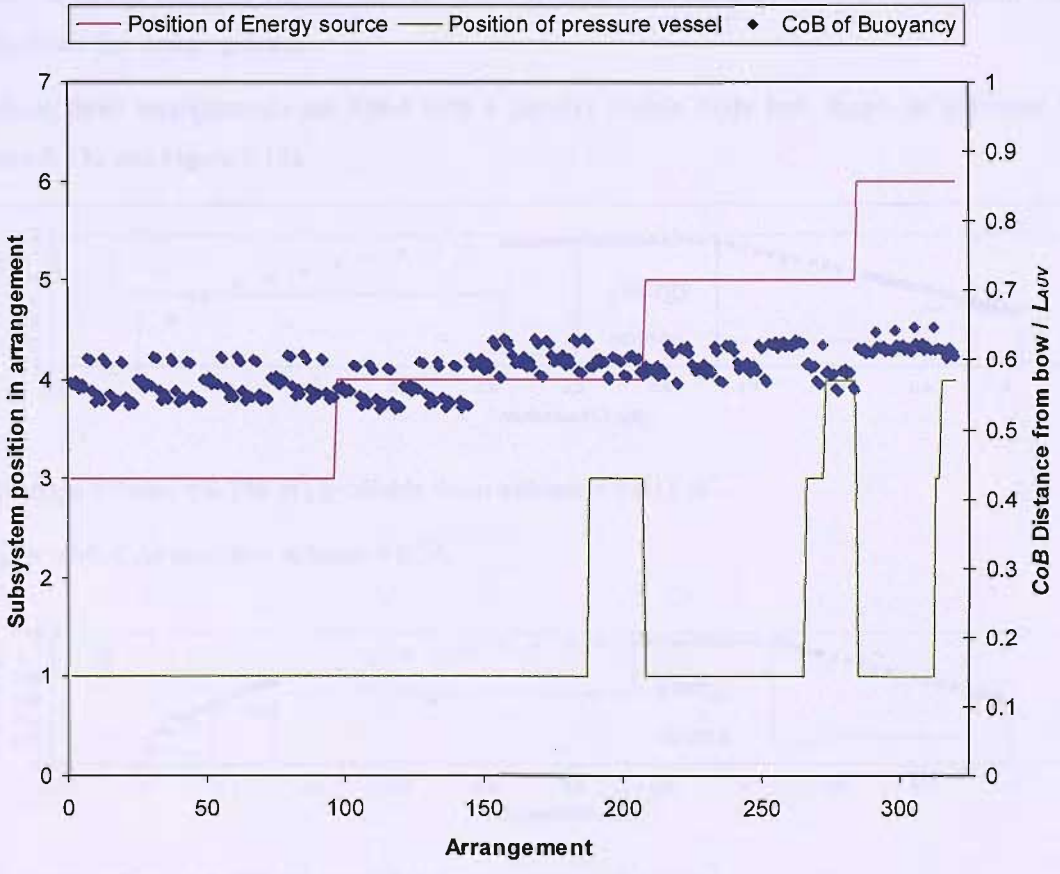

Figure 8.12 Foam *CoG* with subsystem arrangement filtered by hull shape fit for case study B.

325 possible arrangements is a large decrease from 5040 possible arrangements. The hull shape envelops all the subsystems after the first and it is assumed that adjusting the L_{Foam} placement of the first subsystem or the curve over the bow might occur in detailed design.

For all the arrangement possibilities the L_{Foam} occurs between 52.8 % and 64.9 % of AUV body length. All arrangements place the energy source between third and sixth, and 278 place the pressure vessel first. Placing the pressure vessel at the bow has practical implications; any damage to the pressure vessel will reduce its structural strength. However, the pressure vessel has spherical endcaps, and so may align with the bow curvature at the leading edge. The remaining 47 arrangements place the pressure vessel either third of fourth with the energy source behind. None of the possible arrangements placed the largest subsystem (energy source) first. As example candidate designs, one arrangement with the pressure vessel first and two arrangements from the 47 which placed the energy source third or fourth, are selected and have a hull shape fitted. A design engineer should consider more arrangements but only three are considered here to illustrate the design process.

These three arrangements are fitted with a parallel middle body hull shape, as indicated in Figure 8.13a and Figure 8.13b.

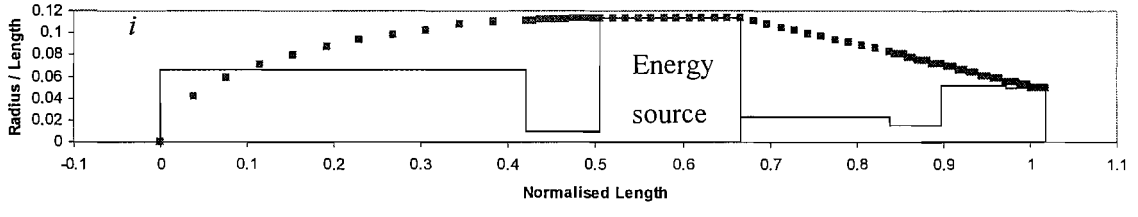

Hull shape volume = 0.759 m^3, available foam volume = 0.411 m^3.

L_{Foam} = 0.54, *CoB* available volume = 0.54.

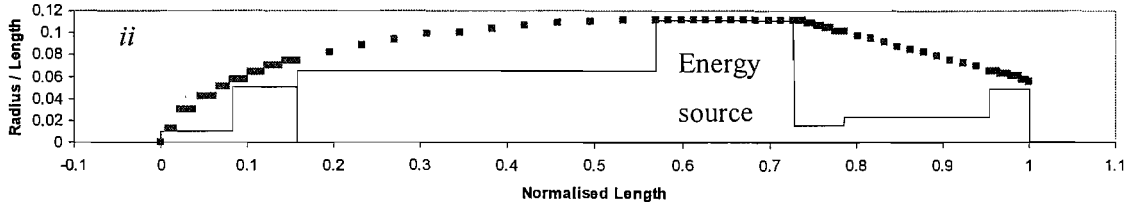

Hull shape volume = 0.780 m^3, available foam volume = 0.430 m^3.

L_{Foam} = 0.60, *CoB* available volume = 0.55.

Figure 8.13a Possible arrangements and selected parallel middle body hull shape.

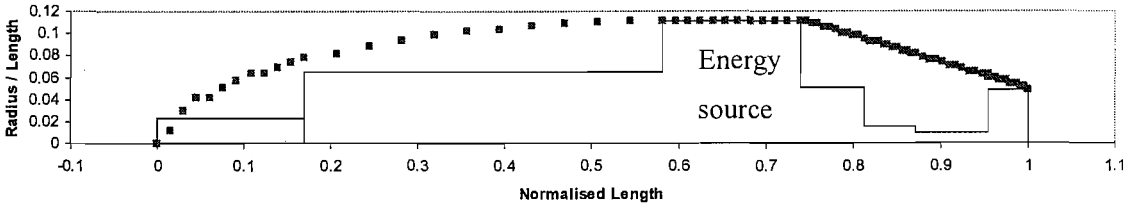

Hull shape volume = 0.782 m^3, available foam volume = 0.434 m^3.

L_{Foam} = 0.59, *CoB* available volume = 0.53.

Figure 8.13b Possible arrangements and selected parallel middle body hull shape.

Figure 8.13a*i* shows an arrangement with the pressure vessel placed first. The hull shape will have to be altered to surround the pressure vessel, but depending on the pressure vessel endcap it may be possible to create a smooth bow. This hull shape has less than 0.444 m^3 of foam, so requires 0.033 m^3 more available volume, but is currently hydrostatically balanced. Figure 8.13a*ii* and Figure 8.13b are very similar hull shapes because of similar subsystem arrangements and there is little to separate these two designs. Both are slightly hydrostatically unbalanced (5 % and 6 %) but both require additional volume for foam (0.014 m^3 and 0.010 m^3). This additional volume might be used to hydrostatically balance the shape. For the first iteration the decision regarding which subsystem to place at the bow may guide the next iteration.

Table 8.30 Estimated $C_{D\nabla}$ for example parallel middle body hull shapes showing non - dimensional parameters for case study B.

Example	BMT	MST	Maximum radius of AUV, R_{Max}	Estimated $C_{D\nabla}$	Difference from base model	Estimated drag at 2.5 ms^{-1}
	m	*n*	*p*			N
Figure 8.13a*i*	0.4958	0.6532	0.1114	0.0095	0.4667	25.3
Figure 8.13a*ii*	0.5698	0.7273	0.1114	0.0088	0.6148	23.9
Figure 8.13b	0.6282	0.7857	0.1114	0.0082	0.7316	22.3

Table 8.30 shows the predicted $C_{D\nabla}$ values of the candidate hull shapes. Estimated drag decreases as R_{Max} moves backwards, as defined by the position of the energy source, caused by the decrease of $C_{D\nabla}$. Figure 8.13b has the largest volume, lowest $C_{D\nabla}$ and lowest overall drag prediction. Based purely on hydrodynamics, this would be the hull shape selected, although it still needs refining. The values of drag prediction are for the bare body using the Schlichting skin

friction estimation. As these shapes have departed from the base model (lowest = 0.4667), the drag result may well change with the hydrodynamic model utilised.

The hull shapes in Figure 8.13a and b appear similar to the laminar hull shape, despite having been filtered for the parallel middle body. This is because the hydrostatic balance places the largest subsystem further than 50 % along the body. Therefore a laminar flow hull shape will be fitted to these arrangements. The C_{D_∇} value will be approximated using the equation found for the Rutherford model in Chapter 6.

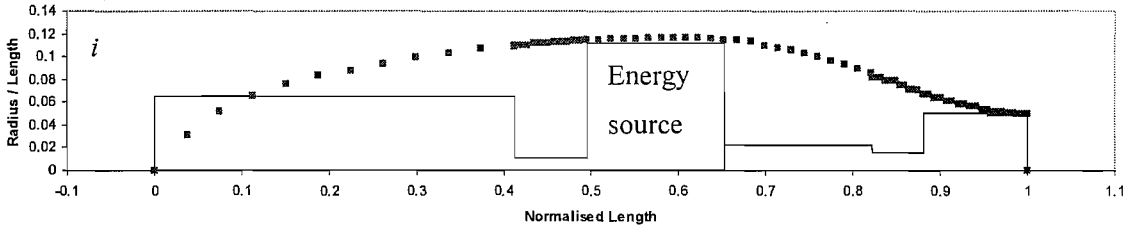

Hull shape volume = 0.785 m^3, available foam volume = 0.420 m^3.

L_{Foam} = 0.53, *CoB* available volume = 0.57.

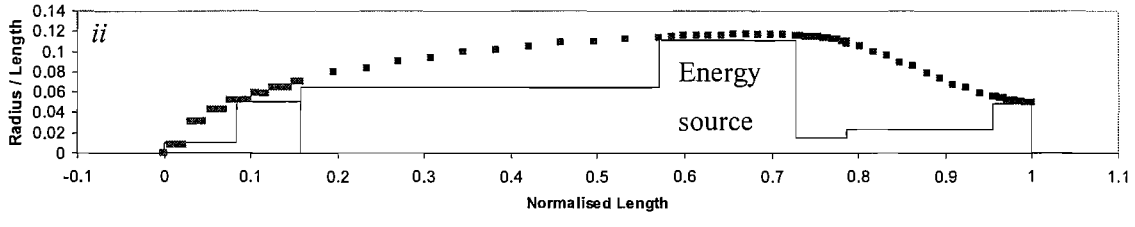

Hull shape volume = 0.798 m^3, available foam volume = 0.419 m^3.

L_{Foam} = 0.60, *CoB* available volume = 0.57.

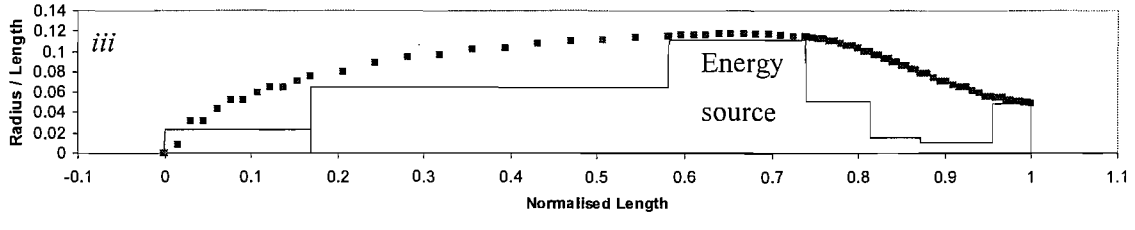

Hull shape volume = 0.796 m^3, available foam volume = 0.424 m^3.

L_{Foam} = 0.59, *CoB* available volume = 0.54.

Figure 8.14 Possible arrangements with Rutherford hull form for case study B.

Figure 8.14*i* has the same problem as the parallel middle body shape; the pressure vessel at the bow affects the hull shape. This will be even more critical when maintaining a laminar boundary layer. All three shapes require additional foam buoyancy to become neutrally buoyant, and are not hydrostatically balanced (within 5 %). This would be addressed in a second iteration used to refine the hull shape. Figure 8.14*ii* and Figure 8.14*iii* produce similar hull shapes, as the energy source defines the hull, and it has not moved greatly along the body. Therefore the C_{D_∇} and drag prediction for all three shapes will be comparable. Table 8.31 shows the predicted C_{D_∇} and drag of the arrangements with a Rutherford hull shape.

Table 8.31 Estimated C_{D_∇} and drag for example Rutherford hull forms showing non-dimensional parameters for case study B.

Example	Bow curvature *m*	MST *n*	Maximum radius of AUV, R_{Max} *p*	Estimated C_{D_∇}	Difference from base model	Estimated drag at 2.5 ms^{-1} N
Figure 8.14*i*	2	0.6169	0.1169	0.0120	0.1059	32.59
Figure 8.14*ii*	2	0.7143	0.1169	0.0119	0.2033	32.68
Figure 8.14*iii*	2	0.6981	0.1169	0.0119	0.1870	32.67

From Table 8.31, the drag estimates are very similar, consequently selection of the hull shape should not be purely based upon drag estimate.

These six hull shapes (both parallel middle body and laminar flow) result from a single iteration of the design method. From the original 5040 arrangements, the concept design has been filtered to 47 arrangements that could be hydrostatically balanced and do not place the pressure vessel at the bow. It might be feasible to pass all these arrangements to the next design iteration.

To continue with the case study, Figure 8.14*ii* will be considered as the preferred candidate design and its performance evaluated. This concept has both a small subsystem at the bow and is the most hydrostatically balanced of the laminar flow hull shapes. The parallel middle body hull shapes give lower overall drag predictions, but has greater differences compared to their base model. Additionally they resemble laminar flow hull shapes due to the long BMT length. Both hull shapes might be selected as candidate designs, and for this example Figure 8.14*ii* was selected.

Further research might investigate a generic expression for $C_{D\nabla}$. A generic expression that can evaluate laminar flow and parallel middle body hull shapes would remove the decision based on hull shape. This would allow the designer to focus on finding a minimal drag prediction for the concept design.

Does concept AUV fulfil mission requirements?

The AUV total volume, energy capacity and $C_{D\nabla}$ have been found as a result of this design method. All the parameters to estimate the range of the AUV are known, and the concept design will be tested against mission objectives. These parameters are summarised in Table 8.32. The AUV volume is the hull shape envelope volume, not the exact displaced volume, and will be used for the $\nabla^{2/3}$ term.

Table 8.32 Concept AUV after one full iteration of design methodology.

Parameter	**Value**
AUV volume	0.798 m^3
AUV mass	744.407 kg
Mass of energy	223.322 kg
Energy capacity	22846 Wh
$C_{D\nabla}$	0.0119
Hotel and navigation power	53 W
Payload power	33.9 W
Thrust power @ 2.5 ms^{-1} with 56.25 % efficiency	145.2 W
Estimated endurance @ 2.5 ms^{-1}	98.411 hours
Estimated optimum velocity	1.67 ms^{-1}
Thrust power @ optimum velocity with 56.25 % efficiency	43.45 W
Estimated endurance at optimum velocity =	257.9 hours

The mission objective is to carry the specified payload to 6000 m depth at a velocity of up to 2.5 ms^{-1}, for 36 hours. The AUV has to have a mass of less than 1000 kg. All these parameters have been met, as shown in Table 8.32. The endurance at maximum velocity is over 2.7 times the required endurance, and the AUV mass is 74.4 % of the maximum mass. This AUV exceeds the mission requirements and improves on the SAMS AUV capabilities. Further refinement and

design iteration is required but there is scope for increasing AUV mass and drag prediction without failing to fulfil a mission requirement.

8.4.1 Case study B conclusions

This case study applied the design method to a deep diving AUV. The size of the energy source is still a key decision, as it became the largest subsystem and controlled the hull shape. The actual capacity of the energy source is then determined using the *Mass Ratio* introduced in Chapter 4. Dimensioning the energy source is still a decision based upon experience, though the radius of the other subsystems should influence the decision.

Earlier work suggested a mass advantage of pressure tolerant batteries over that of a large pressure vessel. This case study further supports this by utilizing pressure tolerant batteries to give increased energy capacity. A pressure sensitive energy source within a constant M_{AUV} would have 47 % of the energy capacity. There will be additional practical issues of maintenance and access of an energy source within a pressure vessel. Economic cost has not been considered as part of this study, and it will affect the selection of energy source.

The hydrodynamic filtering within the method can be automated, such that the list of possible subsystems can be more readily generated. However, this will limit engineer interaction with the hull shape, and might overlook design possibilities. In this case the parallel middle body shape was automatically filtered, but the laminar hull shape was shown to fit example arrangements. There was little difference between the concept hull shapes, and the design method could be iterated to refine the hull shape and produce a concept design. The mission would be completed by a concept from the first iteration, showing that a solution is possible, though more work might be done to the design.

8.5 Chapter conclusions.

This Chapter described two specific missions and introduced navigational and scientific payloads to enable mission completion. The design methodology presented in Chapter 7 is then applied to identify technically feasible candidate designs.

In case study A, possible arrangements were found on a first pass of the design cycle, but were rejected for being too large and only using 5 % of the energy source capacity. Pressure sensitive batteries and pressure tolerant batteries were considered and the dimensioning of these required iteration when fitting a hull shape. As this was a shallow mission, pressure sensitive batteries within a pressure vessel are a suitable option. The capacity of the energy source was based upon an expected propulsion power draw, assuming a specific motor was used. The high velocity

required a large energy capacity and made the energy source the largest subsystem. This greatly over estimated the propulsion power and oversized the AUV. Case study A highlighted that the properties of the energy source are a key decision and the influence the largest subsystem has on the hull shape.

A second iteration within case study A reduced the size of the Panasonic energy source and protective pressure vessel. This iteration improved the energy use over the mission from 5 % of energy capacity to 76 % of energy capacity. The concept found from the second iteration would be passed to detailed design.

For case study B, possible AUV arrangements have been found on a first pass of the design method, but are not hydrostatically balanced and require refinement. The energy source key decision was the selection of pressure tolerant batteries, and estimating the battery mass using the AUV *Mass Ratio*. The pressure sensitive energy source capacity was estimated to be 47 % of the pressure tolerant energy source, as the mass of the pressure vessel was included in the energy source mass. Case study B illustrates the advantage of a pressure tolerant energy source. The design method was successful in creating an AUV that had both greater endurance and less mass than the SAMS AUV.

Both case studies made use of the automated filtering within the design method. Case study A with the Panasonic batteries filtered 720 possibilities to 4 based on hydrostatic balance. Case study B filtered by comparison of the required foam volume and the available volume with the fitted hull shape to reduce 5040 arrangements to 47. This makes the filtered list of arrangements more accessible to an engineer.

Both case studies made use of the hydrodynamic equations generated in Chapter 6 to estimate $C_{D_{\nabla}}$ This gave quick estimates for each hull shape, and allowed the comparison of hull shape alterations at a constant cruising velocity.

The strength of this design method is that it can guide a solution for a concept mission without a pre-conceived AUV. The focus on hydrostatic arrangement means that the overall shape of the AUV need not be decided prior to the design. This makes hull shape less of a key initial decision.

The methodology does rely on quantified inputs from the mission specification. Accurate statements of objectives and estimation of the nested dimensions for included subsystems are needed to improve the candidate solution. The key decision of the energy source capacity will also have a large influence on the time to iterate the method to produce a concept AUV.

Chapter 9
Conclusions and recommendations.

This Chapter summarises the research presented and compares the outcomes to the objectives laid out in Chapter 1. It will highlight the contribution to science and discuss possible industrial applications. Lastly, there will be recommendations for future work.

9.1 Primary objectives.

By achieving the primary objectives set out in Chapter 1 the following contributions have been made to this field of research.

I – Creation of a structured design methodology incorporating energy source and hull shape influences.

A design method has been created that permits sensible arrangement of required subsystems and identification of type and capacity of energy source to fulfil specific mission statements. This facilitates moving AUV design away from variations of existing designs and towards the creation of novel AUVs. The design method is summarized through the flow chart provided. Some stages can be automated to seek out technically feasible solutions and the formal structure provides a clear progression of information through the process. Key decisions and constraints have been identified and discussed.

By analysing the mission requirements carefully it is possible to specify constraints and payload, the AUV design is focussed on completing the mission. This removes the need to retrofit and adjust existing technology and considers other design options.

The energy source is considered as a subsystem. The energy source type can be selected to match the operating depth and influence the mass of any required pressure vessel. The sizing of the energy source is based upon initial estimates of required capacity. The dimensions and arrangement of the energy source will influence the AUV hull shape. This has been illustrated in the presented case studies. The design method encourages iteration to refine the energy source type and size.

Identification of the hull shape is a key output of the design method. Internal subsystem arrangement significantly influences hull shape profile. Therefore understanding hull shape drag is essential. The related hydrodynamic calculations reported and discussed seek to fulfil objective III.

The design method initially considers all possible subsystem arrangements and eliminates those that do not satisfy geometric placement, hydrostatic and hydrodynamic constraints. The proposed design method can produce combinations of volume and shape, that may not have been previously considered but present a unique solution to the particular AUV mission considered.

II – Improve the prediction of lithium polymer battery behaviour at high hydrostatic pressure.

Lithium polymer batteries have been shown to operate at high pressure and their characteristics measured. Determination of internal resistance was based on voltage behaviour at differing temperature, pressure and current draw. These battery performance results have been published and contribute to the understanding of lithium polymer batteries as a pressure tolerant energy source for AUVs.

Lithium polymer batteries have been physically tested at 60 MPa, equivalent to 6000 m depth. No failures were found after 2800 battery hours of testing. The batteries are thus considered to be pressure tolerant and reliable. Further tests gave the voltage performance of the batteries at varying current draw and temperature. An equivalent circuit model of the battery was created to permit comparison of the internal resistance. Comparison of actual and equivalent circuit models at differing environmental conditions and power draws increased the understanding of lithium polymer battery internal resistance.

The equivalent circuit model was able to simulate the recorded voltage curve of Autosub 6000's energy source during a trial mission. This objective is considered to have been met and has direct industrial applications.

III - Investigate the hydrodynamic shape of axis-symmetric AUV hull shapes to parameterise drag change with shape change.

The AUV hull shape drag relationship with the geometric parameters that define the hull shape profile has been described. This relationship is expressed as a truncated multivariable linear Taylor series and readily permits estimation of the volumetric drag coefficient from selected hull profile parameters.

Hydrodynamic research has defined a total of 48 hull shape variants within two families, parallel middle body and laminar flow hull shape. Each hull shape profile is defined as functions of input geometric parameters. The hull shapes have been modelled with a potential theory based computational code at different velocities. Estimates of C_{D_∇} at a single velocity are generated and attributed to hull shape variations. The derived relationship for each hull shape family can be

included in the design methodology. A robust method of predicting hull shape drag was used, based on Schlichting's approximation for skin friction based on Re. This enabled the C_{D_∇} relationship with hull shape to be found and included in the design method.

Objective III has been achieved within the limits of the hull shapes and modelling technique applied. Axis-symmetric AUV hull shapes have been defined and modelled. Parameterised equations of C_{D_∇} have been created as functions of hull shape. However, the flow transition error found within the boundary layer code means that the derived equations for C_{D_∇} are very dependant upon the limitations of the Schlichting skin friction estimation employed.

The objectives laid out in Chapter 1 have been met. The next section considers some industrial applications for these outcomes.

9.2 Industrial applications.

The reported research is now discussed in relation to possible industrial applications and current technology.

It is intended that the adoption of a more structured design method should encourage design innovation by improving the understanding of related decisions. This might be used as a starting point for a new AUV in an unfulfilled niche within an expanding market. Where design experience of similar vehicles exists, the method may be used to quickly generate many alternate concept AUV forms for consideration.

The design method can be used to give estimates of size and hull shape of a concept AUV for extremely challenging missions. The first steps of the design method can be very important and a structured approach will allow the logic process to be followed and repeated.

Autosub 6000 has adopted pressure tolerant lithium polymer batteries and dived to 4556 m, almost three times the depth of Autosub 2. Application of lithium polymer batteries is a direct industrial outcome from this work.

A fuel gauge model has been generated for lithium polymer batteries, which could be carried forward into a full electrical model of an AUV. A mission could be programmed and simulated to predict energy source voltage at any point and to predict remaining energy source capacity to plan for contingencies.

Empirical relationships between coefficient of drag and AUV velocity exist. The next stage would be to refine the volumetric coefficient of drag based upon hull shape and velocity variations. A hydrodynamic expression that can estimate drag force based on hull shape would guide the hull shape design and further refine the concept AUV.

9.3 Recommendations for future work.

This section provides a broad discussion on possible progress of future work to build on the research outcomes reported. Some of these avenues were considered during the research but were not explored, others more directly follow on from the research outcomes.

9.3.1 Design methods.

This research provides for the first time a formal structured axis-symmetric AUV design method expressed by both flow chart and case study example. A design method is an open ended concept and by its nature will undergo further development.

The design effectively considers a 2D model regarding subsystem arrangement with subsystems placed along the AUV centreline. By relaxing the axial constraint, the subsystems could be placed parallel to each other and improve packing within the available volume within a hull shape. Packing research could consider 2D packing methods of irregular shapes within an irregular hull shape. The hull shape might not be defined, so subsystem packing should consider 'clustering' subsystems around a point and a hull shape fit around the subsystem cluster. Overall the AUV fineness ratio ($L_{AUV} / 2R_{Max}$) could influence the shape of such a subsystem cluster. The packing of the foam into the remaining volume would require some method of estimating the available volume. Geometric hull shape parameters could then be determined and the hydrodynamic drag estimated.

Further research might decide to explore the third dimension. Such an arrangement of subsystems might generate packing methods of transverse slices (comparable to packing within a circle, section 2.4). This method would be capable of calculating AUV roll, and might make complete use of available packing volume.

The design method might be updated to allow space between subsystems. Therefore a large subsystem can be placed at the bow, with a 'spacer' between the first subsystem and the hull shape nose. It would control the position of the nose and therefore the curvature of the bow. The length of the 'spacer' would be constrained by the desired overall AUV length and the increase in available volume.

This Thesis has considered examples of subsystems and nested dimensions. As technologies are becoming available, a study might be directed at listing and classifying more common AUV subsystems. Its purpose would be to find any relationships between subsystem type and required connections, for example, power cables and water pipes require AUV volume. The connection bend radius can be significant and might constrain subsystem placement. Such understanding

would generate more accurate nested dimensions, depending on the subsystem and the packing method.

The key decisions have been shown to have a large effect on the design cycle. The intention was to remove bias from the concept design and encourage innovation. Future work might consult AUV designers to find any 'rules of thumb'. If such rules of thumb are inviolate throughout AUV design, then these should be included in the design as constraints to further filter the concept designs.

9.3.2 Energy source.

Lithium polymer batteries are considered to be more accepted by the AUV community and technology has improved during the course of this research. As a direct result of physical tests in Chapter 4, Autosub 6000 has adopted pressure tolerant lithium polymer batteries.

The energy source might be improved by looking at more efficient packing and storage methods. Energy source dimensions have been identified here as a key design decision. The shape of the energy source when it is the largest subsystem has an affect on the hull shape and size of the AUV. Further work might investigate the packing of rectangular batteries to find any size restrictions caused by physical packing, access and construction. Such research could also produce pressure tolerant battery packs with a higher energy density or guidelines for battery pack arrangement within the AUV.

During battery operation heat is generated from the ohmic internal resistance. Most batteries have a maximum safe operating temperature therefore the generated heat requires dissipation. Managing battery pack thermodynamics can be a challenge. In cold environments the battery pack could use the generated heat to warm batteries and decrease temperature based battery internal resistance. In warm environments the heat must be removed from the cells to prevent batteries over heating. The current draw, size of battery pack and insulating surroundings all contribute to the thermal management of the battery pack (for example, Autosub 6000 pressure tolerant packs are filled with oil). It is anticipated that there would be a size constraint on high current battery packs due to the temperature of the core batteries. Research could investigate any relationships between battery pack size and current draw for given insulating materials.

9.3.3 AUV hull shape.

The hydrodynamic research could be improved and the parameterised prediction formula updated or extended to second order. Some recommendations for progress in these areas are made next.

The research has indicated that a short parallel middle body and long bow will resemble a laminar flow hull shape. Further work might attempt to combine the geometric input parameters to create one formula for all hull shapes. This would remove the need to decide between them and remove one of the identified key decisions.

An expression for volumetric drag coefficient has been developed for two hull shape families. Further work might expand the hull shape variants and extend the volumetric drag coefficient expression. Such work might improve accuracy when the hull shape is far removed from the base model, as well as include the influence of velocity. It represents the creation of a large number of models and perhaps provides scope for the application of genetic algorithms.

Palisupan permitted research to create the design method. Resolving the issues found within the hydrodynamic modelling would improve AUV drag prediction within the design method. A more complex boundary layer approach might improve the modelling of the laminar flow hull shape.

The control of the boundary layer is believed to be very important when fitting a laminar flow hull. The linear approximations of C_{D_∇} are calculated using the Schlichting skin friction estimation. Improved transition prediction methods would allow for the Thwaites – Head boundary layer model to be utilised and so the approximation of C_{D_∇} would be improved for laminar flow hulls. A function for velocity would also be useful, to guide the operating velocity of a laminar flow hull and how this velocity range might be altered by changing a hull shape parameter.

Increasing computing power and the improvement of computational methods might allow another modelling approach to be used. For example, a fluid volume model could approximate separation of streamlines to model wake and constrain the gradient of the hull shape stern.

Further work might investigate the placement of control surfaces and propellers and generate constraints on the hull shape stern. This would include a review of published literature on surface ship and submarine propulsion and propeller placement to find similarities. Furthermore, control surfaces or propeller placement might not be restricted to the stern with differing hydrodynamic constraints and manoeuvring effects.

Some firsts have been reported in this Thesis and many challenges await the attention of others.

References

Abu Sharkh, S., G. Griffiths and A. Webb. (2003). "*Power Sources for Unmanned Underwater Vehicles.*" G. Griffiths (Editor), Technology and Applications of Autonomous Underwater Vehicles, Taylor and Francis, pp. 19 - 35.

Akhtman, J., M. Furlong, P. Jantapremjit, A. Palmer, A. Phillips, S. Abu Sharkh, S. Turnock and S. Veres. (2007), "*SotonAUV: University of Southampton Entry into the 2007 Student Autonomous Underwater Challenge - Europe*", SAUC-E 2007, Defence Science and Technology.

Alers, P. B. (1981). "*Tradeoff studies for the Unmanned Free Swimming Submersible (UFSS) Vehicle.*" Oceans '81, pp. 113 - 117.

Allmendinger, E. E. (1990). "*Submersible vehicle systems design.*" The Society of Naval Architects and Marine Engineers.

Anderson, J. D. (2001). "*Fundamentals of Aerodynamics.*" Third Edition, McGraw-Hill.

Babb, R. J. (1994). "*Instrumentation for a low drag hydrodynamic test vehicle.*" Electronic engineering in Oceanography, Vol. 394, pp. 24 - 29.

Banner, J., C. J. Govar and R. Wilson. (2006). "*Navy Safety Testing of Lithium Ion batteries for the Battlespace Preparation Autonomous Underwater Vehicle (BPAUV).*" 42nd Power Sources Conference, Philadelphia, USA, 12th -14th June.

Benham, P. P., R. J. Crawford and C. G. Armstrong. (1996). "*Mechanics of Engineering Materials.*" 2nd Edition, Addison Wesley Longham limited.

Berkley, J. O. and P. Y. Wang. (1987). "*Two-dimensional finite bin packing algorithms.*" The Journal of the Operational Research Society, Vol. 38, Issue 5, pp. 423 - 429.

Birgin E. G., J. M. Martinez, F. H. Nishihara and D. P. Ronconi. (2005). "*Orthogonal packing of rectangular items within arbitrary convex regions by nonlinear optimization.*" Computers and Operation Research, Vol. 33, pp. 3535 – 3548.

Blidberg, D. R. (1997). "*Solar Powered Autonomous Undersea Vehicles.*" Sea Technology Magazine, pp. 45 - 51.

Blidberg, D. R. and D. A. Mikhail. (2003). "*Solar Powered Autonomous Underwater Vehicles.*" G. Griffiths (Editor), Technology and Applications of Autonomous Underwater Vehicles, Taylor & Francis, pp. 59 - 76.

Bradley, A. M., M. D. Feezor, H. Singh and F. Y. Sorrell. (2001). "*Power Systems for Autonomous Underwater Vehicles.*" Journal of Oceanic Engineering, Vol. 26, Issue. 4, pp. 526 - 538.

Burcher, R. and L. Rydill. (1994). "*Concepts in Submarine Design.*" Ocean Technology, Cambridge University Press.

Cebeci, T. and P. Bradshaw. (1977). "*Momentum transfer in boundary layers.*" Hemisphere Publishing Corporation.

Cebeci, T. and A. M. O. Smith. (1974). "*Analysis of Turbulent Boundary Layers.*" F. Frenkiel and G. Temple (Editor), Applied Mathematics and Mechanics, Academic press, New York.

Chettleborough, P. (2002). "*Resistance and Propulsion of the Autonomous Underwater Vehicle Autosub.*" **Bachelor of Engineering**, University of Southampton, School of Engineering Sciences, Supervisor: Prof. G. E. Hearn,

Chiasson, L. and B. Vairamohan. (2003). "*Estimating the state of charge of a battery.*" Proceedings Of The 2003 American Control Conference, Denver, June, pp. 2863 - 2868.

Comstock J. P. (Editor) (1967).*"Principles of Naval Architecture*".6th Edition, Society of Naval Architects.

Cross, N. (2000). "*Engineering design methods - Strategies for Product Design.*" 2nd Edition, John Wiley & Sons.

Curle, N. (1962). "*The laminar boundary layer equations.*" Oxford University Press,

Doerffel, D. and S. Abu Sharkh. (2004). "*Rapid test and non-linear model characterisation of solid-state lithium-ion batteries.*" Journal of Power Sources, Vol. 130, Issue 1-2, pp. 266 - 274.

Dougal, R. A., S.Liu, L.Gao and M.Blackwelder. (2002). "*Virtual Test Bed for Advanced Power Sources.*" Journal of Power Sources, Vol. 110, pp. 285 - 294.

Dowdeswell, J. (2004), "*Cruise report - JR106b*" RSS - James Clark Ross.

Dowsland, K. A. and W. B. Dowsland. (1995). "*Solution approaches to irregular nesting problems.*" European Journal of Operational Research, Issue 84, pp. 506 - 521.

Dress, D. (1989). "*Drag Measurements of a Laminar Flow Body of Revolution.*" American Institute for Aeronautics and Astronautics, Vol. 27, Issue 8, pp. 1081 - 1082.

Ehrlich, G. M. (2002). "*Handbook of Batteries.*" D.Lyndon and T. B. Reddy (Editor), 3rd Edition, McGraw-Hill, p. 35.26.

European Union Directive 76/464/EEC (1976) *"On pollution caused by certain dangerous substances discharged into the aquatic environment of the community*".

Fallows, C. D. (2005). "*Characterisation of the propulsion systems of Autonomous Underwater Vehicles.*" **Doctor of Philosophy**, University of Southampton, School of Engineering Sciences, Supervisor: Prof G. E. Hearn.

Ferguson, J., A. Pope, B. Butler and R. I. Verrall. (1999). "*Theseus AUV - Two record breaking missions.*" Sea Technology Magazine, February.

Fish, F. E., G. V. Lauder, R. Mittal, A. H.Techet and M. S. Triantafyllou. (2003). "*Conceptual Design for the Construction of a Biorobotic AUV Based on Biological Hydrodynamics.*" 13th International Symposium on Unmanned Untethered Submersible Technology (UUST), New England Center, Durham, New Hampshire, USA, 24th - 27th August.

Fox, C. D. M.: "*Small subs provide big payoffs for submarine stealth.*" (2001), The Official Magazine of the US Navy, Vol3, No3, Retrieved May, 2005, from http://www.chinfo.navy.mil/navpalib/cno/n87/usw/issue_11/submarine_stealth.html.

Fukagawa, Y., Y. Shinano, T. Wada and M. Nakamori. (2005). "*Optimum Placement of a Wafer on a Rectangular Chip Grid.*" 6th World Congresses of Structural and Multidisciplinary Optimisation, Rio de Janeiro, 30th May - 3rd June.

Funnell C. (Editor) (2001-2002). "*Janes' Underwater Technology.*", 4th Edition, Thompson.

Furlong, M. (2007 October). "*Autosub 6000 trials.*" K. Rutherford. *Private communication.*

Gitzendanner, R., F. Puglia, C. Martin, D. Carmen, E. Jones and S. Eaves. (2004). "*High power and high energy lithium-ion batteries for under-water applications.*" Journal of Power Sources, Vol. 136, pp. 416 - 418.

Griffiths, G. (2005). "*Cost vs. performance for fuel cells and batteries for AUVs.*" Unmanned Underwater Vehicle Showcase, Southampton, September.

Griffiths, G. (2000). "*Technology needs for Autonomous Underwater Vehicles.*" International Ocean Systems Magazine, Vol. 4, Issue 3, pp. 8 - 15.

Griffiths, G., J. Jamieson, S. Mitchel and K. Rutherford. (2004). "*Energy storage for long endurance AUVs.*" Advances in Technology for Underwater Vehicles, ExCel, London, UK, 16th March 2004.

Hansen, R. J. and J. G. Hoyt. (1984). "*Laminar-To-Turbulent Transition on a Body of Revolution With an Extended Favorable Pressure Gradient Forebody.*" Journal of Fluids Engineering, Vol. 106, pp. 202 - 210.

Hasvold, O. and K. H. Johansen. (2002). "*The Alkaline Aluminium Hydrogen Peroxide semi-Fuel Cell for the Hugin 3000 Autonomous Underwater Vehicle.*" Workshop on Autonomous Underwater Vehicles, 2002, IEEE, June pp. 89 – 94.

Hasvold, O., K. H. Johansen, O. Mollestad, S. Forseth and N. Storkerson. (1999). "*The Alkaline Aluminium / hydrogen peroxide power source in the Hugin II unmanned underwater vehicle.*" Journal of Power Sources, Vol. 80, pp. 254 - 260.

Hasvold, O., N. Storkersen, S. Forseth and T. Lian. (2005). "*Power sources for autonomous underwater vehicles.*" Journal of Power Sources, Vol. 162, Issue 2, pp. 935 - 942.

Hasvold, O. and N. Storkerson. (2001). "*Electrochemical power sources for unmanned underwater vehicles used in deep sea survey operations.*" Journal of Power Sources, Vol. 96, pp. 252 - 258.

Hoerner, S. F. (1965). "*Fluid Dynamic Drag.*" Published by Author.

Hong, J. J. (2002) "*Lithium secondary cell and method of fabricating the same.*" Patent Application Number: 09/518,277.

Hornfeld, W. (2004). "*DeepC, the German AUV development Project.*" Retrieved 2004 from www.imar-navigation.de.

Holt, N. D. A. (1997 May). "*An Investigation Into Alternative Submarine After Hydroplane Configurations, Using a Surface Panel Method.*" M.Eng, University of Southampton, Ship Science, Supervisor: Dr S. R. Turnock.

Houghten, E. L. and P. W. Carpenter. (2003). "*Aerodynamics for Engineering Students*" Fifth Edition, Butterworth-Heinemann.

Huggins, A. and A. R. Packwood. (1994). "*The Optimum Dimensions for a Long-Range, Autonomous, Deep-diving, Underwater vehicle for Oceanographic research.*" Ocean Engineering, Vol. 21, Issue 1, pp. 45 - 56.

Huggins, A. and A. R. Packwood. (1995). "*Wind Tunnel experiments on a fully appended laminar flow submersible for oceanographic survey.*" Ocean Engineering, Vol. 22, Issue 2, pp. 207 - 221.

Hughes, A. W. (2000 April). "*Investigation of Tip-Driven Thruster and Waterjet Propulsion Systems.*" **Doctor of Philosophy**, University of Southampton, Faculty of Applied Science and Engineering, Supervisor: Dr S. R. Turnock.

Jalbert, J., J. Baker, J. Duchesney, P. Pietryka, W. Dalton, D. R. Blidberg, S. Chappell, R. Nitzel and K. Holappa. (2003). "*Solar-powered autonomous underwater vehicle development.*" Unmanned Untethered Submersible Technology, Durham, New Hampshire.

James, G., D. Burley, D. Clemens, P. Dyke, J. Searl and J. Wright. (1996). "*Modern Engineering Mathematics.*" Second Edition, Addison – Wesley.

Katz J. and A. Plotkin (2001). "*Low-Speed Aerodynamics*"Second Edition, Cambridge University Press.

Kimber, N. L. and K. H. Scrimshaw. (1994). "*Hydrodynamic testing of a 3/4 scale Autosub model.*" Oceanology International, Brighton, March.

Kinsey, J. (1998). "*Drag Characterisation in the Autonomous Benthic Explorer.*" Oceans '98, Nice, France.

Kleiner, A. and J. G. Northcutt. (2004). "*AUV Sea Trails and Tribulations; 36 months and 25,000 kilometres later - was it worth it?*" Hydro International.

Kobayashi, Y., S. Seki, , A. Yamanaka, , H. Miyashiro, Y. Mita, and T. Iwahori. (2005). "*Development of high-voltage and high capacity all solid state lithium secondary batteries.* ." Journal of Power Sources, Vol. 146, Issues. 1-2, pp. 719 - 722.

Lodi, A., S. Martello and M. Monaci. (2002). "*Two-dimensional packing problems: a survey.*" European Journal of Operational Research, Issue 141, pp. 241 - 252.

Lutz, T. and S. Wagner. (1998). "*Numerical shape optimisation of natural laminar flow bodies.*" 21st International Council on the Aeronautical Sciences, Melbourne Australia, 13th - 18th September.

MacNaughten, A., R. White and M. Bendzlowicz. (2005). "*Into the deep end.*" International Ocean Systems, January / February.

Mathworks: "*Matlab 7.0.*" (1994), Retrieved May 2005, from http://www.mathworks.com/access/helpdesk/help/techdoc/matlab.html.

McCarthy, K. (2003). "*REMUS - A Role Model for AUV Technology Transfer.*" International Ocean Systems, November.

McPhail, S. (2007a). "*Autosub 6000 - A leap forward in capability: a long range and deep diving AUV.*" National Oceanography Centre, *Unpublished work.*

McPhail, S. (2007b). "*Autosub and the very long range AUV.*" AUV Science in Extreme Environments workshop, 6th February.
McPhail, S. (2006a). "*Lithium Polymer Pressure Balanced Battery System.*" National Oceanography Centre, Southampton, *Unpublished work.*
McPhail, S. (2006b). "*Personal conversation.*" K. Rutherford, *Private communication.*
Millard, N., S. Mcphail, M. Pebody, J. Perrett, J. Riggs, P. Stevenson and A. Webb. (2003). "*Autosub operations during cruise JR84.*" Autosub Under Ice Newsletter, Issue 3, pp. 10 - 11.
Murphy, A. J. (2005). "*Design, Build and Testing of a Laminar Flow Drag Plate.*" **Doctor of Philosophy**, University of Southampton, School of Engineering Sciences, Ship Science, Supervisor: Prof G. E. Hearn.
National Research Council. (2001). "*Future needs in deep submergence science; occupied and unoccupied vehicles in basic ocean research.*", National Academies press.
Newman, P., R. Westwood and J. Westwood. (2007). "*Market Prospects for Autonomous Underwater Vehicles.*" Unmanned Underwater Vehicle Showcase, National Oceanography Centre, Southampton,
Packwood, A. R. and A. Huggins. (1994). "*Afterbody shaping and transition prediction for a laminar flow underwater vehicle.*" Ocean Engineering, Vol. 21, Issue 5, pp. 445 - 459.
Pahl, G. and W. Beitz. (1988). "*Engineering Design - A systematic approach.*" Wallace and Ken (Editor), 1st Edition, The Design Council.
Parsons, J. S., R. E. Goodson and F. R. Goldschmied. (1974). "*Shaping of Axisymmetric Bodies for minimum Drag in Incompressible Flow.*" Journal of Hydronautics, Vol. 8, Issue 3, pp. 100 - 107.
Pashias, C. (2001). "*Shape optimisation of a long range AUV using Computational Fluid Dynamics.*" **Bachelor of Engineering**, University of Southampton, School of Engineering Sciences, Supervisor: Dr. S. R. Turnock.
Phillips, A., M. Furlong and S. R. Turnock. (2007). "*The use of Computational Fluid Dynamics to Assess the Hull Resistance of Concept Autonomous Underwater Vehicles.*" Oceans 07, Aberdeen, 18th – 21st June.
Phillips, S., D. Hook and H. Young. (2007). "*Advanced in unmanned surface vehicle operations.*" Unmanned Underwater Vehicle Showcase, National Oceanography Centre Southampton,
Rand, D. A. J. and R. M. Dell. (2005). "*The Hydrogen economy: a threat or opportunity for lead acid batteries.*" Journal of Power Sources, Vol. 144, Issue 2, pp. 568 - 578.
Rawson, K. J. and E. C. Tupper. (2001). "*Basic Ship Theory.*" 5th Edition, Longman Group limited, Vol. 2.
Rawson, K. J. and E. C. Tupper. (1994). "*Basic ship theory.*" 4th Edition, Addison Wesley Longman Ltd, Vol. 1.
Robinson, K. (2007). "*Li-Poly pressure-tolerant batteries dive deep.*" Bluefin Robotics Corporation.
Ross, C. T. F. (1990). "Pressure vessels under external pressure statics and dynamics." Taylor & Francis books,
Saint-Amour, S. (2007). "*Battery Management System increases UUV capabilities.*" 07 Virtual Acquisition Showcase.
Sato, N. (2001). "*Thermal behaviour analysis of lithium-ion batteries for electric and hybrid vehicles.*" Journal of Power Sources, Vol. 99, pp. 70 - 77.
Sawa, T., T. Aoki, S. Tsukioka, T. Hyakudome, S. Ishibashi and T. Inada. (2004). "*Fuel cell power source will open new AUV generation.*" Underwater Intervention, February.
Schlichting, H. (1968). "*Boundary Layer Theory.*" 4th Edition, McGraw-Hill,
Shukla, A. K., A.S.Arico and V.Antonucci. (2001). "*An appraisal of electric automobile power sources.*" Renewable and Sustainable Energy Reviews, Vol. 5, pp. 137 - 155.

Stevenson, P. (2005). "*Autosub Weights and Volumes.*" National Oceanography Centre, Southampton, *Unpublished work.*

Stevenson, P. and D. Graham. (2003). "*Advanced materials and their influence on the structural design of AUVs.*" G. Griffiths (Editor), Technology and Applications of Autonomous Underwater Vehicles, Taylor & Francis, pp. 77 - 92.

Stevenson, P., G. Griffiths and A. Webb. (2002). "*The Experience and limitations of using Manganese Alkaline Primary Cells in a large Operational AUV.*" Workshop on Power Systems for AUVs, San Antonio, Texas, June.

Stevenson, P. and C. Hunter. (1994). "*Development of an efficient propulsion motor and driver for use in the deep ocean.*" Electronic Engineering in Oceanography, 19th - 21th July.

Tamura, K., T. Aoki, S. Tuskioka, T. Murashima H. Nakajoh and T. Fujita. "*The development of the deep sea cruising AUV Urashima*", Japan Marine Science and Technology Centre (JAMSTEC).

Thwaites, B. (1960). "*Incompressible Aerodynamics.*" Dover publications, Inc. New York.

Turnock, S. R. (1997), "*Technical Manual and User Guide for the Surface Panel Code: Palisupan*", University of Southampton, Ship Science Report 100.

Turnock, S.R. (2004). "*SESS6007 Computational Fluid Dynamics.*" University of Southampton *Unpublished work*

Wazzan, A. R., C. Gazley. and A. M. O. Smith. (1981). "*H-Rx Method for Predicting Transition.*" American Institute for Aeronautics and Astronautics, Vol. 81, pp. 810 - 812.

Webb, D. C., P. J. Simonetti and C. P. Jones. (2001). "*SLOCUM: An underwater Glider propelled by Environmental energy.*" Journal of Oceanic Engineering, Vol. 26, Issue. 4, pp. 447 - 452.

Webb, R.: "*Slocum thermal glider.*" (1999), Retrieved July 2004, from http://www.webbresearch.com/thermal_glider.htm.

Wilson, R. and J. Bales. (2006). "*Development and Experience of a Practical Pressure-Tolerant, Lithium Battery for Underwater use.*" Oceans 06, Singapore.

Woods Hole Oceanographic Institution (2008, February 11), "*New Hybrid VehicleGiven Its First Test Drive In The Ocean.*", Science Daily, Retrieved May 2008 from http://www.sciencedaily.com/releases/2008/02/080207140106.htm

Yeo, R. (2007). "*Surveying the underside of an Arctic ice ridge.*" Unmanned Underwater Vehicles Showcase, National Oceanography Centre, Southampton.

Yoerger, D.: "*ABE AUV.*" (2007), from http://www.dsl.whoi.edu/DSL/dana/abe_serious.html.

Young, A. D. (1939), "*The Calculation of the Total and Skin Friction Drags of Bodies of Revolution at Zero Incidence.*" Aeronautical Research Committee Reports and Memoranda, no.1874.

Web based references

www1: "*International Submarine Engineering Ltd.*" (May 2002), Retrieved April, 2005, from www.ise.bc.ca.

www2: "*Underwater Robotics & Application Laboratory.*" (1995), Retrieved April, 2005, from underwater.iis.u-tokyo.ac.jp/robot/pteroa-e.html.

www3: "*Bluefin Robotics Corporation* ", Retrieved April, 2005, from www.bluefinrobotics.com/index.htm.

www4: "*Hydroid Incorporated.*" 2007, from www.hydroidinc.com/.

www5: "*Kongsburg Maritime.*" Retrieved 2006, from www.km.kongsberg.com/.

www6: "*National Oceaonography Centre, Southampton - Autosub.*" 2006, from www.noc.soton.ac.uk/OED/index.php?page=as.

www7: "*Subsea7 - Geosub.*" from www.subsea7.com/rov_geosub.php.

www8: "*DeepC-AUV.*" 2005, from www.deepc-auv.de/deepc/DeepC.htm.

www9: "*Nekton Research - Ranger/Umap.*" (February 2003), Retrieved April, 2005, from http://www.nektonresearch.com/ranger.html.
www10: "*Deepsea Power & Light 2004 - Press Release on new ceramic buoyancy spheres.*" Retrieved June, 2005, from www.deepsea.com/flotation.
www11: "*Eaglepicher - Kokam.*" Retrieved March, 2007, from www.kokam.com/english/biz/kokam.html.
www12: "*Zebra battery fact sheet.*" 2004, from www.rolls-royce.com/marine/downloads/submarine/Zebra_fact.pdf.
www13: "*Japan Marine Science and Technology Centre - Urashima.*" 2007, from www.jamstec.go.jp/e/about/equipment/ships/urashima.html.
www14: "*Underwater Robotics & Application - R1 Project.*" (June 2005), Retrieved April, 2005, from http://underwater.iis.u-tokyo.ac.jp/robot/r1-e.html.
www15 "*Department of Energy Announces 12 Projects To Increase Vehicle Efficiency.*" (2005), from http://www.energy.gov/engine/content.do?PUBLIC_ID=17464&BT_CODE=PR_PRESSRELEASES&TT_CODE=PRESSRELEASE.
www16: "*Ernesto Birgin homepage.*" 2005, from http://www.ime.usp.br/~egbirgin/.
www17: "*Fluent.*" 2007, from www.fluent.com/.
www18: "*Ansys CFX.*" 2005, from www-waterloo.ansys.com/cfx/.
www19: "*Woods Hole Institute* ", 2005, from www.whoi.edu/oceanus/viewArticle.do?id=4758.
www20: "*Cartographic- Topographic maps.*" 2006, from www.cartographic.com.
www21: "*Reson Offshore Ltd. - SeaBat 7125 200kHz multibeam sonar brochure.*" 2007, from www.reson.com/sw245.asp.
www22: "*The Spray glider.*" 2005, from www.uib.no/People/are062/spray.htm.
www23: "*IXSEA - PHINS Inertial Navigation System data sheet.*" 2007, from www.ixsea.com/en/products/002.001.001.002/Phins.html.
www24: "*Wetlabs BB2F optical backscatter.*" 2007, from www.wetlabs.com/products/ebb/bbvsfindex.htm.
www25: "*Subsea buoyancy systems.*" 2008, from www.trelleborg.com/en/offshore.
www26: "*SubSea Propulsion systems* ", 2007, from www.subseapropulsionsystems.com.
www27: "*Panasonic Lithium Ion Batteries - CR18650E data sheet.*" from www.panasonic.com/Industrial/Battery/oem/chem/lithium.
www28: "*Sea Max THL-404-8 thruster.*" 2008, from www.dssi.globalexplorerrov.com/4000.htm.
www29: "*Edgetech side scan sonar.*" 2007, from www.edgetech.com/sidescan.html.

Appendices.

APPENDIX A

Energy storage for long endurance AUVs

G Griffiths, BA, MSc, CEng, MIEE

Southampton Oceanography Centre, UK

J Jamieson

Subsea7 Ltd., UK

S Mitchell BA

Systems Engineering & Assessment Ltd., UK

K Rutherford MEng

University of Southampton, UK

SYNOPSIS

Energy storage is a key issue for long endurance autonomous underwater vehicles. Mission duration, speed through the water and sensor and payload capabilities are constrained by the energy available, which in turn is governed by the characteristics of the energy source or sources and the mass and volume that the vehicle designer can devote to the energy system. Tensioned against these technical issues are those of cost, operational life, ease of use, maintainability, safety, security and continuity of supply of the items forming the energy system. This paper focuses on primary and secondary electrochemical batteries, how existing vehicles have constructed their energy storage systems and seeks to establish whether electrochemical cells alone will be able to provide the necessary energy at an affordable cost for future long endurance AUVs and the missions being considered.

INTRODUCTION

Energy is a key issue for long endurance autonomous underwater vehicles (AUVs). Mission duration, speed through the water and sensor and payload capabilities are constrained by the energy available, which in turn is governed by the characteristics of the energy source or sources, the mass and volume that the vehicle designer can devote to the energy system and the details of how the weight of the energy system is countered with buoyancy. Most AUVs are dependent on stored energy for their operation. The few exceptions, not considered in this paper, use energy from the environment, either directly as in the case of the thermal engine of the Slocum glider [1] or to recharge onboard supplies as in a solar-powered AUV [2].

Authors' Biography

Gwyn Griffiths is Head of the Underwater Systems Laboratory at the Southampton Oceanography Centre and Professor of Underwater Systems Engineering at the University of Southampton. His research interests include the technology and applications of underwater vehicles and use of acoustics to measure ocean currents and zooplankton abundance.

James Jamieson is employed as a Principal Engineer in the Remote Technology Group of Subsea7 where he presently leads the AUV engineering team. His background is in underwater systems engineering, with over 15 years experience in ROV, AUV, and tooling control system development.

Scott Mitchell is a specialist in analogue and power management electronics at SEA Ltd. He has over 20 year experience in the design of power management systems for spacecraft, now being applied to unmanned underwater vehicles.

Kieran Rutherford is a student on the Engineering Doctorate program at the University of Southampton. His research subject is the Energy and Efficiency of Underwater Vehicles.

Batteries, either primary or secondary, are by far the most common choice of energy storage for past and present AUVs. In Jane's Underwater Technology [3] information on the energy source is available for 61 different AUVs. Batteries, either primary or secondary, were used in 53 of these vehicles (3 primary, 42 secondary, 4 primary or secondary, 4 of unspecified type). Aluminium oxygen semi-fuel cells were used in four vehicles; only one vehicle claimed to use a fuel-cell (hydrogen-oxygen); an air-breathing diesel was used by two semi-submersibles (one an adaptation of the other) and a closed cycle diesel engine was used by one vehicle. Batteries are likely to remain the technology of choice for at least the next five years, despite their limitations. Partly this is because the technical options are tensioned against cost, operational life, ease of use, maintainability, safety, security and continuity of supply of the items forming the energy system.

Given their importance, this paper focuses on primary and secondary electrochemical batteries. A review of the proportion of an AUV's mass given over to the energy source is followed by a description of how four existing vehicles (REMUS, Autosub Geosub and USS *Cutthroat*) have constructed their energy storage systems ranging from secondary lead-acid to primary lithium cells. The paper then tries to answer three key questions:

- How does the choice of buoyancy material affect the proportion of the vehicle's mass that can be assigned to the energy source?

- Will primary or secondary electrochemical cells provide a technical solution to the energy requirements of future long endurance AUVs?

- If so, what will be the likely cost? Given that the relationship between cost of energy and specific energy is shown to be highly non-linear.

The discussion highlights the importance of an iterative design process that can minimise the energy requirement. Alternatives to increasing the stored energy, such as reducing the vehicle drag and reducing the vehicle payload energy requirements are explored in the context of non-linear relationships between battery specific energy and cost.

FACTORS AFFECTING THE MASS AVAILABLE FOR ENERGY STORAGE IN AN AUV

The mass and volume of an energy source within an AUV is a major design factor affecting vehicle size and, as a consequence, handling and platform integration. A simple graph, Fig 1, shows on the ordinate axis what mass the energy source would need to be for total mission power requirements of 1, 10, 100 and 1000 kWh as a function of the specific energy of the energy source. Long endurance propeller-driven AUVs are likely to require at least 100 kWh of energy. While this simple approach can be used to estimate the mass of the energy source knowing its specific energy and the mission energy requirements, assessing what the energy source mass means for the overall mass of the AUV is not straightforward. The following section examines this issue and discusses the ratio of energy system mass to overall mass in present and past generation AUVs.

The overall mass (and hence size, given that it is usual for AUVs to be near neutral buoyancy) of an AUV can be expressed as an equation whose form depends on the configuration of the vehicle. For an AUV composed of multiple pressure vessels, with the energy source within one or more pressure vessels the mass of the vehicle is given by:

$$M_{AUV} = M_E + M_{BE} + \sum_{i=1}^{m} M_i + \sum_{j=1}^{n} M_{Bj} \qquad (1)$$

where M_E is the mass of the energy source, M_{BE} □□ □□□ mass of the pressure vessel(s) containing the energy source, M_i the overall mass of the i^{th} pressure vessel or other component and M_{Bj} is the mass of the j^{th} weight or added buoyancy to achieve near neutral buoyancy overall. For an AUV with a single pressure

vessel this equation can be used, by letting M_{BE} represent □□□ mass of the single pressure vessel, M_i the mass of the i^{th} internal component and M_{Bj} the mass of the j^{th} weight (if any) added to achieve near neutral buoyancy overall.

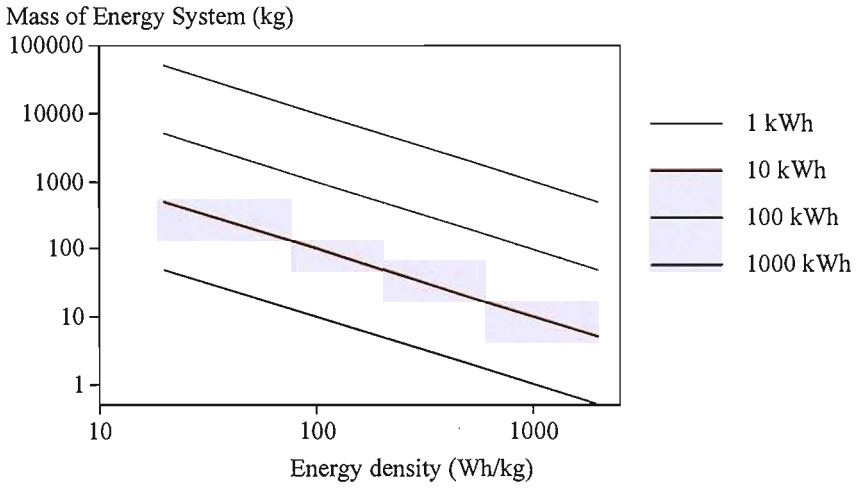

Fig 1 Mass of an energy source needed for mission energy needs from 1 to 1000 kWh against the specific energy of the energy source.

One design objective for a long endurance AUV is to maximise the proportion of the total vehicle mass available for the energy source. That is, the ratio of M_E to M_{AUV} should be as high as possible, subject to other design requirements being met, for example diving depth and payload capacity. While the ratio of M_E to M_{AUV} provides a simple metric, the denominator term contains $m+n+1$ terms, and hence up to $m+n+1$ factors that influence the ratio. Nevertheless, examining the ratio M_E to M_{AUV} for existing vehicles can provide an assessment of the energy-carrying capacity of AUVs that have been built. Fig 2 shows the ratio M_E to M_{AUV} for 30 AUVs using data obtained from [3]. In many cases, M_E was not provided, but has been estimated from the data on energy source capacity and chemistry, hence the error bars on the data in Fig 2. Note that the vehicles are ranked on the abscissa by claimed maximum depth. The most immediate conclusion is that no current vehicle has a M_E to M_{AUV} ratio of greater than 0.5 and that no vehicle capable of diving deeper than 1500 m (Autosub and to the right) has a M_E to M_{AUV} ratio of greater than 0.25.

Other conclusions need to take account of some of the factors within the $m+n+1$ terms in M_{AUV}. For example, many of the vehicles with a ratio of below 0.15 are test or demonstrator vehicles, where there may be little need to provide significant energy, at least in their present configurations; examples include the Twin Burger, Sea Squirt and Urashima. Conversely, the vehicle with the highest M_E to M_{AUV} ratio, the Pilot Fish, is a shallow diving test vehicle, comprising a single plastic pressure vessel, built to demonstrate the effectiveness of an oscillating fin thruster, with little in the way of additional payload and instrumentation, and a target to achieve a similar power-to-weight ratio as marine creatures, in the region of 25 W kg^{-1} [4]. For the Theseus AUV, figures for its test configuration (with a 20 kWh NiCd battery) and its operational configuration (with a 360 kWh AgZn battery) are included, showing a significant increase in M_E to M_{AUV} ratio for the operational vehicle.

For those vehicles with their energy source contained within one or more pressure vessels, the mass of the pressure vessel(s) can be a significant proportion of the total vehicle mass. If the size (mass) of the vehicle is constrained, then the performance and choice of the buoyancy material is important to the energy-carrying capability of the vehicle. Stevenson and Graham [5] give indicative graphs and figures for the mass to displacement ratio and densities of pressure vessels and buoyancy foams. Rearranging to give the mass to buoyancy ratio for ring-stiffened cylinders gives:

$$\frac{M_B}{B} = \left(\frac{S.P_w}{K - S.P_w} \right) \tag{2}$$

where M_B is the mass of the pressure vessel, B the buoyancy provided, S the required safety factor, P_w the maximum working pressure (in MPa) and K a material dependent constant: ~75 for titanium, 100-120 for carbon fibre reinforced plastic (CFRP) and ~67 for aluminium. The resulting mass to buoyancy ratio for titanium and CFRP ring-stiffened cylinders are shown in Fig 3 together with those for a number of different buoyancy foams, a ceramic cylinder [6] and two sizes of borosilicate glass buoyancy spheres.

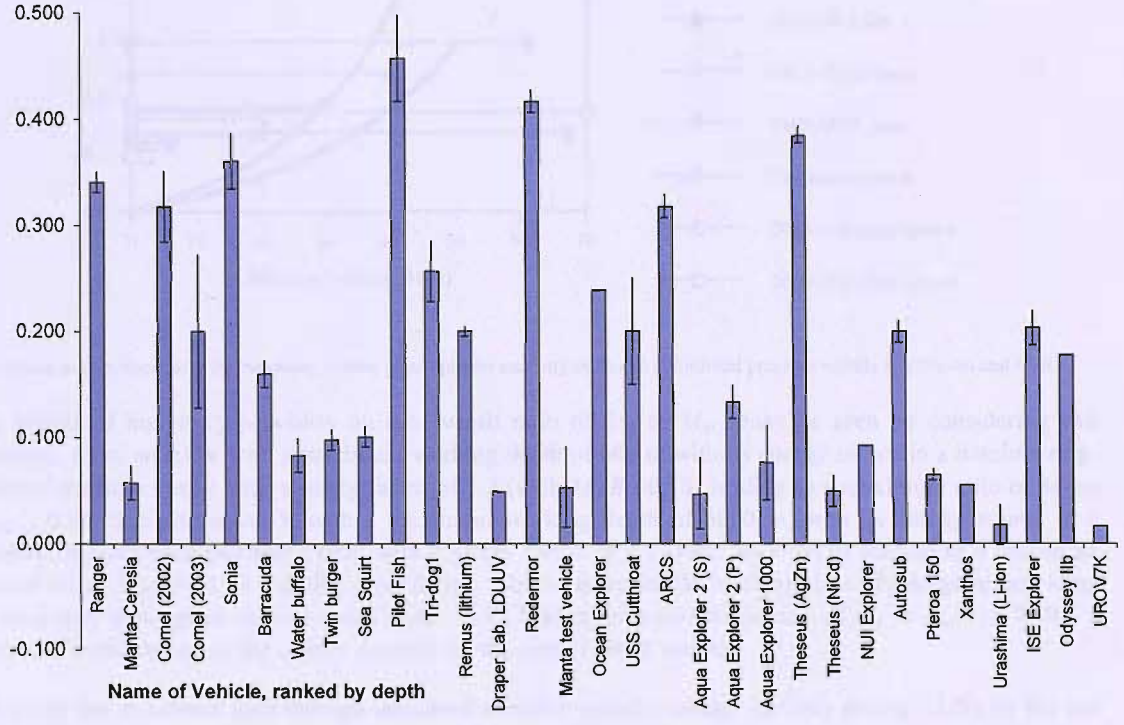

Fig 2 Energy system mass to total vehicle mass for 30 AUVs, ranked by maximum diving depth.

The balance of advantage, in terms of minimising the mass to buoyancy ratio and hence vehicle mass at the required working depth, alters from the ring-stiffened pressure vessels to glass spheres and foam buoyancy above 24-35 MPa (2400-3500m) at a safety factor of 1. More realistically, the cross over point would be at ~ 2000 m for the titanium pressure vessel (at a safety factor of 1.2) and 1750 m for the CFRP if a larger safety factor such as 2 was used.

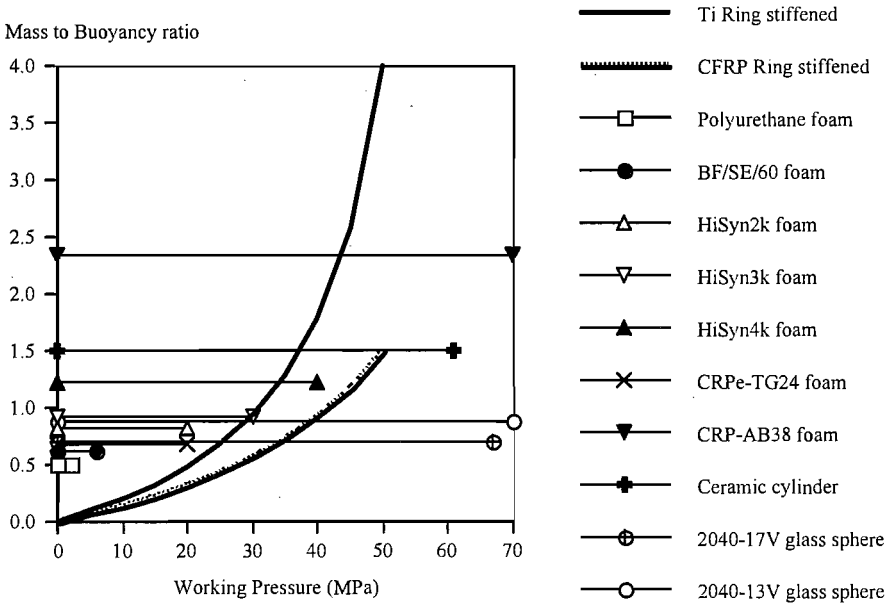

Fig 3 Mass to buoyancy ratio for buoyancy foams, glass spheres and ring-stiffened cylindrical pressure vessels in titanium and CFRP.

The impact of buoyancy provision on the overall ratio of M_E to M_{AUV} may be seen by considering two examples. First, an AUV with a maximum working depth of 600 m with its energy source in a titanium ring-stiffened pressure vessel with a safety factor of 1.2 (with M_B/B =0.10) leading to a maximum ratio of M_E to $M_{AUV\ of}$ 0.90. Second, an AUV with a maximum working depth of 5000 m, with its energy source in a titanium ring-stiffened pressure vessel with a safety factor of 1.2 (with M_B/B =4.0) leading to a maximum ratio of M_E to M_{AUV} of 0.20. For this deep diving vehicle, there would be significant advantage in providing the buoyancy using glass spheres (with M_B/B =0.7), leading to a maximum ratio of M_E to M_{AUV} of 0.59 – a three-fold improvement in the energy payload for the same overall weight.

Achieving the endurance gain through increased effective specific energy for deep diving AUVs by the use of foam buoyancy rather than pressure vessels requires that the energy source should be able to operate at ambient pressure. This severely reduces the choice of cell chemistries and cell construction. Lead acid cells have been used in this mode for many years. More recently lithium solid polymer cells have been operated at pressure [7]. It is an open question as to whether cell chemistries such as lithium carbon monofluoride (LiCF) constructed as pouch cells could be operated in a pressure-balanced mode. In all of these cases, the mass of the protective housing and any inert pressure compensating fluid would decrease the effective specific energy.

Given these different options, how can they be compared? The concept of specific energy at zero buoyancy as a performance metric has been proposed by Mierlo and others. That is, the energy source and the buoyancy needed (in whatever form) is considered as one unit and the energy available per kg of weight in air is compared. Table I shows this comparison for a range of cell types for a 600 m AUV using batteries within a ring stiffened titanium pressure vessel and a 5000 m AUV with (a) batteries within a ring stiffened titanium pressure vessel, (b) batteries within 17" glass spheres and (c) the cells at ambient pressure with the buoyancy provided by empty glass spheres. At 5000 m (50MPa) the latter option provides the highest specific energy for the low gravimetric density lithium cells.

Table I Specific energies of some battery chemistries at zero buoyancy within titanium cylinders and glass spheres.

Chemistry and example type	*Type*	*Specific Energy ($Wh.kg^{-1}$)*	*SE ($Wh.l^{-1}$)*	*SE at ρ=1 Ti PV 6MPa ($Wh.kg^{-1}$)*	*SE at ρ=1 Ti PV 50MPa ($Wh.kg^{-1}$)*	SE at ρ=1 *Glass Spheres at 50 MPa ($Wh.kg^{-1}$)*	*SE cells at pressure, Glass Spheres 50 MPa ($Wh.kg^{-1}$)*
Lead acid Yuasa NPL78-12	Sec	34	85	31	6.8	*(20)*	18.5
Lithium polymer LG Chem Gen III	Sec	95	157	86	19	56	60
Manganese alkaline D cell at 20°C 0.2W $cell^{-1}$	Pri	110	271	100	22	65	*Not suitable*
Lithium ion CGR-18650HG	Sec	160	394	145	32	94	*Not suitable*
Lithium thionyl chloride PT2300	Pri	420	737	382	84	247	*Not suitable*
Lithium CF LCF111	Pri	709	1095	645	142	417	*If achievable: 474*

Note the very poor performance of the cells in the ring stiffened titanium pressure vessel at 50 MPa. In this case the analysis shows that primary manganese alkaline cells would have a similar effective specific energy as lead acid cells within glass spheres. Of course, safety considerations may well rule out the use of lead acid cells in sealed glass spheres, in which case, at a penalty of less than 10% in specific energy, they could be used in pressure balanced mode in conjunction with the glass spheres. Long endurance deep diving vehicles clearly benefit from using pressure tolerant batteries.

BATTERY USE IN FOUR CONTRASTING VEHICLES

REMUS

REMUS is a small AUV that can be configured for different applications, hence not all versions are the same length and volume and different versions may have different energy sources. The basic vehicle is constructed in a single pressure vessel 1.6 m in length and 0.19 m diameter, with a weight of 37 kg [8]. The standard depth rating is 100-150 m. In standard form the energy source is a 1 kWh secondary lithium ion battery, estimated to weigh 7 kg, giving a ratio of M_E to M_{AUV} of 0.19. Versions of REMUS have been fitted with primary lithium cells for longer endurance, providing at least double the 22-hour endurance of the lithium ion pack. In such a small vehicle the high cost of these primary cells may not be such an issue.

The REMUS vehicle, given its small size, comes well equipped with sensors (CTD, light backscatter), navigation instruments (acoustic long baseline, acoustic Doppler velocity log) and all of the necessary systems to provide autonomy. This suggests that the sum of the masses of these components forms a significant part of the overall AUV mass, resulting in a relatively low ratio of M_E to M_{AUV} despite the advantages of its single pressure vessel construction and shallow diving depth. As new technology emerges to replace some of the heavier parts of the vehicle's systems, it is possible that the M_E to M_{AUV} could increase. As an example, the four transducers of the Doppler velocity log can be replaced with a single phased array transducer now under evaluation.

Autosub

At 6.8 m long and 0.9 m in diameter Autosub is a large AUV designed for applications in ocean science [9]. Autosub is constructed as an open frame clad with panels, with a free-flooding internal space for the payload and vehicle systems, most within their separate aluminium, stainless steel or titanium pressure vessels. Many of these pressure vessels are rated to over 3000 m. The largest pressure vessel holds the energy source and its working pressure limits the diving depth of the vehicle. In its first form (Autosub-1) the vehicle was fitted with seven 12 V 80 Ah lead acid batteries providing 6.7 kWh of energy within a 500 m rated glass fibre reinforced plastic (GFRP) pressure vessel (mass 160 kg) that was not ring stiffened. The vessel used titanium

end domes rated to 6000 m (mass of 45 kg). This combination provided a mass to buoyancy ratio of 1.085 – far higher than a ring stiffened pressure vessel with the same depth rating. A ring stiffened titanium pressure vessel with the same buoyancy and a 500 m rating at a safety factor of 1.5 would weigh 39 kg, reducing the overall mass of the vehicle by at least 166 kg. The energy source in Autosub-1 weighed 300 kg and the overall vehicle weighed 1578 kg, a M_E to M_{AUV} ratio of 0. 19.

In 1997 the energy source was upgraded to primary manganese alkaline cells to provide increased energy for the same overall weight. A battery comprising 30 strings of 72 'D' cells in series provided some 30 kWh of energy at 25°C and at a power drain of 500 W typical at that time, sufficient for a 253 km mission [10].

In 2000 the vehicle was further upgraded by exchanging the single GFRP pressure vessel centre section for seven ring stiffened CFRP pressure vessels with a working depth of 1600 m (collapse depth of 3300 m) together with added foam buoyancy segments. The mass to buoyancy ratio of the CFRP tubes was 0.78 (total mass 602 kg) and 1.58 for the foam buoyancy (total mass 294 kg). Seven tubes were used, rather than a single large diameter tube because of the difficulty in manufacturing a single thick-walled CFRP tube and because of uncertainty in the as-built strength. A single ring stiffened CFRP tube with the same displacement as the sum of the seven CFRP tubes in the vehicle and the foam buoyancy, assuming the same mass to buoyancy ratio as that of the smaller tubes, would provide an additional buoyancy of 82 kg; that is, its mass would be 82 kg less.

In practice, Autosub is mass not volume limited. Four of the seven CFRP tubes could be filled with manganese alkaline cells, the other three providing buoyancy and dry space for instrumentation and other vehicle systems. In this configuration the *maximum* battery weight was increased to 700 kg, while the overall vehicle weight increased to 3500 kg, a M_E to M_{AUV} ratio of 0.20. For recent missions, the battery pack was formed of 58 strings of 75 'D' cells in series, 4350 cells in all, weighing 610 kg and providing about 61 kWh of energy at 20°C and the typical Autosub-2 power consumption of 1 kW. Additional instrument payload meant that the battery weight had to be reduced. As described in [11] the use of primary cells proves cost effective for an AUV such as Autosub used in science research campaigns in areas of high risk of loss, such as under sea ice or under ice shelves.

Autosub has a relatively low ratio of M_E to M_{AUV} partly because, as a research vehicle, the design is optimised for flexibility in payload and systems configuration. The use of multiple pressure vessels, many rated to depths exceeding the overall vehicle specification inevitably adds to the overall weight, as does the use of multiple small diameter CFRP pressure vessels. The high safety factor allowed for the CFRP pressure vessels is also a factor.

Geosub

Although derived from Autosub, Geosub has been optimised for routine use in the offshore Oil and Gas industry. As in Autosub, Geosub currently uses CFRP pressure vessels for the batteries, with a depth rating of 2000m but with the ability to upgrade to 3000 m. One of the modifications was to move from primary manganese alkaline cells to a battery of secondary lithium ion cells to suit the day-in, day-out operation of the vehicle. The development of lithium ion batteries for use in the commercial arena presented some significant technical and operational issues. They included:

- Operational safety
- Environmental impact
- Wide temperature performance
- Packaging
- Weight
- Rapid charging systems.

The final solution was developed by a specialist battery contractor* with close attention to the safety and environmental issues. There are four batteries and one charger system. Each battery fits into one of the seven CFRP pressure vessels and comprises a string of 28 sets in series of 33 parallel lithium ion cells. The delivered battery specification is:-

Battery Voltage	100 V (nominal)
Battery Capacity	165 Ah
Total vehicle Capacity	660 Ah (four batteries)
Battery Weight	150 kg
Total Weight	600 kg (four batteries)
Charge time	6 hours from empty

Battery protection system

- Over / under voltage
- Over current (charge / discharge)
- Over temperature

The Geosub vehicle fitted with four battery packs has a weight of 2400 kg. This gives the Geosub vehicle a M_E to M_{AUV} ratio of 0.25. This gives a vehicle total of 3696 cells, and provides about 66kWh of energy across a wide temperature range.

The use of lithium ion cells has provided Geosub with a M_E to M_{AUV} ratio and total available power slightly greater to that of Autosub and at a depth rating of 2000 m compared to 1600 m. In addition, the move to secondary cell technology has successfully and safely added the day-in, day-out operations capability demanded in the commercial market.

USS *Cutthroat*

USS *Cutthroat* is the world's largest AUV at 34 m long, 3 m diameter and weighing 196 tons. She was built as a 0.294 scale model of a US *Virginia* class submarine and contains in her single pressure vessel an energy system weighing some 38 tons, a M_E to M_{AUV} ratio of 0. 19. The primary propulsion energy system comprises 1680 Valve Regulated Lead Acid (VRLA) cells arranged as four parallel stacks of 420 cells in series giving an operational voltage of 742-900 [12]. An auxiliary battery for instrumentation comprises a single stack of 186 cells. Power density rather than specific energy is the most pressing specification for *Cutthroat's* energy supply. The main propulsion motor is rated at 3000 hp (2.2 MW), requiring 1300 W per cell during discharge. The installed energy is sufficient for two runs at flank speed (about 20 minutes at >10 m s^{-1}), three at 75% power and seven at 50% power. *Cutthroat* is also fitted with a 15 hp loiter motor; loiter speed and duration are not available, but are estimated at 1.5 m s^{-1} and up to 95 hours. The performance of *Cutthroat* underlines the energy required for high speed in a large vehicle, with the corollary that a large vehicle is needed to house the energy source when it is a battery that is economic, but of low specific energy. Indeed, low specific energy is an advantage in this case, as the shallow diving AUV with its large single pressure hull would need to have lead ballast added to achieve near neutral buoyancy.

DISCUSSION

Lithium ion secondary cells as in REMUS and Geosub are the state of the art for the modern AUV. Although their specific energy is lower than silver zinc cells, their better cycle life and lower cost of ownership make them the cell of choice where the capital cost can be offset against a large number of missions. However, it would take over 6000 kg of lithium ion cells to provide 1000 kWh for a long endurance AUV. Converting that energy source mass to a vehicle mass at the ratio of 0.2 found in a number of current generation vehicles implies an AUV weighing over 30 tonnes. For most purposes such a vehicle would be impractical, except, perhaps, when shore-based.

---

* AEA Technology Ltd.

Battery chemistries with higher specific energy than lithium ion are available. Commercial lithium carbon monofluoride cells have a specific energy of over 700 Wh kg^{-1} (Table I), over four times that of lithium ion. However, they are single use primary cells. Moreover, they are very costly. Whilst a Watt-hour of energy from a primary manganese alkaline cell costs £0.07, a Watt-hour from Li CF cells costs over £7. The increase in specific energy is at an enormous monetary cost. Therefore, while there are technically feasible battery solutions for providing an AUV with 1000 kWh of energy at a mass of less than 1500 kg (overall AUV mass of 7000 kg) such a vehicle would not be economic.

What are the realistic options for long endurance AUVs? There are several, many of which have been, and remain, topics of research. They include:

- Improve the energy efficiency of the onboard systems and instruments;
- Improve the efficiency of propulsion;
- Reduce the vehicle drag, and maintain low drag throughout missions;

and, following the arguments made in this paper, increase the ratio of M_E to M_{AUV} by:

- Rigorous control of the mass of each component at the design stage;
- Appropriate choice of materials;
- Not over specifying the depth rating of the vehicle or its components;
- Choosing the optimum form of buoyancy for the working depth of the vehicle;
- Further research into reducing the uncertainty of the actual collapse pressure of FRP cylinders;
- Further research into affordable high specific energy electrochemical cells capable of operating at ambient pressure (for deep-diving vehicles) and
- Research into hybrid energy sources, combining the simplicity and reliability of electrochemical batteries with the high specific energy of other sources such as combustion-based systems.

ACKNOWLEDGEMENTS

This work forms part of the Energy and Propulsion topic within the Battlespace Access UUV programme sponsored by the Capability Manager (Manoeuvre) of the UK Ministry of Defence and was carried out under Contract No. RT/COM/2/013. We gratefully acknowledge their support. The views in this paper are those of the authors and do not necessarily reflect those of the Ministry.

REFERENCES

[1] R. E. Davis, C. C. Eriksen and C. P. Jones, 'Autonomous buoyancy-driven underwater gliders', pp. 37-58 in 'The technology and applications of autonomous underwater vehicles', G. Griffiths, (editor), Taylor and Francis, London, ISBN 0415-30154-8, (2003).

[2] D. R. Blidberg and M. D. Ageev, 'Solar powered underwater vehicles', pp. 77-92 in 'The technology and applications of autonomous underwater vehicles', G. Griffiths, (editor), Taylor and Francis, London, ISBN 0415-30154-8, (2003).

[3] C. Funnell (editor), 'Jane's Underwater Technology', Jane's Information Group Ltd., Coulsdon, (4th edition), ISBN 0-7106-2332-1, (2001).

[4] Nektor Research web site at http://www.nektonresearch.com/nektor.html

[5] P. Stevenson and D. Graham, 'Advanced materials and their influence on the structural design of AUVs', pp. 77-92 in 'The technology and applications of autonomous underwater vehicles', G. Griffiths, (editor), Taylor and Francis, London, ISBN 0415-30154-8, (2003).

[6] J. D. Stachiew and R. R. Kurkchubasche, 'Ceramics show promise in deep submergence housings', Sea Technology 34(12): 35-41, (1993).

[7] Bluefin Robotics web site at http://www.bluefinrobotics.com/products.htm

[8] Hydroid Inc web site at http://www.hydroidinc.com

[9] N. W. Millard, G. Griffiths, G. Finnegan, S. D. McPhail, D. T. Meldrum, M. Pebody, J. R. Perrett, P. Stevenson, and A. T. Webb, 'Versatile autonomous submersibles - the realising and testing of a practical vehicle', Underwater Technology 23(1): 7-17, (1998).

[10] G. Griffiths, A. Knap and T. Dickey, 'The Autonomous Vehicle Validation Experiment', Sea Technology 41(2): 35-43, (2000).

[11] P. Stevenson, G. Griffiths and A.T. Webb, 'The Experience and Limitations of using Manganese Alkaline Primary Cells in a large Operational AUV', pp. 27-34 in Proceedings AUV 2002: A workshop on AUV energy systems, Piscataway, IEEE, ISBN 0-7803-7572-6/02, (2002).

[12] K. R. Sette and J. R. Spina, 'Energy storage systems for large vehicles', pp. 19-26 in Proceedings AUV 2002: A workshop on AUV energy systems, Piscataway, IEEE, ISBN 0-7803-7572-6/02, (2002).

PERFORMANCE OF LITHIUM-POLYMER CELLS AT HIGH HYDROSTATIC PRESSURE

K. Rutherford[*a], D. Doerffel[a]

[a]*School of Engineering Sciences, University of Southampton, Highfield, Southampton, SO17 1BJ, UK*

Abstract

Lithium polymer cells are an attractive energy source for underwater vehicles due to their high specific energy and possible operation at hydrostatic pressure. Their behaviour at pressures experienced in the deep ocean is of particular concern to designers. This paper presents test results that show how the voltage during discharge is affected by temperatures between 4°C and 28°C, and pressures of 0.1 MPa and 60 MPa. A simple non-linear equivalent circuit to model the internal resistance of the cell is shown and the effect of temperature on resistance is found. The main conclusions are that lithium polymer cells can operate at 60 MPa, and their performance is similar to that at 0.1 Mpa. Underwater cold temperature and high current reduce the performance of the cell more than high pressure.

Keywords: Lithium polymer batteries, AUV, high pressure, equivalent circuit.

* Corresponding author. Tel: +44 (0)2380-596004 Fax: +44 (0)2380-596149; E-mail address: K.Rutherford@soton.ac.uk

Nomenclature

C_{12}	Double layer capacitance	F
C_{long}	Diffusion capacitance	F
I_C	Charge current	A
I_D	Discharge current	A
Q_0	Rated capacity of a cell at full charge	Ah
R_{01}	Total ohmic resistance	Ω
R_{12}	Charge transfer resistance on discharge	Ω
R_{Long}	Diffusion resistance	Ω
R_P	Self discharge resistance	Ω
S_B	Battery specific energy	Wh kg^{-1}
SOC	State of charge	%
S_S	System specific energy	Wh kg^{-1}
V_0	Voltage at beginning of pause in discharge	V
V_1	Voltage at the end of instantaneous voltage rise	V
V_2	Voltage after 900 seconds of pause.	V

1. Introduction

The motivation for this study was to investigate a potential power source for use within battery-powered autonomous underwater vehicles (AUVs), in particular AUVs that dive deep, to over 5000 m. The Southampton Oceanography Centre's Autosub AUV has operated with batteries assembled from manganese alkaline 'D' size primary cells since 1998, completing over 300 missions for marine science [1]. In the current design, the batteries, made up from up to 5000 cells, are housed in four carbon fibre reinforced plastic tubes, rated to an operating depth of 1600 m [2]. The longest mission to date has been 253 km, limited by the energy that was available [3]. As reliability of the vehicles' systems has improved over the last six years the mission endurance becomes limited by the energy available on board rather than by system failures. AUVs are subject to the limitations of terrestrial electric vehicles, but have additional constraints, such as the need to design for near neutral buoyancy, while providing sufficient energy for missions. Autosub requires over 150 MJ for a 250 Km mission, with typically 500 W in propulsion and 500 W in control system and sensors. In turn, choice of power source affects the mass, shape, performance, and cost of operation of the vehicle.

To date, most AUVs use batteries as their power source. These batteries are usually enclosed within pressure vessels, providing dry space at one atmosphere pressure. However, Stevenson and Graham [4] show that the mass to displacement ratio of pressure vessels increases with diving depth. There is an increasing mass penalty in providing space at one atmosphere for the energy system as a whole (batteries and pressure vessel) for deep diving vehicles.

As a consequence, especially for deep diving vehicles, the option to remove the need for the pressure vessels by operating the batteries at ambient pressure would prove highly advantageous [5]. The batteries would displace their own volume of water, reducing the mass of buoyancy required to float the battery system.

However, not all cell chemistries or forms of construction are amenable to operation at ambient pressures of up to 60 MPa (6000 m water depth). Pressure compensated lead-acid cells are in routine use within instruments and vehicles used in the deep sea, for example the valve-regulated Seabattery [6]. However, their specific energy is low (e.g. 21 Wh kg^{-1} for the 12V 48Ah Seabattery). One candidate cell chemistry with a high specific energy and a form of construction expected to be tolerant to pressure is the lithium-polymer cell (e.g.194 Wh Kg^{-1} for the Kokam SLPB526495 [7]).

As yet, there appears to be no open-literature papers on the performance of lithium-polymer cells at high pressure. This paper reports the results of experiments to evaluate the electrical and mechanical

performance of one type of lithium-polymer pouch cells (Kokam SLPB526495 cells rated at 3.27 Ah [7]) under hydrostatic pressure, with a view towards their use in a new deep-diving AUV Autosub-6000.

Cells were first tested at atmospheric pressure and at ambient temperature. This established typical cell capacity and discharge performance, and provided the parameters of a simple equivalent circuit model used previously for lithium-ion cells by AbuSharkh and Doerffel [8]. Furthermore this data provided a reference to compare the performance and characteristics of cells tested at high pressure (60 MPa) or at low temperature (4°C), typical of the deep ocean. Due to practical constraints it was not possible to alter the temperature of the pressure vessel, preventing the determination of cell performance at the combination of low temperature and high pressure.

2. Methods.

2.1 Test procedures

The experiments under pressure were made within a water-filled cylindrical pressure vessel. The cell was placed within deformable bags filled with oil to ensure electrical insulation and isobaric pressure. The cell was tested with a Digatron universal battery tester as described by Doerffel and Abu Sharkh [8]. The temperature was measured with a thermistor attached to the cell terminal. The same cell was used for the atmospheric pressure tests at 18°C and the tests at 60MPa. A separate cell had to be wired up to test the differing temperature effects.

For reasons of safety, the initial survival test pressurised one cell only to 60 MPa for 1 hour. On depressurisation, the cell was inspected for signs of damage and its terminal and on load voltages checked. These tests showed that this type of lithium-polymer cells would be able to survive the test procedure physically and electrically. Further tests where conducted where batches of 50 cells were pressurised for a total of 12 cycles and then tested electrically, zero failures gave additional confidence that the cells would be suitable for use in pressure compensated batteries.

The electrical test cycle consisted of a full charge with a current of 1 A, until the terminal voltage reached 4.2 V. Charging then continued at this voltage until the current fell below 0.327 A. At this point the cell was considered to be fully charged (100%) SOC. During charging, pauses for 15 minutes were inserted after each 0.327 Ah of charge, representing 10% SOC increase.

During discharge the current was held at a constant value. The cell was considered to be discharged when the on-load voltage reached 3V, above the absolute minimum of 2.5 V as recommended by manufacturer [7]. During discharge pauses of 15 minutes at 0.327Ah intervals meant the peaks in the voltage recovery would align, easing the calculation of OCV using the procedure suggested in [8]. The cell was allowed to rest for 2 hours after a discharge, or at least 4 hours after a charge, to allow the cell to reach close to equilibrium state

One cell, chosen as reference, underwent electrical cycles at 26°C and atmospheric pressure to establish baseline charge discharge characteristics and capacity (section 3.1). Further tests varied the temperature of the air surrounding the cell and the current drawn during discharge at atmospheric pressure (section 3.1) and at 60 MPa (section 3.2)

A simple method was used to calculate state of charge (SOC), which assumes each cell was fully charged before the start of each

test, and that subsequent cycles charged to the same point. Q_o is assumed to be the nominal cell capacity of 3.27 Ah.

$$SOC(t) = 100 \frac{Q_o - \int_0^t I_D(t)dt}{Q_o} \quad (1)$$

2.2 Derivation of the equivalent circuit parameters

As well as determining any effect of hydrostatic pressure on capacity, experiments sought to identify any changes in the internal resistance of the cell. The equivalent circuit of the cell is modelled as a simple linear passive network (Fig. 1) based on a Randles configuration. As this representation does not account for complex nonlinearities, the circuit parameters are functions of temperature, current, state of charge and perhaps pressure.

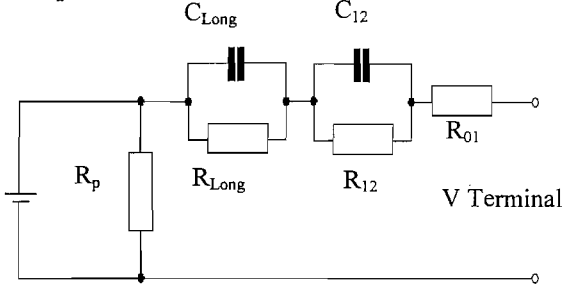

Fig. 1. Equivalent circuit model for the lithium-polymer cells during discharge.

With the exception of R_p, circuit parameters were estimated from discharge test measurements. R_{01} was obtained from: $R_{01} = |V_1-V_o|/I$ (Fig 2.). This is an instantaneous measurement, and although the equipment was set to a high sampling rate it is likely that the value of V_1 includes the beginning of the kinetic overpotential. The first second of discharge is assumed to be the instantaneous voltage drop though it is likely that, after 100ms or so, the kinetic over potential and double layer capacitance have an effect. The kinetic overpotential is affected by temperature and in turn affects the voltage (Tafel equation). The time constant is small so this should have limited effect over these scales.. In the equivalent circuit of Fig. 1, the voltage rise from V_1 to V_2 (Fig 2.) is described by a double exponential:

$$V(t) = V_1 + iR_{12}(1 - e^{-\frac{t}{R_{12}C_{12}}}) + iR_{Long}(1 - e^{-\frac{t}{R_{Long}C_{Long}}}) \quad (2)$$

These values were estimated from the data using a least squares procedure in Maple (version 9) to minimise the difference between V(t) as modelled using equation 2 and the actual data. R_{12} and C_{12} were determined from the first 300 s of the voltage rise after each pause (Fig. 2). The least squares procedure took these values and then estimated R_{long} and C_{long}. R_{12} and C_{12} found from the 15 minute pauses at the end of each 10% discharge (typically 87 mΩ and 11494 F) were significantly less than those estimated from the 2 hour pause at the end of the discharge cycle (e.g. 130 mΩ and 16026 F at 4°C and one atmosphere). Causes for this are discussed in section 3.1. Alternative battery model options are available as given by [10], though this requires many parameters that cannot be found from the limited information available from these tests. Non-linear elements have been considered, and initial tests are encouraging. These have not been utilised here as they require high resolution tests of recovery voltage as a function of time, which has not been possible with the Digatron machine as its sampling rate is limited.

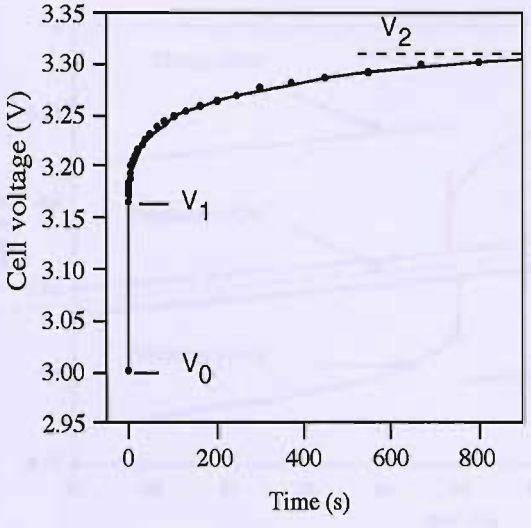

Fig. 2. Voltage-time graph of the reference cell with load of 1 A removed at T=0 showing the voltage points used to estimate the equivalent circuit parameters.

3. Analysis of Results

3.1 Electrical performance at atmospheric pressure

The cell voltage against SOC for a discharge and charge current of 1 A is shown in Fig. 3. with 15 minute pauses at intervals of $Q_0/10$. If the cell voltage reached equilibrium within each pause, then the off load voltage during discharge would be equal to the off load voltage during charge. That is not the case in these tests, for example Fig. 4 shows an enlargement graph of the data from Fig. 3. around the pause at 60% SOC.

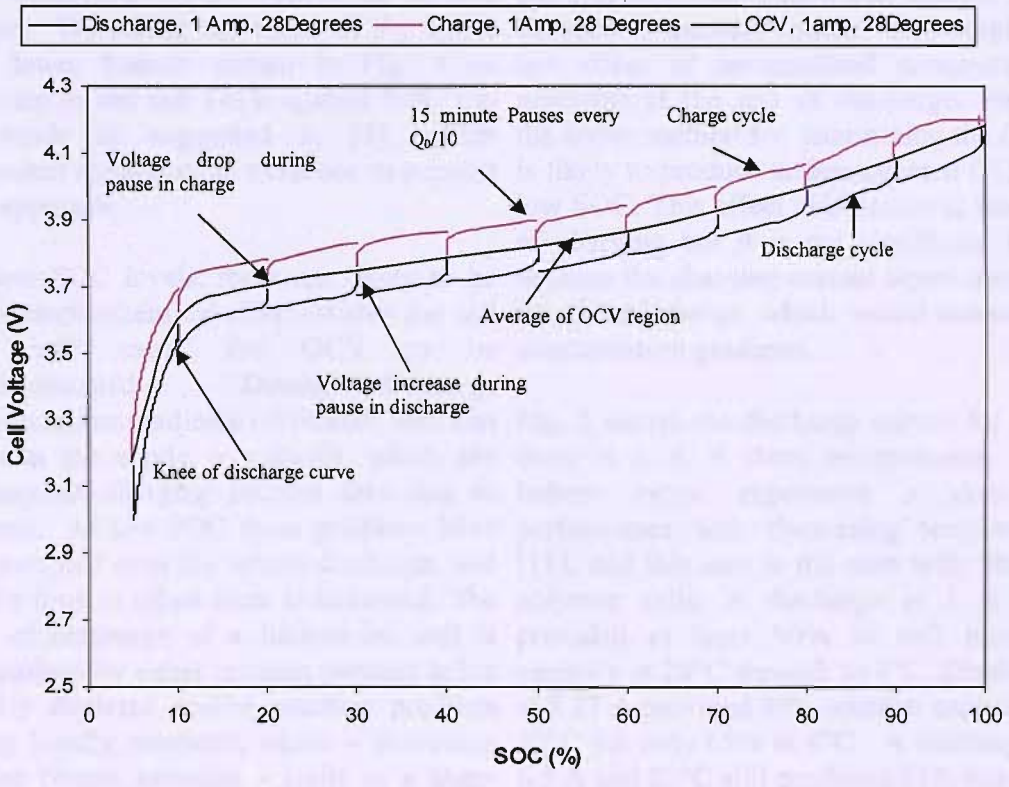

Fig. 3. Cell Voltage with state of charge during charge and discharge at 1A at a mean temperature of 28 °C at one atmosphere.

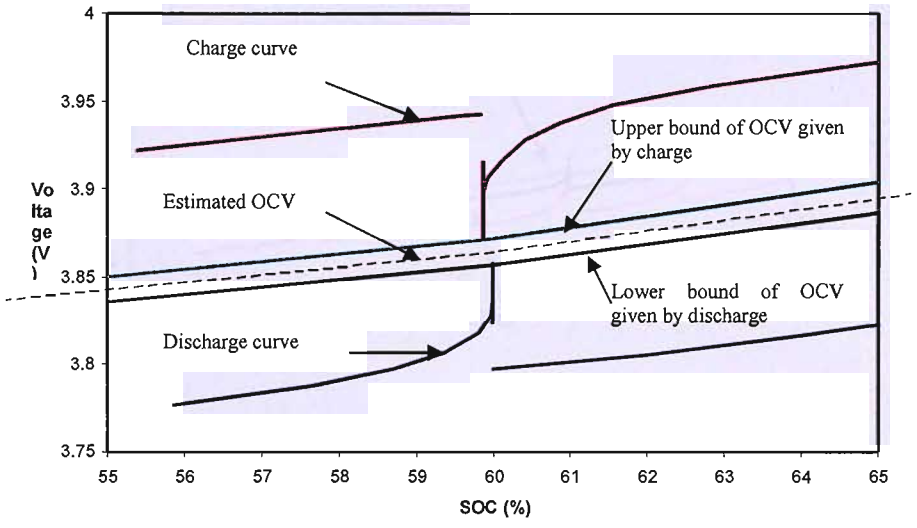

Fig. 4. Cell Voltage at 60% SOC, 1 A and mean temperature of 28 ° C showing upper and lower limits of OCV.

The gap between the cell voltages at the end of discharge and charge pauses was 14 mV. The equilibrium OCV would lie in this region. By taking the mean of the upper and lower bounds shown in Fig. 4 an estimate of the cell OCV against SOC can be made as suggested in [8], which presented experimental evidence to support this approach.

At low SOC levels, there are likely to be some electrochemical affects within the cell that will cause the OCV to be underestimated. During discharge concentration gradients of lithium ions can form at the anode or cathode, which the subsequent charging process then has to reverse. At low SOC these gradients have accumulated over the whole discharge, and so the time to offset them is increased. The end of discharge of a lithium-ion cell is determined by either reaction partners being locally depleted and/or reaction products being locally saturated, which – according to the Nernst equation - leads to a sharp decrease in the equilibrium potential of the cell. This is observed as a knee in the discharge curve and means that small changes in concentration can exhibit large changes in the cell voltage. This amplifies the effect of accumulated concentration gradients at the end of discharge. Hence, the above method for determining the OCV is likely to produce underestimated OCV at low SOC. This effect also occurs at the end of charging but it is not significant here, because the charging current tapers down at the end of charge, which would reduce the concentration gradients.

Fig. 5 shows the discharge curves for tests done at 1 A at three temperatures. All battery types experience a drop in performance with decreasing temperature [11], and this also is the case with lithium polymer cells. A discharge at 1 A still provided at least 90% of cell nominal capacity at 28°C through to 4°C. Discharge at 3.27 A provided 90% nominal capacity at 22°C yet only 65% at 4°C. A discharge at 6.5 A and 23°C still produced 85% nominal capacity, yet only 17% at 3°C.

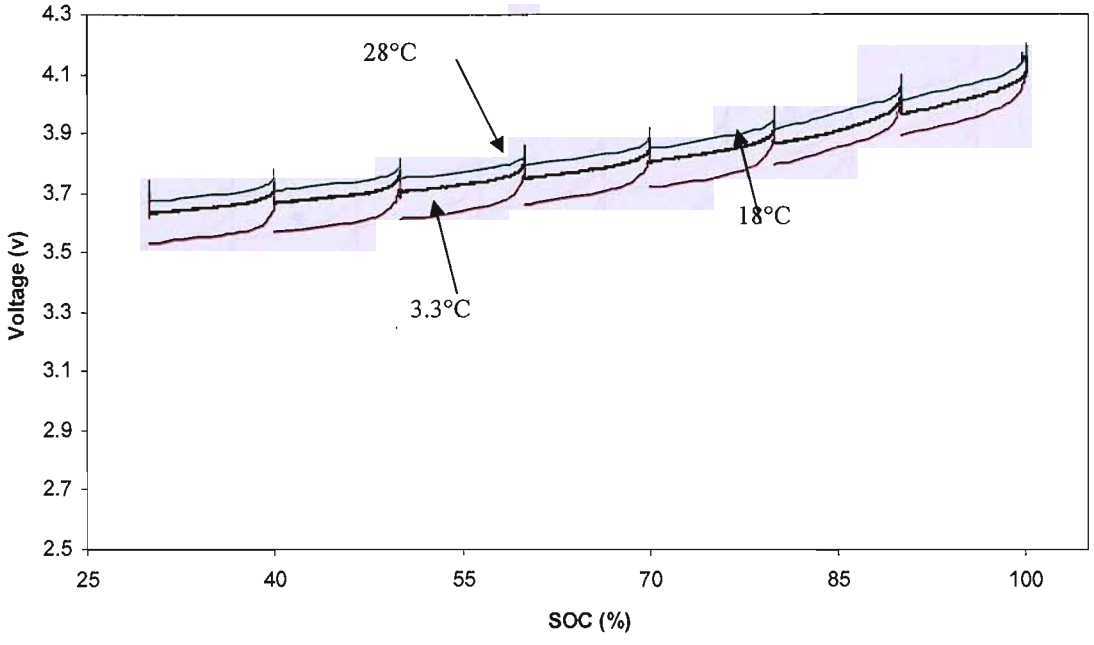

Fig. 5. Discharge curves for 1 Amp, at 28, 18, and 3.3 °C compared to SOC

After a pause the voltage rises to almost the same point at all temperatures (Fig. 5), though the estimated OCV is not quite the same. The Nernst equation in [11] shows that the equilibrium voltage is affected by a temperature coefficient, though this does not seem to be significant as the cell recovered, given 900 seconds, to the same voltage irrespective of temperature.

The drop from V_2 to the on-load voltage at the beginning of each discharge period in Fig. 7 is much larger than observed for the same current load in Fig. 6, implying an increase in R_{01} at the lower temperature. The increase of ohmic resistance (immediate voltage drop) is due to the decrease of ionic conductivity in the polymer electrolyte [12]. The increasing gradient of the discharge curve with increasing current draw is evidence of higher internal resistance R_{12} and will be explored in section 3.3. At 60% SOC, the total voltage drop at 3.27 A and 22°C is 249 mV, while at 4°C and 3.27 A the voltage drop increases to 783mV.

The exact capacity removed from the cell is influenced by the 'knee' of the discharge curve (Fig. 3.). The cell capacity is almost fully exhausted after this knee is reached during discharge. The voltage drops quickly and only little capacity can be discharged before the cut-off voltage is reached as shown in the low current discharge in Fig 7. Fig 7 also shows that this knee is not yet reached when discharging at high currents and at a low temperature (4°C). The reason for smaller capacities obtained in these tests is not that the cell capacity is exhausted (depletion of reactants or saturation of reaction products), but that simply the cut-off voltage is reached prematurely due to high voltage drops, probably as a result of poor ionic conductivity of the polymer electrolyte.

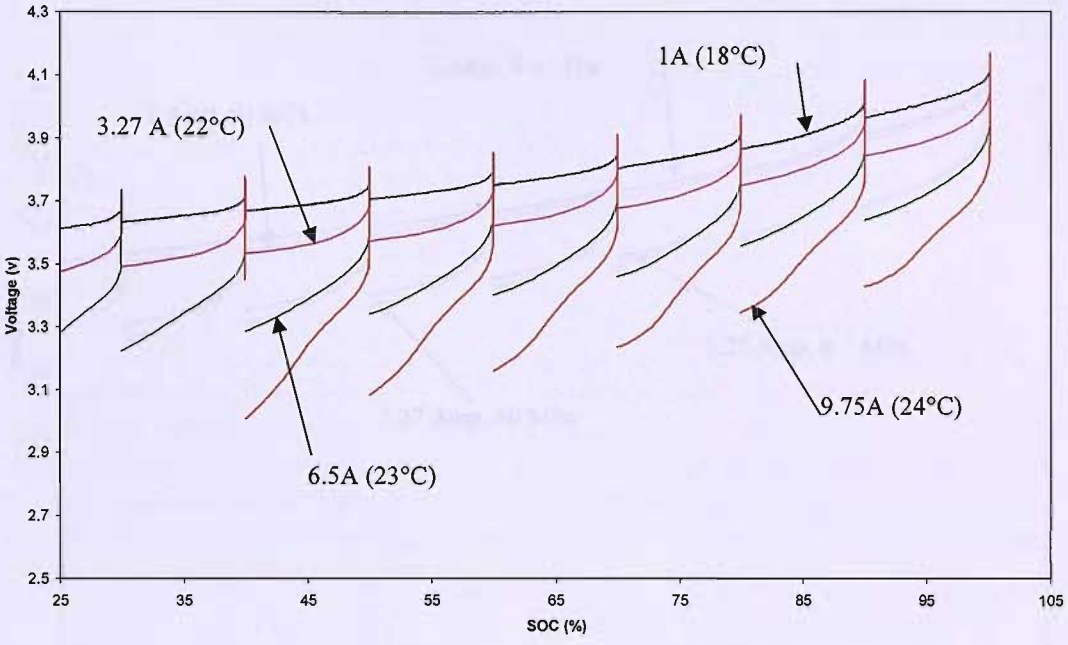

Fig. 6. Cell voltage with SOC at 1, 3.27, 6.5 and 9.75 Amp discharge between 18 and 24° C and at one atmosphere pressure.

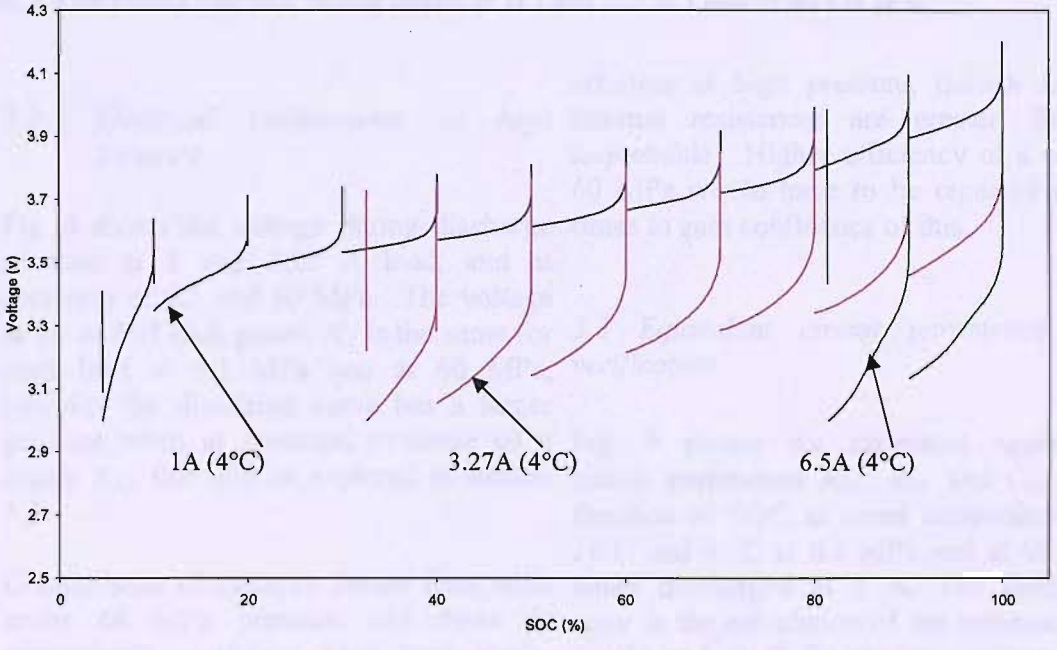

Fig. 7. Cell voltage with SOC during discharge at 1, 3.27 and 6.5 Amps, at 4° C and atmosphere pressure

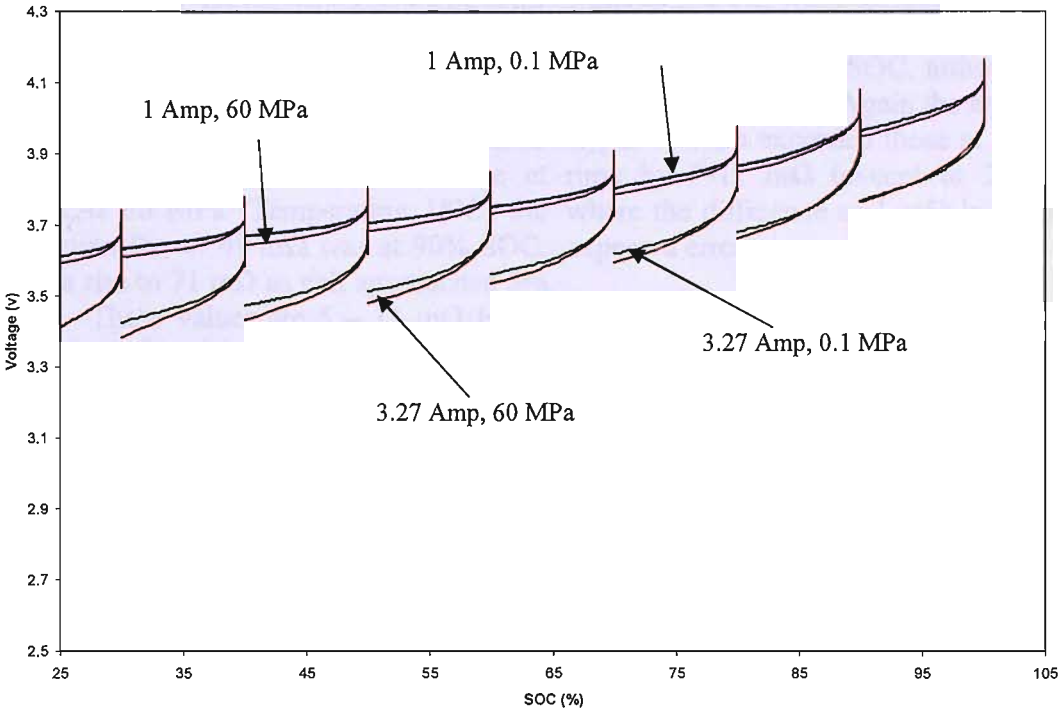

Fig. 8. Cell voltage with SOC during discharge at 1 and 3.27 A, 1 and 60 MPa at 18°C

3.2 Electrical performance at high pressure

Fig. 8 shows the voltage during discharge of tests at 1 and 3.27 A load, and at pressures of 0.1 and 60 MPa. The voltage at the end of each pause, V_2 is the same for each load at 0.1 MPa and at 60 MPa, however the discharge curve has a larger gradient when at pressure, evidence of a higher R_{12}, this will be explored in section 3.3.

Comparisons of capacity drawn from cells under 60 MPa pressure and those in atmospheric conditions have been made. At 1 A load, the capacity of the cell is 90%, slightly lower than at 60 Mpa, 91%, however an error of $\pm$ 1% is not unlikely. At 3.27 A the 60 MPa capacity is 92%, 6% higher than at 0.1 MPa, 86%, which is unlikely to be an error. This would suggest that the electrochemistry of the cell is more efficient at high pressure, though as the internal resistances are greater, this is improbable. Higher efficiency of a cell at 60 MPa would have to be repeated many times to gain confidence of this.

3.3 Equivalent circuit parameters and verification

Fig. 9 shows the estimated equivalent circuit parameters R_{01}, R_{12} and C_{12} as a function of SOC at mean temperatures of 28°C and 4 °C at 0.1 MPa and at 60 MPa when discharged at 1 A. The estimated error in the calculation of the resistances is 1 mΩ and 50 F for the capacitance. The ohmic resistance R_{01} changes in both magnitude and behaviour as a function of SOC and temperature. At 28°C R_{01} varied little with SOC, increasing from 25-26 mΩ at 100% - 30% SOC to 27-31 mΩ at 20% SOC and below. In contrast, the minimum R_{01} at 4°C was 89 mΩ, with a rise to 164

mΩ as the cell approached 5% SOC. This ohmic voltage rise should not vary with temperature, but as discussed above in section 2.3, it is likely that this value includes a fraction of the charge transfer resistance, and so is more noticeable at 4°C.. At 60 MPa (Temperature 18°C) the minimum R_{01} of 49 mΩ was at 90% SOC, with a rise to 71 mΩ as cell approached 5% SOC. These values are 5 – 11 mΩ larger than those found for the cell at atmospheric pressure at the same temperature.

The charge transfer resistance R_{12} behaved differently. The estimates at 0.1 MPa and 60 MPa showed higher resistances at 90% and 5% SOC than at intermediate points. At 28°C and 0.1 MPa, R_{12} was greater than R_{01} while at 4°C R_{12} was less than R_{01} except at 90% SOC. Also at 18°C 60 MPa R_{12} exceeded R_{01} at 90% SOC, although not at 10% SOC and lower. Again the estimates of R_{12} at 60 MPa exceeded those at 1 bar, this time by 7-12 mΩ (except at 20% SOC where the difference of 1 mΩ is within the expected error).

Estimates of the double layer capacitance C_{12} showed lower values at the lower temperature, and highest near 50% SOC. Here tests at 18°C and 28°C have approximately the same values of C_{12}, though at pressure C_{12} could have a lower value, but still have the same curve shape.

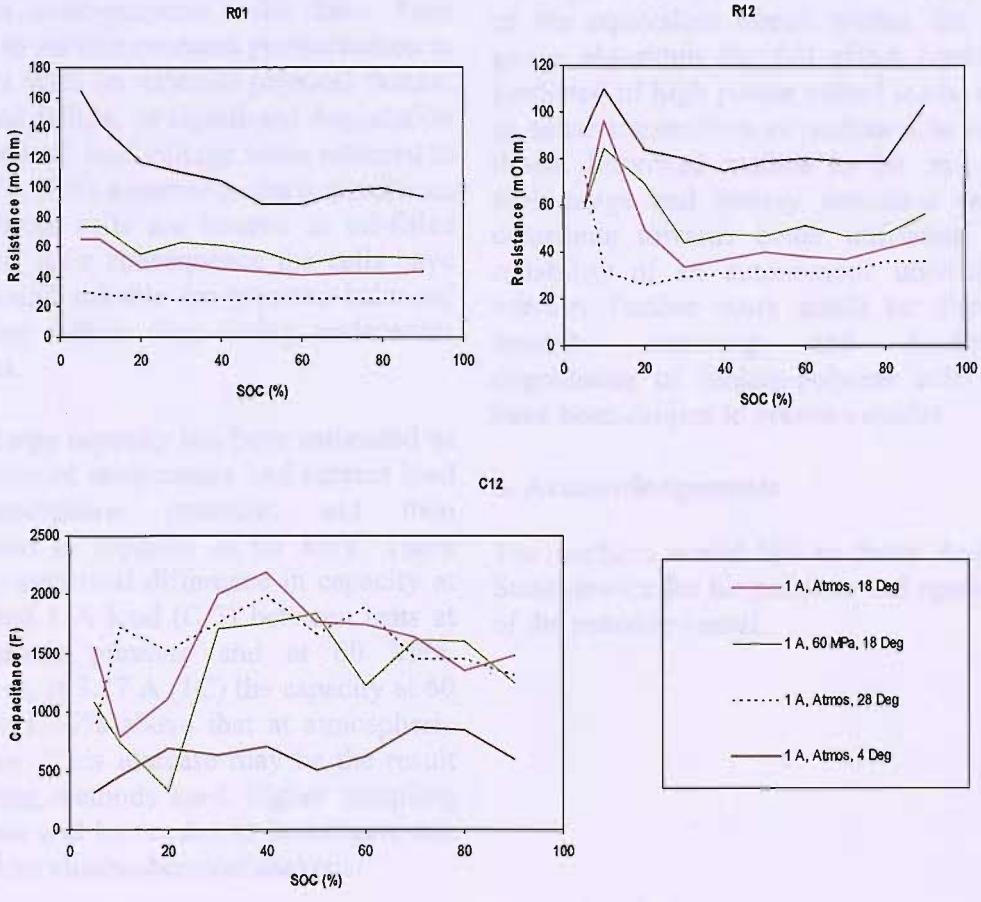

Fig. 9 Estimated Equivalent Circuit parameters R_{01}, R_{12} and C_{12} for cycles at 1 Amp and varying temperature and pressure.

The first minute of the recovery period will include the double layer capacitance, included in the Tafel equation and represented by C12, and though this value

is useful for the simulating, it is not an accurate representation of the electrochemistry. The increases in resistance with pressure may also be explained by error in separating ohmic resistance and overpotentials. For the deep ocean application the cells would be far more affected by the reduction of temperature from the ocean surface to 6000 m than for the increase in pressure from 0.1 to 60 MPa. There is a small increase of resistance at pressure, but were the current draw to be kept small, the cell would still produce more than 90% of its rated capacity.

5. Conclusions

Lithium solid-polymer cells have been shown to survive repeated pressurisation to 60 MPa with no external physical failure, electrical failure, or significant degradation to on and off load voltage when returned to 0.1 MPa. This assumes isobaric conditions when these cells are housed in oil-filled pouches. As a consequence the cells have been found suitable for pressure-balanced operation within deep-diving underwater vehicles.

Cell charge capacity has been estimated as a function of temperature and current load at atmospheric pressure, and then compared to capacity at 60 MPa. There was no statistical difference in capacity at 18°C and 1 A load (C/3) between tests at atmospheric pressure and at 60 MPa. However, at 3.27 A (1C) the capacity at 60 MPa was ~5% above that at atmospheric pressure. This increase may be the result of testing methods used, higher sampling rate tests will be needed to investigate this with more electrochemical analysis.

Analysis of charge and discharge voltage data enabled the parameters of a simple equivalent circuit model to be estimated as a function of temperature, state of charge and pressure. Temperature had a greater effect than pressure on the values of the equivalent circuit parameters. On average, the values of R_{01} and R_{12} at 60 MPa were higher, by 5-11 mΩ at atmospheric pressure at the same temperature, while cooling the cells from 18°C to 4°C increased R_{01} by ~60 mΩ and R_{12} by ~40 mΩ.

The equivalent circuit parameters described in this paper, will enable a model of the cell to be created, in order to then produce a fuel gauge algorithm. This algorithm would be able to predict capacity and terminal voltage based on current load, temperature and pressure. By incorporating the capacitive as well as resistive elements of the equivalent circuit within the fuel gauge algorithm the full effect could be predicted of high power pulsed loads, such as sonar transmitters or variation in AUV thrust. Improved realism in the on-board fuel gauge and battery simulator would contribute towards better utilisation and reliability of an autonomous underwater vehicle. Further work could be directed towards assessing and modelling degradation of lithium-polymer cells that have been subject to pressure cycles.

6. Acknowledgements.

The Authors would like to thank Andrew Staszkiewicz for his patience and operation of the pressure vessel.

7. References.

[1] N.W. Millard and 26 others, Multidisciplinary ocean science applications of an AUV: The Autosub science missions programme. In: Griffiths, G. (Ed.), The technology and applications of autonomous underwater vehicles. Taylor and Francis, London, 2003, pp. 139-159.

[2] P. Stevenson, G. Griffiths, A.T. Webb, The experience and limitations of using manganese alkaline primary cells in a large operational AUV. Proc. AUV 2002: A workshop on AUV energy systems, IEEE, Piscataway, 2002, pp. 27-34.

[3] G. Griffiths, G., A. Knap, T. Dickey, The Autonomous Vehicle Validation Experiment, Sea Technology, 41(2) (2000) 35-43.

[4] P. Stevenson, D. Graham, Advanced materials and their influence on the structural design of AUVs, In: Griffiths, G. (Ed.), The technology and applications of autonomous underwater vehicles, Taylor and Francis, 2003, pp. 77-92.

[5] G Griffiths, J Jamieson, S Mitchell, K Rutherford, Energy storage for long endurance AUVs. Proc. ATUV conference, IMarEST, London, 16-17 March 2004. pp. 8-16.

[6] http://www.deepsea.com/seabatry.html#summary accessed on 29 September 2004.

[7] http://www.kokam.com/product/battery_main.html accessed on 20th July 2004.

[8] S. Abu-Sharkh, D. Doerffel, Rapid test and non-linear model characterisation of solid-state lithium-ion batteries. J. Power Sources, 130 (2004) 266-274.

[9] H.Jan Bergveld, W.S.Kruijt, P.H.L.Notten, Battery Management Systems: Design by modelling, Kluwer Academic Publishers, Dordrecht, 2002.

[10] D.Lyndon, T.B.Reddy (Eds)., Handbook of Batteries, third ed., McGraw-Hill, New York, 2002, pp. 22.18

[11] G.M.Ehrlich, in: D.Lyndon, T.B.Reddy (Eds)., Handbook of Batteries, third ed., McGraw-Hill, New York, 2002, pp. 35.26

[12] http://vtb.engr.sc.edu/ last accessed on 25/02/05

[13] J. J. Hong, Lithium secondary cell and method of fabricating the same, .US Patent No. US6,423,449, 2002.

APPENDIX B

Pressure vessel creation.

B.1 Theory.

This appendix presents a summary of pressure vessel design. Pressure vessels are a well understood technology and more detail can be found in reference books (Ross 1990).

A pressure vessel will always be present to protect pressure sensitive components. Some components cannot operate at pressure, such as hard-drives, because of different construction materials (semiconductors and dielectrics) which may have a elastic property mismatch of structural materials or an internal void may be present (Research Triangle Institute 1973, White 2005). In the future it may be possible to run AUVs from solid memory, removing the hard drive, making it possible to remove all pressure sensitive electronics.

There are two main stresses within a cylinder with domed ends when subjected to pressure; longitudinal stress and radial stress. The circumferential stress is twice that of the longitudinal stress and so dominates the collapse of the pressure vessel and gives rise to equation 1, also known as the boiler pressure equation (Benham, et al. 1996, Burcher and Rydill 1994).

$$P_{Yield} = S_F \sigma_{Yield} \frac{t}{R} \qquad 1$$

Equation 1 is a valid pressure vessel design equation, given a thin wall and a small fineness ratio. R is the average radius of the pressure vessel and wall thickness, σ_{Yield} is the yield stress of the pressure vessel material. If the wall thickness becomes greater than 10% of the radius, the pressure vessel is said to be thick-walled, and another equation represents the $P_{Collapse}$ (equation 2) (Benham, et al. 1996 pg. 387, Saw 2005).

$$P_{Yield} = \frac{-S_F \sigma_{Yield} \frac{1}{2}\left(R_{PVo} + R_{PVi}\right)\left(R_{PVo}^{\ 2} + R_{PVi}^{\ 2}\right)}{R_{PVo}^{\ 2}\left(R_{PVi}^{\ 2} + \frac{1}{4}\left(R_{PVo} + R_{PVi}\right)^2\right)} \qquad 2$$

When the fineness ratio is large enough (the cylinder is long and thin) the pressure vessel might fail by buckling rather than material yield. Exploring this leads to another set of equations. Equation 3 is derived from a version of the Von Mises equation presented by Ross (Ross 1990 pg. 76) and is also presented in DeHart (DeHart 1969 pg. 9-5). DeHart's version is only recommended for values of n greater than 5, and so will give a conservative estimate of the failure of a pressure vessel. n is the number of lobes of the pressure vessel cross section at failure, an ellipse has $n = 2$, a cross has $n = 4$. The Von Mises equation used by Ross is given in equation 3.

$$P_{Buckle} = \left(\frac{E\left(\frac{t}{R}\right)}{n^2 - 1 + \left(\frac{\pi R}{2L}\right)^2} \right) \left(\frac{1}{\left(n^2\left(\frac{L}{\pi R}\right)^2 + 1\right)^2} + \left(\frac{t^2}{12R^2\left(1-\upsilon^2\right)}\right)\left(n^2 - 1 + \left(\frac{\pi R}{2L}\right)^2\right)^2 \right) \quad 3$$

As L tends towards infinity, then this produces equation 4

$$P_{Buckle} = S_F \frac{Et^3}{12\left(1-\upsilon^2\right)R^3}\left(n^2 - 1\right) \quad 4$$

and for n = 2; $P_{Buckle} = S_F \frac{Et^3}{4\left(1-\upsilon^2\right)R^3}$. 5

P_{Buckle} is the pressure by which the pressure vessel will fail due to buckling of the cylinder walls, rather than the material yielding and collapsing. E is the Youngs' modulus of the material, υ is the Poisson's ratio. Equation 5 shows the equation for when n = 2, and requires the lowest P_{Buckle}.

Figure B.1 shows the effect of n on pressure factor. Pressure factor is based on equation 3, after E has been removed, making pressure factor general to any chosen material. For values of L / D greater than 2.0, the lowest buckling factor (and hence lowest $P_{Collapse}$) occurs when n = 2. In this methodology the pressure vessel is assumed to have a L / D ratio greater than 2.0 meaning that n=2 and equation 5 is appropriate.

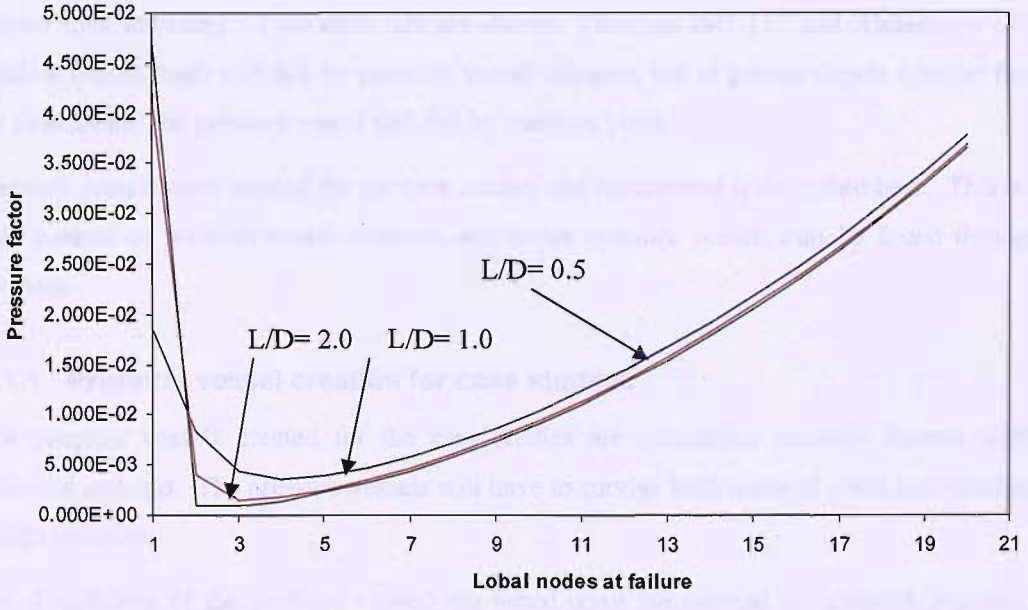

Figure B.1 Buckling pressure factor variation with lobal failure nodes, *n*.

Ring stiffeners will help prevent the collapse of the pressure vessel due to buckling by reducing the effective length. It would be possible to increase the wall thickness, but ring stiffeners can achieve

the same strength with less mass. This level of design is used for the final detailed design iteration to save a small percentage of pressure vessel mass.

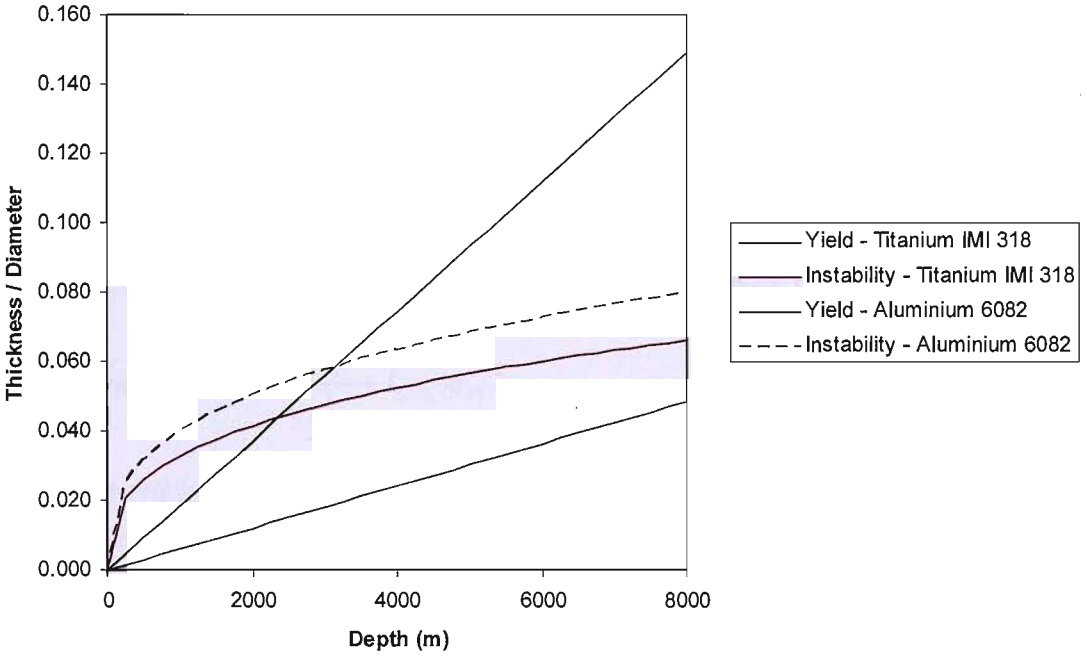

Figure B.2 Pressure vessel thickness/diameter increase with depth given n=2 and L = infinite.

Figure B.2 shows the increase of ratio of thickness to diameter with increasing diving depth. To resist failure, either by collapse or buckling, the thickness /diameter of the pressure vessel must be greater than indicated. Two materials are shown, Titanium IMI 115 and Aluminium 6082. At shallow depths, both will fail by pressure vessel collapse, but at greater depths (greater than 3000 for aluminium) the pressure vessel will fail by material yield.

Pressure vessels were created for the case studies and the method is described here. This is not the only method of pressure vessel creation, and better pressure vessels may be found through other methods.

B.1.1 Pressure vessel creation for case studies.

The pressure vessels created for the case studies are cylindrical pressure vessels with hemi-spherical endcaps. The pressure vessels will have to survive both material yield and buckling at the design pressure.

The dimensions of the pressure vessels are based upon the internal components required radius, length or volume. In some instances not all these are given and the pressure vessel design is iterated to produce a feasible solution.

The process is split into two main stages, design to resist material yield and then to resist buckling. Equation 1 can be rewritten to give pressure vessel wall thickness, t, equation 6.

$$t = \frac{P_{Yield} R}{S_F \sigma_{Yield}} \qquad 6$$

P_{Yield} σ_{Yield} are known from the operating depth and the chosen material properties. S_F can be specified (1.2, of 20 % is customary for metals) and R depends on internal components.

The required internal volume of subsystems needs to be enclosed. Equation 7 is taken from Chapter 2 and shows the internal volume of the pressure vessel available for packing.

$$Internal\ Volume = \frac{8 r_{PVi}^3}{3^{\frac{3}{2}}} + L_{PVC} \pi r_{PVi}^2 \qquad 7$$

Assuming the required volume of subsystems is known, then L_{PVC} can be found by rearranging equation 7 to give equation 8.

$$L_{PVC} = \left(Internal\ Volume - \frac{8 r_{PVi}^3}{3^{\frac{3}{2}}} \right) \frac{1}{\pi r_{PVi}^2} \qquad 8$$

Now the pressure vessel displacement volume and mass can be found from equations 9 and 10.

The second stage checks whether this pressure vessel will fail by buckling at the required operating depth. The pressure vessel dimensions found are put into the full Von Mises' equation (equation 3). The full version of Von Mises' is used as the pressure vessels in the case studies have L / D less than 10.

Figure B.2 indicates that titanium will fail by buckling for long cylinders for depths up to 8000 m. If the pressure vessel fails by buckling, either the wall thickness or radius can be increased. Increasing the wall thickness is an option if the radius is constrained and will increase strength at the expense of mass. Increasing the radius will reduce L_{PVC} and strengthen the pressure vessel. This is the preferred method if only a volume is defined by the internal subsystems. This method can be iterated many times in order to create a pressure vessel for each case study.

B.2. Pressure vessel volume and mass.

Packing the pressure vessel and determining its length is more of a challenge, and shows scope for packing algorithms. Hemi-spherical ends can be used for packing, and smaller sub-systems should be placed towards the ends to fit within the radius. The largest subsystem should be placed within the cylindrical section, and the heaviest subsystem placed at the *CoB* of the pressure vessel.

Figure B.3 shows the nomenclature used to define the geometry of the pressure vessel.

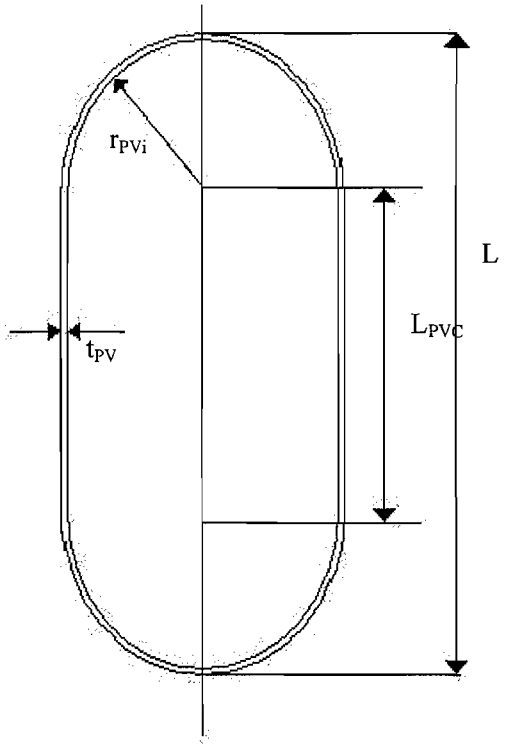

Figure B.3 Pressure vessel nomenclature.

The displacement and mass of the pressure vessel is given in equations 9 and 10, the total mass of the pressure vessel with pressure sensitive subsystems is given in equation 11.

Given that: $r_{PVo} = r_{PVi} + t$.

$$\nabla_{PV} = \frac{4}{3}\pi r_{PVo}{}^{3} + L_{PVC}\pi r_{PVo}{}^{2} \qquad 9$$

$$Mass_{PV} = \rho_{Material}\left(\frac{4}{3}\pi\left(r_{PVo}^{3} - r_{PVi}^{3}\right) + L_{PVC}\pi\left(r_{PVo}^{2} - r_{PVi}^{2}\right)\right) \qquad 10$$

$$M_{Pv} = Mass_{PV} + Mass_{internal\ systems} \qquad 11$$

From these equations it can be shown, in Figure B.4, that there is no volume benefit in splitting the pressure vessel into multiple smaller vessels. To get the same available volume with smaller pressure vessels, their combined mass would be the same as one pressure vessel as both mass and volume are $R_{PVo}{}^{3}$ functions.

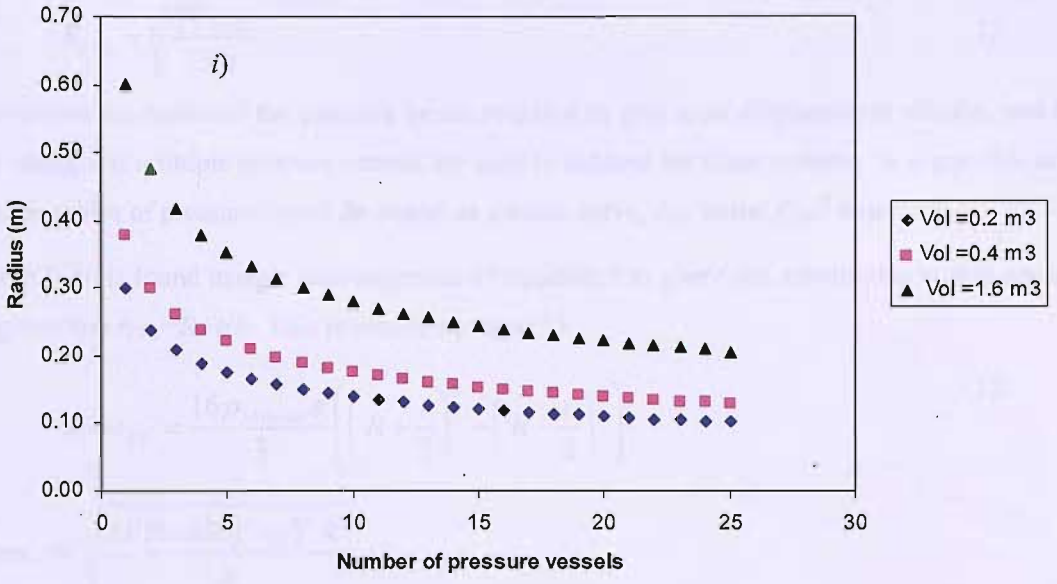

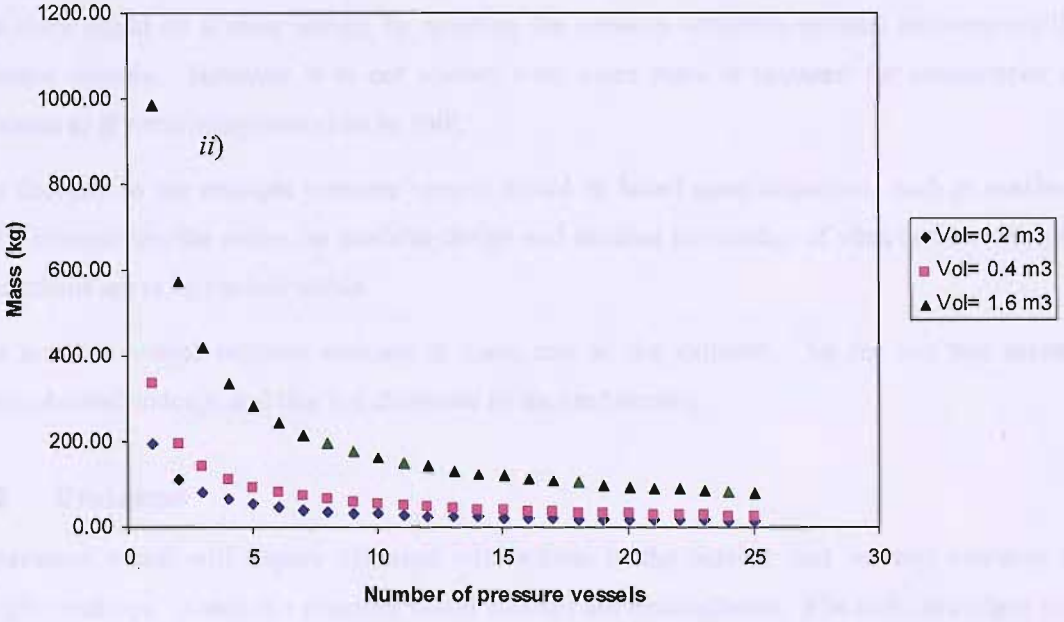

Figure B.4 *i*) Required radius of each pressure vessel to obtain a fixed volume and *ii*) Total mass of pressure vessels for a given volume.

Figure B.4 shows the size and mass comparisons of using multiple pressure vessels to achieve a set volume. Figure B.4*i* is found by rearranging equation 9 to give R_{PV_o} given the assumption that $L=4R_{PV_o}$ to give equation 12 α is the number of pressure vessels required to make up the total volume ∇_{Total}.

$$R_{PVo} = \sqrt[3]{\frac{3\nabla_{Total}}{7\pi\alpha}} \qquad 12$$

This shows the radius of the pressure vessel required to give a set displacement volume, and how this changes if multiple pressure vessels are used to achieve the same volume. It is possible to see that the radius of pressure vessel decreases as a cubic curve, due to the R_{PVo}^3 term.

Figure B.4*ii* is found using a rearrangement of equation 5 to give t and substituting within equation 10 given that $r_{PVo}=R+t/2$. This produces equation 13

$$Mass_{PV} = \frac{16\rho_{Material}\pi}{3}\left(\left(R+\frac{t}{2}\right)^3 - \left(R-\frac{t}{2}\right)^3\right) \qquad 13$$

where $t = \sqrt[3]{\frac{4PBuckle(1-\upsilon)^2 R^3}{E}}$.

This shows that the mass of the pressure vessel is a function of R, $\rho_{Material}$, E and υ. This means that there could be a mass saving by splitting the pressure sensitive systems between multiple pressure vessels. However it is not known what extra mass is required for connections and structure or if some subsystems can be split.

The decision to use multiple pressure vessels would be based upon constraints such as maximum AUV dimensions, the desire for modular design and detailed knowledge of what pressure sensitive subsystems are to be packed within.

The pressure vessel requires endcaps at each end of the cylinder. So far this has assumed hemispherical endcaps and this is a discussed in the next section.

B.3 Endcaps

A pressure vessel will require electrical connections to the outside, and so have complex and weighty endcaps. Autosub's pressure vessel endcaps are hemi-spheres. Flat end caps might allow improved packing and placement within the concept AUV, but are a weakness of the pressure vessel.

For simple ends $P_{Yield} = S_F \frac{8\sigma_{Yield}t^2}{3r^2\left(\frac{3}{\upsilon}+1\right)}$ 14

For fixed ends $P_{Yield} = S_F \frac{4\sigma_{Yield}t^2}{3r^2}$ 15

Equations 14 and 15 show equations for the pressure at which flat ends will fail by material yield. For steel, the fixed pressure vessel end will fail before the cylinder body until 15500 m. The

simple endcaps will fail before the cylinder until 2050 m. In practice flat endcap failure pressure is between these two equations due to the real flat endcap connection having both simple and fixed components.

Hemispherical endcaps will fail when the cylinder does, but all these methods are dependant on the actual construction method (bolts or welding). In this example hemispherical endcaps will be used, with the construction and the electrical connections designed in the detailed design stage.

B.4 Spherical pressure vessel.

Spherical pressure vessel creation is more simple. However the presence of connections though the pressure vessel wall will compromise the structural strength and require special attention when designing. The stress at any point is given in equation 16 (Benham, et al. 1996), pg54) and internal volume and displacement given by equations 17 and 18.

$$P_{Collapse} = 2S_F \sigma_{Yield} \frac{t}{R} \quad 16$$

$$Internal\,Volume = \frac{4}{3}\pi r_{PVi} \quad 17$$

$$\nabla_{SphericalPV} = \frac{4}{3}\pi r_{PVo} \quad 18$$

To define the spherical pressure vessel, only the radius, safety factor and construction material need to be decided, as the collapse pressure is defined by the mission parameters. The wall thickness can then be calculated by rearranging equation 16. The internal components mostly consist of printed circuit boards, wiring and other electronic components, hence can be designed to fit almost any space. The constraint placed here is that the internal volume of the pressure vessel matches the volume of the pressure sensitive components.

B.4 References.

Benham, P. P., R. J. Crawford and C. G. Armstrong. (1996). "*Mechanics of Engineering Materials.*" 2nd Edition, Addison Wesley Longham limited.

Burcher, R. and L. Rydill. (1994). "*Concepts in Submarine Design.*" Ocean Technology, Cambridge University Press.

DeHart, R. C. (1969). "*Handbook of ocean and underwater engineering.*" J. J. Myers, C. H. Holm and R. F. Mcallister (Editor), McGraw Hill.

Research Triangle Institute. "*Study of contemporary electronic components under a fluid pressure environment.*" (1973), Research Triangle Institute, Naval Ship Research and Development Laboratory.

Ross, C. T. F. (1990). "*Pressure vessels under external pressure statics and dynamics.*" Taylor & Francis books.

Saw, K. (2005). "*Pressure vessel design.*" K. Rutherford, *personal communication.*

White, D. (2005). "*Pressure testing of internal components.*" K. Rutherford, *personal communication.*

APPENDIX C

Least squares approximation for battery internal resistance.

This Appendix describes the least squares method used to find the equivalent circuit values to model a lithium polymer battery.

D.1 Theory.

Figure D.1 shows the battery voltage rise during a pause in discharging.

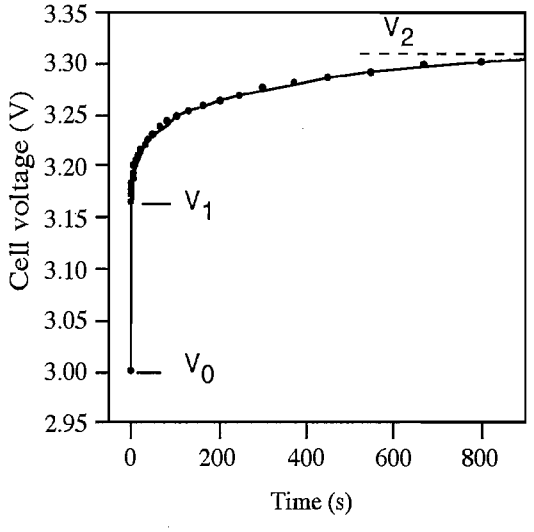

Figure D.1 Voltage-time graph over 15 minutes of the reference battery with load of 1 A removed at T=0 showing the voltage points used to estimate the equivalent circuit parameters.

The instantaneous rise is V_0 to V_1 is due to ohmic resistance and can be modelled with a single resistor, R_{01}. R_{01} is calculated by $V_1 - V_0 / i$. The curve from V_1 to V_2 is the dynamic voltage response and is described by a pair of exponentials,

$$V(t) = V_1 + iR_{12}(1 - e^{\frac{t}{R_{12}C_{12}}}) + iR_{Long}(1 - e^{\frac{t}{R_{Long}C_{Long}}}). \quad 1$$

The task is to find the values of R_{12}, C_{12}, R_{Long} and C_{Long} to approximate $V(t)$. $V(t)$ is the experimental voltage rise over a pause in discharge, $V_2 - V_0$, and i is the current draw.

When $t = \infty$ equation G.1 can be rewritten as,

$$V(t) = V_1 + iR_{12} + iR_{Long}. \quad 2$$

The challenge is at what time (t) will equation G.1 become G.2? Doerffel's (Doerffel D and S. Abu Sharkh 2004) method only had R_{12} and not R_{Long}, so R_{12} was found by;

$$R_{12} = \frac{V_2 - V_1}{i} \quad 3$$

However this approach assumes that the capacitor has little impact, or has a very short time constant. For this research a least squares approach was used, to fit a curve and allow for different capacitor time constants.

From $V=iR$, equation G.1 can be re-written as;

$$V(t) = V_1 + V(1 - e^{-\frac{t}{R_{12}C_{12}}}) + V(1 - e^{-\frac{t}{R_{Long}C_{Long}}}). \quad 4$$

Assuming that R_{12} / C_{12} and R_{Long} / C_{Long} have sufficiently different time constants, then R_{12} / C_{12} can be found over the first 300 seconds of discharge pause;

$$V(t) = V_1 + V_{300}(1 - e^{-\frac{t}{R_{12}C_{12}}})\Big|_{300\ seconds} \quad 5$$

A model $V(t)$ can then be found by estimating V_{300} and $1/R_{12}C_{12}$. The squared difference between the model $V(t)$ and the experimental $V(t)$ quantifies the curve similarity. The aim is to minimise the sum of the squared differences.

$$Least\ Squares = \sum \left(V(t) - model\ V(t)\right)^2 \quad 6$$

R_{12} is then found from the estimate of V_{300} and C_{12} is then found from $1/R_{12}C_{12}$. R_{Long} is then;

$$R_{Long} = \frac{V_2 - V_1}{i} - R_{12} \quad 7$$

The process will work over any time span, allowing it to be used on batteries with different RC time constants.

D.2 Worked example.

As an example, consider the data set in Table 1. The pause time and voltage rise (V_2-V_1) are experimentally determined. Model $V(t)$ and the difference are respectively found by equations G.5 and G.6. V_{300} and $1/RC$ are estimated and varied to give a local minimum sum of least squares.

		V_{300}	$1/RC$
		0.054	**0.014**
Pause time (secs)	**voltage rise (V_2-V_1)**	**Model $V(t)$**	**Difference^2**
3	0.006	0.002	1.42806E-05
9	0.011	0.006	2.12263E-05
20	0.017	0.013	1.45338E-05
33	0.022	0.020	4.08528E-06
48	0.028	0.026	2.4871E-06
62	0.033	0.031	2.78448E-06
93	0.038	0.039	1.72315E-06
132	0.044	0.045	2.22664E-06
178	0.049	0.050	2.82819E-07
302	0.055	0.053	3.19481E-06
		Least Squares	6.6825E-05

Table 1 Fitting model $V(t)$ to experimental data set.

The voltage rise from V0 to V1 was 0.044 V. At 1 A this gives R_{01} = 44 mΩ. R_{12} is found using equation G.3, R_{12} = 54 mΩ. As $1/RC$ is known, C_{12} = 1322.75 F.

These results are plotted in Figure D.2. The model underestimates the time constant of the RC for the model curve. This only models a single RC pair, including the second RC pair from equation G.4 would require a data set over a greater time.

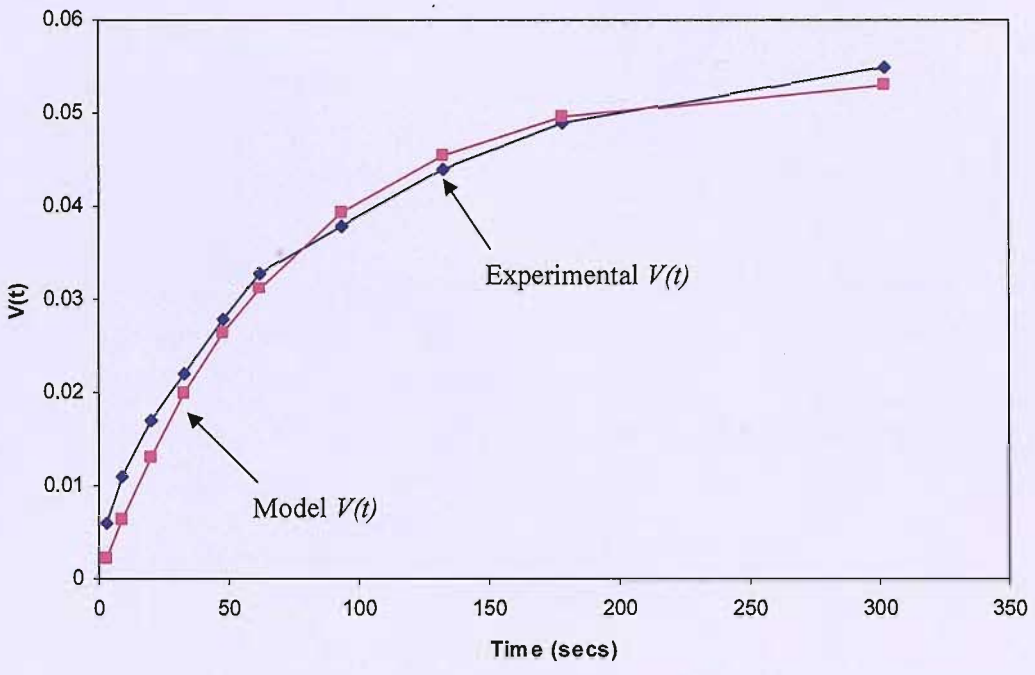

Figure D.2 Experimental *V(t)* and model *V(t)* over the first 300 seconds after 1 A current draw removed.

The experimental results used for this thesis have more data points over the 300 seconds as the measurement resolution was increased.

D.3 References.

Doerffel, D. and S. Abu Sharkh. (2004). "*Rapid test and non-linear model characterisation of solid-state lithium-ion batteries.*" Journal of Power Sources, Vol. 130, Issue1-2, pp. 266 - 274.

APPENDIX D

D.1.1 Modelling a transom stern.

Pashias found that the coupled boundary layer model would sometimes not solve, and attributed it either to the transom stern or the boundary layer approximation (Pashias 2001). Chettleborough found that hull shape profiles with large stern gradients would have a low drag estimate (Chettleborough 2002). D'Alembert's paradox was that a sphere within an invisicid flow would have a net drag force of zero.

An early challenge in this research was to address the modelling of the stern to enable successful boundary layer solution and increase stability of results. The instability caused by the transom stern can be seen when looking at the lengthwise variation of C_P in Figure D.1. With the transom stern the C_P has an large negative peak at the stern, reducing the predicted drag of the shape. The value of the negative C_P peak varied with velocity and panel count.

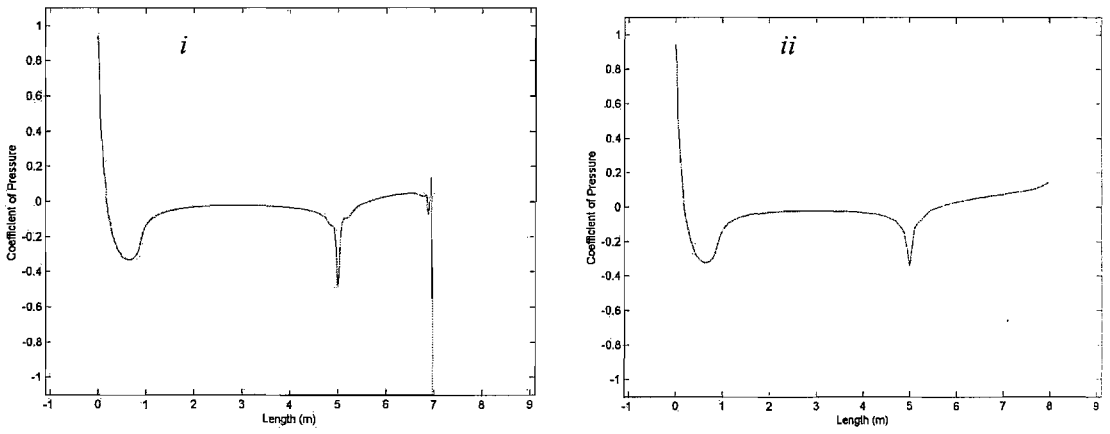

Figure D.1 C_P of Autosub model with i) transom stern and *ii*) tail at a forward velocity of 2ms^{-1}.

When the stern is extruded to a point, forming a tail, the flow is not forced around the sharp geometry change and the negative C_P spike does not occur (Figure D.1*ii*).

On a physical model the flow streamline would separate at the transom stern and form a wake downstream of the body. Extruding the stern to create an artificial tail follows the streamline over the recirculating region and approximate a short wake. This prevents separation and does not require the coupled potential method to either model separation or the C_P around a large geometry change. The altered profile for the hull shape is shown in Figure D.2.

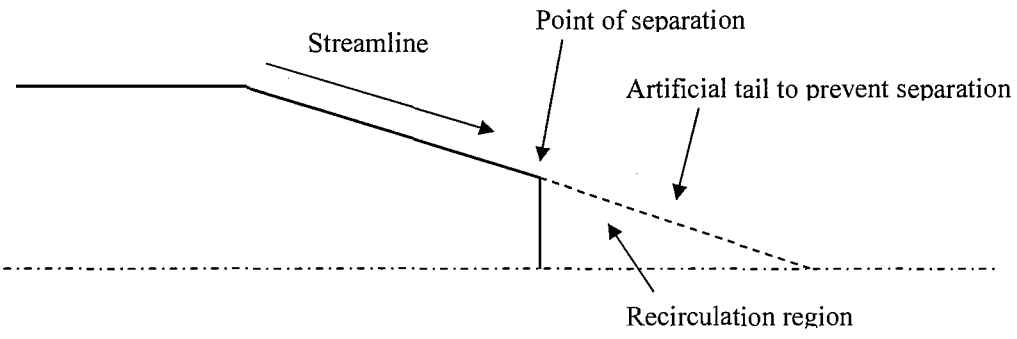

Figure D.2 Profile of an AUV transom stern showing artificial tail.

The drag prediction of a transom stern can be approximated by analysing the C_P over the artificial tail. Although the recirculation region within the separated streamlines is chaotic, the overall pressure acting on the transom stern is relatively constant due to conservation of mass. Therefore as the C_P at the separation point is known, the overall affect on pressure drag can be estimated by integrating C_P over the whole transom stern.

The tail can either be kept a constant radius and vary independently of stern gradient, or kept at the same gradient as the stern. Keeping the tail at a set radius gives a constant increase in volume and surface area for each hull shape variant. A constant and known increase in volume and surface area attributable to the tail, allows a more direct comparison in hull shape drag variation resulting from hull shape changes. Keeping the tail at the same gradient as the stern might be a more faithful model of the wake for a limited range of stern gradients. Both versions are tested and commented on in Chapter 6.

In this thesis the drag predictions include the presence of the tail. The primary reason for the tail was to stabilise the boundary layer model, and this was achieved. Further work should resolve the boundary layer transition modelling error to improve estimation of C_P over the stern and then the tail approximation can be removed.

D.1.2 Thwaites' laminar boundary layer approximation.

Thwaites boundary layer approximation has been shown to give a 5% error in θ and a 10% error in δ^*. This is considered, by Hughes, to be acceptable, and the approximation has been used to model real systems (Hughes 2000). Both the Thwaites and the Head method are based on the momentum integral equation (equation **Error! Reference source not found.Error! Reference source not found.**1).

$$\frac{1}{2}C_F = \frac{\theta}{U}(H+2)\frac{dU}{dx} + \frac{d\theta}{dx} \qquad 1$$

If H and C_F are functions of θ and u then equation 1 can be integrated and an approximation made. To find these functions of H and C_F, consider the thin shear layer equation for a two dimensional, steady, laminar flow which is derived from Bernoulli's equation (equation 2). u is the external velocity local to the surface, not to be confused with the velocity upstream U or the velocity in the x direction, u_x.

$$u_x\frac{\partial u_x}{\partial x} + v\frac{\partial u_x}{\partial y} = -\frac{1}{\rho}\frac{dp}{dx} + v\frac{\partial^2 u_x}{\partial y^2} \qquad 2$$

$$y=0 \qquad \frac{\delta^2 u_x}{\delta y^2} = -\frac{u}{\theta^2}\lambda \qquad \frac{\delta u_x}{\delta y} = -\frac{u}{\theta}l \qquad 3$$

Then apply the above boundary conditions (equation 3) and use equation 2 to give equation 4. It was found that l and H both adhered to a universal function of λ (equation 5) which Thwaites denoted by $l(\lambda)$ and $H(\lambda)$ respectively.

$$\frac{1}{2}C_F = \frac{\tau_w}{\rho u^2} = \frac{v}{u^2}\left(\frac{\delta u}{\delta y}\right)_w = \frac{vl(\lambda)}{u\theta} \qquad 4$$

$$\lambda = \frac{\theta^2}{v}\frac{du}{dx} \qquad 5$$

The mathematical Falkner –Skan transformation can be used to give approximations of $l(\lambda)$ and $H(\lambda)$, allowing equation 1 to be rewritten as equation6 (Cebeci and Bradshaw 1977 pg. 108 - pg.110).

$$\frac{u}{v}\frac{d\theta^2}{dx} = 2\{-[H(\lambda)+2]\lambda + l(\lambda)\} = F(\lambda) \qquad 6$$

Here $F(\lambda)$ is an universal function, for which Thwaites derived an expression that best fit equation 2.

$$F(\lambda) = 0.45 - 6\lambda = 0.45 - 6\frac{\theta^2}{v}\frac{du}{dx} \qquad 7$$

Substituting equation 6 into equation 7, multiplying by u^5 and some rearrangement:

$$\frac{1}{v}\frac{d}{dx}\left(\theta^2 u^6\right) = 0.45u^5 \qquad 8$$

And after integration:

$$\frac{\theta^2 u^6}{v} = 0.45\int_0^x u^5 dx + \left(\theta^2 \frac{u^6}{v}\right) \qquad 9$$

Using non-dimensional numbers defined by:

$$x^* \equiv \frac{x}{L} \qquad u^* = \frac{u}{U} \qquad \mathrm{Re} = \frac{UL}{v}$$

Equation 9 can then be written as:

$$\left(\frac{\theta}{L}\right)^2 \mathrm{Re} = \frac{0.45}{\left(u^*\right)^6}\int_0^x \left(u^*\right)^5 dx + \left(\frac{\theta}{L}\right)^2 \mathrm{Re}\left(\frac{u_0^*}{u^*}\right)^6 \qquad 10$$

In calculations starting from a stagnation point flow the last term becomes zero as $u_0^* = 0$ at the 1st station, in this case equation 10 becomes equation 11.

$$\left(\frac{\theta}{L}\right)^2 \mathrm{Re} = \frac{0.075}{\left(\frac{du^*}{dx^*}\right)_0} \qquad 11$$

Once θ is calculated for a specific external velocity (u_e), the boundary layer parameters H and C_f can be determined: This is while the parameter λ stays within -0.1 and 0.1. Outside these limits the laminar boundary layer becomes unstable.

For $0 \le \lambda \le 0.1$

$$l = 0.22 + 1.57\lambda - 1.85\lambda^2$$

$$H = 2.61 + 3.75\lambda - 5.24\lambda^2 \qquad 12$$

For $-0.1 \le \lambda \le 0$

$$l = 0.22 + 1.402\lambda + \frac{0.018\lambda}{0.107 + \lambda}$$

$$H = \frac{0.0731}{0.14 + \lambda} + 2.088 \qquad 13$$

D.1.3 Head's turbulent boundary layer approximation.

In the Palisupan boundary layer approximation the Thwaites' approximation is run first, then a transition prediction is made, then Head's approximation for turbulent flow initiates and C_f is predicted.

Head presented an integral method for modelling the growth of a turbulent boundary layer assuming that the dimensionless entrainment velocity v_E/u is a function of the shape factor, H_1. The entrainment velocity is the component of the velocity normal to the streamline at the edge of the boundary layer (Cebeci and Bradshaw 1977 pg. 54). Where H_1 is defined as equation 14.

$$H_1 = \frac{\delta - \delta^*}{\theta} \qquad 14$$

And the dimensionless entrainment velocity is:

$$\frac{v_E}{u} = \frac{1}{u}\frac{d}{dx}\left[u\left(\delta - \delta^*\right)\right] \qquad 15$$

Using equation 14, equation 15 can be written as:

$$uF = \frac{d}{dx}\left[u\theta H_1\right] \qquad 16$$

Where F is a best fit function dependant on H_1, and H_1 is assumed to be a best fit function (G) of H. The functions F and G are determined experimentally:

$$F = 0.036\left(H_1 - 3.0\right)^{-0.6169} \qquad 17$$

$$G = 0.8234(H - 1.1)^{-1.287} + 3.3 \qquad \text{When } H \leq 1.6 \qquad 18$$

$$G = 1.55001(H - 0.6778)^{-3.064} + 3.3 \qquad \text{When } H \geq 1.6 \qquad 19$$

From the momentum integral equation (equation 1) it can be observed that there are three unknowns; θ, H and C_F for a given external velocity distribution. Using equations 16 to19 will show a relationship between θ and H. Head used the coefficient of friction law given by Ludwieg and Tillmann (Ludwieg and Tillmann 1949) to relate θ and H to C_F.

Where

$$C_F = 0.246 \times 10^{-0.678H} R_\theta^{-0.268} \qquad R_\theta = \frac{\theta u_e}{\nu} \; R_\theta = \frac{\theta u}{\nu} \qquad 20$$

Thus there are two ordinary differential equations that can be solved numerically for a specified external velocity distribution. This is solved iteratively, with an initial guess of θ and H that gets updated with each iteration.

D.2 References.

Cebeci, T. and P. Bradshaw. (1977). "*Momentum transfer in boundary layers.*" Hemisphere Publishing Corporation,

Chettleborough, P. (2002). "*Resistance and Propulsion of the Autonomous Underwater Vehicle Autosub.*" **Bachelor of Engineering**, University of Southampton, School of Engineering Sciences, Supervisor: Hearn and G. E.

Hughes, A. W. (2000 April). "*Investigation of Tip-Driven Thruster and Waterjet Propulsion Systems.*" **Doctor of Philosophy**, University of Southampton, Faculty of Applied Science and Engineering, Supervisor: S. R. Turnock.

Ludwieg, H. and W. Tillmann. (1949). "*Investigations of the wall-shearing stress in turbulent boundary layers.*" NACA report TM 1285.

Pashias, C. (2001). "*Shape optimisation of a long range AUV using Computational Fluid Dynamics.*" **Bachelor of Engineering**, University of Southampton, School of Engineering Sciences, Supervisor: S. R. Turnock.

APPENDIX E

Matlab arrangement code.

This is the code used to automate parts of the design method. There are three functions. The first generates a matrix of all the possible unique arrangements for a given number of subsystems. This can be time consuming so the output is saved as a combination file for later reference.

The code in appendix F generates the possible arrangement combinations within a matrix. The subsystem arrangement number is the row number within the matrix. Each subsystem is assigned a matrix column, and the number within the arrangement indicates the position of that subsystem.

For example, three subsystems would have a matrix of 3 columns by 27. [111, 112, 113.. etc] This is then filtered for any rows with repeated numbers to give 3! final combinations. The final matrix for three subsystems is shown in Table F.1. Arrangement 2 would mean that the three subsystems are arranged in the order, 2 3 1.

3	2	1
2	3	1
3	1	2
1	3	2
2	1	3
1	2	3

Table A.1 Final matrix for three subsystems.

Program 2 is a run file that assigns all the subsystems a place according to the combination file and inputs them into the third file.

Program 3 processes the body of the work described in the presented design method. It assesses the arrangement size, volume and mass. Neutral buoyancy if verified, then the foam lever arm for hydrostatic balance is created. A parallel middle body hull shape is fit over the arrangements and the volume of foam estimated. The program filters for any error flags that were raised during the program and then outputs a list of arrangements that are possible.

F.1 Program 1

```
% this function creates the unique arrangement list. It is not written efficiency, so will take some
time to run. The repmat function allowed faster solution of big matricies than nested for loops
clear all
N=8; %N is the number of subsystems
M=N-1;
M2=M/2;
M3=M/3;
M4=M/4;
M5=M/5;
M6=M/6;
M7=M/7; %repeat columns for each row of N
```

```
A(M7,M)=zeros;
C=1
n=1
%repeat this block of array B for N-3, then end on the last
%1
bit = 1:M;
A(1:M,C)=bit
A=repmat(A,M,1);
clear B
B(1:length(A)) = 1;
B((length(A)/M)+1:(length(A)/M2))=2;
B((length(A)/M2)+1:(length(A)/M3))=3;
B((length(A)/M3)+1:(length(A)/M4))=4;
B((length(A)/M4)+1:(length(A)/M5))=5;
B((length(A)/M5+1):(length(A)/M6))=6;
B((length(A)/M6+1):(length(A)))=7;
C=C+1
A(:,C)=B(:);

%2
A=repmat(A,M,1);
clear B
B(1:length(A)) = 1;
B((length(A)/M)+1:(length(A)/M2))=2;
B((length(A)/M2)+1:(length(A)/M3))=3;
B((length(A)/M3)+1:(length(A)/M4))=4;
B((length(A)/M4)+1:(length(A)/M5))=5;
B((length(A)/M5+1):(length(A)/M6))=6;
B((length(A)/M6+1):(length(A)))=7;
C=C+1
A(:,C)=B(:);

%3
A=repmat(A,M,1);
clear B
B(1:length(A)) = 1;
B((length(A)/M)+1:(length(A)/M2))=2;
B((length(A)/M2)+1:(length(A)/M3))=3;
B((length(A)/M3)+1:(length(A)/M4))=4;
```

```
B((length(A)/M4)+1:(length(A)/M5))=5;
B((length(A)/M5+1):(length(A)/M6))=6;
B((length(A)/M6+1):(length(A)))=7;
C=C+1
A(:,C)=B(:);

%4
A=repmat(A,M,1);
clear B
B(1:length(A)) = 1;
B((length(A)/M)+1:(length(A)/M2))=2;
B((length(A)/M2)+1:(length(A)/M3))=3;
B((length(A)/M3)+1:(length(A)/M4))=4;
B((length(A)/M4)+1:(length(A)/M5))=5;
B((length(A)/M5+1):(length(A)/M6))=6;
B((length(A)/M6+1):(length(A)))=7;
C=C+1
A(:,C)=B(:);

%5
A=repmat(A,M,1);
clear B
B(1:length(A)) = 1;
B((length(A)/M)+1:(length(A)/M2))=2;
B((length(A)/M2)+1:(length(A)/M3))=3;
B((length(A)/M3)+1:(length(A)/M4))=4;
B((length(A)/M4)+1:(length(A)/M5))=5;
B((length(A)/M5+1):(length(A)/M6))=6;
B((length(A)/M6+1):(length(A)))=7;
C=C+1
A(:,C)=B(:);

%6
A=repmat(A,M,1);
clear B
B(1:length(A)) = 1;
n=n+1
B((length(A)/M)+1:(length(A)/M2))=2;
n=n+1
```

```
B((length(A)/M2)+1:(length(A)/M3))=3;
n=n+1
B((length(A)/M3)+1:(length(A)/M4))=4;
n=n+1
B((length(A)/M4)+1:(length(A)/M5))=5;
n=n+1
B((length(A)/M5+1):(length(A)/M6))=6;
n=n+1
B((length(A)/M6+1):(length(A)))=7;
n=n+1
C=C+1
A(:,C)=B(:);

% now start comparing and removing rows with duplicate numbers
Arrangement_combos=A;
x=0;
y=0;
m=1;
for x=1:M-1
   for y=x+1:M
      m=1;
      n=1;
   Consider1 =Arrangement_combos(:,x);
   Consider2 =Arrangement_combos(:,y);
   ConsiderLength=length(Consider1);
      for m =1:ConsiderLength
         ConsiderLength=length(Consider1);
         if Consider1(m)==Consider2(m);
            Arrangement_combos(m,1)=0;
         else
            m=m+1
         end
      end
   end
end
n=1;
clear m
ArrayLength=length(Arrangement_combos);
for m =1:ArrayLength
```

```
  ArrayLength=length(Arrangement_combos);
  if Arrangement_combos(m,1)==0
    m=m+1;
    else
    Keepers(n,:)=Arrangement_combos(m,:);
    n=n+1
    m=m+1;
  end
end
Keepers
length(Arrangement_combos)
length(Keepers)

%Create Combos.txt for other programs to use.
f=fopen('combos.txt','at'); % file ID = f
  fprintf(f,'%g\t',Keepers);
fclose(f);
```

F.2 Program 2

This calls the combos.txt and applies a subsystem to each column for every arrangement. Then the third program is called to analyse that arrangement.

```
Arrangement_combos=dlmread('combos_this_run.txt');
for q=1:length(Arrangement_combos)
  This_arrangement=Arrangement_combos(q,:);
  ADCP300kHz = This_arrangement(1);
  Altimeter = This_arrangement(2);
  CTD = This_arrangement(3);
  WetlabsBB2F = This_arrangement(4);
  Sidescan = This_arrangement(5);
  Pressure_vessel = This_arrangement(6);
  Energy = This_arrangement(7);
  Motor = This_arrangement(8);

Hydrodynamic_filter_Deep(ADCP300kHz,Altimeter,CTD,WetlabsBB2F,Sidescan,Pressure_vessel,
Energy,Motor);
end
```

F.3 Program 3

This analyses the arrangement of subsystems given by the function in program 2. Each subsystem's properties are specified in this file, and are the only required change when altering a subsystem.

```
% this is to Automate the hydrodynamic filtering of the AUv arrangements. 1st step -> define %hull
shape around sub-systems. 2nd step -> check for sub-systems which protude beyond %the hull
shape. 3rd step -> Find trapezoidal available foam volume. 4th step -> filter %arrangements.
%This file is to hydrostatically balance an AUV internals from a minimum number of %subsystems.
The idea is to have a matrix of N rows, where N is the number of %subsystems. The x position of
each component within the vehicle can then be calculated %and placed into a vector of size N.
The COG, COB and max Radius can be found after %the matrix and vector have been solved.

function [ADCP300kHz,Altimeter,CTD,WetlabsBB2F,Sidescan,Pressure_vessel,Energy,Motor] =
hydrodynamic_filter_Deep(ADCP300kHz,Altimeter,CTD,WetlabsBB2F,Sidescan,Pressure_vessel,
Energy,Motor);
Run_code= [ADCP300kHz,Altimeter,CTD,WetlabsBB2F,Sidescan,Pressure_vessel,Energy,Motor];

Rho_water=1025;
Rho_foam=580;
N=8;
clear Sub_systems;
clear ID;
clear a;

%matrix where each row is a subsystem (n,Mass,Volume,Length,Radius,breath,height)
%y and z are only non-zero if shape is not cylindrical)
%___________[N  mass  volume  L    rad  b h]
Sub_systems=[ADCP300kHz        14.5 0.0029 0.228 0.0 0.228 0.211;
    Altimeter          2.60 0.0013 0.180 0.0480 0 0;              %altimeter
    CTD                20.7 0.0085 0.520 0.070 0 0;               %CTD
    WetlabsBB2F        1.30 0.00054 0.256 0.0315 0 0;             %Wetlabs backscatter
    Sidescan           7.30 0.00225 0.0 0.0 0.0 0.0;              %Length set to zero to simulate
mounting alongside vehicle.
    Pressure_vessel    189.095 0.1431 1.271 0.2002 0 0;           %pressure vessel
    Energy             223.3224 0.11394 0.485147 0 0.485147 0.485147;  %energy
    Motor              28.0 0.0096 0.1400 0.1500 0 0];            %motor
N=size(Sub_systems,1);
```

```
% Find any non cylindrical subsystems and place bounding box about them
for a =1:N-1
   if Sub_systems(a,6)>0;
      Sub_systems(a,5)=((Sub_systems(a,6)^2+Sub_systems(a,7)^2)^(1/2))/2;
   else
      Sub_systems(a,5)=Sub_systems(a,5);
   end
end

ID(ADCP300kHz)={'ADCP300kHz'};
ID(Altimeter)={'Altimeter'};
ID(CTD)={'CTD'};
ID(WetlabsBB2F)={'WetlabsBB2F'};
ID(Sidescan)={'Sidescan'};
ID(Pressure_vessel)={'Pressure_vessel'};
ID(Energy)={'Energy'};
ID(Motor)={'Motor'};
ID=sortrows(ID);

Sub_systems=sortrows(Sub_systems);
X_position_sub_system_centre=zeros(N,1);
X_position_sub_system_interface=zeros(N,1);

% Find the lengthwise position of each subsystem
n=1;
X_temp=0.0;
while n<=N
   X_position_sub_system_centre(n)=Sub_systems(n,4)/2 + X_temp;
   X_position_sub_system_interface(n) = X_position_sub_system_centre(n) + Sub_systems(n,4) /
2;
   X_temp = X_position_sub_system_centre(n) + Sub_systems(n,4) / 2;
   n=n+1;
end
clear n

% now have to find the maximum radius and moments of the sub_systems
Max_temp = max(Sub_systems);
R_max = Max_temp(5);
```

```
Mass_sub_systems = sum(Sub_systems(:,2))
Volume_sub_systems = sum(Sub_systems(:,3))
Buoyancy_sub_systems = -((Rho_water * Volume_sub_systems) - Mass_sub_systems);
Mass_moment_without_foam = sum( Sub_systems(:,2) .* X_position_sub_system_centre );
Volume_moment_without_foam = sum( Sub_systems(:,3) .*X_position_sub_system_centre);

CoG_without_foam = Mass_moment_without_foam / Mass_sub_systems;
CoB_without_foam = Volume_moment_without_foam / Volume_sub_systems;

%now to find the amount of foam required
Volume_foam = Buoyancy_sub_systems / (Rho_water-Rho_foam);
Mass_foam = Volume_foam*Rho_foam;

%total mass and volume of the AUV
Mass_AUV = Mass_sub_systems + Mass_foam;
Volume_AUV = Volume_sub_systems + Volume_foam;
Buoyancy_AUV = (Volume_AUV * Rho_water) - Mass_AUV;

%now to find the position of the foam to balance the shape
X_foam = (Mass_AUV * Volume_moment_without_foam - Volume_AUV *
Mass_moment_without_foam) / (Mass_foam * Volume_AUV - Volume_foam * Mass_AUV);

Length_AUV = sum(Sub_systems(:,4));

Mass_moment_AUV = sum( Sub_systems(:,2) .* X_position_sub_system_centre ) + Mass_foam *
X_foam;
Volume_moment_AUV = sum( Sub_systems(:,3) .* X_position_sub_system_centre ) +
Volume_foam * X_foam;
CoG_AUV = Mass_moment_AUV / Mass_AUV;
CoB_AUV = Volume_moment_AUV / Volume_AUV;

%knowing the position of the CoG_foam, where is it within the shape and can i set it to %detect
collision with maximum radius subsystem.  I need it to report back the sub-system %where X_foam
< Xposition

X_R_max_row = find(Sub_systems(:,5) == R_max)
if X_R_max_row <= 1
   Boundary_fore = 0;
else
```

```
   Boundary_fore = X_position_sub_system_interface(X_R_max_row-1);
end
Boundary_aft = X_position_sub_system_interface(X_R_max_row);


% Hull shape arrays:  Slot Number(N), Interfacepoint, Radius, Hull Radius, Error?
Stern_gradient= (Sub_systems(N,5)- R_max) / (Length_AUV - Boundary_aft);
Bow_end= Boundary_fore;
Bow_majorA= Boundary_fore;
%Y_offset= Sub_systems(1,5);
Y_offset= 0.0;
Bow_minorB= R_max-Y_offset;

%now to find the available volume for foam. need to make the array big enough such that all %the
subsystems can fit within.
Big_array_X(N*10+1)=zeros;
Big_array_SS_radius(N*10+1)=zeros;
Big_array_hull_radius(N*10+1)=zeros;
Big_array_volume(N*10+1)=zeros;
Big_array_moment(N*10+1)=zeros;
i=1;
   N_start= 0.0;
   N_end= X_position_sub_system_interface(1);
   if N_start==N_end;
      Big_array_X((i:i+10))= N_end;
   else
      H_step= (N_end-N_start)/10;
      Big_array_X((i:i+10))= N_start:H_step:N_end;
   end
   Big_array_SS_radius((i:i+10))= Sub_systems(1,5);
i=i+11;

for n= 2:N
   N_start= X_position_sub_system_interface(n-1);
   N_end= X_position_sub_system_interface(n);
   if N_start==N_end;
      Big_array_X((i:i+10))= N_end;
   else
      H_step= (N_end-N_start)/10;
```

```
    Big_array_X((i:i+10))= N_start:H_step:N_end;
  end
  Big_array_SS_radius((i:i+10))= Sub_systems(n,5);
  i=i+11;
end

clear i

%now to find the hull radius on a row by row basis
I_R_max_row = find(Big_array_SS_radius(:) == R_max);
for i=1:I_R_max_row
  Big_array_hull_radius(i)= ((Bow_minorB^2 * (1 - ((Big_array_X(i) - Bow_end) ^2 / (Bow_majorA
^2) ))) ^ 0.5) + Y_offset;
end

for i=I_R_max_row:I_R_max_row+10;
  Big_array_hull_radius(i)= R_max;
end

for i=I_R_max_row+10:length(Big_array_X);
  Big_array_hull_radius(i)= (Big_array_X(i) - Boundary_aft) * Stern_gradient + R_max;
end
clear i

% now to find volume available
for i=2:length(Big_array_X)
  if Big_array_SS_radius(i) > Big_array_hull_radius(i)
    Big_array_volume(i)= 0.0;
  else
    Big_array_volume(i)= pi * (Big_array_hull_radius(i)^2 - Big_array_SS_radius(i)^2) *
(Big_array_X(i) - Big_array_X(i-1));
  end
end

Buoyancy_volume= sum(Big_array_volume);
Big_array_moment= Big_array_X .* Big_array_volume;
Total_moment= sum(Big_array_moment);

Buoyancy_centre_of_buoyancy= Total_moment / Buoyancy_volume;
```

```
Enough_volume_for_foam= Buoyancy_volume - Volume_foam;
Hydrostatic_balance= Buoyancy_centre_of_buoyancy - X_foam;

f=fopen('hydrostatic.txt','at'); % file ID = f
fprintf(f,'##########################################\n','a');
fprintf(f,'%g\n',Run_code,'a');
fprintf(f,'\n'); % Text break
fprintf(f,'%s\n',ID{:});
fprintf(f,'\n'); % Text break
fprintf(f,'Centre of Gravity of each sub system in meters from bow\n');
temp=X_position_sub_system_centre';
fprintf(f,'%6.3f\n',temp);
fprintf(f,'\n'); % Text break
fprintf(f,'X position of sub-system interface in meters from bow\n');
temp=X_position_sub_system_interface';
fprintf(f,'%6.3f\n',temp);
fprintf(f,'\n'); % Text break
fprintf(f,'Length of AUV =\n %6.3f\n',Length_AUV');
fprintf(f,'Maximum radius =\n %6.3f\n',R_max');
fprintf(f,'Maximum radius occurs between \n %6.3f \n %6.3f \n',Boundary_fore,Boundary_aft);
fprintf(f,'Mass of Foam =\n %6.3f\n',Mass_foam);
fprintf(f,'Volume of foam =\n %6.3f\n',Volume_foam);
fprintf(f,'Volume available for foam =\n %6.3f\n',Buoyancy_volume);
fprintf(f,'Total AUV mass =\n %6.3f\n',Mass_AUV);
fprintf(f,'Total AUV volume =\n %6.3f\n',Volume_AUV);
fprintf(f,'Total AUV Centre of Buoyancy =\n %6.3f\n',CoB_AUV);
fprintf(f,'Total AUV Centre of Gravity =\n %6.3f\n',CoG_AUV);
fprintf(f,'Foam CoG occurs at \n %3.3f \n',X_foam);
fprintf(f,'Volume CoG occurs at \n %3.3f \n',Buoyancy_centre_of_buoyancy);

if (Boundary_fore <= X_foam) & (X_foam <= Boundary_aft);
   fprintf(f, 'ERROR: Foam CoG occurs at the same place as maximum radius at sub-system
number\n %f \n', Sub_systems(X_R_max_row));
elseif (Length_AUV < X_foam) | (X_foam < 0.0);
   fprintf(f, 'ERROR: Foam CoG occurs outside the AUV body\n')
   fprintf(f,'\n'); % Text break
else
   X_temp = find(Sub_systems(:,5) <= R_max);
   X_foam_sub_system = X_temp(1);
```

```
    fprintf(f, 'Foam CoG occurs at sub-system \n %3f',X_foam_sub_system);
    fprintf(f,'\n'); % Text break
end
fclose(f)
end
```